MANOEUVRING PREDICTION OF FOIL-ASSISTED VESSELS: A Mathematical Model Assisted by CFD

DAVID A. FIDALGO DOMINGOS

MANOEUVRING PREDICTION OF FOIL-ASSISTED VESSELS:
A MATHEMATICAL MODEL ASSISTED BY CFD

DAVID A. FIDALGO DOMINGOS

FEBRUARY, 2019

TO OBTAIN THE DEGREE OF MASTER OF SCIENCE IN MARITIME TECHNOLOGY
AT DELFT UNIVERSITY OF TECHNOLOGY

TO BE DEFENDED PUBLICLY ON FRIDAY, FEBRUARY 22ND, 2019 AT 10:45 A.M.

THESIS COMMITTEE:

PROF. DR. IR. A.P. VAN'T VEER
DELFT UNIVERSITY OF TECHNOLOGY, PROFESSOR OF SHIP HYDROMECHANICS

IR. M. BONCI (SUPERVISOR)
DELFT UNIVERSITY OF TECHNOLOGY, PHD. CANDIDATE, SHIP HYDROMECHANICS

IR. V. JACOBS (SUPERVISOR)
VAN OOSSANEN NAVAL ARCHITECTS, HYDRODYNAMICIST

DR. IR. A. VRIJDAG
DELFT UNIVERSITY OF TECHNOLOGY, ASSISTANT PROFESSOR OF SHIP DESIGN

DELFT UNIVERSITY OF TECHNOLOGY
FACULTY OF MECHANICAL, MARITIME AND MATERIALS ENGINEERING
SHIP HYDROMECHANICS AND STRUCTURES

ABSTRACT

The competitiveness of the maritime sector together with energetic and environmental challenges have promoted a demand for **more efficient marine vehicles**. In response to this, research campaigns have been conducted, with the aim of developing new technologies. One of these technologies is the application of **hydrofoils** (*e.g.:* a Hull Vane) to marine vehicles. Although these allow a significant increase in efficiency, challenges and concerns rise due to their influence on seakeeping and **manoeuvring** performance. As a starting point, for a better understanding of the impact of hydrofoils on the dynamic behaviour of vessels, this research was focused on the:

"Development of knowledge, methodologies and tools to perform manoeuvring predictions of vessels equipped with a Hull Vane."

For this, ***Virtual Captive Tests*** *(VCT)* were combined with a ***4 DOF*** **manoeuvring model**, to perform manoeuvring predictions of vessels equipped with a **Hull Vane**. The convergence of the ***CFD*** solutions, for *VCT*, proved to be a challenging task with a lot of room for improvement. This is caused by the presence of complex flow features, *e.g.*: fore and aft-body vortices. In the end, an **Adaptive Grid Refinement** (*AGR*) algorithm, allowed an equilibrium between computational cost and discretization uncertainties.

Two types of *VCT* were performed and compared: Oblique Towing Tests *(OTT)* and Planar Motion Mechanism (*PMM)* tests. Due to the strong non-linear nature of hydrodynamic forces and moments, a ***Discrete Spectral Method*** was developed for the analysis of the *PMM* tests. On one hand, *PMM* tests represent an advantage in the determination of unsteady forces/moments compared to semi-empirical models. On the other hand, virtual *PMM* tests are more complex and more vulnerable to sources of errors, *e.g.:* flow memory effects and higher numerical residuals. At last, this research showed that the gain in accuracy in the determination of unsteady effects, hardly compensates the loss in accuracy in the determination of steady effects. Furthermore, it was shown that the **uncertainties** of captive tests can be amplified by the manoeuvring model, which can significantly penalize the precision of manoeuvring predictions. For the **validation** of manoeuvring predictions, a 25 m **patrol vessel** equipped with a Hull Vane (*RPA8*) was considered, for which **experimental data** is available. By comparing the results of the manoeuvring prediction with the experimental ones, it was shown that the manoeuvring prediction process over-estimates the **course stability**. Resulting in 20% (≈20 m) over-estimation of the 35° **turning circle** diameter and 50% (≈ 0.4°) under-estimation of the 3°-3° **zig-zag** overshoot. Regarding the impact of the Hull Vane on the manoeuvring performance, it was concluded that the Hull Vane increases the course stability of *RPA8,* leading to 7% increase of the 35° turning circle diameter and 18% decrease of 10°-10° zig-zag yaw overshoot. This is the result of a combination between: **interaction phenomena**, an increase in yaw damping caused by the Hull Vane struts and an increase in *Munk* moment caused by the change in dynamic trim. Therefore, the extrapolation of these results for other vessels is not trivial, due to the interaction between these effects.

With the aim of reducing the cost of manoeuvring assessments, a ***Linear Pressure Distribution Method*** *(LPDM)* was developed, to model the effects of the Hull Vane on manoeuvring. This model was successfully validated, using the results of an integrated approach, *i.e.:* **hydrodynamic coefficients** determined using captive tests with the Hull Vane. The results show about 1% (≈1 m) difference in the prediction of the dimensions of a 35° turning circle, and less than 11% (≈ 0.3°) difference in the prediction of the 10°-10° zig-zag yaw overshoot.

Finally, this research provides knowledge, tools and methodologies for a better understanding of the dynamic behaviour of **foil-assisted vessels**, particularly vessels equipped with a Hull Vane. The results of this research provide a solid foundation for further research in this field.

ACKNOWLEDGEMENTS

When I was 19, I moved to Lisbon to study *Marine Engineering and Naval Architecture* at *Instituto Superior Técnico.* At that time, my knowledge about vessels and maritime structures was no more than the *Archimedes Principle.* Six years later, here I am, writing the final words to obtain the *Master's Degree* in *Maritime Technology,* at exactly 2219 km from where everything started, in *Suela (Lisbon)*.

In first place, I want to thank to my parents, Alberto and Orlanda, which have made the impossible possible, to ensure that I could get here. To my sister, *Liliana,* for being always there for me, even when my parents can't, for her limitless patience to correct almost every important document I write and, of course, for letting me use her *Netflix* account. Getting here would have been hardy possible without the unconditional support of my family.

Thanks, *Raquel*, for all the special moments, being always present, limitless patience and love. Aldo, for those "30 min. skype calls" which always end up in endless conversations and, the fantastic years as flat-mates together with *Botas* e *Labisa*. *"Afilhado" Miguel*, for being my right hand in anything. *Diva, Lenny* and *Ticha* for the "family" weekends in *Delft. Raffo, Fede* and *"Big D"* for those fantastic movie nights and delicious food. *Luigi* for the geography lessons, and for all the parties together. Furthermore, a big "thank you" to the rest of my friends in *Portugal* and in *The Netherlands,* who made this journey full of the unforgettable moments.

I want to thank *Matteo,* my supervisor at *TUDelft,* for his guidance, dedication and transmission of knowledge. *Prof. Riaan van't Veer,* the coordinator of this thesis, for his important feedback over the course of the research. *Nico van der Kolk* for his interest and initial support. And finally, thank you *Dr. ir. A. Vrijdag,* for accepting to be part of the graduation committee.

A special thanks to my supervisor at *Van Oossanen, Vincent,* for his help, dedication and critical thinking. I also want to thank him and *Alie* for working late hours, without them I would still be writing this thesis. I want to thank *Niels Moerke* for this fantastic opportunity, *Mark Peter* for the support, dedication and interesting conversations, and *Kasper Uithof* for guiding me in the beginning of this project. The support and knowledge of *Van Oossanen Naval Architects* were fundamental to get here, thank you for making me feel at home.

I also want to thank *Serge Toxopeus* for his interest and willingness to help. His *Phd.* work was a good starting point for this research.

To finalize, I want to thank to all the people who have significantly contributed for my education. I dedicate this research to you.

The result of this journey is not just some extra knowledge beyond the *Archimedes Principle,* but also unforgettable moments and very special friendships. This is not the end of the student life, just the beginning.

I hope this research inspires you.

"Nobody who ever gave his best regretted it."

-George Halas

February 12th, 2019

David A. Fidalgo Domingos

TABLE OF CONTENTS

LIST OF FIGURES

LIST OF TABLES

NOMENCLATURE

a_H	Rudder-hull interaction fraction	$[-]$
C_B	Block Coefficient	$[-]$
c_d	Wing section drag coefficient	$[-]$
C_D	Finite wing drag coefficient	$[-]$
C_l	Wing section lift coefficient	$[-]$
C_L	Finite wing lift coefficient	$[-]$
C_Y^{R0}	Rudders' loading coefficient	$[-]$
c_R	Mean rudder chord	$[m]$
D	Finite wing drag	$[N]$
D_P	Propeller Diameter	$[m]$
D_R	Propeller slipstream diameter at the rudder location	$[m]$
e	Span efficiency factor	$[-]$
e_R	Mean distance between the rudder leading edge and the aft of the vessel	$[m]$.
F_n	Froude Number	$[-]$
g	Gravitational acceleration (constant)	9.81 $[m/s^2]$
GM	Metacentric height	$[m]$
J	Propeller advance ratio	$[-]$
K_Q	Propeller torque coefficient	$[-]$
K_T	Propeller thrust coefficient	$[-]$
K^{HD}	Roll moment due to hydrodynamic forces acting on the hull	$[N.m]$
K^{HS}	Roll moment due to hydrostatic forces (righting moment)	$[N.m]$
K_p	Number of propellers	$[-]$
L	Finite wing lift	$[N]$
M_n	Mach number	$[-]$
n_p	Propeller rate	$[1/s]$

p, q, r	Roll, pitch and yaw rates, respectively	$[rad/s]$
Q	Torque required by the propeller	$[N.m]$
R	Bare Hull straight ahead resistance	$[N]$
R_n	Reynolds number	$[-]$
S	Wing lateral projected area	$[m^2]$
S^S	Strut lateral projected area	$[m^2]$
S^{HV}	Hull Vane horizontal projected area	$[m^2]$
t	Propeller thrust deduction factor	$[-]$
t_R	Steering resistance deduction factor	$[-]$
T_{accel}	Acceleration period of a *CFD* computation	$[s]$.
T	Axial thrust produced by the propulsion system	$[N]$
T_d	Vessel's draft	$[m]$.
u, v, w	Advance, sway and heave speeds, respectively	$[m/s]$
u_w	Maximum flow velocity due to actuator disk	$[m/s]$
U	Freestream velocity	$[m/s]$
V_s	Ship reference speed (often advance speed)	$[m/s]$
V_a	Propeller inflow speed	$[m/s]$
V_{prop}	Flow speed at the propeller plane	$[m/s]$
V_2	Maximum velocity of the propeller slipstream	$[m/s]$
V_r	Propeller slipstream speed at the rudder location	$[m/s]$
x_{RH}	Rudder-hull interaction force application abscissa	$[m]$
(x^P, y^P, z^P)	Coordinates of the propeller(s) in the non-inertial frame of reference (x, y, z)	$[m]$
(x^R, y^R, z^R)	Coordinates of the rudders' stock in the non-inertial frame of reference (x, y, z)	$[m]$
(x^S, y^S, z^S)	Coordinates of the centroid of the strut(s) in the non-inertial frame of reference (x, y, z)	$[m]$
(x^{HV}, y^{HV}, z^{HV})	Coordinates of the centroid of the Hull Vane horizontal part in the non-inertial frame of reference (x, y, z)	$[m]$
X, Y, N, K	Total surge, sway, yaw and roll forces/moments, respectively	$[N]$ and $[N.m]$,

X^E, Y^E, N^E, K^E	Surge, sway, yaw and roll excitation forces/moments, respectively	$[N]$ and $[N.m]$
X^H, Y^H, N^H, K^H	Surge, sway, yaw and roll forces/moments acting on the hull, respectively	$[N]$ and $[N.m]$
X^P, N^P	Total surge force and yaw moment developed by the propulsion system, respectively	$[N]$ and $[N.m]$
$X^{P,PS}, X^{P,SB}$	Surge force of the propeller at the PS and SB respectively (twin screw)	$[N]$
X^R, Y^R, N^R, K^R	Total steering forces/moments in surge, sway, yaw and roll, respectively	$[N]$ and $[N.m]$
X^{R0}, Y^{R0}	Pure rudder force in surge and sway direction, respectively	$[N]$
$X^{R,PS}, X^{R,SB}$	Surge force of the rudder at the PS and SB respectively	$[N]$
w_f	Wake fraction [-]	$[-]$
α	Angle of attack	[°]
α_0	Hydrodynamic inflow angle	[°]
α_E	Effective rudder angle	[°]
β	Drift angle	[°]
$\beta_p, \beta_R, \beta_S$	Propeller, rudder and struts geometric inflow angles	[°]
δ	Rudder deflection	[°]
Δ	Displacement	$[kg]$
Δt	Time step	[s]
ϕ, ψ, θ	Heel, heading and trim angles, respectively	[°]
θ^S	Shaft angle	[°]
η_o	Open water efficiency of propellers	$[-]$
γ_R	Flow straightening factor	$[-]$
Γ	Irrotational vortex strength	$[m^2/s]$
Γ_R	Hydrodynamic inflow angle at zero geometric inflow angle	$[rad]$
Γ_s	Rudder to strut flow bending coefficient	$[-]$
ρ	Water density (constant)	1025 $[kg/m^3]$

ACRONYMS

ADT	Actuator Disk Theory
AGR	Adaptive Grid Refinement
AoA	Angle of Attack
AR	Aspect Ratio
A_{pp}, F_{pp}	Aft and forward perpendiculars, relative to the *CoG [m]*
CoG	Centre of gravity
CFD	Computational Fluid Dynamics
DOF	Degree(s) of Freedom
EFD	Experimental Fluid Dynamics
$FDHF$	Fast Displacement Hull Form, see [1].
FFT	Fast Fourier Transform
HTC	Hamburg Test Case
IMO	International Maritime Organization
LAR	Low Aspect Ratio
$LARWT$	Low Aspect Ratio Wing Theory
LLT	Lifting Line Theory
$LPDM$	Linear Pressure Distribution Method
ODE	Ordinary Differential Equations
OTT	Oblique Towing Test(s)
PMM	Planar Motion Mechanism
PS, SB	Portside and Starboard
$RANSE$	Reynolds Averaged Navier-Stokes Equations
RAT	Rotating Arm Test
$RPA8$	25m Patrol Vessel equipped with a Hull Vane
rpm	Rotations per minute

1. INTRODUCTION

1.1 MOTIVATION

The application of hydrofoils to marine vehicles started in the beginning of the 20th century with the Italian inventor Enrico Forlanini, [2]. At that time, due to technical limitations, safety issues and maintenance, this technology was not reliable enough for most of the maritime industry. However, in the last decades, as result of many technological advances, the use of hydrofoils has become more attractive for some maritime sectors (*e.g.:* defense sector), since they allow to combine speed with efficiency and comfort. However, this technology still rises challenges and concerns regarding its impact on seakeeping and manoeuvring performance. Therefore, the goal of this research is the:

"Development of knowledge, methodologies and tools, which will contribute for the development of a new generation of seagoing vessels."

As a starting point, to reach this goal, this research focuses on calm water manoeuvring prediction of foil-assisted vessels. Particularly vessels equipped with a Hull Vane[1]. The Hull Vane is an hydrofoil placed at the stern which aims to reduce resistance and improve seakeeping. Which has been studied and optimized for more than 25 years by *Van Oossanen Naval Architects*. However, its impact on manoeuvring performance is still not clear. For the purpose of this research, the *RPA8* is considered. This is a 25 [m] patrol vessel equipped with a Hull Vane, for which experimental data is available:

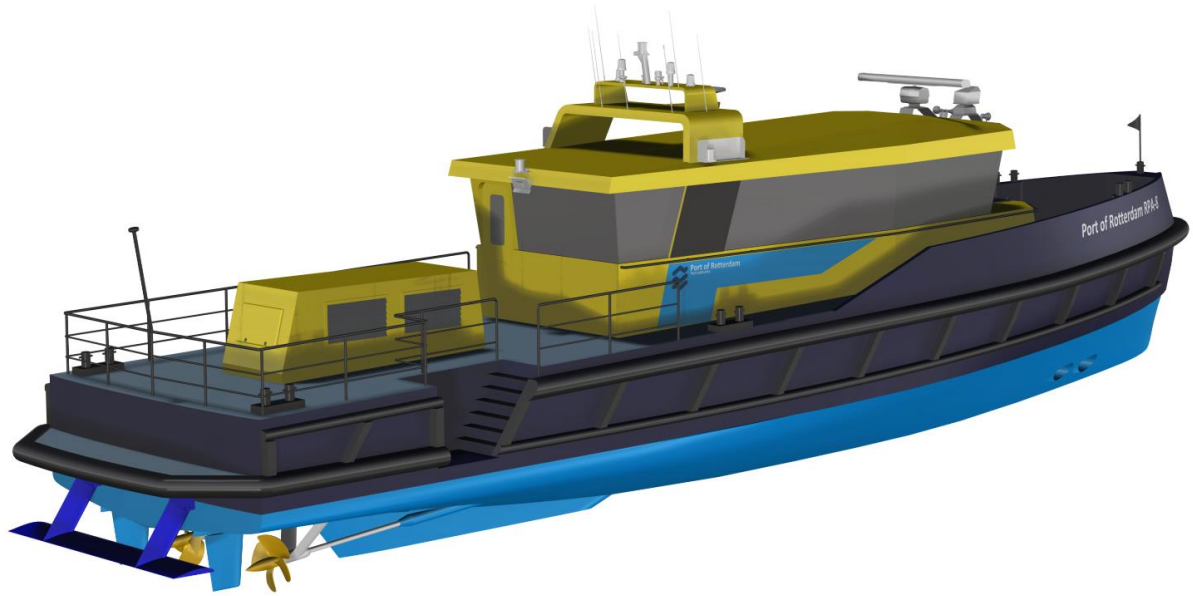

Figure 1.1: RPA8, 25[m] patrol vessel equipped with a Hull Vane (at the stern in dark blue).

[1] Hull Vane® is a registered trademark of *Van Oossanen Naval Architects B.V.*

1.2 STATE OF THE ART

Manoeuvrability is an important aspect to consider in the design of a vessel, to ensure safety, comfort and adequate dynamic behavior. However, due to the complexity of the physical phenomena involved, the assessment of manoeuvring characteristics is an expensive and challenging task. Advances in *Computational Fluid Dynamics* (*CFD*), allow to reduce experimental time and costs, comparative to traditional model scale experiments. However, the accuracy of this type of numerical methods is still a concern.

Since the late 90's, multiple researchers have been trying to use *CFD* to determine hydrodynamic coefficients for manoeuvring. However, only in 2006 one of the first successful validations of *Virtual Captive Tests* (captive tests performed in *CFD*) was presented, see *Hochbaum* in [3]. Later in 2011, *Toxopeus* in [4], presented a complete study on the application and validation of *CFD* for the determination of hydrodynamic coefficients for manoeuvring. Although *Hochbaum* and *Toxopeus* conducted their studies without considering free surface effects, both found challenging the validation of the results, due to the presence of complex flow phenomena. More recently, *Bonci et al.* in [5] combined a system identification algorithm with free running *CFD* simulations, with the aim of improving manoeuvring predictions. Despite promising results were obtained, it was concluded that the free running *CFD* results still required improvements.

Some of the current challenges in the fields of manoeuvring and foiling/foil-assisted vessels are:

- Validation of *Virtual Captive Tests,* including free surface effects*;*
- Validation of free running manoeuvres in *CFD;*
- Manoeuvring prediction of foil-assisted vessels;
- Foiling vessels in stern-quartering waves and following seas, see *Faltinsen* in [6];
- Effects of ventilation and cavitation on the dynamic behavior of foiling vessels, see *Faltinsen* in [6].

1.3 RESEARCH OBJECTIVES

This research focuses on the development of knowledge, methodologies and tools which will allow to perform manoeuvring predictions, at early design stages, of vessels equipped with a Hull Vane. For this, *Virtual Captive Tests* are combined with a manoeuvring model (1st and 3rd research topics of the previous list), in the following way:

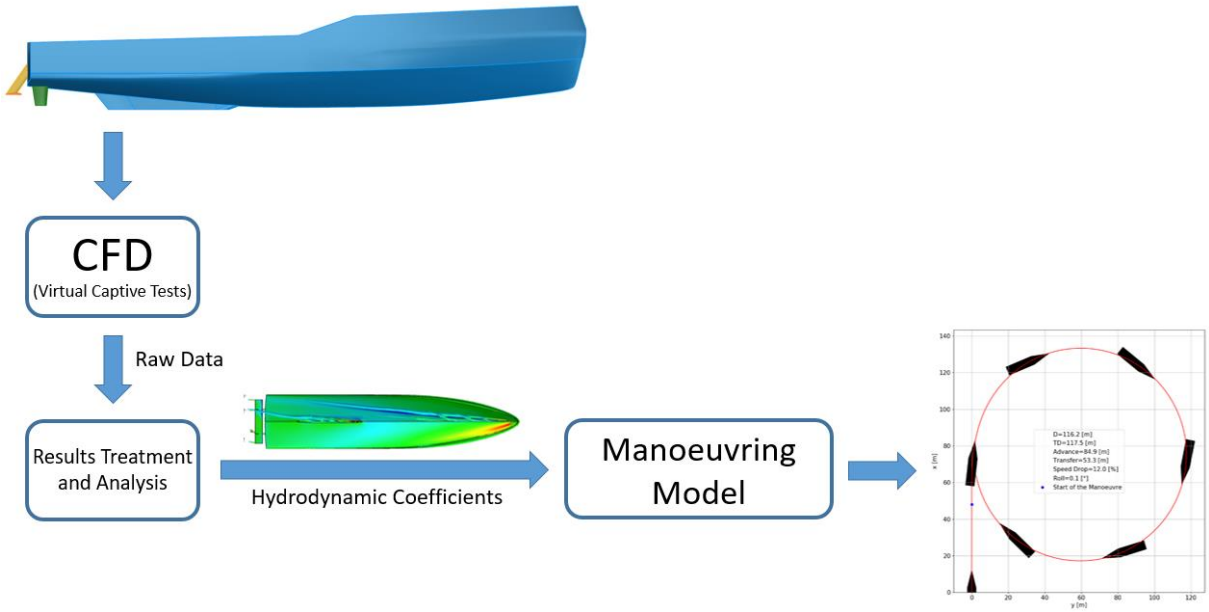

Figure 1.2: Manoeuvring prediction process.

In the course of this research, this manoeuvring prediction process will be developed from beginning to end, *i.e.:* development of methodologies to perform and analyze virtual captive tests, and the development of a manoeuvring model. This will establish a solid foundation for future development in this field, which will allow *Van Oossanen Naval Architects* to study, assess and optimize the manoeuvring performance of conventional vessels and vessels with hydrofoils. To reach this goal, three research objectives are defined, and presented in the following three subsections of this chapter.

Due to time constrains, a detailed assessment of roll motion prediction, during manoeuvring, is left for future research.

1.3.1 FIRST RESEARCH OBJECTIVE: DETERMINATION OF HYDRODYNAMIC COEFFICIENTS

Traditionally, hydrodynamic coefficients for manoeuvring were determined using semi-empirical models or model-scale experiments (captive tests). However, semi-empirical models are not always applicable and model-scale experiments are expensive. Thanks to advances in numerical methods and hardware, it is now possible to perform the same captive tests using *CFD* (*i.e.: Virtual Captive Tests*). This is not only less expensive (comparative to physical experiments), but also avoids scaling effects and allows a more detailed analysis of the flow field. However, the setup and validation of these simulations is still challenging. Therefore, the first research objective is to:

> *"Establish methodologies for the determination of hydrodynamic coefficients using virtual captive tests, including free surface effects."*

Toxopeus in [4], showed that it is possible to improve manoeuvring predictions of merchant ships by using hydrodynamic coefficients derived from *CFD.* Although *Toxopeus* neglected free surface effects (low *Froude* numbers), this assumption is not valid for *RPA8* ($F_n \approx 0.5$).

In this research, multiple mesh topologies and *Virtual Captive Tests* will be compared. Considering parameters such as: computational cost and discretization errors. In the end, manoeuvring predictions of *RPA8* will be compared to experimental data and the impact of discretization uncertainties, on manoeuvring predictions, will be assessed.

1.3.2 SECOND RESEARCH OBJECTIVE: MANOEUVRING MODEL

The available literature concerning manoeuvring prediction and mathematical modelling of foil-assisted vessels is scarce. Although *Hackett et al.* in [7], briefly assessed this, it was for a very specific case, where the foils were located beheath the hull. However, the Hull Vane is placed behind the stern making it subjected to different flow field. To fill this gap in the manoeuvring prediction of foil-assisted vessels, this research aims to:

"Develop and implement a manoeuvring model, for calm water manoeuvring predictions of vessels with Hull Vane."

This objective shall be accomplished, by assessing and mathematically modelling relevant hydrodynamic forces/moments and interaction effects. Then, these mathematical models will be implemented in *Python 3.6* and the equations of motion solved using a time-marching algorithm. In the end, a sensitivity analysis is performed to assess the importance of each hydrodynamic coefficients on the manoeuvring performance of *RPA8.*

1.3.3 THIRD RESEARCH OBJECTIVE: HULL VANE MATHEMATICAL MODEL

Since the Hull Vane is a fixed foil it can be considered as part of the hull, like a skeg (*i.e.:* integrated approach). This avoids the need of modeling the Hull Vane separately from the hull, which can be a challenging task due to complex hull-Hull Vane interaction. However, this makes the assessment of the impact of the Hull Vane on the manoeuvring performance, considerably expensive, since the *Virtual Captive Tests* need to be performed twice, *i.e.:* for the case with and without Hull Vane. Therefore, this research aims to develop a mathematical model for the Hull Vane, which eventually allows a less expensive assessment of the impact of the Hull Vane on the manoeuvring performance. Having said this, the third and last research objective is to:

"Develop a Hull Vane mathematical model and assess its impact on the overall manoeuvring prediction process."

This objective will be accomplished by performing *Virtual Captive Tests,* with and without Hull Vane. Then, the results of these tests will be compared, and the effect of the Hull Vane on the manoeuvring performance assessed and modelled. The impact of the use of this model on the manoeuvring prediction process, will be determined by comparing it with the integrated approach, considering aspects such as complexity and accuracy.

1.4 REPORT OUTLINE

Chapter 2 presents the literature review. This consists on presenting the underlying knowledge and assumptions for a good understanding of this research together with the state of the art.

Chapters 3, 4* and *5 complete the **first research objective**, by setting up *Virtual Captive Tests* for the determination of hydrodynamic coefficients, and performing an analysis of the results. ***Chapter 3*** presents the main modelling assumption and the setup of the *CFD* simulations. ***Chapter 4*** presents a solution verification study of the numerical setup, and hull hydrodynamic coefficients that are derived from the results of the *Virtual Captive Tests.* ***Chapter 5*** focuses on the study and modelling of interaction effects.

Chapters 6* and *7 complete the **second research objective.** Here a manoeuvring model for vessels with Hull Vane is described in detail.

In ***Chapter 8*** the manoeuvring model is verified, and the manoeuvring prediction process validated, together with Hull Vane mathematical model. This leads to the achievement of the **third research objective.** Finally, the effect of the Hull Vane on the manoeuvring performance of *RPA8* is assessed.

Chapters 9 *and* ***10:*** Present the main conclusions of this research, recommendations and future work.

2. LITERATURE REVIEW

This chapter aims to review the current literature, introduce topics, definitions and assumptions that are essential for a good understanding of this research. It starts with the introduction of the *Hull Vane*, and then stability and standard manoeuvres will be introduced, giving a fundamental overview of manoeuvring and how it can be accessed. After this, a mathematical perspective of manoeuvring will be presented, where frames of reference will be introduced together with the mathematical representation of forces. Then, fundamental *CFD* related topics will be presented, and finally an overview of some of the current methods to determine hydrodynamic manoeuvring coefficients. This chapter allows any person with a good knowledge of differential calculus, algebra and mechanics, to understand the main aspects involved in manoeuvring predictions of vessels.

At this point it is important to clearly define “manoeuvring”. This definition slightly changes among the scientific community. As an example, *S.Sutulo* in [8] defines “manoeuvring” as the ability to change the direction and amplitude of a motion, while *M.S.Triantafyllou et al.* in [9] assume that “manoeuvring” does not include any controlled speed changes. Here, “manoeuvring” is defined in accordance to *S.Sutulo*, which can also include controlled speed changes.

2.1 THE HULL VANE

The Hull Vane was invented by *Pieter Van Oossanen* in the early 90’s. Its first application was on a catamaran, to reduce its excessive running trim and increase the vessel’s top speed. Since then the Hull Vane’s resistance and motion reduction properties have been studied and optimized. Currently, the Hull Vane is mainly applied to monohulls sailing at moderate to high non-planing speeds.

According to *Kasper et al.* in [10], the Hull Vane can reduce the resistance up to 25.5%, or increase up to 9.5%, depending on the hull form, speed, sea state, and running trim. The calm water resistance reduction is mainly caused by 3 different physical phenomena:

- Transom wave reduction: The low-pressure region created by the Hull Vane, interacts with the wave crest created at the stern, reducing it.
- Thrust generation: The Hull Vane uses the up-wash at the ship’s stern to create forward thrust.
- Trim correction: It’s common in ships to have excessive trim aft due to the low-pressure region created by the rocker. In these cases, the Hull Vane also corrects the trim, reducing the resistance.

Besides resistance reduction, the Hull Vane also improves seakeeping. In [11] *de Jonge* showed that it can reduce the trim motion up to 20.5%.

Although, the Hull Vane has been studied and optimized for more than 25 years, its impact on the manoeuvring performance is not clear yet. *Kasper Uithof et al.* in [12] found that the application of a Hull Vane in a 55m fast supply vessel decreased the turning ability of the vessel. The most plausible hypothesis for the origin of this effect, is the increase in lateral area at the stern caused by the Hull Vane struts, which contributes for a decrease of the turning ability. However, due to complex flow phenomena and the effect of the Hull Vane on dynamic trim, it is not likely that an extrapolation of these results to any other case it is correct.

2.2 MOTION STABILITY

Manoeuvring performance in the end is all about motion stability. This concept is essential for a good understanding of manoeuvring and controllability of marine crafts. Therefore, the aim of this section is to introduce the different types of motion stability. Later in *Section 2.3* a practical perspective of this is given, when explaining the standard manoeuvres to assess the controllability and dynamic characteristics of a vessel.

Later, in *section 2.8,* a control theory perspective of stability will be presented, briefly showing how to assess the directional stability of a vessel and how to relate this to some of the vessel's characteristics.

2.2.1 COURSE STABILITY (OR STRAIGHT-LINE STABILITY)

Course stability defines the ability of a vessel without control, to return to a straight path after a disturbance in yaw. However, assuming a course stable case, the final direction of the vessel will be different from the initial one since there are no restoring forces in yaw, as mentioned by *Fossen* in [13].

Figure 2.1: Trajectory of a course stable vessel, [14].

Often a skeg is used to increase the straight-line stability, since it moves the application point of the transverse hydrodynamic forces towards the stern, stabilizing the vessel. From a practical perspective can be seen as the skeg trying to correct drift angle, by creating a yaw moment in an attempt to align the vessel axis with the incoming flow.

2.2.2 DIRECTIONAL STABILITY

This criterion is more significant than course stability, since it considers the ability to control the vessel. Directional stability defines the capability of a vessel to recover the initial heading after a disturbance in yaw. This can happen with or without oscillations, depending on the control and system characteristics. *Fossen* in [13] mathematical describes this behaviour.

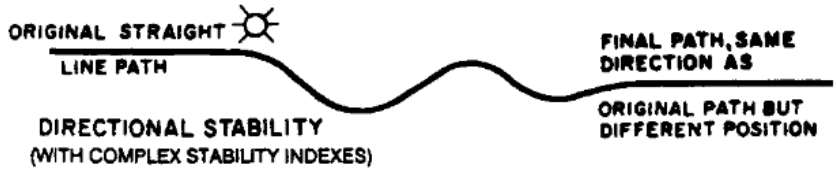

Figure 2.2: Trajectory of a directionally stable vessel, with oscillatory behaviour, [14].

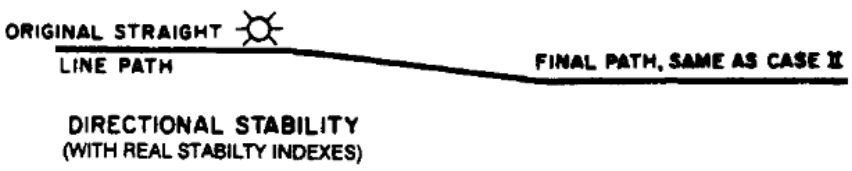

Figure 2.3: Trajectory of a directionally stable vessel, without oscillatory behaviour, [14].

The directional stability is closely correlated with the controllability of a vessel. Increasing the rudders tends to improve this characteristic, until a certain limit. Over this limit it makes the system unstable. In control systems theory this is called the gain margin, which is the maximum gain of the system transfer function in open loop before it becomes unstable, *see Franklin et al.* in [15]. However, note that the rudder size has almost no effect on the course stability, since this one implies no action of steering devices, as mentioned by *Fossen* in [13]. A practical example of this can be seen later in *Figure 2.9.*

2.2.3 POSITIONAL MOTION STABILITY

Positional motion stability is a stronger requirement than any of the ones previously presented. This one implies not only recovery of heading but position as well after a disturbance in yaw. Also, it considers the action of steering devices since there is no restoring forces in yaw.

Figure 2.4: Trajectory of a vessel with positional motion stability and oscillatory behaviour, [14].

Note that this characteristic requires active control of the steering devices. This behaviour is dependent on different characteristics, from the rate of turn of the rudder, to the course stability and directional stability. Therefore, to improve this behaviour more advanced technics are required. For instance, a course stable vessel will have less overshoot in yaw than a less stable one. However, if it is too course stable it will take a lot of time to get back to the original path. If the rudder size or rudder rate is too large, it will cause overshoot and eventually the system to become unstable, as previously mentioned.

2.3 STANDARD MANOEUVRES

Some specific manoeuvres were adopted as standard to allow a quantitative assessment of the manoeuvring characteristics of vessels. Here, just the most widely known and recognized manoeuvres are going to be describe and used (turning circle, zig-zag and spiral). These manoeuvres are not considered normal nautical manoeuvres, since they were specifically developed to assess the manoeuvring performance.

2.3.1 TURNING CIRCLE

The turning circle manoeuvre has always been of interest because of its practical applicability. As mentioned in [14], the turning circle manoeuvre assesses the turning ability of a vessel. This consists on steering the vessel in a steady circular motion, by keeping the rudders with a constant deflection. As shown below (*Figure 2.5*), this manoeuvre can be described by four parameters: advance, transfer, tactical diameter and steady turning diameter.

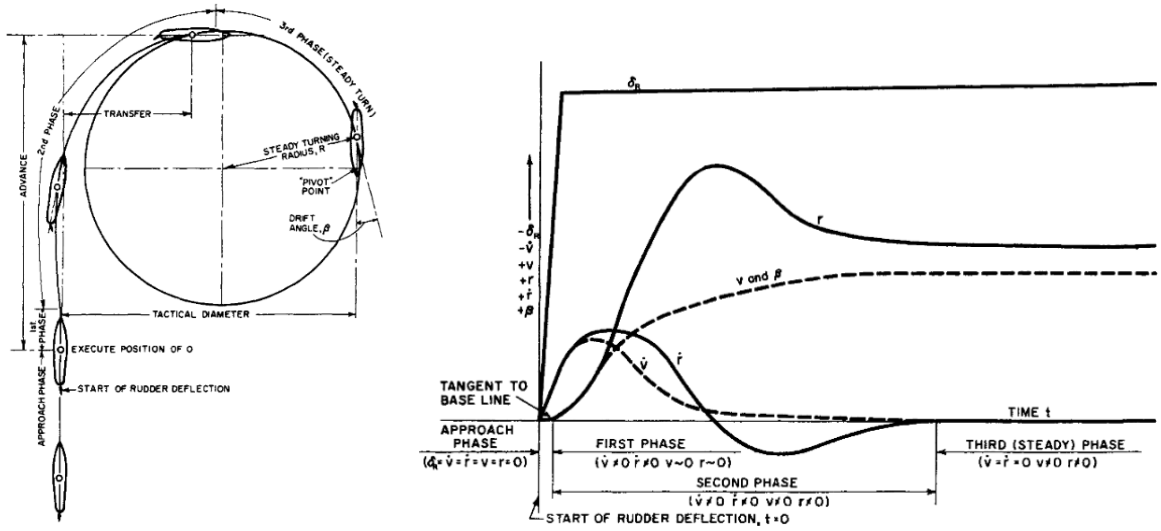

Figure 2.5: ***Left:*** *Trajectory turning circle manoeuvre.* ***Right:*** *Characteristics of the phases of a turn.* ***Source****: [14].*

As it can be observed in *Figure 2.5*, the first phase of the turning circle is the approach phase. This phase occurs before the rudder is deflected and is required to make sure the vessel is sailing in a straight course with constant speed in steady state conditions. Then the so called first manoeuvring phase follows the approach phase, it occurs while the rudder is being deflected (according to *Sutulo* in [8], it should be deflected at the maximum rate). Once the rudder reaches the desired deflection the second manoeuvring phase starts, this phase is characterized by a transient behaviour of the vessel with a constant rudder angle. The third and last phase is characterized by a steady circular motion of the vessel. As shown by *Lewis* in [14], the turning circle diameter increases with the directional stability and length of the ship and decreases with the steering force.

A practical example of turning circle requirements is given by *IMO* in [16], for ships over 100 [m] in length (L), chemical tankers and gas carriers. In this case the *IMO* requires:

- **Test speed (V)**: 90% of the ship's maximum speed;
- **Rudder Angle:** 35° to portside and starboard or the maximum rudder angle;
- **Advance:** Should not exceed more than 4.5 ship lengths;
- **Tactical Diameter:** Should not exceed 5 ship lengths.

2.3.2 ZIG-ZAG MANOEUVRE

The zig-zag manoeuvre (first proposed by *Kempf* in 1944, [17]) aims to generate a periodic unsteady motion in order to determine the control characteristics of a vessel, as explained in [14]. This manoeuvre is mainly characterized by the time histories of two parameters, a desired heading and a rudder angle. Often the desired heading is set to the rudder angle, in other words it consists in steering the vessel until its heading reaches the rudder angle and then steering to the other side and repeating this multiple times. The results of a zig-zag manoeuvre are strongly dependent on the course stability of the vessel and on the effectiveness of the rudder, as referred in [14]. For conventional displacement ships the process is expected to become periodic after 4-5 cycles of 10°-10° or 20°-20°, [8]. Furthermore, according to [8], conclusions about the course keeping ability can be draw by doing a 5°-5°zig-zag

manoeuvre, this will later explained in *Section 2.8*. *Figure 2.6* shows a time trace of this manoeuvre and its parameters:

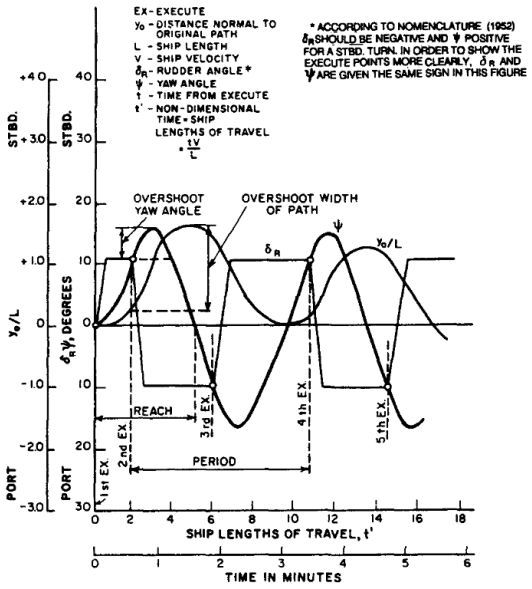

Figure 2.6: Zig-Zag manoeuvre, [14].

The principle parameters that characterize the result of zig-zag manoeuvre are:

- The 'Reach' time;
- The overshoot in yaw angle;
- The overshoot width of path.

The reach time assesses the ability of a ship to change its course direction (turning ability). The reach time is reduced with an increase in speed, rudder effectiveness (generated force per angle of attack) and/or a decrease in the vessel course stability, as explained by *Arentzen* and *Mandel* in [18].

In [14] *Lewis* explains that the *overshoot* in yaw angle and the overshoot width of path assess the counter-manoeuvring ability of a marine vehicle (ability of changing manoeuvre). The *yaw angle overshoot* increases with an increase in speed, an increase of rudder effectiveness and a decrease in course stability of the vessel. The *overshoot width of path* increases with an increase in speed, a decrease in rudder effectiveness and a decrease in course stability of the vessel. More details about this can be found in [14].

A practical example of zig-zag requirements is also given by *IMO* in [16], for ships over 100 [m] in length (L), chemical tankers and gas carriers. In this case the *IMO* requires:

- **Test speed (V):** 90% of the ship's maximum speed;
- **Zig-zag characteristics:** 10°-10° or 20°-20°;
- **First overshoot (10°-10°):** It should not exceed 10° if $\frac{L}{V} < 10\ [s]$, $(5 + \frac{L}{2.V})°$ if $10[s] < \frac{L}{V} < 30\ [s]$, otherwise 20°;
- **Second overshoot (20°-20°):** It should not exceed 25° if $\frac{L}{V} < 10\ [s]$, $(17.5 + \frac{3.L}{4.V})°$ if $10[s] < \frac{L}{V} < 30\ [s]$, otherwise 40°;
- **First overshoot (20°-20°):** Should not exceed 25°.

2.3.3 SPIRAL MANOEUVRE

The spiral manoeuvre was first proposed by *Dieudonne* and can be found in [19]. It aims to mainly assess the course stability of a vessel but also the directional stability. According to [20], the manoeuvre consists on: after having a straight and steady course for one minute, the rudder is then deflected at $15°$, and it is kept like this until one more minute has passed with steady yaw rate. After this, the rudder angle is then decreased about $5°$ and it is kept like this for one more minute in steady state. This procedure is repeated until the rudder angle reaches $-15°$ and then the increment of rudder angle becomes positive and the process is repeated. For a course stable vessel, every rudder deflection is associated with only one rate of turn. While for a course unstable vessel, is possible to have different rates of turn for the same rudder deflection (hysteresis). The picture below shows a plot of the rate of turn according to the rudder angle, for a course stable and unstable vessel:

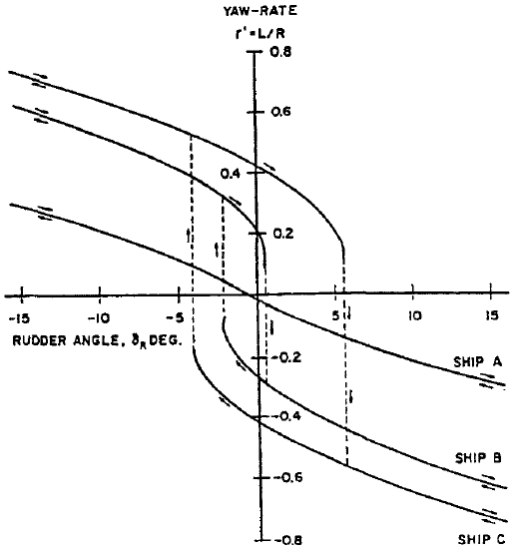

Figure 2.7: Spiral Manoeuvre results for 3 different ships (A, B and C), [21].

In Figure 2.7ship A shows to be course stable, while ship B and C unstable. From here is also possible to understand that C is more unstable than B, since it has a larger hysteresis. Another important fact is that for dynamically symmetrical ships this plot is antisymmetric. However, this is not the case in Figure 2.7, this dynamic asymmetry is often encountered in ships with an odd number of propellers, as mentioned by *Fossen* in [13]. The height of the hysteresis is a numerical measure of the degree of dynamic instability of the hull while the width of the hysteresis is a measure of the directional stability of an unstable ship. *S.Sutulo* showed in [8], that by trimming the vessel bow down is possible to make a ship become directionally unstable:

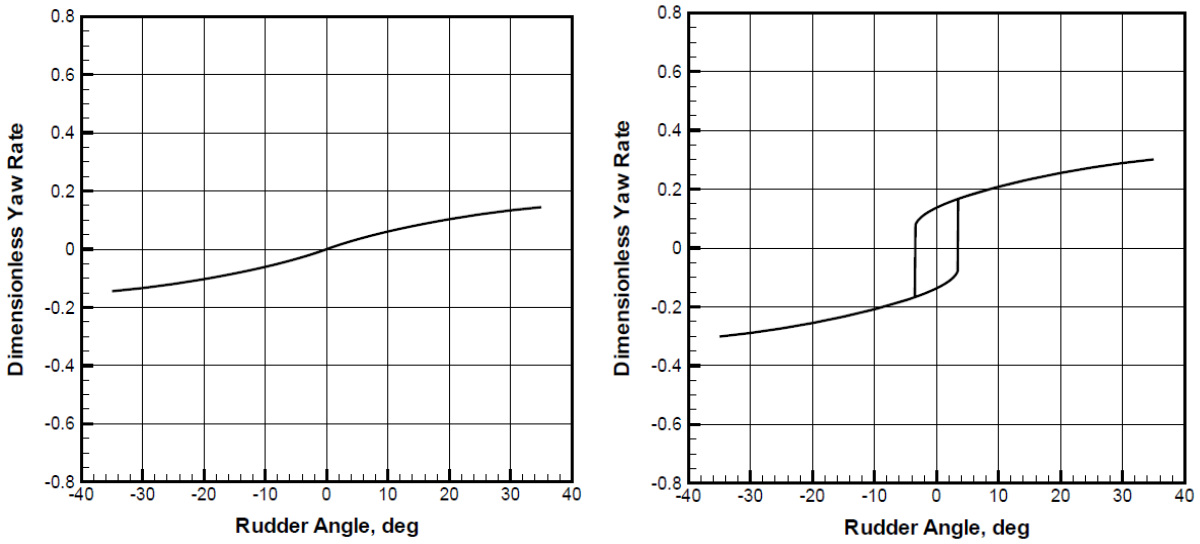

Figure 2.8: Spiral manoeuvre result without trim (left) and with trim by the bow(right), [8].

The vessel becomes directionally unstable when trimmed forward because the centre of lateral pressure when drifting is moved forward (associated to an increase of the *Munk Moment, or yaw moment,* as explained by *Kornev* in [22]), what destabilizes the vessel, since the moment created on the hull will tend to further increase its angle of attack instead of correcting it. It is also important to note that an unstable vessel has better turning ability than a stable one, this can be verified in Figure 2.8

Furthermore, *S.Sutulo* also shows in [8], the relation between the size of the rudder and the directional stability of the vessel:

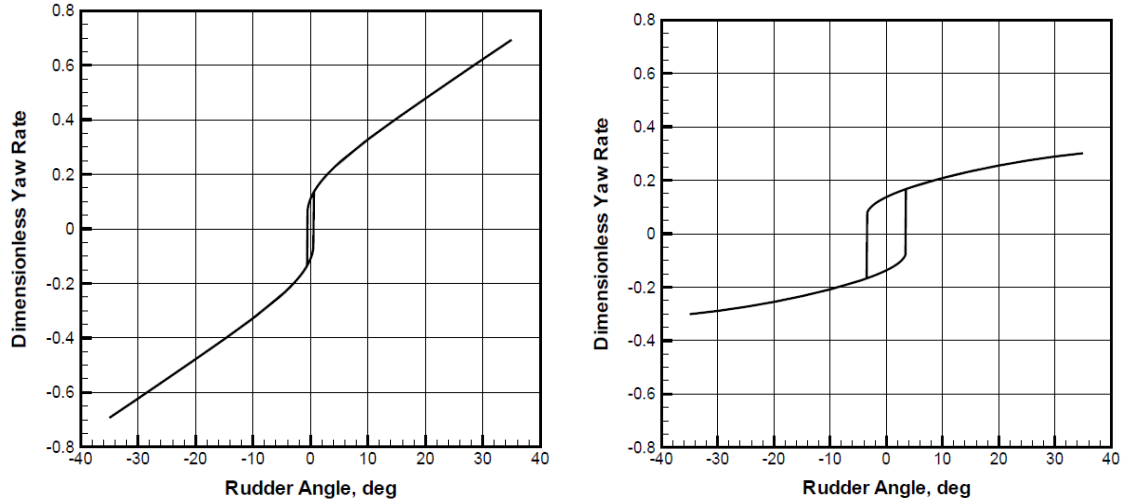

Figure 2.9: Spiral manoeuvre results with a large rudder (left) and a small rudder (right), [8].

As can be seen by changing the rudder size, the height of the hysteresis loop practically did not change, only the width. This shows that the vessel is more controllable with a larger rudder, although is still unstable.

2.3.4 PULL-OUT MANOEUVRE

The so-called *Pull-out Manoeuvre* was first introduced by *Roy Burcher* in 1969. This manoeuvre aims to determine if a vessel is course stable or not. Consists in after doing a turning circle to set the rudder to zero and analyse the behaviour of the vessel. This procedure needs to be done to portside and starboard. If the rate of turn of both tests decay to the same value, it means that the vessel is course stable, otherwise it is not. The figure below shows the result of this test for a stable and unstable vessel:

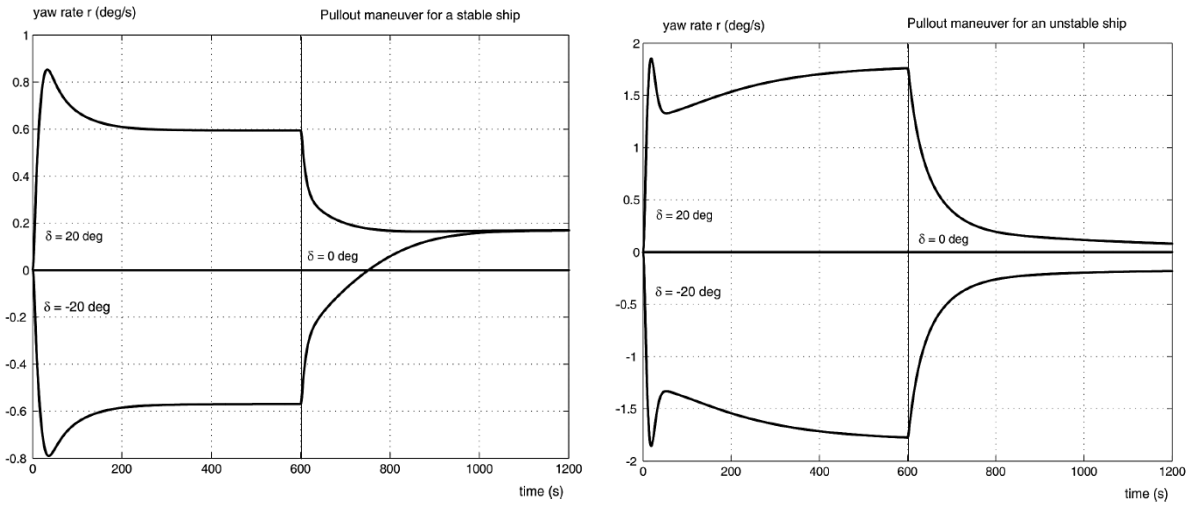

Figure 2.10: Pull-out test result for a course stable (left) and unstable vessel (right), [13].

In *Figure 2.10,* is possible to see that the rate of turn of the stable vessel, it is not converging to zero, this means that the vessel is not dynamically symmetric. This asymmetry is also revealed in the spiral test results by a vertical shift of the curve. For the case of a course unstable vessel, the difference in the converged values of yaw rate corresponds exactly to the height of the hysteresis loop of the spiral manoeuvre, as referred in [13]. At the end the pull-out test can be seen as a particular case of the spiral manoeuvre.

2.4 MOTIONS AND MATHEMATICAL REPRESENTATION OF FORCES

2.4.1 MATHEMATICAL MODELLING APPROACHES

In general, there are two ways to mathematically model manoeuvring of vessels, the *integrated approach* and the *modular approach*. The *integrated approach* considers a total force/moment acting on the system, which is dependent on all the relevant system variables, as explained by *Sutulo* in [8]. The *modular approach* decomposes the main system in elements, where the force of every element is dependent only on the relevant parameters for the element itself, and in the end combines all the forces/moments by using interaction coefficients, [8]. This last approach is the most commonly used because, it is more versatile, it allows to assess the influence of each element on the system behavior and to consider local flow phenomena. However, this last approach makes it difficult to compare the coefficients of different vessels since their individual value hardly gives any useful information about the system, because this one is composed by multiple parts, as mentioned by *Toxopeus* in [4]. The first objective of this research is to develop a mathematical model to study foil-assisted vessels. Therefore, the *modular approach* is the most convenient in this context since it allows to test different appendage configurations without significant changes in the model.

2.4.2 RIGID BODY MOTION AND FRAMES OF REFERENCE

A vessel is considered a rigid body with $6DOF$ under the influence of external forces/moments, [21]. It moves in an earth fixed frame of reference (inertial: ξ, ζ, η) and it contains a body fixed frame of reference on its CoG (non-inertial: x, y, z).

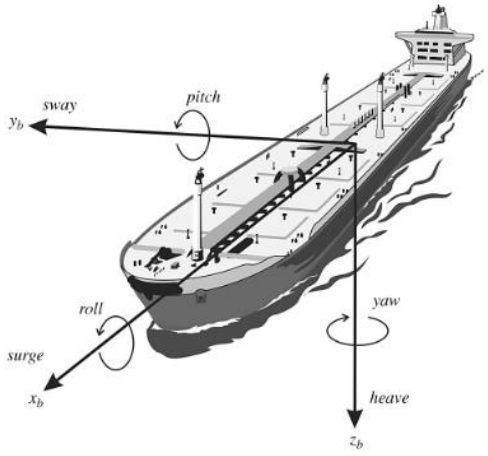

Figure 2.11: Motions in 6DOF, [13].

The ship motions and forces/moments in the inertial frame of reference (ξ, ζ, η) are mathematically represented in the non-inertial frame of reference (x, y, z) in the following way, [8]:

x – position in surge;	u – Advance speed;	X – external surge force;
y – position in sway;	v – sway speed;	Y – external sway force;
z – position in heave;	w – heave speed;	Z – external heave force;
ϕ – heel angle;	p – roll speed;	K – external roll moment;
θ – trim angle;	q – pitch speed;	M – external pitch moment;
ψ – heading angle;	r – yaw rate;	N – external yaw moment.

The motion of a rigid body is governed by the *Euler* equations of motion, [20]. These equations create a time domain coupled second order linear system of ODE's (Ordinary Differential Equations). More details about this type of equations can be found in [23] or other fundamental literature of differential calculus:

$$m.(\dot{u} + w.q - v.r) = X \qquad \textit{Eq. 2.1}$$

$$m.(\dot{v} + u.r - w.p) = Y \qquad \textit{Eq. 2.2}$$

$$m.(\dot{w} - u.q + v.p) = Z \qquad \textit{Eq. 2.3}$$

$$I_{xx}.\dot{p} + (I_{zz} - I_{yy}).q.r = K \qquad \textit{Eq. 2.4}$$

$$I_{yy}.\dot{q} + (I_{xx} - I_{zz}).p.r = M \qquad \textit{Eq. 2.5}$$

$$I_{zz}.\dot{r} + (I_{yy} - I_{xx}).p.q = N \qquad \textit{Eq. 2.6}$$

These equations assume a non-inertial frame of reference located at the CoG (Centre of Gravity). Furthermore, it is important to note that the linearity of this system of ODE's is dependent on the mathematical description of the external forces/moments. In free running manoeuvring the most significant forces/moments are aero/hydrodynamic. However, these depend on many variables, especially the ones acting on the hull. Therefore, in order to describe them mathematically, it is necessary to make approximations and assumptions. These approximations are considered to be the main source of errors in the mathematical description of ship motions, as mentioned by Lewis in [14]. The aerodynamic forces are less predictable and less important than hydrodynamic ones (just from the fact that the density of the water is roughly 1000 times larger than the density of the air), and so they will be neglected for the purpose of this research.

2.4.3 MATHEMATICAL REPRESENTATION OF HULL FORCES

As previously referred, hydro and aerodynamic forces/moments acting on the hull are dependent on multiple variables. By assuming that these forces/moments are k times differentiable, an approximation of $(n+m)$ order in the vicinity of a point can be done using *Taylor Series* expansion, [14]:

$$F(x_1,\dots,x_k) \approx F(x_1^0,\dots,x_k^0) + (x_1 - x_1^0).\frac{dF}{dx_1}|_{x_1^0} + \cdots + \frac{(x_k - x_k^0)^n.(x_{k-1} - x_{k-1}^0)^m}{n!\ m!}.\frac{d^{(n+m)}F}{dx_k^n dx_{k-1}^m}|_{(x_k^0,\ x_{k-1}^0)} \quad k \in \mathbb{N} \qquad \textit{Eq. 2.7}$$

More details about the multivariable *Taylor Series* expansion can be found in [24].

In order to simplify the mathematical representation, the following notation is adopted:

$$\frac{dF}{dx_1} = F_{x_1}, \qquad \frac{d^2F}{dx_1^2} = F_{x_1x_1}, \qquad \frac{d^2F}{dx_1dx_2} = F_{x_1x_2}, \qquad etc\ \dots$$

$$\frac{dx_n}{dt} = \dot{x}_n$$

Note that, here F represents a generic multivariable function and x_k generic variables. In the context of hydrodynamics these derivatives (except the purely time domain ones) are often called *hydrodynamic derivatives* and they represent hydrodynamic coefficients.

Linear hydrodynamic coefficients can represent damping forces (*e.g.:* Y_v), added masses (*e.g.:* $X_{\dot{u}}$), reaction forces due to couplings in motions (*e.g.:* N_v), etc... However, higher order terms (*e.g.:* Y_{vr}, X_{rvu}) do not have such a direct physical meaning, but they represent the interaction between variables. For instance, Y_{vr} represents the influence of r (yaw rate) on Y_v, as illustrated in Figure 2.12.

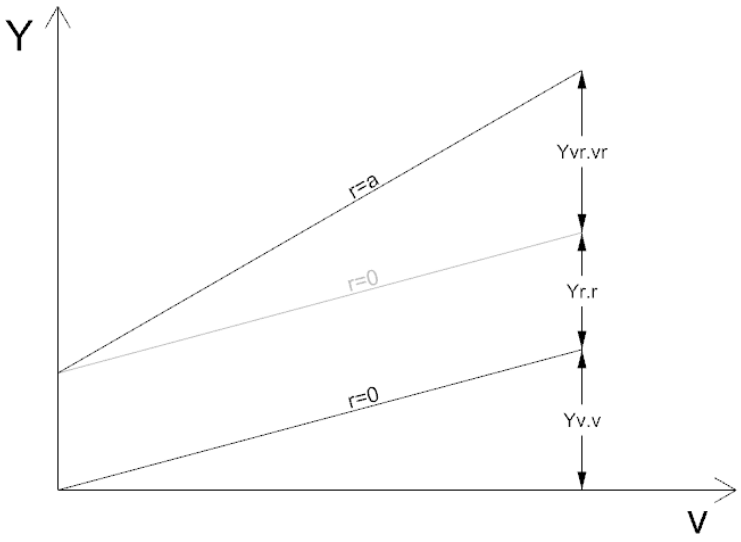

Figure 2.12: Illustration of the meaning of some terms of the Taylor expansion for sway.

Higher order terms lead to higher accuracy. However, an increase in the order implies a significant increase in the number of hydrodynamic coefficients that are necessary to determine. However, it is important to note that the *Taylor* approximation is a purely mathematical representation, what can lead to unnecessary coefficients. For instance, some valid assumptions are:

- In case of a vessel with port-starboard symmetry, $X(v)$ and $X(r)$ are even functions. Therefore, the odd terms of their *Taylor* expansion are assumed to be zero, *e.g.*:

$$X_v = X_r = X_{vvv} = X_{rrr} = 0$$

- $X(u)$ and $Y(v)$ are odd functions. Therefore, the even terms of their *Taylor* expansion are assumed to be zero, *e.g.*:

$$X_{vv} = X_{rr} = 0$$

A more detailed analysis of this can be found in *Section 4.4* where the results of the *Virtual Captive Tests* are discussed.

2.5 PROPULSION SYSTEM

The propulsion system plays an important role on manoeuvring performance. Since it is often placed upstream of the rudders it strongly influences their effectiveness. Depending on the type of manoeuvre of interest, some propulsive hydrodynamic phenomena can be neglected, allowing the use of simplified mathematical models, such as *Actuator Disk Theory,* [25]. In this research, just shaft line systems with fixed pitch propellers are considered.

In order to take propeller characteristics into account and better represent propeller to rudder interaction in the mathematical manoeuvring model it is necessary to determine the working point of the propeller. As mentioned by *Bonci* in [26], the propeller rate can be assumed constant during manoeuvring. This section aims to introduce not only Actuator Disk Theory, which is particular important when considering propeller-rudder interaction, but also the methodology to determine the working point of the propeller and consequently the propeller rate.

Actuator disk theory (*ADT*) was first introduced by *Rankine (1865)* and later studied by *Froude(1889),* [9]. In this theory, a propeller is represented by a permeable disk with zero thickness that introduces a uniform jump in total pressure of the flow passing through it, creating thrust, as illustrated in Figure 2.13. Due to the fact that this research is focused on the manoeuvrability at moderate speed (no stopping manoeuvres), local flow asymmetries created by the propeller are considered not to be important, as referred by *S.Sutulo* in [8]. Therefore, no tangential velocities, swirl or *Glauert* forces (side forces created by propellers) are considered, [9].

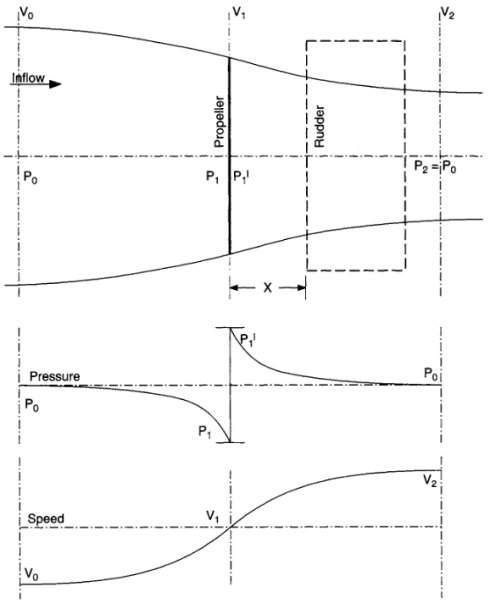

Figure 2.13: Dynamics of a flow through an actuator disk, [25].

The *ADT* assumes an actuator disc operating in an inviscid and unbounded flow, under a uniform axial inflow speed V_A and static pressure p_∞. These assumptions fulfil the requirements for *Bernoulli equation, therefore it can be applied between a point far upstream and downstream,* [9].

$$p_\infty + \frac{1}{2}\rho V_A^2 + \Delta p = p_\infty + \frac{1}{2}\rho(V_A + u_w)^2 \Rightarrow \Delta p = \rho . u_w . (V_A + \frac{u_w}{2}) \qquad \textit{Eq. 2.8}$$

With this, the total thrust created by the actuator disk is given by the jump in total pressure times the area of the disk:

$$T = \Delta p . A_D = \rho . u_w . \left(V_A + \frac{u_w}{2}\right) . \pi . R_D^2 \qquad \textit{Eq. 2.9}$$

The thrust can also be computed by defining a control volume and using conservation of mass and momentum.

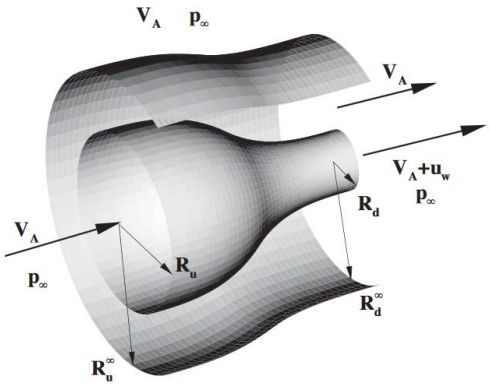

Figure 2.14: Control volume for actuator disk, the stream tube contraction has been exaggerated for the sake of clarify, *[9].*

The integral form of mass and momentum conservation in a fixed control volume, with incompressible and inviscid flow, are the following:

$$Mass\ Conservation: \int \vec{u} \cdot \vec{n}\, dA = 0 \qquad \textit{Eq. 2.10}$$

$$Momentum\ Conservation: \int \rho . \vec{u} . (\vec{u} \cdot \vec{n}) dA + \int p . [I] dA = 0 \qquad \textit{Eq. 2.11}$$

Where $[I]$ represents an identity matrix. More details about the derivation of these conservation laws can be found in fundamental literature of fluid mechanics, like [27].

This momentum conservation method also shows that the flow velocity at the propeller plane is:

$$V_{Prop} = V_A + \frac{u_w}{2} = \frac{V_A + V_2}{2} \qquad \textit{Eq. 2.12}$$

Where V_2, is the maximum velocity of the propeller slipstream, see *Eq. 2.23*. This becomes particularly useful later, when determining the flow speed at the rudders' plane.

To determine the working point of the propeller(s), open water characteristics and interaction coefficients are used. To explain this, it is useful to first introduce the following parameters:

$$Thrust\ deduction\ factor\ (t): R = (1 - t) . k_p . T \qquad \textit{Eq. 2.13}$$

$$Wake\ fraction\ (w): V_A = \left(1 - w_f\right) . V_s \qquad \textit{Eq. 2.14}$$

$$Advance\ Ratio: J = \frac{V_A}{n_p . D_p} \qquad \textit{Eq. 2.15}$$

$$Thrust\ coefficient: K_T = \frac{T}{\rho . n_p^2 . D_p^4} \qquad \textit{Eq. 2.16}$$

$$Torque\ Coefficient: K_Q = \frac{Q}{\rho . n_p^2 . D_p^5} \qquad \textit{Eq. 2.17}$$

$$Open\ Water\ Efficiency: \eta_o = K_T . \frac{J}{2\pi . K_Q} \qquad \textit{Eq. 2.18}$$

The *thrust deduction factor* represents a propeller-to-hull interaction and the *wake fraction* a hull-to-propeller interaction, more details about these interaction effects can be found in *Section 2.7*. The *Advance Ratio* represents the non-dimensional velocity at the propeller plane, and the open water efficiency, the amount of thrust that it is possible to generate with a certain torque. More information about these coefficients can be found in *Woud and Stapersma* (2003), [28]. *Figure 2.15* shows an example of a typical open water diagram, the evolution of K_T, K_Q and η_o with the advance ratio.

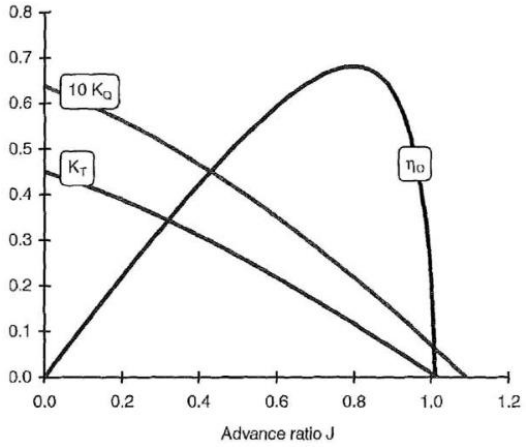

Figure 2.15: Example of a propeller open water diagram, *[28]*.

In order to determine the working point of the propeller in a certain condition ("condition 0" here) it is necessary to match the thrust produced by the propeller with the thrust required by the ship. This is done following the procedure described in [28]. This approach consists in creating a *thrust coefficient* for the ship, *Eq. 2.19*, when traveling at condition 0, and then determine the intersection point with the propeller K_T – curve, in the open water diagram. From here it is then possible to determine *J* (advance ratio) and consequently n_p (propeller frequency), as illustrated in *Figure 2.16*.

$$K_{T,ship} = \frac{T_0}{\rho . V_{A,0}^2 . D_p^2} . \left(\frac{\mathrm{V_{A,0}}}{\mathrm{n_p . D_p}} \right)^2 = \frac{T_0}{\rho . V_{A,0}^2 . D_p^2} . J^2 \qquad \textit{Eq. 2.19}$$

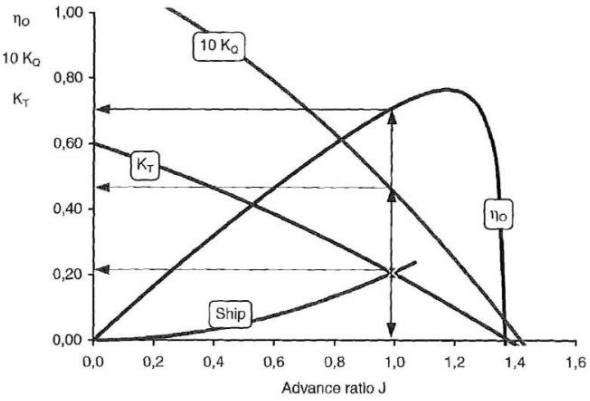

Figure 2.16: Illustration of the procedure to determine the propeller working point, [28].

Note that this method only considers steady conditions. However, for manoeuvring purposes, it can be assumed a constant propeller frequency during manoeuvring in the absence of controlled speed changes, as mentioned by *M.Bonci* in [26]. Once the advance ration is determined for the condition before the start of the manoeuvre, it is then possible to determine the propeller rate for the entire manoeuvre. However, during manoeuvring there is the well know speed drop phenomena, which decreases the advance speed and consequently the advance ratio (*J*). In this case the thrust and torque coefficients can be updated according to the open water characteristics of the propelled, wake fraction and thrust deduction fraction.

2.6 STEERING SYSTEM

The steering system is responsible for controlling the direction of a vessel. Since this research is specially focused on the *RPA8* case, the only steering device considered will be conventional rudders. Often rudders are placed at the stern, in the slipstream of the hull and propellers to allow good manoeuvring characteristics and increase their effectiveness (more lift at lower ship speeds). However, this makes them subjected to strong flow disturbances, that requires careful mathematical modelling.

The forces on the rudders are mainly dependent on the inflow speed and angle. Furthermore, once these flow conditions are known, forces can be determined and converted to the vessel's frame of reference. Thus, this section is divided in three subsections: Rudder Inflow Speed, Rudder Inflow Angle and Rudder Forces.

2.6.1 RUDDER INFLOW SPEED

As previously referred, rudders are often in the wake of the hull and propeller. According to *Molland et al.* in [25], swirl and tangential velocities can be neglected for the ship manoeuvrability at moderate speed. This assumption is no longer valid for vessels working at high thrust loading condition (low advance ratio, J), since the tangential speed of the propeller's slipstream is relatively high when compared to the axial speed. In certain cases, this can lead to a thrust production by the rudders, as illustrated below:

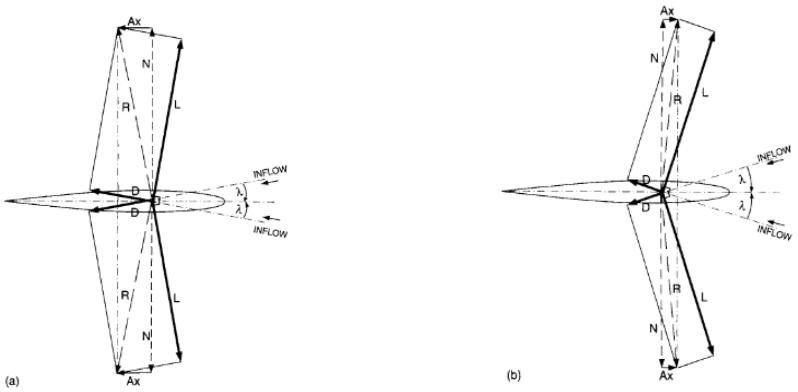

Figure 2.17: (a) Rudder forces in a usual free sailing condition. (b) Rudder forces for a high thrust loading condition, [25].

Moreover, due to non-uniform hull wake and higher speed of the tip of the propeller blades, the slipstream velocity distribution is not uniform, as can be observed in *Figure 2.1 b*. However, for most of manoeuvring studies, this effect can be represented by an averaged uniform velocity distribution (*Figure 2.18 a*), as suggested by [25]. This allows to considerably simplify the mathematical modelling of the propeller wake.

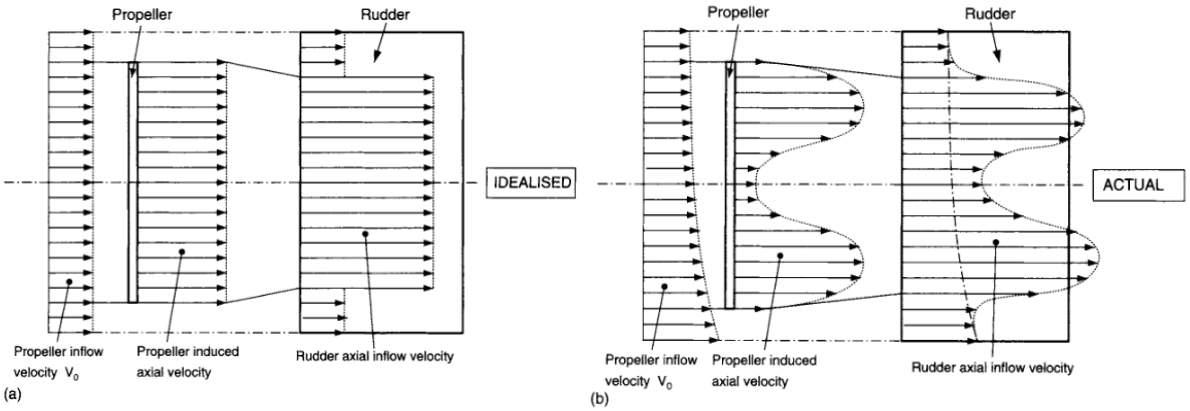

Figure 2.18: (a) Idealized propeller slipstream. (b) Real propeller slipstream, [25].

The propeller-induced velocity on the rudder can be obtained by computing the axial flow velocity at the rudder location, using actuator disk theory. When combining actuator disk theory with a *Gutsche*-type correction (C_R) it is possible to obtain the following approximation for the propeller-induced axial velocity at the rudder, as explained in [25]:

$$C_R = 0.5 + \frac{0.5}{1 + \left(\frac{0.15.D_P}{x_R}\right)} \qquad \textit{Eq. 2.20}$$

$$V_r = V_0 \left[1 + C_R.\left(\sqrt{1 + \frac{8.K_T}{\pi.J^2}} - 1\right)\right] \qquad \textit{Eq. 2.21}$$

As a result of mass conservation, the propeller slipstream is narrower downstream than the propeller diameter, due to the acceleration of the flow (*Figure 2.14*). Thus, the rudders are often not fully immersed in the propeller slipstream. By applying mass conservation *Eq. 2.10*, it is possible to estimate the size of the propeller slipstream at the rudder location:

$$D_R = D_P.\sqrt{\frac{V_{prop}}{V_r}} \qquad \textit{Eq. 2.22}$$

V_r (flow velocity at the rudder location) is known, from *Eq. 2.21*. And V_{prop} (flow velocity at the propeller plane) is given by *Eq. 2.12*. Where, according to [25], V_2 (maximum propeller slipstream velocity) can be computed by:

$$V_2 = V_0.\sqrt{1 + \frac{8.K_T}{\pi.J^2}} \qquad \textit{Eq. 2.23}$$

Note that V_r is only applicable to the region of the rudder affected by the propeller slipstream. For the rest of the rudder it is often assumed V_A (propeller advance velocity), as described by [8].

2.6.2 RUDDER INFLOW ANGLE

As mentioned in the beginning of this section, the flow at the rudder is often disturbed by the presence of the hull and propulsion system. As it can be expected, this causes changes on the rudder's inflow angle. This chapter presents a systematic approach to mathematically model these effects. More details about the interaction between hull and rudder will be later discussed in *Section 2.7.* In order to approach the mathematical description of the rudder's inflow angle, it is necessary to introduce the following definitions:

- **Rudder deflection** (δ): Angle between the rudder chord and longitudinal ship axis
- **Geometric inflow angle** (β_R): Drift angle at the rudders' location. Considering an *Eulerian* frame of reference, it is given by:

$$\beta_R = -atan\left(\frac{v + x_R.r}{u - y_R.r}\right) \qquad \textit{Eq. 2.24}$$

- **Hydrodynamic inflow angle** (α_0): Inflow angle relative to the longitudinal ship axis.
- **Effective rudder angle** (α_E): Angle between the rudder axis and the Hydrodynamic inflow angle.

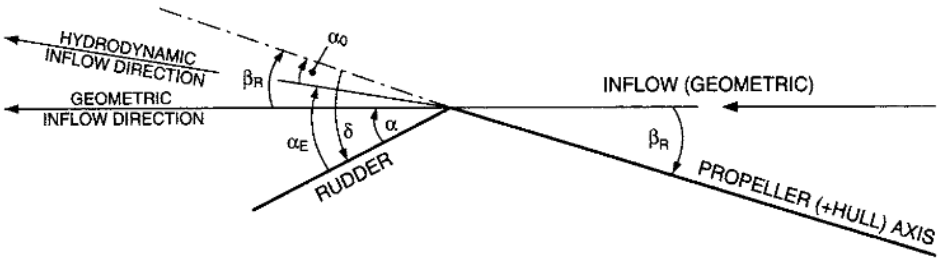

Figure 2.19: Flow straightening terminology, [25]

The rudder forces are dependent on effective rudder angle (α_E). This one is given by:

$$\alpha_E = \delta + \alpha_0 \qquad \textit{Eq. 2.25}$$

The rudder deflection (δ) is known but the hydrodynamic inflow angle (α_0) is not. However, in [25], it is assumed that α_0 is given by:

$$\alpha_0 = \gamma_R.\beta_R \qquad \textit{Eq. 2.26}$$

Where γ_R, is the flow straightening factor. The combination of *Eq. 2.25* and *Eq. 2.26* results in:

$$\alpha_E = \delta + \gamma_R.\beta_R \qquad \textit{Eq. 2.27}$$

The determination of the flow straightening coefficients for this research will explained in *Section 5.*

2.6.3 RUDDER FORCES

The previous sections aimed to introduce methods to determine rudders' inflow speed and angle. This section will be focused on the determination of rudders' forces during maneuvering. Throughout the years multiple methods have been proposed to compute forces on 3D finite wings. However, few of them are able to combine simplicity with accuracy in the way *Lifting Line Theory (LLT)* does. Therefore, this section will be focused on this method, since it is widely used for manoeuvring models, see [29].

The *Lifting Line Theory* was the first successful quantitative model used to predict aerodynamic forces on finite wings. This theory allows practical computations of the properties of finite 3D wings. According to [30], the main assumptions of this theory are:

- The thickness and chord are much shorter than the span;
- The wing is unswept (leading edge perpendicular to free stream flow);
- The flow is inviscid, steady and perpendicular to the span.

The underlying hypothesis of *LLT* is that a finite wing can be represented by a superposition of an infinite number of vortex filaments of strength Γ fixed in space (bound vortices). However, by the *Helmholtz's Theorem*, a vortex filament cannot end in the fluid (assuming inviscid flow). Therefore, at the extremities of each filament the bound vortex is extended downstream to infinity, this is often called a horse-shoe vortex, [30].

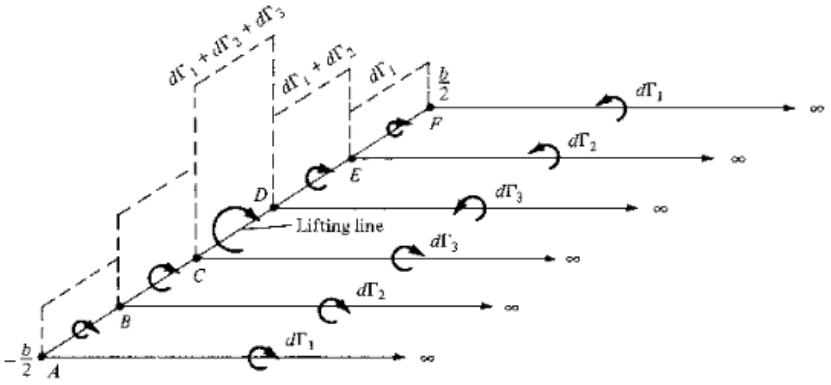

Figure 2.20: Superposition of a finite number of horseshoe vortices along the lifting line (span of the wing), [30].

The superposition of infinite horse-shoe vortices creates a continuous distribution of vorticity $\Gamma(y)$, leading to a continuous variation of downwash created by the trailing vortices, which induces a variation of angle of attack along the wing span. This allows not only to take into account the lift distribution over the wing span but also to compute the induced resistance due to the trailing vortices. In the end the *LLT* relates lift distribution with induced drag and shows that an elliptical chord distribution and a high aspect ratio are beneficial. Furthermore, it also shows that the drag scales with the lift squared, [30].

$$C_D = c_d + \frac{C_L^2}{\pi . e . AR} \qquad \textit{Eq. 2.28}$$

Where c_d is the drag coefficient of the foil section, e is the span efficiency factor (1 for elliptical chord distribution, <1 for other type of chord distribution), AR is the aspect ratio and C_L the 3D lift coefficient that (according to [30]) for an elliptical wing can be approximated by:

$$C_L = C_l \left(\frac{AR}{AR + 2} \right) \qquad \textit{Eq. 2.29}$$

Note that for conventional foil sections C_l and C_d can be easily found in the literature, for instance [31]. However, this formulation is only valid for high aspect ratio wings ($AR > 4$), which is often not the case for rudders. Therefore, *Fujii et al.* presented in [32], an approximation based on lifting line theory for the 3D lift coefficient for small aspect ratio rudders:

$$C_L = \frac{6.13.AR.\sin(\alpha_E)}{2.25 + AR} \qquad \textit{Eq. 2.30}$$

Note that the *AR* here considered is the effective aspect ratio, *i.e.*: including mirror effects when close to walls. Standard factors for different situations can be found in [25].

The simplicity of this theory allows a good comprehension of the inviscid phenomena involved in the flow over an idealized finite wing with moderate to high aspect ratio. This is the main reason to be often used to mathematically model control surfaces, *e.g.:* rudders.

However, near the stalling region these predictions based on lifting line theory are inappropriate. This is mainly due to the occurrence of flow separation (viscous effects) and spanwise flows, as can be seen in *Figure 2.21*. Therefore, it is necessary to be careful when modelling rudders with *LLT*, since these ones are often subjected to stalling.

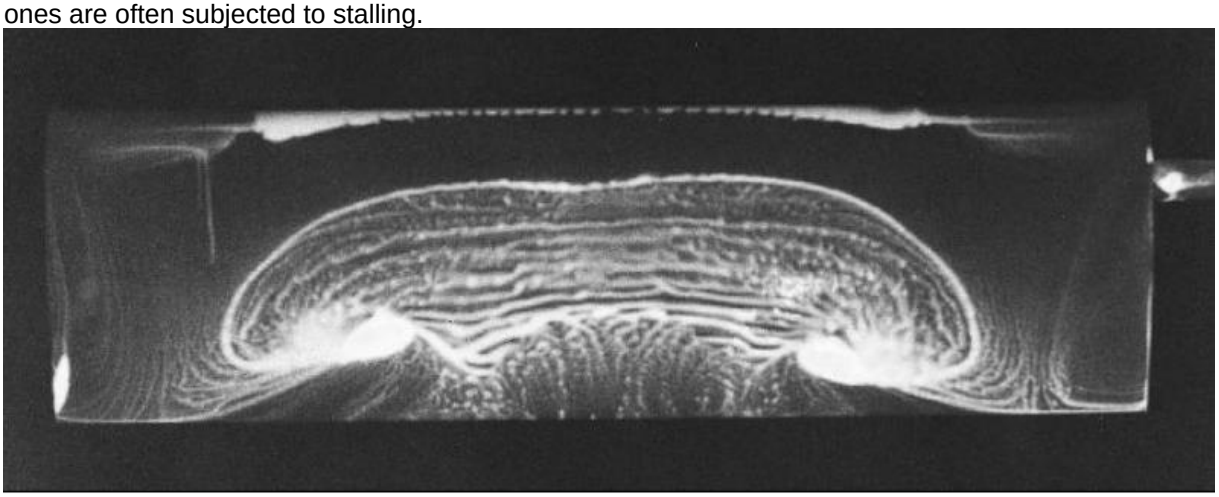

Figure 2.21: Spanwise flow over Clark Y-14 foil section after stall. $AR = 3.5$, $\alpha = 22.8°$, $Re = 245\,000$ (based on chord length), [30].

Once the lift and drag coefficients are known, the rudders' forces are given by:

$$D = \frac{c_D.\rho.U^2.S}{2} \qquad \textit{Eq. 2.31}$$

$$L = \frac{c_L.\rho.U^2.S}{2} \qquad \textit{Eq. 2.32}$$

Recall that, drag force is a force aligned with the freestream while a lift force is a force perpendicular to the free stream (frame of reference of the external flow). Therefore, to determine their effect on frame of reference of the vessel, it is necessary to translate them. When considering 4 DOF (surge, sway, yaw and roll), this becomes:

$$X^{R0} = -D.\cos(\alpha_0) + L.\sin(\alpha_0) \qquad \textit{Eq. 2.33}$$

$$Y^{R0} = (D.\sin(\alpha_0) + L.\cos(\alpha_0)).\cos(\phi) \qquad \textit{Eq. 2.34}$$

The convention used in this research assumes $D > 0$.

2.7 INTERACTION EFFECTS

As mentioned in *Section 2.4.1,* interaction coefficients are a fundamental part of a modular manoeuvring model. These ones are responsible for making the connection between the different constitutive elements of the vessel. This section aims to introduce the most significant interaction effects and the mathematical formulations to evaluate them.

2.7.1 HULL TO PROPELLER INTERACTION

The most significant example of hull to propulsion interaction is the wake fraction (w_f). This one is caused by the fact that the flow at the propeller plane is disturbed by the presence of the hull. Often resulting in a deceleration of the propeller's inflow.

This coefficient can be determined experimentally or using numerical methods. According to *Larsson and Raven* in [33], experimentally, it consists on measuring the wake field of the bare hull (nominal wake field) using: a pitot tube rake that can be rotated around the propeller shaft, or *LDV(Laser Doppler Velocimetry)/PIV (Particle Image Velocimetry)*. With CFD (numerically) it consists on doing an average of the normalised inflow speed at the propeller location.

This effect is sensitive to the motion of the vessel. The influence of the drift angle on the wake fraction has been a relevant topic of research in the last decades, leading to the development of semi-empirical formulations. One of these formulations that relates the wake fraction with the drift angle was proposed by *Inoue et al.* in [34], for single-screw container vessels:

$$w_f(\beta_p) = w_f(0).e^{-4.\beta_p^2} \qquad \textit{Eq. 2.35}$$

However, this kind of semi-empirical formulations have a rather limited range of applicability. Since the *RPA8* is a twin-screw vessel, the previous formulation is not applicable in the context of this research. Therefore, the influence of drift on the wake fraction is determined numerically using virtual captive tests (*Section 5.1*).

2.7.2 PROPELLER TO HULL INTERACTION

The thrust deduction factor (t) is a propulsion to hull interaction coefficient. In general, a propulsion system close to the hull is responsible for increasing the flow speed at the stern, decreasing eventual flow separation at stern but at the same time increasing the viscous resistance. Therefore, $t > 0$ when the presence of the propulsion system increases the vessel's resistance and vice-versa.

The most common way to determine t is to compare the resistance of the vessel in towing and self-propelled condition, or the resistance with actuator disk in CFD. This can be done by measuring the resistance on the hull using CFD or by measuring the thrust delivered by the propeller experimentally.

However, according to *S.Sutulo* in [8], the thrust deduction factor (t), is weakly affected by transverse velocity at moderate manoeuvring speeds. Thus, this one is often assumed constant for manoeuvring prediction purposes.

2.7.3 HULL & PROPULSION TO RUDDER INTERACTION

In *Section 2.6.2*, γ_R was introduced as the flow straightening factor. This factor accounts of the disturbances caused by hull and propulsion on rudder inflow angle. Generally, in the literature it is assumed that the hull and propulsion system tend to straighten the flow, as illustrated below:

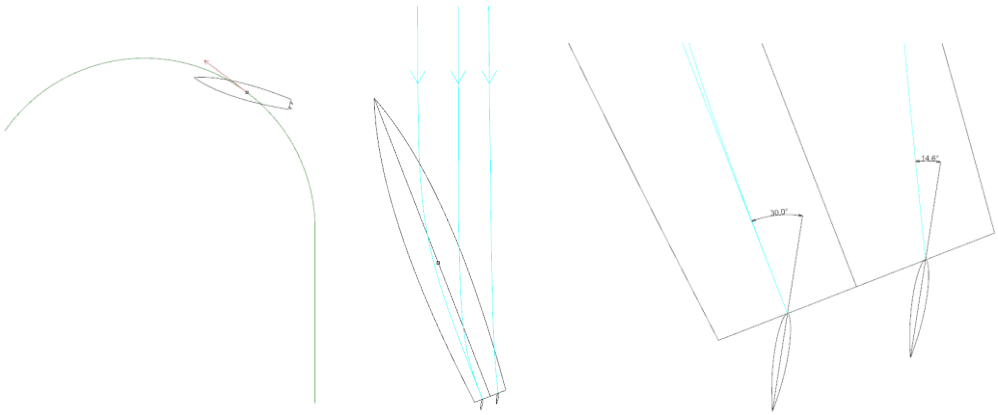

Figure 2.22: Illustration of flow straightening effects for a twin rudder ship.

The determination of flow straightening coefficients is discussed in *Chapter 5.*

2.7.4 RUDDER TO HULL INTERACTION

The deflection of the rudder changes the pressure field around the hull, increasing its lift, analogously to wing-flap interaction, as described by *H.Yasukawa et al.* in [35] and where the following illustration is provided:

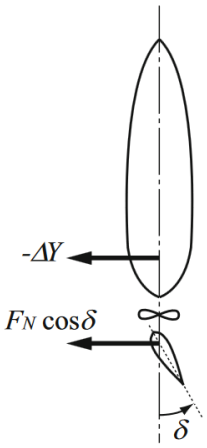

Figure 2.23: Illustration of rudder to hull interaction phenomenon, [35].

This effect on the sway force can be mathematically described by using a coefficient a_H that represents the ratio between the lateral force induced by the rudder on the hull and the lateral rudder force (Y^{R0}), as done in [35]:

$$Y^R = Y^{R0}.(1 + a_H) \qquad \textit{Eq. 2.36}$$

Furthermore, to determine the yaw moment caused by this effect, it is necessary to define the application point of this force, x_{RH}. This results in the following simplified formulation for the yaw moment due to rudder deflection:

$$N^R = Y^{R0}.(x^R + a_H.x_{RH}) \qquad \textit{Eq. 2.37}$$

Rudder-to-hull interaction forces in surge are in general represented using a so-called steering resistance deduction factor, t_R. According to *Yasukawa* and *Yashimura* in [35], the total surge force caused by the rudder (X^R) can be represented by:

$$X^R = X^{R0}.(1 - t_R) \qquad \textit{Eq. 2.38}$$

However, this effect is often neglected, since the x-projected area of the hull's affected region is considerably small, leading to forces much smaller than the rudder's drag. In this case X^R becomes:

$$X^R = X^{R0} \qquad \textit{Eq. 2.39}$$

Note that X^{R0} and Y^{R0} represent just the forces acting on the rudder.

Kose K. et al. in [36] showed that for crude carriers the rudder-hull interaction effect can be significant with $0.3 < a_H < 0.4$, meaning that this interaction effect represents $30\% - 40\%$ of the total rudder force. Furthermore, *Söding in* [37], developed semi-empirical formulations of a_H and x_{RH} for container vessels:

$$\begin{cases} a_H = \dfrac{1}{1 + \left(\dfrac{4.9.e_R + 3.c_R}{T_d}\right)^2} \\ \dfrac{x^R + a_H.x_{RH}}{1 + a_H} = x^R + \dfrac{0.3.T_d}{\dfrac{e_R}{T_d} + 0.46} \end{cases} \qquad \textit{Eq. 2.40}$$

Where T_d represents the draft, $e_R$the mean distance between the front edge of the rudder and the aft of the hull and c_R the mean rudder chord. Although this type of formulation is practical, it might not be correct when applied to different vessels' types, namely patrol vessels like the *RPA8.*

For the same reason presented in the previous section, the determination of these interaction coefficients will be discussed in *Chapter 5.*

2.7.5 RUDDER TO PROPULSION INTERACTION

Rudder to Propulsion interaction, is the influence of the rudder on the propeller performance. Since for most of the cases the rudder is in the wake of the propeller, this interaction is expected not to be relevant and therefore hard to find in the literature.

2.8 MOTION STABILITY FROM A SYSTEMS AND CONTROL THEORY PERSPECTIVE

The application of systems and control theory to assess manoeuvring performance is a very interesting and important topic. It provides good understanding of the manoeuvring characteristics, often being utilized for optimization of dynamic behavior of vessels. Although most of the common methods of system's analysis are only applicable to linear systems, it is possible to apply them to non-linear systems if these ones are linearized, as explained by *Franklin et al.* in [15]. The linearity assumption is not often fully applicable to the maneuverability of vessels. However, systems and control theory helps to draw conclusions about the vessel's motion stability. For this reason, this research will not focus on this topic, however the topic is introduced for a good understanding of vessel's dynamics.

From the control theory perspective, operating a vessel is a feedback and feedforward type of control. It is feedforward control because the helmsman can take an action before the system notices any change (e.g.: avoid a collision). It is feedback if the helmsman is aiming to control the heading of the vessel, see *Figure 2.24*. For the stability analysis of the motion of the vessel, only the feed-back is relevant, for heading control.

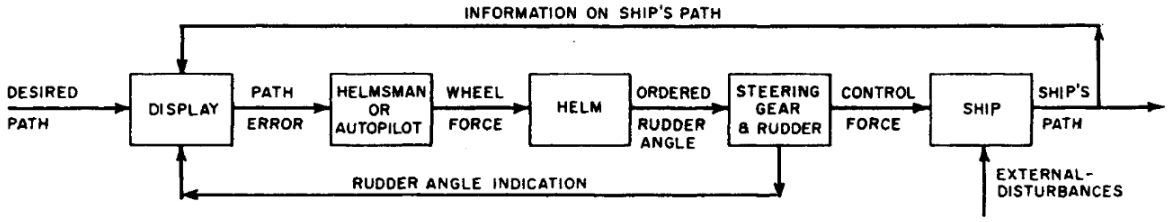

Figure 2.24: Control theory perspective of a vessel, [14].

Assuming a linear model (for simplicity) the dynamics of a hull in yaw can be described using a transfer function $G(s)$, in the *Laplace* space, as done in [13]. $G(s)$ defines a simple linear relation between a yaw moment and a yaw rate. The position of its roots in the complex plane characterize the stability of this system, as shown below:

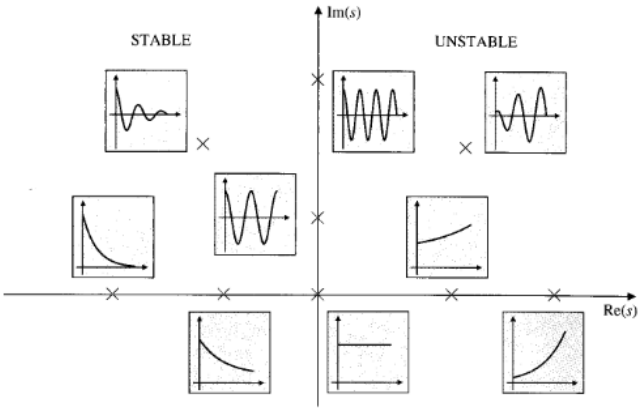

Figure 2.25: Influence of the position of the system's roots on its response, [15].

As can be seen in *Figure 2.25*, a stable system has the roots on the negative part of the real axis, while an unstable system has the roots on the positive side of the real axis. To decrease the response time of a system (time to reach the desired heading or rise-time in control theory), it is necessary to increase the gain of the controller (e.g.: larger rudders) or increase the gain of $G(s)$ (e.g.: reduce the skeg, increase trim forward). This moves the dominant root of the system to the right, closer to the imaginary axis, reducing the system damping. However, if the gains are too big, the system becomes unstable or the overshoot becomes too large, what leads to an increase of the zig-zag period (related to the settling-time in control theory). Therefore, at the end the parameter that mostly influences the controllability (directional stability or handling) of the vessel is the damping in yaw. A critically damped vessel combines a quick response with no overshoot, see *Figure 2.26*.

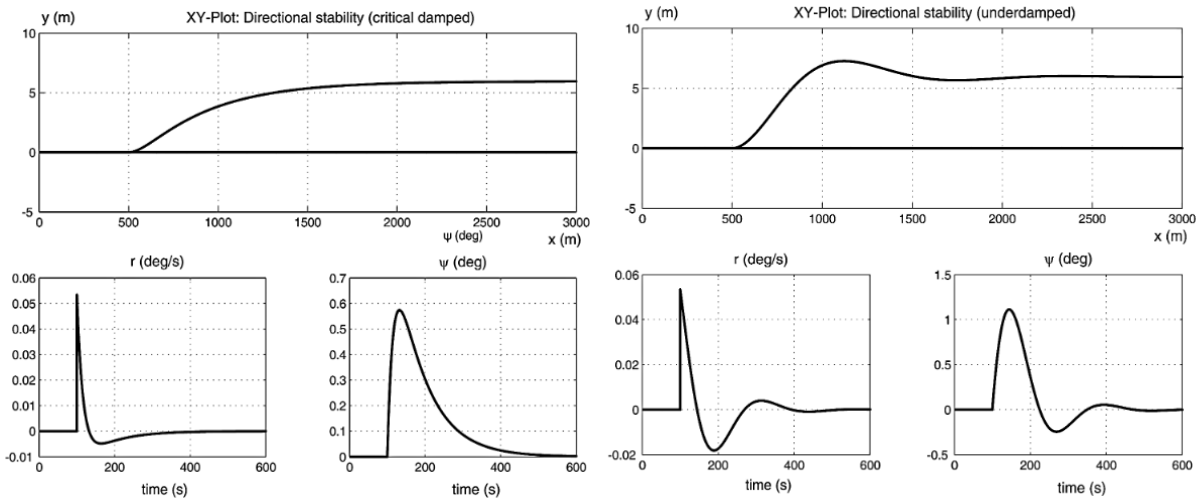

*Figure 2.26: **Left**: Critically damped vessel response to perturbation in yaw. **Right**: Underdamped vessel response to perturbation in yaw. [13]*

Conclusions about the course keeping capability can also be reached by doing gentle zig-zag manoeuvres such as 5°-5°, as referred in [8]. The aim of this test is to evaluate the behavior of the vessel at higher frequencies of steering. Since every system has a delay in response, it is expected that at certain frequencies the system enters in resonance. This can be analyzed in detail by a frequency domain analysis using a *Bode Diagram*, this one shows the amplitude and phase angle of the system's response with the variation of the input frequency.

By applying linear control theory to a vessel, it is possible to find a relatively simple way to assess whether a vessel is course stable or not. For this a fully linear sway-yaw system is assumed:

$$\begin{bmatrix} m - Y_{\dot{v}} & 0 \\ 0 & I_{zz} - N_{\dot{r}} \end{bmatrix} \begin{Bmatrix} \dot{v} \\ \dot{r} \end{Bmatrix} + \begin{bmatrix} -Y_v & -(Y_r - m.U) \\ -N_v & -N_r \end{bmatrix} \begin{Bmatrix} v \\ r \end{Bmatrix} = \begin{Bmatrix} Y_\delta \\ x^R.Y_\delta \end{Bmatrix} \delta \qquad \textit{Eq. 2.41}$$

Note that U is assumed to be a constant longitudinal speed. The right-hand side term represents external forces and moments, in this case a rudder linear model where $Y_\delta.\delta$ represents the sway force created when the rudder is deflected by δ and x^R represents the x-position of the rudder in relation to the centre of gravity. This is a *Single Input Multiple Output* (*SIMO*) system. To simplify the mathematical manipulation of this system, this one is represented in the following way:

$$[M].\{\dot{v}\} + [B].\{v\} = \{F\}.\delta \qquad \textit{Eq. 2.42}$$

Since it is a linear system, it can be solved in the *Laplace* domain:

$$[M].s.V(s) + [B].V(s) = \{F\}.\Delta(s) \qquad \textit{Eq. 2.43}$$

The transfer function of this system is then given by:

$$G(s) = \frac{V(s)}{\Delta(s)} = \frac{\{F\}}{[M].s + [B]} \qquad \textit{Eq. 2.44}$$

As previously explained, a stable system has its roots in the negative part of the real axis. In this case to assess this it is necessary to determine the characteristic equation of the system. This one is given by (see *Fossen* in [13]):

$$\det([M].s + [B]) = A.s^2 + B.s + C = 0 \qquad \textit{Eq. 2.45}$$

Where:

$$\begin{cases} A = \det([M]) = (m - Y_{\dot{v}}).(I_{zz} - N_{\dot{r}}) \\ B = -Y_v.(I_{zz} - N_{\dot{r}}) - N_r.(m - Y_{\dot{v}}) \\ C = \det([B]) = Y_v.N_r - (Y_r - m.U).N_v \end{cases} \quad \textit{Eq. 2.46}$$

According to the criteria of *Routh-Hurwitz* (see *Franklin et al.* in [15] or *Fossen* in [13]), a necessary and sufficient condition for the stability of this system is that:

$$A, B, C > 0 \quad \textit{Eq. 2.47}$$

By the definition of mass, added mass and damping A and B are always positive in the context of ship manoeuvring, as mentioned by *Fossen* in [13]. Therefore, the non-trivial condition for course stability boils down to $C > 0$:

$$Y_v.N_r - (Y_r - m.U).N_v > 0 \quad \textit{Eq. 2.48}$$

Since Y_v and N_r represent a reaction force/moment due to a motion and this one is in the opposite direction of the motion, these two coefficients in the context of ship manoeuvring are always negative, therefore:

$$Y_v.N_r > 0 \quad \textit{Eq. 2.49}$$

In *Eq. 2.59*, N_v represents the yaw moment due to sway, also known as the *Munk Moment*, see the following picture:

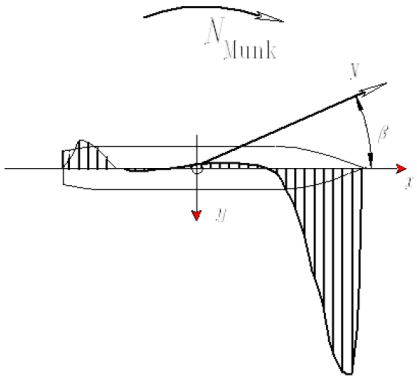

Figure 2.27: Lateral force distribution for real fluid and consequent *Munk Moment, [8].*

For conventional vessels, a negative drift angle leads to a positive *Munk Moment,* as shown in the previous picture. In this condition the *Munk Moment* is a destabilizing moment in yaw, since it tends to further increase the drift angle instead of correcting it. Therefore, N_v is often negative:

$$N_v < 0 \quad \textit{Eq. 2.50}$$

As previously mentioned in *Section 2.2.1,* the skeg decreases this destabilizing moment, by increasing N_v (making it less negative). Regarding Y_r this one represents the sway force due yaw rate, it is not necessarily negative or positive.

According to *Sutulo* in [8], a more physical interpretation of *Eq. 2.48* can be found by making a simple mathematical transformation:

$$Y_v.N_r > (Y_r - m.U).N_v \Leftrightarrow \frac{N_r}{(Y_r - m.U)} > \frac{N_v}{Y_v} \Rightarrow l_r > l_v \quad \textit{Eq. 2.51}$$

This relation is only true for $(Y_r - m.U).Y_v > 0$. Here l_r represent the arm of the yaw moment due to yaw rate (a stabilizing moment) and l_v the arm of the yaw moment due to sway speed (a destabilizing moment, see *Figure 2.27*). Therefore, for a course stable vessel the stabilizing arm (l_r) needs to be larger than the destabilizing one (l_v).

More details about systems and control theory and its applications to dynamics of vessels, can be respectively found in [15] and [13].

2.9 COMPUTATIONAL FLUID DYNAMICS

Computational Fluid Dynamics (*CFD*) is a general term that englobes any algorithm to solve fluid flows. One of the first applications was for weather forecasting, it was done by *Richardson* in 1922, [38]. At this time *Richardson* solved by hand a grid over Europe with cells of 200x200 km. At the end the solution diverged, turbulence was pointed as the cause. Nowadays, thanks to advances in the fields of fluid dynamics, numerical schemes and computer science, it is possible to use these methods for research and practical engineering applications. In the end *CFD* allows to reduce experimental costs and to have access to many flow field properties without disturbing the flow with the presence of sensors. However, if it is not properly set up, it can lead to inaccurate results.

S.Hickel in [39] presents the following diagram explaining the multiple steps involved in CFD simulations:

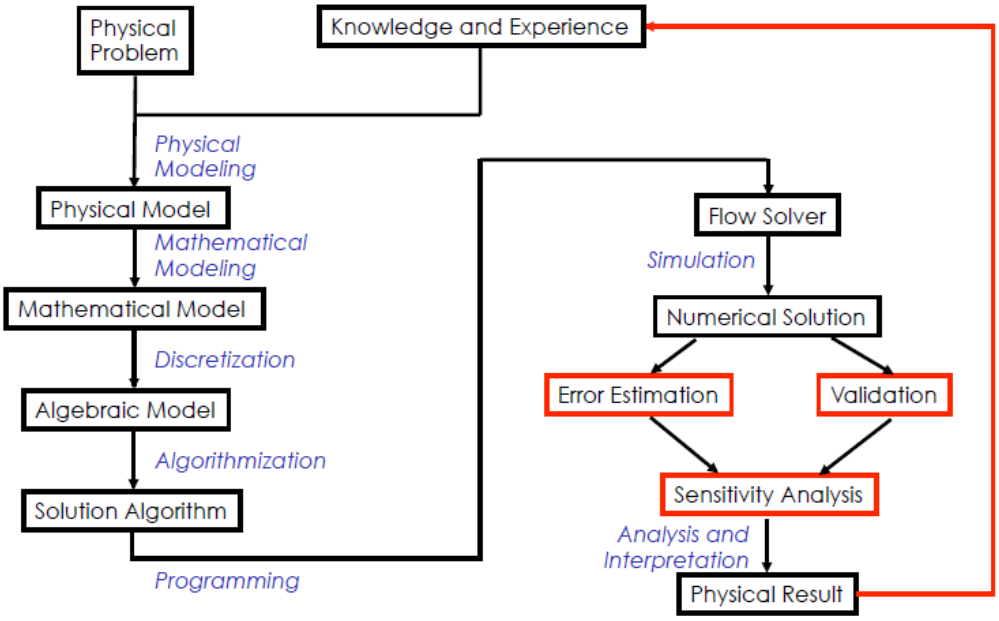

Figure 2.28: Diagram of the execution and analysis of CFD, [39].

This section aims to briefly explain what is behind of some of the main blocks of Figure 2.28, namely the physical, mathematical and algebraic models. Verification and validation (V&V) will also be introduced and a validation method will be presented.

2.9.1 PHYSICAL MODEL

The physical modeling aims to define which physical aspects are relevant for the problem and which ones can be neglected. This is often done with the help of non-dimensional coefficients such as *Reynolds* number (R_n), *Froude* number (F_n), *Mach* number (M_n), among others. Giving a simple example, in the case of a vessel sailing at moderate speed, where L is the ship length and V its speed:

- $R_n = \frac{V.L}{\nu} \gg 1$: Indicating that inertial effects are dominant over viscous effects, what may lead to high turbulence levels especially when $R_n > 5 \times 10^5$ (see *Kundo* in [27]). Therefore, turbulent flow should be taken into account.

- $F_n = \frac{V}{\sqrt{g.L}} \approx 1$: This shows that inertial effects are about of the same level of relevance as gravitational effects. This shows that for instance gravity waves might play an important role on a flow around a ship, therefore free surface should be considered.

- $M_n = \frac{V}{c} \ll 1$: This shows that the inertial effects of the problem are not strong enough to be comparable to the celerity of sound. Therefore, compressibility effects can be negligible.

This type of analysis allows to build a simplified physical model of the problem of interest, where some effects are neglected. It is important to reach a balance between the level of simplification and the desired accuracy. A too complex physical model leads to expensive computations without a significant increase of accuracy, while a too simplified model leads to cheap computations but not enough accuracy.

2.9.2 MATHEMATICAL MODEL

The second step is to mathematically describe the physical model previously defined. Although, currently this is an important topic of research in many fields, it is not the focus of this research. Therefore, only the main equations and steps will be explained here. More details about this can be found in general fluid mechanics and *CFD* literature, for example [27] and [40], respectively.

This section will focus on the principal laws of fluid dynamics, on the mathematical representation of turbulent flows and briefly on boundary conditions

2.9.2.1 Mass Conservation

Mass conservation, states that there is no production or destruction of mass. Therefore, the rate of change of mass inside a control volume is equal to the net mass flow through the boundaries. For a control volume, this can be represented in the integral form (weak form) by:

$$\frac{d}{dt}\iiint_{CV} \rho \, dV = -\oint_{CS} \rho(\vec{u}.\vec{n}) \, dS \qquad \textit{Eq. 2.52}$$

Here $\vec{u} = (u, v, w)$ represents a velocity vector and $\vec{n}$ a unitary normal vector to the surface.

However, this statement is strictly defined for a control volume, to generalize it and facilitate mathematical manipulation, it should be transformed in its differential form (strong form). This can be achieved by considering an infinitesimal small control volume and applying the divergence theorem, leading to the so called continuity equation, see [24] and [27]:

$$\frac{d\rho}{dt} + \nabla.(\rho.\vec{u}) = 0 \qquad \textit{Eq. 2.53}$$

From *section* 2.9.1, it is known that the flow around a vessel at moderate speed, can be considered incompressible, with this assumption the mass conservation condition can be simplified to:

$$\nabla . \vec{u} = 0 \qquad \textit{Eq. 2.54}$$

2.9.2.2 Momentum Conservation

The *Newton's* second law, states that the sum of the forces acting on moving object (considering an inertial frame of reference) is causes a variation of momentum in time, mathematically this is represented by:

$$F = \frac{d}{dt}(m.v) \qquad \textit{Eq. 2.55}$$

The application of this law to a control volume is called momentum conservation law. This law states that the rate of change of momentum in a control volume is equal to the rate of flow of momentum through the control volume boundaries, plus forces acting on the boundary surfaces, plus body forces in the control volume. The mathematical representation of this, is given by the *Cauchy Momentum Equation,* the derivation can be found in [27]:

$$\frac{d}{dt}\iiint_{CV} \rho.\vec{u}\, dV = -\oint_{CS} \rho.\vec{u}.(\vec{u}.\vec{n})\ dS + \iint_{CS} \vec{t}(\vec{n})\, dS + \iiint_{CV} \vec{f}\ dV \qquad \textit{Eq. 2.56}$$

Here $\vec{t}$ represents the stress vector and $\vec{f}$ a body force per unit volume. Note that, so far, no assumption has been made for the specific case of fluids. Therefore, the *Cauchy Momentum Equation* is a general form of *Newton's Second Law* for continuum. If the stress vector is modeled for fluids (no shear stiffness) it will lead to the *Navier-Stokes Equations* (explained below), otherwise $\vec{t}$ can be modelled for solids (shear stiffness) leading to a generalized differential form of Hook's Law*,* see [41].
The *Navier-Stokes Equations* is not more than the strong (differential) form of the *Cauchy Momentum Equation* for fluids, for an incompressible and Newtonian fluid is:

$$\rho\left(\frac{d\vec{u}}{dt} + u.\frac{d\vec{u}}{dx} + v.\frac{d\vec{u}}{dy} + w.\frac{d\vec{u}}{dz}\right) = -\nabla p + \mu\nabla^2\vec{u} + \vec{f} \qquad \textit{Eq. 2.57}$$

Or in a more compact notation:

$$\rho\frac{D\vec{u}}{Dt} = -\nabla p + \mu\nabla^2\vec{u} + \vec{f} \qquad \textit{Eq. 2.58}$$

Here p represents pressure and μ the dynamic viscosity of the fluid. It can be observed that the inertial forces (left hand side term) is equal to the sum of pressure, viscous and body forces. The derivation of these equations can be found in [27].

2.9.2.3 Mathematical Representation of Turbulent Flows

According to *Batchelor* in [42], turbulence is a flow regime characterized by chaotic changes in velocity and pressure. It is such a complex phenomenon that *W.Heisenberg* said:

"*When I meet God, I am going to ask him two questions: Why relativity? And why turbulence? I really believe he will have an answer for the first*"

By directly solving *Eq. 2.53* and *Eq. 2.57*, it is possible to accurately represent turbulence, even at small scales, this is called *Direct Numerical Simulation (DNS).* However, this is very computationally expensive and not often necessary. Therefore, to make the simulation of fluid flows more accessible, in the beginning of the 20th century, *Prandtl* proposed to model turbulence. This is particularly interesting for problems which only depend on the overall turbulent effects and not on the accurate modeling of turbulence, which is often the case when studying flow around ships. The fundamental assumption of turbulence modeling was earlier proposed by *Reynolds,* suggesting that the velocity at a fixed location in a turbulent flow is given by:

$$\vec{u} = \langle \vec{u} \rangle + \vec{u}' \qquad \textit{Eq. 2.59}$$

Where $\langle \vec{u} \rangle$ represents an average velocity vector and $\vec{u}$ a velocity fluctuation vector. By substituting this in *Eq. 2.53* and *Eq. 2.57*, and averaging, it is possible (with some mathematical manipulation) to derive the so called *Reynolds Averaged Navier-Stokes Equations (RANSE),* see [40]:

$$\nabla . \langle \vec{u} \rangle = 0 \qquad \textit{Eq. 2.60}$$

$$\frac{d\langle \rho \vec{u} \rangle}{dt} + \nabla . (\rho \langle \vec{u} \rangle \langle \vec{u} \rangle) + \nabla \langle p \rangle - \mu \nabla^2 \langle \vec{u} \rangle = -\nabla . (\rho \langle \overrightarrow{u'}\, \overrightarrow{u'} \rangle) \qquad \textit{Eq. 2.61}$$

Note that all the terms in the left-hand side of *Eq. 2.61* are known, since they are only dependent on averaged flow quantities. However, the term on the right-hand side is unknown, since it is an average of the product of two fluctuations. This term is called the Reynolds Stress Tensor (RST), and it is responsible for the production of turbulence! Therefore, the modeling of turbulence boils down to the modeling of the RST. Until these days many turbulence models have been developed and so far none of them is applicable to all types of turbulent flows, the choice of turbulent model can have a significant impact on the simulation results. Often a URANSE is used to define solution methods that include slow unsteady effects, as explained by Hickel in [39].

In case of a flow that is moderately influenced by turbulent structures, it possible to use other methods than RANSE and DNS, such as Large Eddy Simulation (LES). LES aims to accurately solve the most energetic scales (large scales), and to model the small turbulent scales (less energetic). This is done by applying a filter to the turbulent energy cascade:

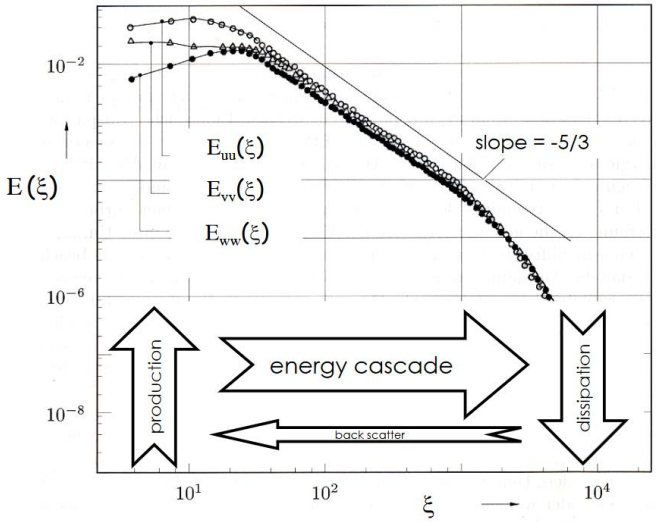

Figure 2.29: Turbulent energy cascade, [43].

Note that $E(\xi)$ represents the energy of the turbulence frequency ξ.

Although *LES* provides an increase in accuracy, it is still considered expensive and not necessary for most of engineering applications. Therefore, in this research *RANSE* will be used.

DNS, LES and *RANSE* are the 3 main methods in *CFD.* Other hybrid and zonal models have been developed with the aim of combining properties of these 3 (*e.g.: Detached Eddy Simulation-DES*).

2.9.2.4 Boundary Conditions

Boundary conditions are necessary in order to close the mathematical problem and allow finding a unique solution. In this section two types of boundary conditions will be briefly explained. According to *Ferzinger* and *Perić* in [40] their definition is:

- ***Dirichlet BC**:* Imposes a constant value for a variable at the boundary, *e.g.:* no slip condition:

$$u = v = 0 \qquad \textit{Eq. 2.62}$$

- ***Neumann BC:*** Imposes a gradient in a particular direction for a variable at the boundary, *e.g.:* slip condition:

$$\frac{du}{dy} = 0 \qquad \textit{Eq. 2.63}$$

More information about mathematical modelling of fluid dynamics for *CFD* can be found in *Ferzinger* and *Perić,* [40].

2.9.3 ALGEBRAIC MODEL

The previous mathematical models together form a system of non-linear coupled partial differential equations. To solve this system, it is required to use numerical methods. Actually, finding an analytic solution for this, it is considered one of the seven *millennium prize problems*. Solving this numerically, means discretising the domain of the equations (space and time) and making approximations to solve this system of equations for every element of the domain individually.

The most common numerical method applied for fluid dynamics is the *Finite Volume Method (FVM)* due to the nature of the equations, since all were derived from control volume approach, see [40]. In this method the computational domain is decomposed in non-overlapping control volumes (finite volumes). Then for every finite volume, the momentum and continuity equations are numerically solved, see [43]. However, to solve these equations in a discretised domain it is necessary also to discretize them, this means numerically representing their differential operators. For example, a first order upwind discretization scheme for the unsteady term of *Eq. 2.57*, is given by:

$$\frac{d\vec{u}}{dt} = \frac{\vec{u}^{(t+\Delta t)} - \vec{u}^{(t)}}{\Delta t} + \epsilon \qquad \textit{Eq. 2.64}$$

Here ϵ, represents the error, it can be estimated with *Taylor* expansion. The discretization errors can strongly influence the final solution in multiple ways (*e.g.:* numerical viscosity and divergence of the solution). One way of decreasing the discretization error, is to use higher order discretization schemes, however this increases the computational time.

Considering a simple example of an incompressible flow and an upwind discretization scheme, it is possible to note that the momentum equation has 2 unknowns: $\vec{u}^{(t+\Delta t)}$ and $p^{(t+\Delta t)}$. Therefore, one more equation is needed to close the problem. For this the *Poisson* equation is used. This equation is nothing more than the combination of the continuity equation *Eq. 2.53* with the momentum equation *Eq. 2.57*, what would ensure mass conservation. The following diagram shows a simple example of the final algorithm to solve incompressible flows:

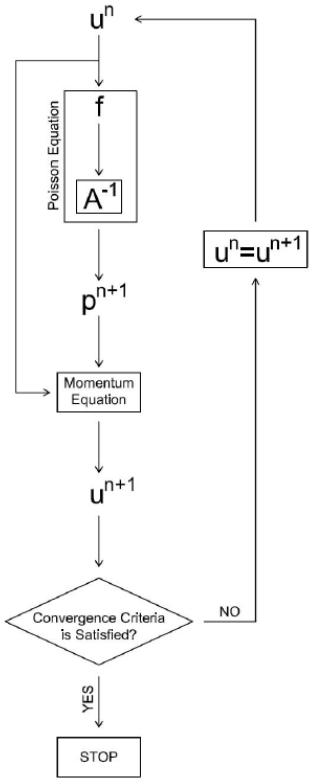

Figure 2.30: Example of a numerical algorithm of an upwind CFD scheme, [44]

More information about algebraic models and discretization techniques can be found in [40].

2.9.4 VERIFICATION AND VALIDATION

To ensure that the physical, mathematical and algebraic models are correct it is necessary to proceed to verification and validation of the simulation. According to *Roache* in [45], verification assesses whether the equations are being properly solved, while validation assesses whether the right equations are being solved. According to *Toxopeus* in [4], verification can be split in two parts: code verification (whether the code is solving the equations right) and solution verification (determination of numerical uncertainty). Since for this research there are no relevant experimental results for *CFD* validation and it is assumed that code verification has already been done by the developers (*NUMECA*), here just solution verification will be assessed. Solution verification can be assessed by means of grid and time step convergence studies. For this research, time step analysis will not be considered since it is assumed that the time step standards suggested by *NUMECA* and *Van Oossanen* are adequate.

Any measurement of a continuous variable cannot determine its true value, that would require infinite precision. Therefore, the only way of dealing with this is to determine a confidence interval (uncertainty) where the true value is expected to be. According to *Coleman and Steele* in [46], there are three main sources of errors *in CFD*:

- **Modelling Errors:** Errors due to geometry defects or even assumptions made when defining the physical and mathematical models
- **Input Errors:** Errors when defining the flow (*e.g.:* flow and fluid(s) properties)
- **Numerical Errors:** Round-off errors, iterative errors and discretization errors.

According to *Eça* and *Hoekstra* in [47], solution verification focuses just on the numerical errors. Round-off error is due to the finite precision of computers. Iterative error is related to the residual error associated to the convergence of the iterative process. Finally, the discretization error is due to the numerical approximations made (*e.g.: finite volume method*). According to [47], this last one is the only one decreasing with the grid refinement and it is the most dominant one in practical *CFD* applications. Therefore, in [47], it is assumed that the round-off and iterative errors are negligible when compared to the discretization error.

Eça and *Hoekstra* in [47], proposed a procedure to estimate the numerical uncertainty based on a *least square root* method and systematic grid refinements. For reliable results this method requires at least 4 different grids with systematic refinement steps preferably. Here the discretization error is represented by power series expansions. At the end it provides a systematic and practical approach to determine uncertainties, with a 95% confidence interval. The following scheme was proposed by *Xin* and *Stern* in [48] and it represents the method described in [47]:

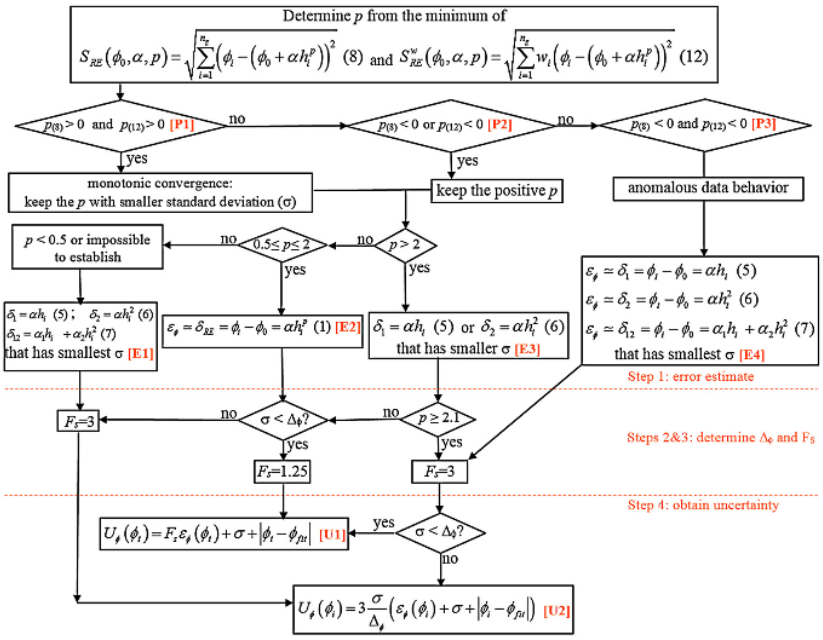

Figure 2.31: Block diagram of the Least Square Root method, [48].

Although this method was developed for structured and geometrically similar grids, often unstructured grids are used due to their capability of describing complex shapes. In this case there are no established methods to determine the uncertainty of the results. However, in this research it will be assumed that this method can be applied to unstructured grids if they have similar characteristics, *e.g.:* orthogonality, skew and aspect ratio distribution. More information about verification and validation can be found in the literature mentioned above.

2.10 DETERMINATION OF HULL HYDRODYNAMIC COEFFICIENTS

Due to the complex physical nature of manoeuvring, mathematical models can lead to considerable offsets from reality. In general modeling errors (*e.g.:* wrong assumptions) and errors in the determination of hydrodynamic coefficients constitute the two main sources of errors in mathematical models for manoeuvring. Modeling errors can be assessed by validating the mathematical model with relevant test cases. However, for errors in the determination of hydrodynamic coefficients, it is not practical, from an engineering perspective, to “validate” every hydrodynamic coefficient, since this would require determining the same coefficients multiple times using different approaches. Therefore, the method to determine hydrodynamic coefficients should be carefully chosen.

This section aims to give an overview of some methods generally used for ship manoeuvring. It first introduces *Semi-Empirical and Analytical Methods*, then goes for *Experimental Methods,* later to *Virtual Captive Tests* and finally *Alternative Methods* where the idea behind system identification will be explained.

2.10.1 MODEL TESTING (CAPTIVE TESTS)

There are multiple experimental techniques to determine hydrodynamic derivatives, which are often called captive tests. The first ones being developed were the oblique towing test and rotating arm test. These two complement each other in the sense that the aim of the oblique towing test is to determine hydrodynamic derivatives that are only dependent on sway motion, while the rotating arm test aims to determine hydrodynamic derivatives related with yaw rate. Although these experimental techniques can lead to accurate results, they are expensive and time consuming. Therefore, in the 50's the *David Taylor Research Centre,* developed a mechanism called Planar Motion Mechanism (*PMM*), that is able to determine hydrodynamic coefficients in a less expensive way. More details about these techniques will be further discussed in this section.

2.10.1.1 Oblique Towing Test (OTT)

The oblique towing test aims to determine hydrodynamic derivatives related to sway speed. It requires a simple set up, where the model is towed in a towing tank at constant drift angle and the forces are measured and decomposed on the model's frame of reference. This procedure is repeated for multiple drift angles (*e.g.:* $\beta = 0°, 5°, 10°, 15°$), keeping the advance speed constant. The drift angle of the vessel is defined as:

$$\beta = \operatorname{atan}\left(\frac{v}{u}\right) \qquad \textit{Eq. 2.65}$$

This allows to make regressions of the measured forces/moments against sway speed and from there to determine hydrodynamic derivatives, as explained in [14].

2.10.1.2 Rotating Arm Test (RAT)

The rotating arm test is a more complex experiment than the oblique towing test. It requires a special basin with a rotating arm. The purpose of this test is to determine hydrodynamic derivatives related with yaw rate, as describe in [14]. The idea behind it is to rotate the model, with or without drift angle, and to measure the forces/moments on its frame of reference. Some of the most common experiments are:

- Multiple yaw rates at constant drift. This evaluates the influence of the yaw rate on the hydrodynamic loads. By adjusting the radial position of the model, advance speed can be kept constant.

- Fixed yaw rate multiple drift angles. This evaluates the influence of drift on the hydrodynamic loads while rotating.

This mechanism allows to determine many coefficients related to yaw rate, even non-linear coupled terms such as Y_{vr} and N_{vr}. The major drawback of this mechanism is that it needs to be considerably large to avoid flow memory effects, for instance, disturbances caused by wave radiation and every run cannot complete more than a full turning circle. This leads to very expensive and time-consuming tests.

2.10.1.3 Planar Motion Mechanism (PMM)

The planar motion mechanism has been invented in the 50's to test marine vehicles with complex sinusoidal trajectories in the horizontal plane, as explained by *Kornev* in [22]. This mechanism allows to substitute the conventional oblique towing test or the rotating arm test, by imposing a sinusoidal motion where yaw rate and sway speed can be combined. Furthermore, since the motion is sinusoidal it does not require to make multiple tests for different sway speeds or yaw rates. Although it is possible to combine in multiple ways a sinusoidal sway motion with a yaw motion, the conventional PMM tests are:

- Pure sway test (r=0):

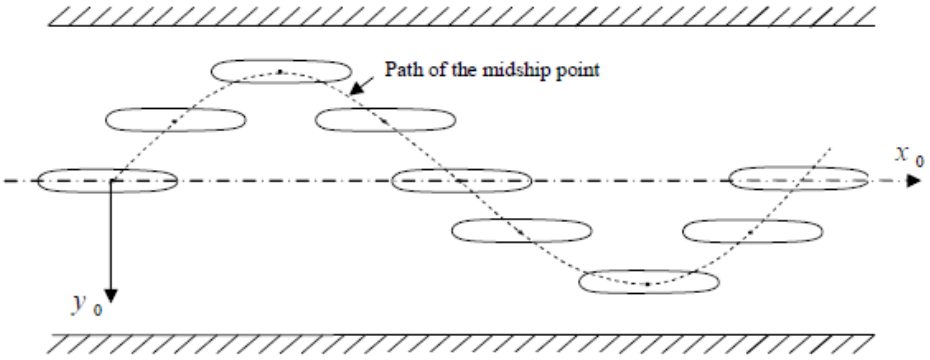

Figure 2.32: PMM, pure sway test, [49].

This test aims to determine added mass and damping coefficients dependent on the sway motion, at a certain advance speed.

- Pure yaw test (r=0):

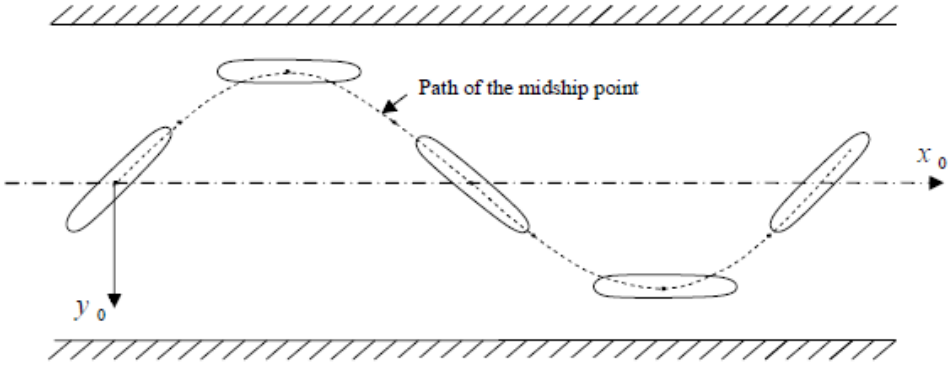

Figure 2.33: PMM, pure yaw test, [49].

This test aims to determine the added mass and damping coefficients dependent on the yaw motion, at a certain advance speed.

The conventional PMM tests are characterized by four parameters: advance speed, motion frequency, sway amplitude and yaw amplitude. As referred by *Perez* in [50], manoeuvring involves low frequency type of motion. Therefore, a careful choice of these parameters is very important, [35]. Otherwise the results might become polluted by flow memory effects. In general, the sway amplitude is defined by the towing tank dimensions, the motion amplitude by the maximum sway speed and the yaw amplitude is equal to the maximum drift in the pure sway test.

Hydrodynamic derivatives can be determined by computing the in-phase part of the forces with acceleration (added mass) and with velocity (damping), similar to what is done for forced heave motion tests by *Journée et al.* in [51]. This can be done solving the motion equation, a simple example for pure sway is:

$$\begin{cases} (\Delta - Y_{\dot{v}}).\dot{v} + Y_v.v = F_y(t) \\ v = y_a.\omega.\cos(\omega.t) \\ F_y = F_{y_a}.\sin(\omega.t + \epsilon) \end{cases} \qquad \text{Eq. 2.66}$$

Here $F_y(t)$ represents the time-trace of the force measured in sway and ϵ represents the phase angle of the force comparative to the sway motion. By solving this system of equations with the help of some trigonometric relations it is possible to determine the hydrodynamic derivatives. A more detailed and complete analysis of this procedure can be found in *Section 4.3.*

Although this mechanism reduces the experimental time and allows to determine added masses (in contrast to the previous experimental techniques presented), the tests' results are very sensitive to the accuracy of the measurements and to their settings/characteristics, as referred by [35]. Furthermore, the results analysis is more complex, what makes them subjected to more sources of error when compared the analysis of oblique towing tests or rotating arm tests.

2.10.2 ANALYTICAL AND SEMI-EMPIRICAL METHODS

The general idea behind most of the analytical and semi-empirical methods is to correlate vessel's particulars with hydrodynamic coefficients. This characteristic makes these methods easy and quick to use, which is particularly attractive in the early design stages. However, since they are only tuned to capture the physical phenomena relevant for certain types of vessels, their range of applicability can be rather limited.

In the past decades multiple attempts were done to analytically describe forces/moments acting on a vessel during manoeuvring. One of the most relevant ones, that later lead to the development of some semi-empirical formulations, was the *Low Aspect Ration Wing Theory (LARWT).* According to *Edward* in [14], the underlaying assumptions of this theory are:

- A ship is a very low *AR* wing of large area (chord=ship's length, span= ship's draft and thickness = ship's beam)
- The wing section is defined as the shape of the water plane at half-draft
- Potential Flow (inviscid and irrotational flow)
- Low Froude Number (no wave making resistance), $F_n < 0.25$
- The free surface can be considered a mirror plane, as proposed by *Tsakonas* in [52] .

The range of applicability of this kind of methods is rather limited, due to big underlaying assumptions. However later they were used to develop semi-empirical methods. These ones aim to improve the accuracy of analytical methods by tuning them with the help of statistical data.

Regarding empirical or semi-empirical methods, the most common and studied ones were developed for merchant ships with "more or less usual particulars" as referred by *S.Sutulo* in [8], when introducing *Inoue's et al.* empirical method, described in [53]. This method was developed based on regression analysis of model tests' results, and it is only applicable for merchant ships with $0.6 < C_B < 0.8$

While empirical methods are just based on statistics, semi-empirical methods aim to improve analytical methods by tuning them with statistical data, as previously referred. An example of this were the formulations introduced by *Clarke* in 1972, [14], for linear hydrodynamic derivatives. These ones are based *LARWT* and were tuned using statistical data from model tests, which lead to more accurate formulations than the purely analytical ones. Another example of a semi-empirical method is the one proposed by *Ankudinov* in [54]. This method is also a correction of *LARWT,* including the effects of appendages. As mentioned by *G. Dubbioso et al.* in [29], this kind of methods are too inaccurate to draw quantitative conclusions about manoeuvring performance, however they can be used to provide qualitative indications.

In conclusion, most of the empirical or semi empirical formulations were developed for merchant vessels and navy vessels, since the vessels inside these groups have similar characteristics, which is not the case for smaller vessels, such as patrol marine crafts. Furthermore, there are more economical incentives to do research about merchant (or military) vessels, since these are the markets where the largest investments are. Therefore, there are no well-established mathematical models that suit the purpose of this research, since it is focused on the specific case of a 25 m Patrol Vessel with a fast displacement hull form.

2.10.3 VIRTUAL CAPTIVE TESTS

In last decades significant improvements have been made to viscous flows solvers, making them able to better solve complex flows. This motivated many researchers in the late 90's to use *CFD* for the determination of hydrodynamic derivatives by replicating captive tests, see *T.Ohmori et al.* [55], *B.Alessandrini and G.Delhommeau* [56] or *A.Cura Hochbaum* in [57]. This development allows to considerable costs reduction in the determination of hydrodynamic coefficients for manoeuvring and to have better understanding of local flow phenomena. One of the first successful attempts of performing and validating virtual PMM tests was presented by *A.Cura Hochbaum* [58] in 2006. *S. Toxopeus,* 6 years later showed that it is possible to use *CFD* to improve manoeuvring predictions when compared to empirical models, [4]. For this *S.Toxopeus* conducted a detailed verification and validation studies using free sailing data of the *Hamburg Test Case (HTC,* a container vessel*)*, in his work free surface effects were also neglected. One of *S.Toxopeus'* conclusions was that the determination of hydrodynamic derivatives using CFD was challenging, often leading to validation studies to fail (mainly due to mesh limitations and separation prediciton), further research is required. In general, it was observed that the transverse force was under-predicted while the *Munk* moment (yaw moment due to sway speed) was over-predicted. Another conclusion was that for manoeuvring studies in early design stages, the comparison errors were acceptable.

This method is the most suited for this research since it allows to have detailed information about the flow, which is important from the to study interaction phenomena. Furthermore, it reduces the costs of the determination of hydrodynamic coefficients. However, in contrast to the previously mentioned researches, free surface effects will be included due to the moderate *Froude number* common to foil-assisted vessels.

2.10.4 SYSTEM IDENTIFICATION

According to *L.Ljung* in [59] system identification is "the art and science of building mathematical models of dynamic systems from observed input-output data". Having said this, it is understandable why the interest and the potentiality of using system identification to determine hydrodynamic manoeuvring coefficients. A simple example of the application of this, is to record the motions of a vessel and the rudder deflection while manoeuvring. Then by using a for instance genetic algorithm, it is possible to find the most suitable mathematical model and the best combination of coefficients to describe the vessel's behavior. *M.Bonci* in [26], concludes that an optimal compromise between accuracy and cost of manoeuvring predictions can be reached by using system identification. However, the physical meaning of the hydrodynamic coefficients might be lost since this procedure is based on a purely mathematical optimization process. Although this method is considered very promising, it is out of the scope of this research. More information about this method can be found in [26].

2.11 MANOEUVRING OF FOIL ASSISTED VESSELS

In 2006 *St. Pierre et al.* [60] compared the motion stability and controllability of a high-speed craft with and without lifting bodies, *CHSV and HSV* respectively. *CHSV* consisted on a double chine hull form with two sets of lifting bodies, forward and aft of the *CoG*, as can be seen in the picture below:

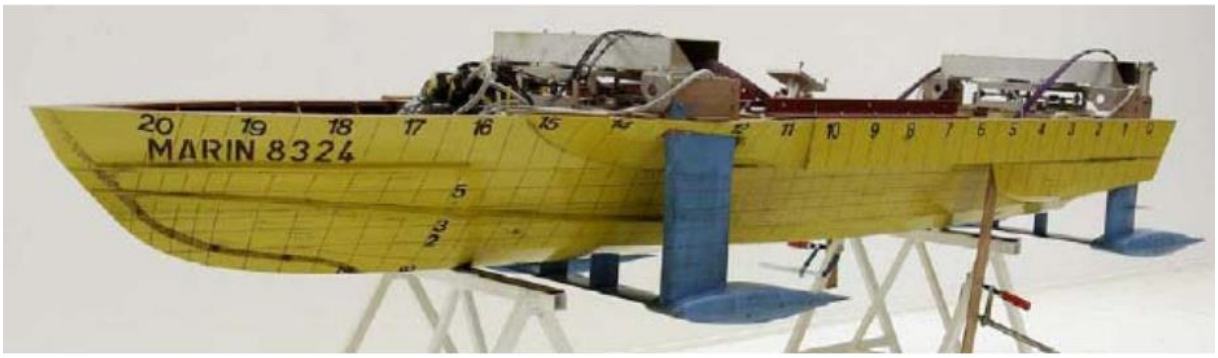

Figure 2.34: Scale model of CHSV, [60].

The *CHSV model* was equipped with 4 horizontal foils, 3 waterjets, trim flaps, fin stabilizers and 2 control flaps on the aft outboard struts. This research presented interesting results, it showed that *HSV* (vessel without foils) was course unstable, but once the foils were installed (without active control) it became stable. Furthermore, significant improvements of the dynamic behavior of the vessel were achieved by using control algorithms for the foils. Namely broaching and bow diving in following seas was mitigated. It was also observed that at higher speed (40 knots) the control system needed to compensate the loss of metacentric height (GM) created by the lifting bodies.

One year later (2007), *Hackett et al.*in [7], presented a comparison of model testing with computational predictions for calm water resistance, manoeuvring and seakeeping. Here a non-linear mathematical model (*FREDYN*) was used to simulate the manoeuvring behavior of *CHSV.* The hydrodynamic coefficients were determined using model captive tests. At the end the results were compared with the results from a free surface panel method (*PANSHIP, irrotational and inviscid flow*) and with free sailing experiments. *PANSHIP* showed to under-predict the yaw rate at big rudder angles and over-predict heel. However, it was still considered to be a valuable tool at early design stages. It was also observed that the forces on the 4 struts were dominant relatively to the forces acting on the hull. When sailing with drift angle, the forward struts produced about 2.5 times more horizontal lift than the aft struts, matching with the expected results. This showed that the interaction between hull, struts and lifting bodies plays an important role. At the end, the mathematical modeling of the water jet steering forces showed to be responsible for a big part of the discrepancies between initial and final manoeuvring calculations. Furthermore, a more detailed study of the interaction phenomena between hull, lifting bodies and struts was performed using *CFD (CFX* solver*)*. However, this last one was focused on calm water straight ahead performance.

More recently, in 2016, *K.Uithof et al.* in [12], presented results of full scale manoeuvring trials of a 55m supply vessel with and without *Hull Vane.* It was observed that the *Hull Vane* increased the turning circle diameter in about 4% (from 313 [m] to 326 [m]) and decreased the averaged zig-zag overshoot with approximately 50 % (from 3.5 [deg] to 1.8 [deg]), showing an increase in course stability. It is expected that this effects is mainly caused by the vertical struts connecting the *Hull Vane* to the hull, what matches the results obtained by *Hackett et al.* in [7].

2.12 CASE STUDY DEFINITION (*RPA8*)

As mentioned in *Chapter 1,* for the purpose of this research *RPA8* will be considered. This is a 25 [m] fast displacement vessel equipped with a Hull Vane. Its main characteristics are described in the table below:

Table 2.1: General RPA8 characteristics.

Characteristic	Value	Units
(L_{wl}, B_{wl}, T_d)	(24.470, 5.170, 1.215)	m
LCF, LCB	9.770, 10.430	m
Δ	58931	kg
(x_G, y_G, z_G)	(10.410, 0.000, 1.810)	m
$(I_{xx}^G, I_{yy}^G, I_{zz}^G)$	(98954.870, 734210.200, 655771.200)	Kg.m ^{2}
$\overline{GM}_t, \overline{GM}_l$	1.980, 48.200	m
V_D	6.5	m/s
V_M	9.7	m/s

Note that the coordinates of the center of gravity are in relation to the intersection of the baseline with the symmetry plane and aft-perpendicular. The remaining coordinates are relative to the center of gravity.

The manoeuvring performance of this vessel was assessed at model and full-scale. The model scale tests were performed with a 4 [m] long model, appended and self-propelled, see Figure 2.35. Turning circle, pull-out and zig-zag manoeuvres were carried out in deep and calm water conditions at 2.5 [m/s] and 6.11 [m/s] (full scale). The rudder rate during the tests was set to 10 [deg/s]. In the end the results were extrapolated to full scale, see 0.

Figure 2.35: Model scale of RPA8, [61].

Turning circle manoeuvres were also performed at full scale, in deep and calm water conditions at 2.5[m/s] at 9.42 [m/s]. The tactical diameter at model scale shows to be overestimated by 20-30% (relatively to full-scale), for the 2.5 [m/s] case with 60° rudder angle. However, it is only possible to compare the results for this case, since this was the only one tested at model and full scale. It is not clear which test is the most accurate. The model test results are subjected to scaling effects, which can be significant when modeling rudders and the Hull Vane, since these ones should be scaled with R_n instead of F_n. However, in the report of the full-scale tests, there is no information about wind, current and precision of the measuring devices, which can have a significant influence on the results. The results of both tests can be found in 0.

For this research moderate speed manoeuvring is the most relevant case since the effect of the Hull Vane is more present at these speeds ($L \approx V^2$). Furthermore, extreme rudder angles (*e.g.: 60*°) is left to be studied in further researches, due to added complexity of the flow and the time constrain associated to this research. Therefore, the only experimental results considered in this research for validation purposes are:

- **Mode-scale**: 3° - 3° zig-zag manoeuvre at 6.11[m/s].
- **Full-scale**: Turning circle at 9.42[m/s] with 30° rudder deflection.

3. VIRTUAL CAPTIVE TESTS – SETUP

In this research, the forces/moments acting on the vessel are split in two types: caused by pure-sway and by pure-yaw. For the first type (*i.e.:* pure-sway), *PMM* tests and *OTT* are performed. For the second type (*i.e.:* pure-yaw), only *PMM* tests are performed. As explained in *Section 2.10.1, PMM* tests assess steady and unsteady forces/moments, while *OTT* only assess steady forces/moments. However, according to *Yasukawa* and *Yoshimura* in [35], *PMM* tests are expected to be subjected to more sources of errors, *e.g.:* flow memory effects, higher numerical residuals due to the unsteady motion. Therefore, to have an indication of the magnitude of the *PMM* error, *OTT* are performed, and the results of the steady forces/moments compared with the ones from *PMM*. In the end the steady forces/moments from *OTT* are considered since these ones are subjected to less sources of errors. The following figure summarizes the experimental setup here described:

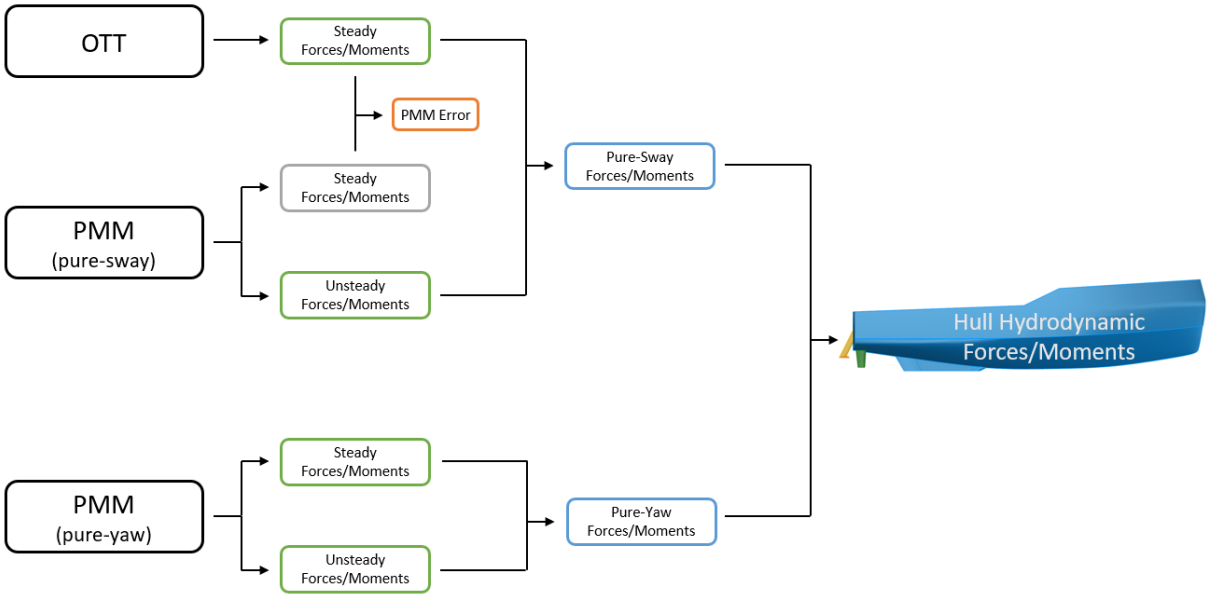

Figure 3.1: Scheme of the experimental setup.

The assessment of cross terms such as Y_{vr}(effect of yaw rate on sway damping) and N_{rv} (effect of sway speed on yaw damping) requires a more complex experimental setup. Furthermore, these ones are not of primary concern. Therefore, their assessment is left for future research due to the time constrains. In *Section 8.3.5,* the impact of this assumption is discussed.

Having said this, the aim of this chapter is to describe the setup of the virtual captive tests. In the first two subsections, the characteristics of the captive tests are presented. Then, the third and last subsection, describes the setup of the *CFD* computations. The results of these virtual captive tests are presented and analysed in *Chapter 4.*

Following the recommendations of *Toxopeus* in [4], the virtual captive tests are performed at full scale and include propulsive effects, using an actuator disk model. This prevents scaling and modelling errors. Since the impact of the Hull Vane on heave and pitch is small enough to avoid the need of mathematically modelling these motions, in the captive tests the vessel is free to trim and sink. Furthermore, according to *Sutulo* in [8], in canonical conditions it can be assumed that the metacentric height is large enough to neglect the influence of roll on other motions. Therefore, the roll motion is fixed to avoid numerical errors and instabilities due to mesh deformation in the *CFD* simulations. This also allows to assess and model roll motions during manoeuvring.

3.1 OTT (OBLIQUE TOWING TEST)

Based on experimental results, the drift angle is expected to do not overcome 15° at moderate speed manoeuvring. Therefore, this test is performed for drift angles ranging from 0°-15° in steps of 5°. The motions of this test are described in the following table:

Table 3.1: Characteristics of the oblique towing tests.

Motions	Constraints
Drift Angles (β)	$(0°, 5°, 10°, 15°)$
Advance Speed (u)	$6.5\ [m/s]$
Sway Speed (v)	$u.tan(\beta) = (0;\ 0.569;\ 1.146;\ 1.742)\ [m/s]$
Yaw Rate (r)	$0\ [rad/s]$
Roll (p)	Fixed
Heave (w), Pitch (q)	Free

Note that the advance speed was chosen according to the experimental data available, which will be used for validation purposes.

3.2 PMM (PLANAR MOTION MECHANISM)

The characteristics of a *PMM* test (*Section 2.10.1.3*), that is performed in a towing tank, are mainly defined by the size of the towing tank. However, in CFD there are no spatial limitations. Therefore, in this research these characteristics are determined using the maximum drift angle and the expected turning circle radius and speed.

The sway motion is described by:

$$\begin{cases} y = y_a.sin(\omega.t) \\ \dot{y} = y_a.\omega.cos(\omega.t) \\ \ddot{y} = -y_a.\omega^2.sin(\omega.t) \end{cases} \quad \textit{Eq. 3.1}$$

The yaw motion in a pure-yaw *PMM* test is 90° out of phase from the sway motion in the pure-sway test. Therefore, it is described by:

$$\begin{cases} \psi = \psi_a.\cos(\omega.t) \\ \dot{\psi} = -\psi_a.\omega.\sin(\omega.t) \\ \ddot{\psi} = -\psi_a.\omega^2.\cos(\omega.t) \end{cases} \quad \textit{Eq. 3.2}$$

The characteristics of the pure-sway and yaw *PMM* tests are obtained by solving the following system of equations:

$$\begin{cases} \dot{y}_a = y_a.\omega \\ \dot{\psi_a} = r = \psi_a.\omega \\ \dot{y}_a = u.\tan(\beta_{max}) \\ \dot{r} \approx \dfrac{u}{R} \\ \psi_a = \beta_{max} \end{cases} \quad \textit{Eq. 3.3}$$

The 4th equation assumes that the sway speed is considerably smaller than the advance speed, which is often the case at moderate speed manoeuvring, here *R* represents a reference turning circle radius (in this case chosen according the full-scale trials). The 5th equation defines the pure-sway condition. By simplifying the previous system of equations, it is possible to obtain the following relations:

$$\begin{cases} \omega = \dfrac{u}{R.\beta_{max}} \\ y_a = R.\beta_{max}.\tan(\beta_{max}) \\ \psi_a = \beta_{\max} \end{cases} \qquad \text{Eq. 3.4}$$

The previous set of equations fully describes a pure-sway and yaw motions. Note that R is estimated from the full-scale trials, and β_{max} represents the maximum expected drift angle. The following table resumes the characteristics of the *PMM* tests realized in this research:

Table 3.2: Characteristics of the PMM tests.

Characteristics	Values
$\boldsymbol{R}$	$50\ [m]$
$\boldsymbol{\beta_{max}}$	$15° = 0.262\ [rad]$
$\boldsymbol{u}$	$6.5\ [m/s]$
$\boldsymbol{y_a}$	$3.507\ [m]$
$\boldsymbol{\psi_a}$	$\beta_{max} = 0.262\ [rad]$
$\boldsymbol{f_{PMM}}$	$0.0791\ [1/s]$
Motions: $\boldsymbol{(w;\ p;\ q)}$	$(Free;\ 0\ [rad/s];\ Free\ )$

3.3 CFD SETTINGS

This section aims to define the setup of the *CFD* simulations for the virtual captive tests. Since this type of computations is considerably expensive it is necessary to find a balance between accuracy and computational cost. The first step for this, is to remove some details of the *RPA8* geometry. This allows to decrease the number of mesh elements without a significant penalty in the results.

Figure 3.2: **Top:** Original model of *RPA8.* **Bottom:** Simplified model of *RPA8.*

In Figure 3.2 it is possible to compare the original model with the simplified one. The simplified version does not contain the bow thrusters' tunnels, the propellers' shaft lines, A-brackets and the propulsion tunnels. The shaft lines and A-brackets are expected to slightly increase the course stability of the vessel. However, this effect is assumed not to be relevant in the context of this research, since these ones are significantly smaller than the lateral are of the hull and located in a region where the flow is highly straightened by the propulsion system, reducing their lateral lift component. For the specific case

of the bow thrusters, when manoeuvring at moderate speed they are not used, and since the flow through them is limited by the presence of the propeller, it seems reasonable to exclude them.

As mentioned in the beginning of this chapter, to prevent scaling and modelling errors, the virtual captive tests are performed at full scale and include propulsive effects by using an actuator disk model.

3.3.1 PHYSICAL MODEL

In this section, an overview of the main physical aspects and assumptions will be provided. A good understanding of the physics of the problem is essential for an appropriate setup of *CFD* simulations.

The size of the computational domain is important to ensure that the flow field around the vessel is not disturbed by the domain boundaries. Since the virtual captive tests for manoeuvring imply asymmetric flow, the full domain is considered. Its dimensions are in accordance to the recommendations of the software developer (*NUMECA*) and the *Van Oossanen* standards. The following figure illustrates the domain dimensions:

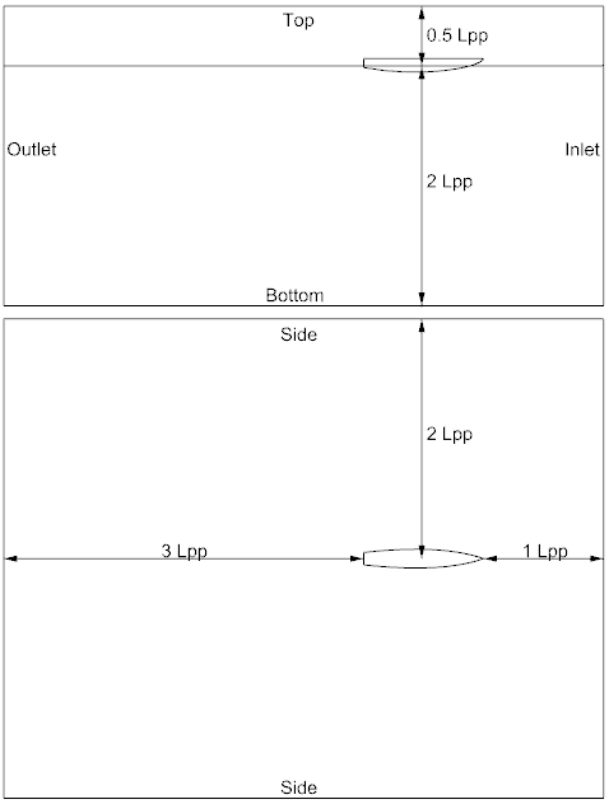

Figure 3.3: Dimensions of the computational domain.

The R_n of the of these tests is in the order of 10^8. This shows that turbulent flow must be expected with eventual flow separation phenomena. Furthermore, to make an estimation of how important is laminar to turbulent transition for this case, a flat plate without pressure gradient is considered, which in general is a conservative assumption. According to *White* in [62], for this case, the boundary layer transition region is approximately between $5 \times 10^5 < R_{n_x} < 8 \times 10^7$, where R_{n_x} represents the *Reynolds* number based on the distance from the leading edge. This means that for a 6.5 [m/s] hydrodynamic flow: $10^{-2} < x[m] < 10^0$, while $L_{pp} \approx 10^1$. Therefore, laminar to turbulent transition is assumed not to be important. This assumption holds also for the rudders and the Hull Vane since these ones are subjected to highly disturbed flow, from the hull and propulsion system.

A advance speed of 6.5[m/s], for this case, corresponds to $F_n = 0.4$, meaning that the length of the wave produced by the vessel is approximately equal to the length of the vessel, as explained by *Larsson et al.* in [63]. Therefore, free surface effects cannot be neglected, which means that unsteady flow should be considered. Furthermore, *PMM* motions are also unsteady, reinforcing the need of considering unsteady effects.

As mentioned in the previous sections, propulsive effects are considered since they can have a significant influence on pitch and heave. Furthermore, sea water is considered an incompressible *Newtonian* fluid (definition can be found in *Kundu et al.* [27]) and for sake of simplicity cavitation effects are neglected.

3.3.2 MATHEMATICAL MODEL

3.3.2.1 Turbulence and Boundary Layer Modeling

Since viscous resistance and flow separation is expected to be important, viscosity must be considered. Therefore, the simulations are performed with unsteady *RANSE* coupled with the equations of motion. This method, in general, provides a good combination of accuracy and computational cost. However, *Toxopeus* in [4] described difficulties in the validation of the virtual captive tests when using this method. The same difficulties were found by *Vink* in [64], where the discretization uncertainties showed to be dominant, for the case of a tug under drift.

Separation phenomena are strongly related to near wall flows subjected to pressure gradients, but at the same time, external flows are also important to properly capture the wakefield of the vessel. Therefore, the 2 equations turbulence model $k-\omega\ STT$ is used since it combines the ability to solve these two types of flow, as explained by *Hickel* in [39]. The same turbulence model was found to be the most adequate one by *Toxopeus* in [4], for virtual captive tests purposes.
For flows subjected to strong pressure gradients and separation, it is recommended to solve the boundary layer (*i.e.:* not using a wall-function). However, for this research, it is assumed that the accuracy penalty of using a wall function does not significantly affect the global hydrodynamic forces acting on the hull. The use of a wall function introduces modelling errors, especially in the prediction of flow separation. This one models the inner sublayer of the boundary layer, making it less sensitive to adverse pressure gradients, see *Wilcox* in [65]. However, in the context of this research, solving the boundary layer leads to a prohibitive amount of cells as explained by *Pas* in [66].

3.3.2.2 Boundary Conditions

To solve the flow, it is necessary to impose boundary conditions (*BC*) at the boundaries of the numerical domain and on solid walls (vessel's surface), *Section 2.9.2*. For the virtual captive tests, 3 types of boundary conditions are used:

- **Far Field *BC*:** According to the Fine/Marine's user guide, [67], this *BC* locally defines a *Dirichlet* or *Neumann* condition based on local flow properties. This allows to have smaller domains since it does not impose a uniform condition for the entire boundary, what could artificially affect the solution. This *BC* is applied to the inlet, outlet and sides of the domain.

- **Prescribed pressure:** This is a *Dirichlet* boundary condition which prescribes a pressure value for a boundary. In this case it is applied to the top and bottom of the domain. Due to the presence of gravity waves (multiphase flow), it is necessary to update this condition with the hydrostatic pressure variation

- **Wall-function:** This condition specifies the use of a wall function (previously explained) to solid walls, in this case it is applied to the vessel.

3.3.2.3 Propulsion Modeling

As mentioned in the previous section, propulsive effects must be considered, for this, actuator disks with swirl are implemented in *CFD.* The thrust is updated every 10 time-steps and the torque is computed based on a constant open water efficiency (η_0). Although in *Section 2.5,* an actuator disk was defined as a zero-thickness disk, here it has a thickness of $0.2\,[m]$ (see Figure 3.4) to avoid numerical instabilities and singularities in flow.

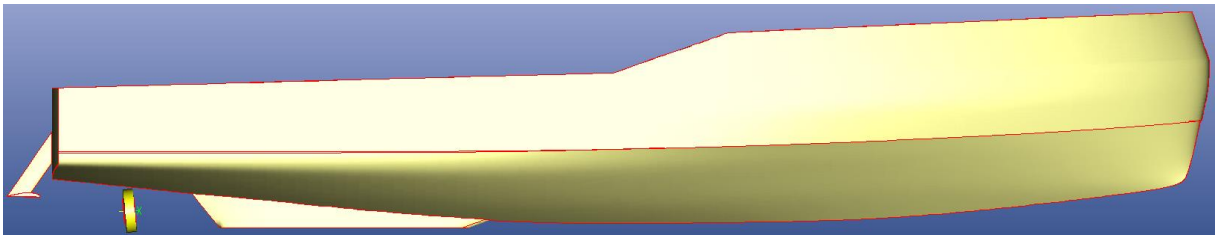

Figure 3.4: Actuator disk setup in *CFD.*

3.3.3 ALGEBRAIC MODEL

3.3.3.1 Mesh Generation

The governing equations are discretized using a *Finite Volume Method* and the computational domain is meshed using an unstructured grid of hexahedrons with *HEXPRESS* (meshing software). Although this type of grid increases the computational cost, it is more flexible and adequate to complex geometries when compared to structured grids, as mentioned by *Hickel* in [43]. The mesh setup is divided in the following steps:

- **Initial Mesh:** Here the domain is divided in a structured way with hexahedrons. These initial elements represent the largest element size. Later, refinements in regions of interest will be applied relatively to this initial mesh.

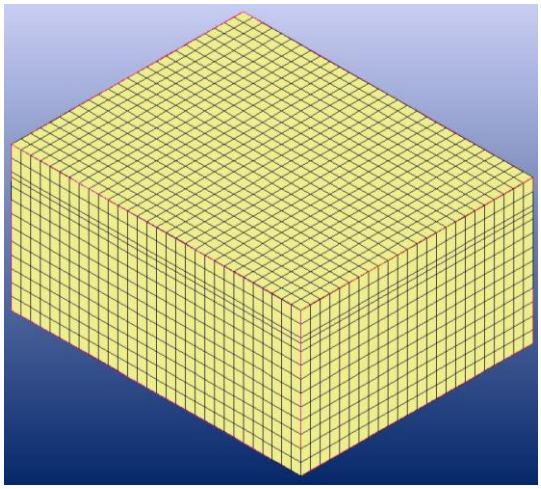

Figure 3.5: Initial Mesh

- **Adapt to Geometry:** In this step, regions of interest are refined. Every refinement level divides a cell in 8, since it is split in 2 in every direction. The 3 main types of refinement are: line, surface and volumetric refinements. Besides refinement levels, it is also possible to define minimum cell sizes, aspect ratio of cells and refinement diffusion for certain regions.

In this step, an extra refinement is applied to a box containing the hull (see *Figure 3.6*), for a better to capturing of fore-body and aft-body vortices, see *Fureby et al.* in [68]. Note that the triangular refinement region, on the top of the domain in Figure 3.6, is the result of a triangular refinement at the free surface to properly capture the *Kelvin* wave pattern.

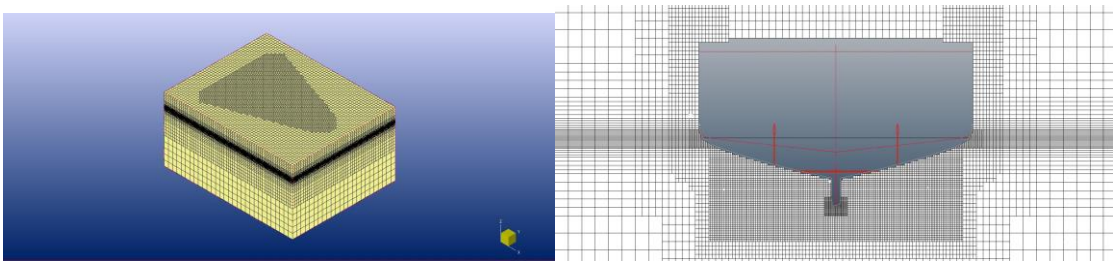

Figure 3.6: Mesh after creation of refinement regions.

- **Snap to Geometry:** This step adapts the grid to the geometry, by fitting the elements close to the surface of the object (*e.g.:* hull and appendages) to the object. This step also creates additional cells in regions where the existing ones are not enough to adequately represent the surface of the object.

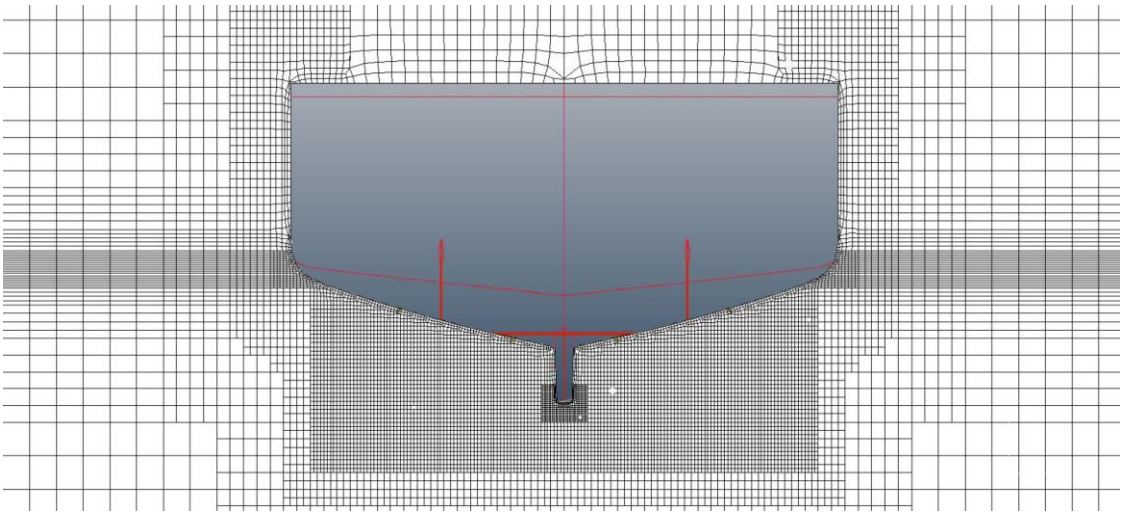

Figure 3.7: Mesh snapped to geometry.

- **Optimization:** During the previous steps low quality mesh elements might have been generated, what can lead to instabilities in the simulation or poor results, *e.g.:* negative volumes, highly twisted cells or concave cells. The optimization step aims to improve the grid quality by correcting these imperfections.

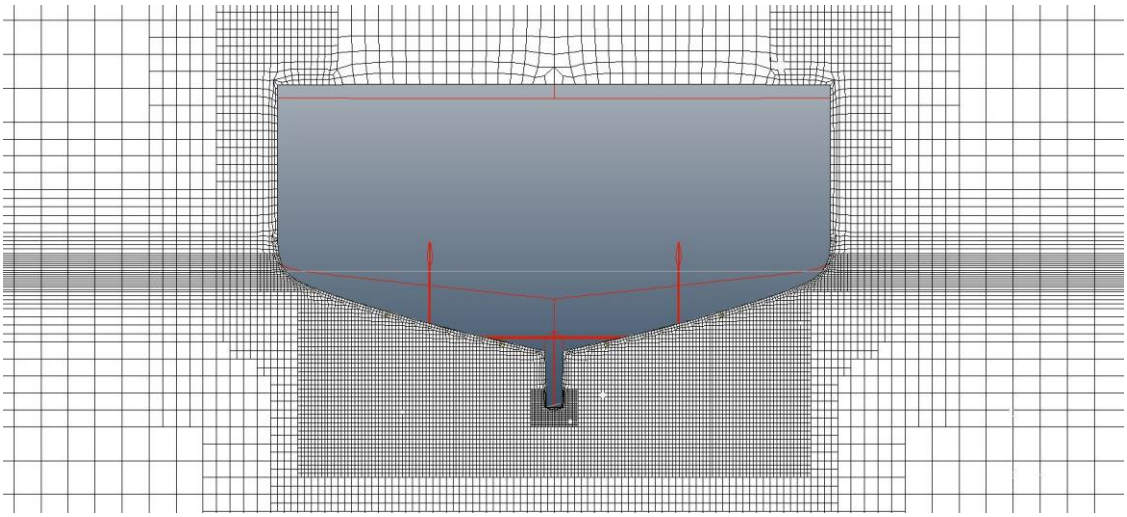

Figure 3.8: Optimized mesh.

- **Viscous Layers Insertion:** Due to viscosity, there is a significant velocity gradient next to walls (Boundary Layer), which is the cause of viscous drag. To properly capture this, it is necessary to create extra refinement layers next to solid walls. These ones are characterized by high aspect ratio cells since it aims to refine the cells mainly in the direction perpendicular to the wall. The size of the viscous layers increases towards the fluid bulk, where the velocity gradients are smaller. To decrease numerical diffusion, the cells' surfaces should be as much as possible orthogonal (or parallel) to the flow direction, as mentioned by *Hickel* in [39]. The following figure shows the final mesh including viscous layers.

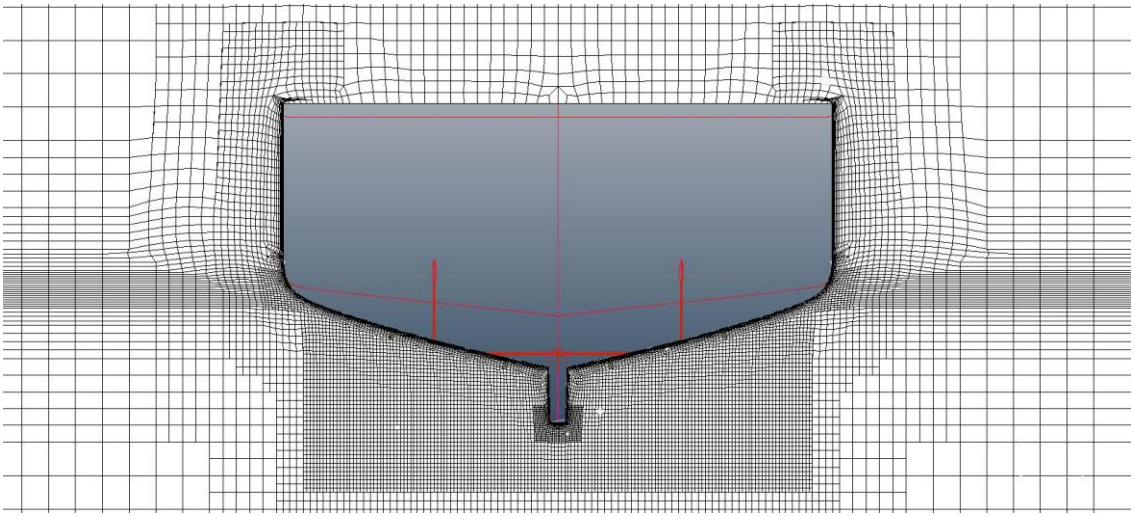

Figure 3.9: Mesh with viscous layers.

According to *Pas* in [66], when using a wall function with $k-\omega\ SST$, it is recommended to have the first cell at the wall with a height comprehended between $50 < y^+ < 100$. In this case was set to $y^+ = 80$, to cover the shear layer of the boundary layer ($y^+ < 80$), see *Pope* in [69]. This cell height corresponds to the beginning of the log-law region of a turbulent boundary layer, as can be seen in the following illustration:

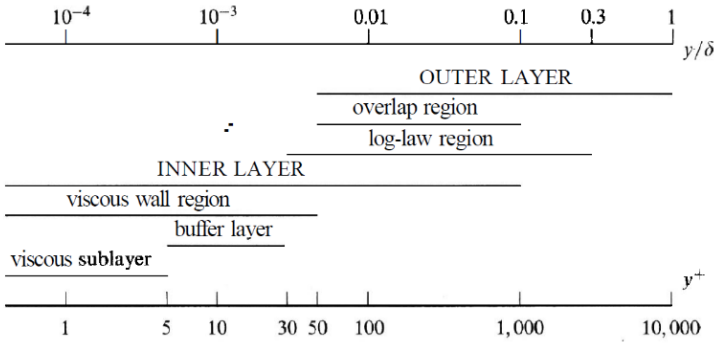

Figure 3.10: Illustration of the different regions of a turbulent boundary layer, *[69]*.

According to [66], if the boundary layer was being solved without a wall function, it would be necessary set the height of the first cell to $y^+ \approx 1$.

Once the mesh is finalized it is convenient to check its quality. The following table summarizes the quality criteria:

Table 3.3: Summary of the mesh quality criteria.

Criteria	Values
Orthogonality	$> 10°$
Negative volumes	None
Twisted cells	None
Concave cells	None

The orthogonality represents the minimum angle between two surfaces of a cell. As mentioned *Hickel* in [39], the mesh elements should be as much orthogonal as possible, this is to avoid stability problems, especially when deforming the mesh. The following figure represents a typical mesh orthogonality distribution:

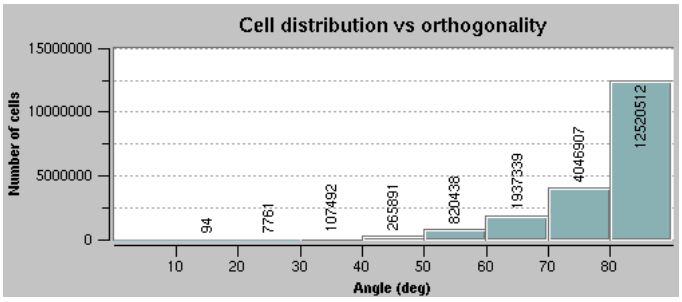

Figure 3.11: Mesh orthogonality distribution.

Negative volumes, twisted cells and concave cells are removed in the optimization step, these types of cells destabilize the simulations. Note that, negative volumes are a purely mathematical concept, it is related with the orientation of cells' surfaces.

Note that the mesh presented in this section is not necessarily the same mesh of the *Virtual Captive Tests.* This one will be defined according to the results of the solution verification study performed in *Section 4.1*.

3.3.3.2 Body Motion

The fluid solver is coupled with the equations of motion of the body to allow multiple degrees of freedom. Therefore, to allow the body to move, during the computation, there are two different methods available: rigid body motion and mesh deformation. According to the software developer in [67], in rigid body motion "The mesh follows the body during the computation according to the imposed motion (…)". While mesh deformation assumes small displacements caused by the movement of a solid wall boundary, which deform the mesh but do not modify the mesh topology. The following table resumes the type of method applied to each degree of freedom during the virtual captive tests:

Table 3.4: Methods used in this research for body motions.

Method	Motions
Rigid Body Motion	$u, v,$ r
Mesh Deformation	w, q
None	p

3.3.3.3 Time Laws

According to the *Van Oossanen* standards, the acceleration period must follow a ¼ sinusoidal ramp and is given by:

$$T_{accel} = \frac{2.L_{pp}}{V_s} \qquad \textit{Eq. 3.5}$$

The same period is used for the *OTT.* For the *PMM* tests, it is defined 1 motion period to initialize the final motion, this was verified to be enough to reach a stable result.

The time step is in accordance to the *Van Oossanen* standards, this one follows a physical time-step law (same time step everywhere in the domain) and it is generally given by:

$$\Delta t = \frac{0.005.L_{pp}}{V_s} \qquad \textit{Eq. 3.6}$$

This time-step is half of what is recommended by the software developer (*NUMECA)* in [67]. Therefore, it is assumed to be adequate in the context of this research.

In order to make the solution converge within the same time step, non-linear iterations are used, and a target reduction in order of magnitude of the residuals is set. For the virtual captive tests, where the flow is highly unsteady (special in *PMM* tests), the number of maximum non-linear iterations is set to 12, aiming for a reduction of 3 orders of magnitude of the residuals. According to *NUMECA's* recommendations, for straight ahead runs, the number of maximum non-linear iterations is about 8, aiming for a reduction in order of the residuals of 2.

4. VIRTUAL CAPTIVE TESTS – RESULTS ANALYSIS

This chapter starts with a solution verification analysis of the *Virtual Captive Tests* setup. For this, multiple grids topologies and methods are tested and the *CFD* discretization uncertainties assessed. According to the outcome of the solution verification analysis, *Virtual Captive Tests* are performed, and hydrodynamic coefficients derived, following the experimental setup presented in *Chapter 3:*

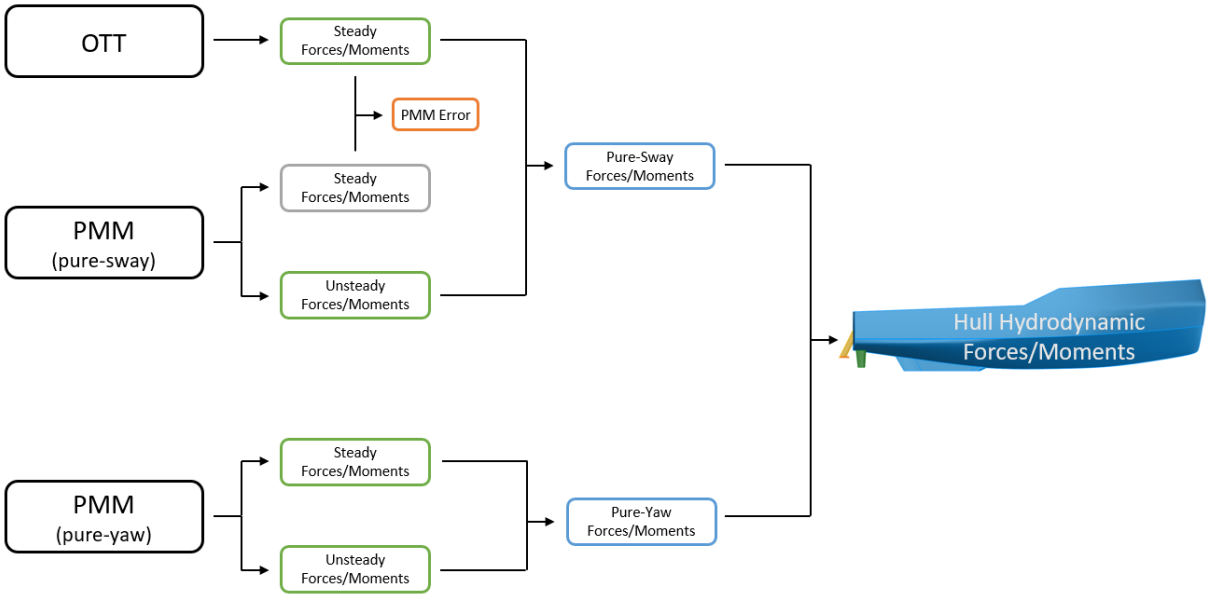

Figure 4.1: Scheme of the experimental setup.

For more details of the experimental setup, see *Chapter 3.* Interaction phenomena is assessed in *Chapter 5.*

A common practice in the scientific community is to non-dimensionalize the equations of motion, and consequently the hydrodynamic derivatives (or coefficients). This allows a more direct comparison between different hydrodynamic coefficients and physical phenomena. For this, the dynamic pressure is considered. Therefore, the force equations are divided by $\frac{1}{2}\rho V^2 L^2$ and the moment equations by $\frac{1}{2}\rho V^2 L^3$, see *Lewis* in [14]. The non-dimensional values, in this report, assume $V = 6.5\ [m/s]$, $L = 25\ [m]$ and $\rho = 1025\ [kg/m^3]$ and are represented with an apostrophe, *e.g.:* Y'_v.

Note that, the results presented in this chapter consider a frame of reference located at the center of gravity of the vessel. Furthermore, for the sake of clarity, at the end of every section of this chapter a summary of the results is presented.

4.1 SOLUTION VERIFICATION ANALYSIS

As mentioned in *Section 2.9.4,* the iterative errors and round-off errors are assumed to be much smaller than the discretization errors. The discretization uncertainties are assessed using the method proposed by *Eça* and *Hoekstra* in [47] and described in *Section 2.9.4.*

Since in the context of this research it is not practical to reproduce every virtual captive test for at least 4 grids (minimum required for reliable results), it is considered one standard case, which is representative of the general virtual captive tests. Similarly, to what was done by *Toxopeus* in [4], a pure drifting case with Hull Vane is defined as a standard manoeuvre for solution verification purposes. The following table summarizes the characteristics of this standard case:

Table 4.1: Characteristics of the standard case for solution verification.

Standard Case	
$\boldsymbol{u}$	$6.5\ [m/s]$ (design speed)
$\boldsymbol{\beta}$	$15°$
$\boldsymbol{DOF}$	heave and pitch
Acceleration period	8.01 [s]
Final time	30 [s]
Time step (Δt)	0.019 [s]

The final time was defined to 30 [s] since it was observed to be enough to reach stable results. The remaining parameters are in accordance with the settings presented in *Chapter 3.*

Due to the presence of strong fore and aft-body vortices in drift (see *Fureby et al.* in [68]), it is challenging to define a grid topology able of combining computational cost and a proper capturing of the flow field. Therefore, the following three types of grids are going to be studied:

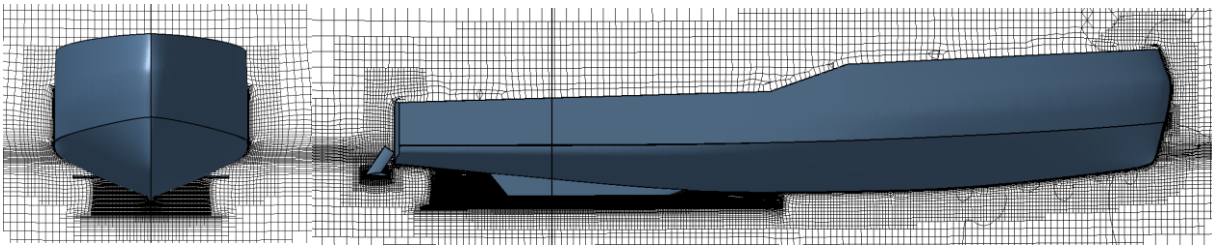

Figure 4.2: Grid topology 1 (*t1*).

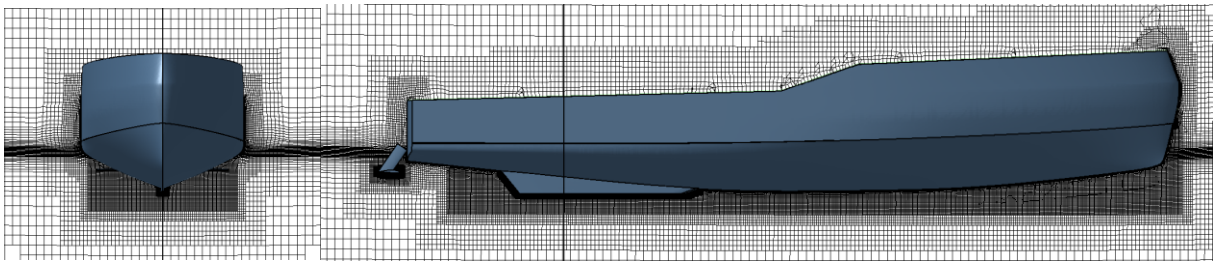

Figure 4.3: Grid topology 2 (*t2*).

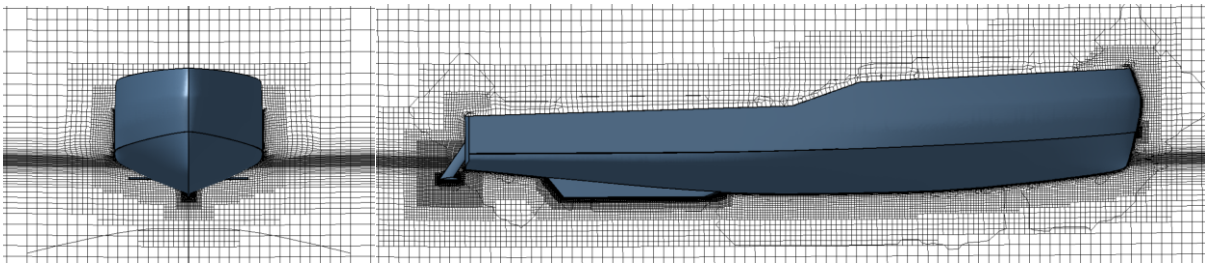

Figure 4.4: AGR grid.

For grid topologies 1 and 2, five grids with different levels of refinement are generated. Since these grids are unstructured, it is difficult to ensure geometrical similarity between them. In an attempt to keep the mesh geometrical properties as much constant as possible between grids, only the number of initial cells is changed, and the refinement levels are kept constant. Since this research is specially focused on the surge forces, sway forces and yaw moments, the solution is verified using these quantities.

4.1.1 GRID TOPOLOGY 1

Grid topology 1 (*t1*) assumes that the fore-body vortex can be well resolved without any extra refinement at the bow and that this one is less important than the aft-body vortex. Therefore, *t1* is characterized by a refinement box around the skeg, with 8 levels of refinement (see Figure 4.2).

The following table summarizes the main characteristics the 5 different grids of *t1* and their discretization uncertainties. More details can be found in *Appendix A.2.1*.

Table 4.2: Characteristics of the grids of *t1*.

Topology 1							
Mesh Reference	**Number of Cells**	h_i	h_i/h_1	**Initial Mesh (x, y, z)**	**U(F_x) [%]**	**U(F_y) [%]**	**U(M_z) [%]**
t1G0.5	7,419,808	0.472	1.268	(10, 8, 4)	132.7	73.5	62.3
t1G0.75	10,638,897	0.419	1.124	(15, 12, 6)	141.6	71.7	61.5
t1G1	15,113,452	0.373	1	(20, 16, 8)	143.3	69.1	58.7
t1G1.5	23,074,552	0.324	0.878	(30, 24, 12)	140.1	65.5	55.7
t1G2.75	39,607,004	0.270	0.725	(55, 44, 22)	126.5	59.9	51.0

Note that the number of the “Mesh Reference” represents the factor applied to the number of initial elements of the mesh.

As can be seen, the uncertainties associated to *Topology 1*(*t1*), are considerably high, because the solutions are not behaving asymptotically (*i.e.:* converging), see uncertainty plots in appendix A.2.1. This gives an indication that important flow features are not being properly captured by the current grid topology. By carefully analyzing the results, it is possible to verify that about 90% of the forces acting on the vessel are produced by the hull. By splitting the hull in portside and starboard, it is possible to conclude that the major source of uncertainty is the starboard part of the hull, see *Table 11.3* in *Appendix A.2.1*. Which is the one expected to be more subjected to complex flow phenomena such as vortices. To check this hypothesis, the results of the *CFD* simulations are post processed, see *Figure 4.5* in the next page.

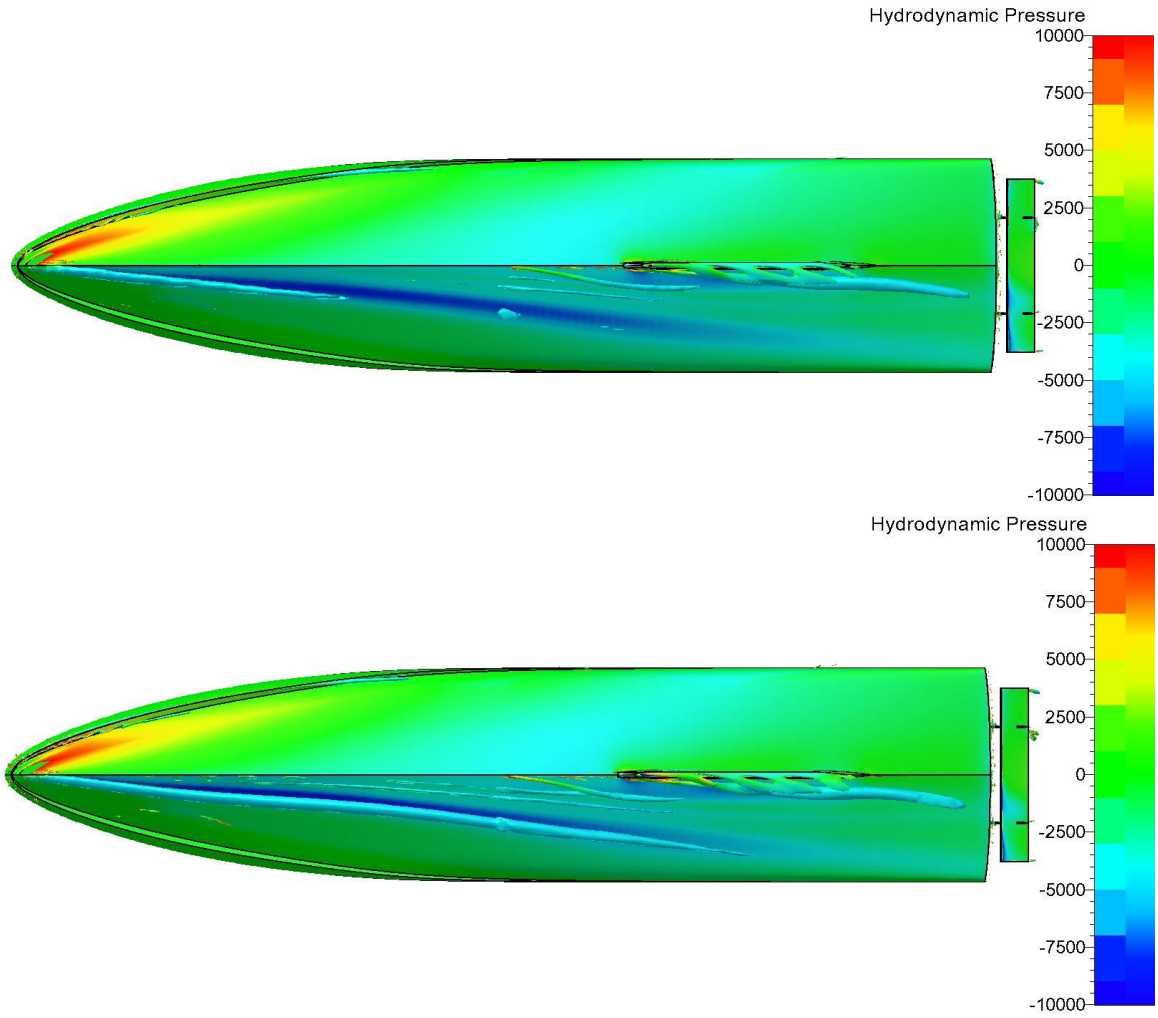

Figure 4.5: Bottom view, vorticity iso-surfaces correspondent to Q=100 (Q-criterion) and coloured according to $|\nabla \times \vec{u}| < 75\ [1/s]$. Hull surface coloured according to hydrodynamic pressure. **Top:** Mesh *t1G1*. **Bottom:** Mesh *t1G1.5*.

Figure 4.5 shows that the lack of mesh resolution forward the skeg results in an under-prediction of the fore-body vortices and consequently a different pressure distribution on the hull surface. In contrast to this, the region around the skeg shows to be relatively well solved, even for coarser meshes (*G0.5* and *G0.75*), see *Appendix* A.2.1.

4.1.2 GRID TOPOLOGY 2

For a better capturing of the fore body vortices, the refinement box around the skeg is extended to cover the entire length of the hull, see *Figure 4.3*. Since 8 levels of refinement showed to be able to capture the aft body vortex even for coarser grids, to reach a compromise between the capturing of flow features and computational cost, the refinement box of topology 2 (*t2*) consists of 7 levels of refinement.

The following table summarizes the main characteristics the 5 different grids of *t2* and their discretization uncertainties. More details can be found in *Appendix A.2.2*.

*Table 4.3:*Characteristics of the grids of *t2.*

Topology 2							
Mesh Reference	**Number of Cells**	h_i	h_i/h_1	**Initial Mesh (x, y, z)**	**U(F_x) [%]**	**U(F_y) [%]**	**U(M_z) [%]**
t2G0.5	7,098,964	0.479	1.266	(10, 8, 4)	9.5	23.2	33.3
t2G0.75	9,972,816	0.428	1.130	(15, 12, 6)	7.1	18.8	30.1
t2G1	14,408,034	0.378	1	(20, 16, 8)	5.6	15.3	26.7
t2G1.5	22,753,167	0.325	0.859	(30, 24, 12)	3.2	11.6	23.7
t2G2	33,066,039	0.287	0.758	(40, 32, 16)	2.5	9.0	20.9

The uncertainties of this grid topology are considerably lower than the ones of *t1*, even though the number of mesh elements remains approximately the same. *Toxopeus* in [4], found the uncertainties to be 10 to 15% on average for an equivalent case. Based on this, he concluded that this level of uncertainty was acceptable for manoeuvring studies in an early design stage. To confirm that the flow field is being better captured, the solutions are post processed, see Figure 4.6 in the next page.

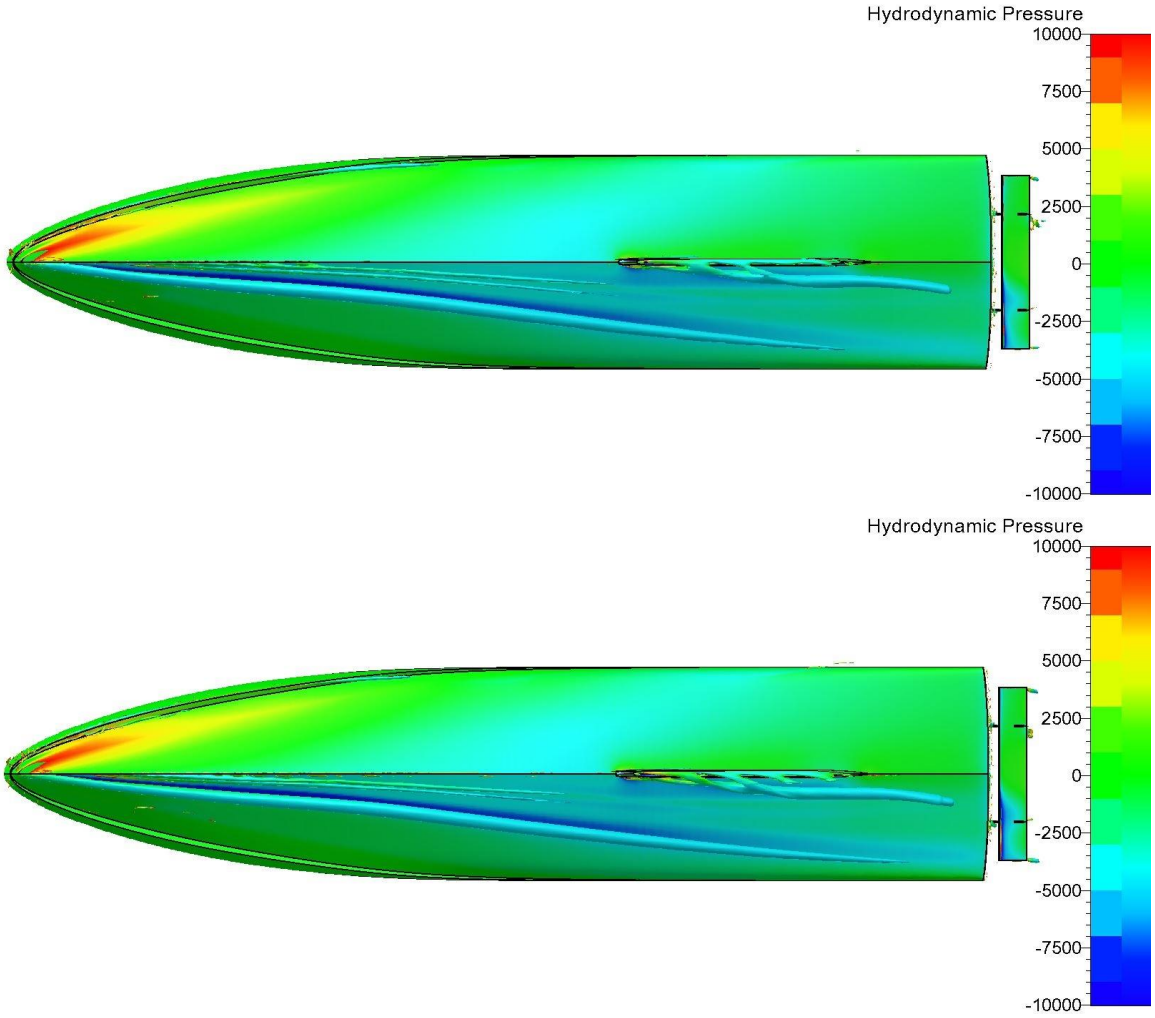

Figure 4.6: Bottom view, vorticity iso-surfaces correspondent to Q=100 (Q-criterion) and coloured according to $|\nabla \times \vec{u}| < 75\ [1/s]$. Hull surface coloured according to hydrodynamic pressure. **Top:** Mesh G1, topology 2 (*t2G1*). **Bottom:** Mesh G1.5, topology 2 (*t2G1.5*).

As can be seen in *Figure 4.6,* this mesh topology allows a better capturing of the fore-body vortices, even for *t2G0.75* (see *Appendix A.2.2*). However, due to a lower refinement level of the refinement box (relatively to *t1*), the aft-body vortex is not being captured as well as for *t1*. Although *t2* significantly reduces the uncertainties, the number of mesh elements still represents a constrain from the computational cost point of view.

4.1.3 ADAPTIVE GRID REFINEMENT *(AGR)*

AGR stands for *Adaptive Grid Refinement* and consists of a numerical method to refine regions of interest during the simulation. This allows to solve local flow details without substantially increasing the computational cost. *Visonneau et al.* in [70], made use of *AGR* to capture ventilation of the fore-body vortex in *RANS*. For the purpose of this research the *AGR* settings were chosen in accordance to the recommendations of the software developer (*NUMECA*). The aim is to decrease the computational cost and to better capture the fore and aft-body vortices, which are one of the main sources of uncertainty in the previous mesh topologies. The following table summarizes the *AGR* settings:

Table 4.4: Adaptive Grid Refinement settings.

AGR Settings	
Base Mesh	14.4M cells
Final Mesh	18.1M cells
Refinement Criteria Type	Flux Component Hessian
Refinement Criteria Threshold	3.75
Minimum Size Limit for Refined Cells	0.015 [m] (Equivalent to refinement level 8 in G1)
Number of Layers Copying Full Criterion Value	2
Number of layers Copying fraction of value	1
Fraction	0.5
Refinement Box Edges	(-1.5, -2.8,2); (25,2.8,0.5), Containing the underwater part of the vessel
Number of time-steps between refinement calls	10

According to *NUMECA* in [67], the 'Flux Component Hessian' is adequate to wake flows and to vortex-wake interaction phenomena, which is the case for vessels under drift. The threshold defines whether a region should be refined or not, the lower the most sensitive it gets. In this case 3.75 corresponds to what *NUMECA* in [67] considers a medium refinement. A lower value was tested but led to the creation of too many cells (25M +). A level 7 refinement box is placed around the Hull Vane to avoid damping of flow properties (due to discretization errors) in the region between the vortex and the Hull Vane, see *Figure 4.4.* The following figures show the final mesh:

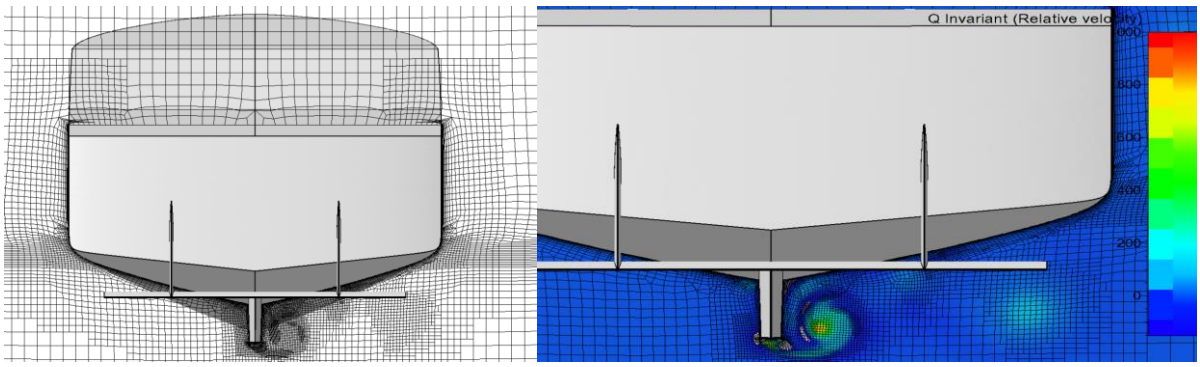

Figure 4.7: Final mesh,18.1M cells. **Left:** Mesh cross section at 5 [m] from the stern. **Right:** Same cross section including Q-criterion of the relative velocity from -150 to 150.

As can be seen, in the regions of more vorticity, the mesh is being refined. The following picture compares the results of *t2G2* (most refined mesh of *t2,* 33.0M cells) and the *AGR* result (18.1M cells):

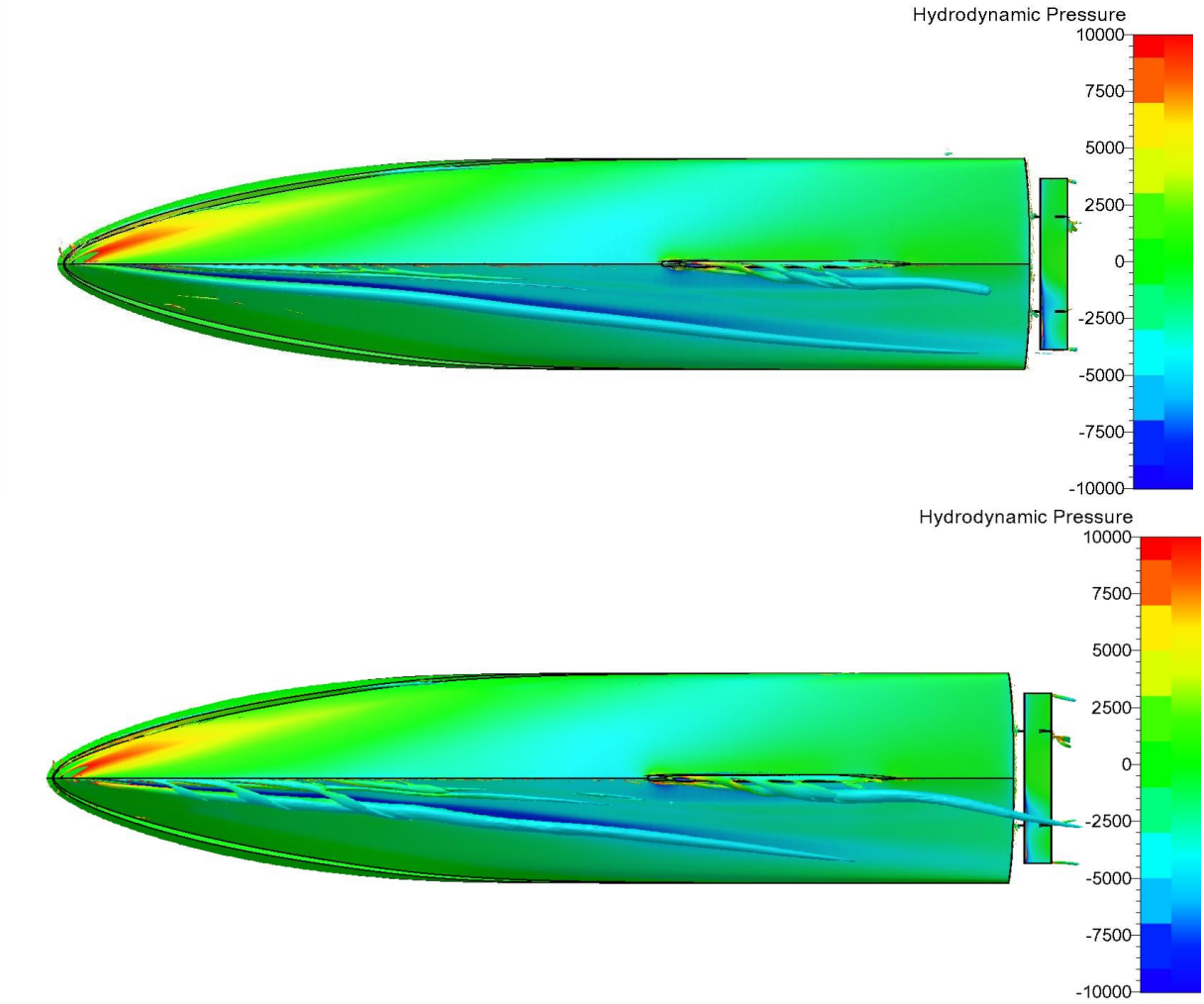

Figure 4.8: Bottom view, vorticity iso-surfaces correspondent to Q=100 (Q-criterion) and coloured according to $|\nabla \times \vec{u}| < 75\ [1/s]$. Hull surface coloured according to hydrodynamic pressure. **Top:** *G2t2*, 33.0M cells. **Bottom:** *AGR,* 18.1M cells.

From the pictures above, it is possible to see that the current *AGR* setting is capable of capturing vorticial structures that are not captured by *t2G2*, mainly in the beginning of the fore-body vortex. Furthermore, it is also possible to see that the *AGR* better captures the aft-body vortex. In *G2t2* this one ends abruptly, which is not physical according to *Helmholtz's Theorem*, see *Section 2.6.3.* This abrupt end of the vortex is caused by strong numerical diffusion due to the end of the refinement box. The following figure compares the mesh at the Q=100 iso-surface of the *G2t2* grid, with the *AGR* grid:

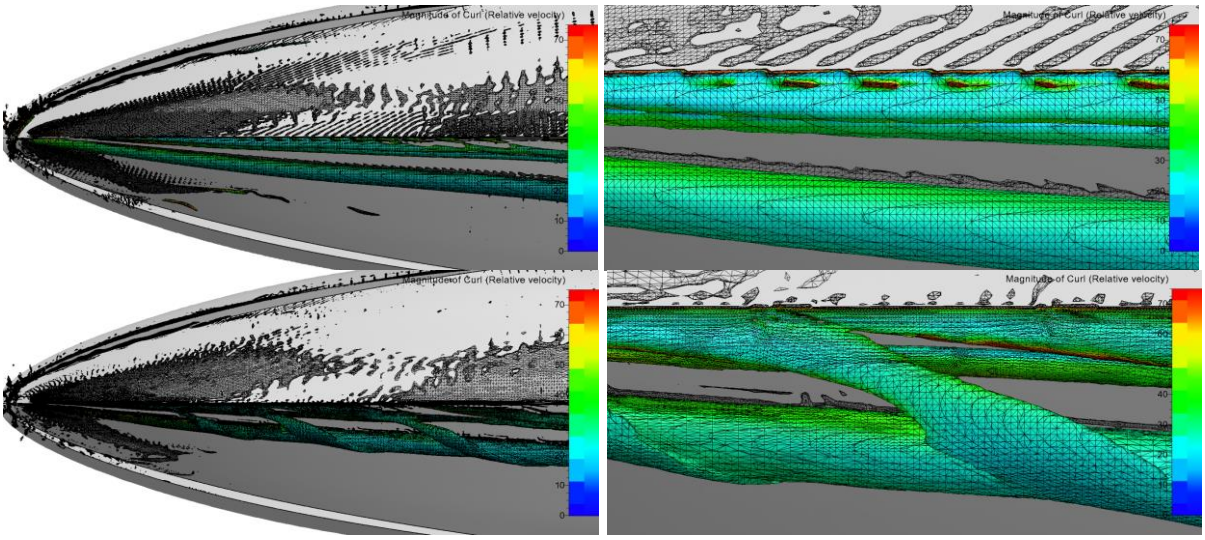

Figure 4.9: Fore body vortex (Q=100) mesh. **Top:** *G2t2* mesh. **Bottom:** *AGR* mesh. **Left:** Global view. **Right:** Local view.

As can be seen in the previous figure, since *AGR* targets high vorticity regions, it allows to capture vortices using a finer mesh than *G2t2* mesh, while keeping the total number of elements significantly lower, reducing the computational cost in about 60%. The difference in refinement is better noticed in the periphery of the vortices' filaments. The following table shows the difference between the results of *t2G2* and the *AGR* mesh:

Table 4.5: Comparison of the results of *G2t2* and *AGR.*

	***t2G2* (33M cells)**	***AGR* (18M cells)**	***AGR Relative Difference***
F_x	22428,25 [N]	22278,45 [N]	-0.67 %
F_y	102037,3 [N]	101565,5 [N]	-0.46%
M_z	614565,3 [N.m]	608815,8 [N.m]	-0.94%

The difference encountered between the results of *AGR* and *t2G2* is not considered significant for manoeuvring simulation purposes. However, the uncertainty of *t2G2* must be simply extrapolated to the *AGR* mesh, since the topology is considerably different.
Wanckers et al. in [71] shows that it is possible to produce geometrically similar grids for uncertainty estimation using *AGR,* in this article the authors also refer that: "*In principle, the adaptive refinement of a coarse, unstructured hexahedral grid using a procedure based on metric tensors is ideal for grid convergence studies*". *Wanckers et al.* applied the method proposed by *Eça* and *Hoekstra* in [47], for the solution verification of the flow around an airfoil and a *KVLCC2* (very large crude carrier). This was done by keeping the smallest cell size considerably small and constant, and by varying the *AGR* threshold by a factor 2. Although, for *KVLCC2* was found to be more challenging to reach the solution asymptotic range, this method for creation of geometrically similar grids for uncertainty estimation was considered successful.
Due to time and computational constraints, the uncertainty assessment of the *AGR* method described in *Table 4.4* is left for future research. Therefore, the uncertainty of mesh *t2G1.5* will be considered as a reference uncertainty when analysing the results. This is considered to be a conservative assumption, taking into account the results presented in *Table 4.5.*

4.1.4 RESULTS DISCUSSION

The solution verification of the grid topology 1 and 2, showed that a proper capturing of vortices is necessary for a solution convergence. In this sense, the *AGR* settings described in *Table 4.4,* are able to combine a better capturing of vortices with a decrease of 60% in computational cost. Therefore, for this research, the *AGR* settings *described in* Table 4.4 will be considered. Assuming that the uncertainties of this method are the equal to the uncertainties *t2G1.5,* and that the influence of these ones on the prediction of the manoeuvring is not significant. The validity of this assumption is addressed in *Chapter 8.*

4.2 VIRTUAL OTT RESULTS ANALYSIS

This section aims to present the results of the virtual oblique towing tests and the determination of hull hydrodynamic coefficients dependent on sway speed. The characteristics of these tests can be found in *Section 3.1.* Since the virtual model is free to heave and pitch, the hydrodynamic forces/moments are in equilibrium with the hydrostatic ones. Therefore, it is not relevant to analyze heave forces and pitch moments.

In the end the results of the virtual *OTT* tests are compared with the *PMM* results, since these last ones are often disturbed by flow memory effects, as mentioned by *Yasukawa* and *Yoshimura* in [35].

4.2.1 LONGITUDINAL ADDED RESISTANCE DUE TO SWAY SPEED

4.2.1.1 Bare Hull

The following plot shows the results and a polynomial regression of the longitudinal added resistance for the bare hull:

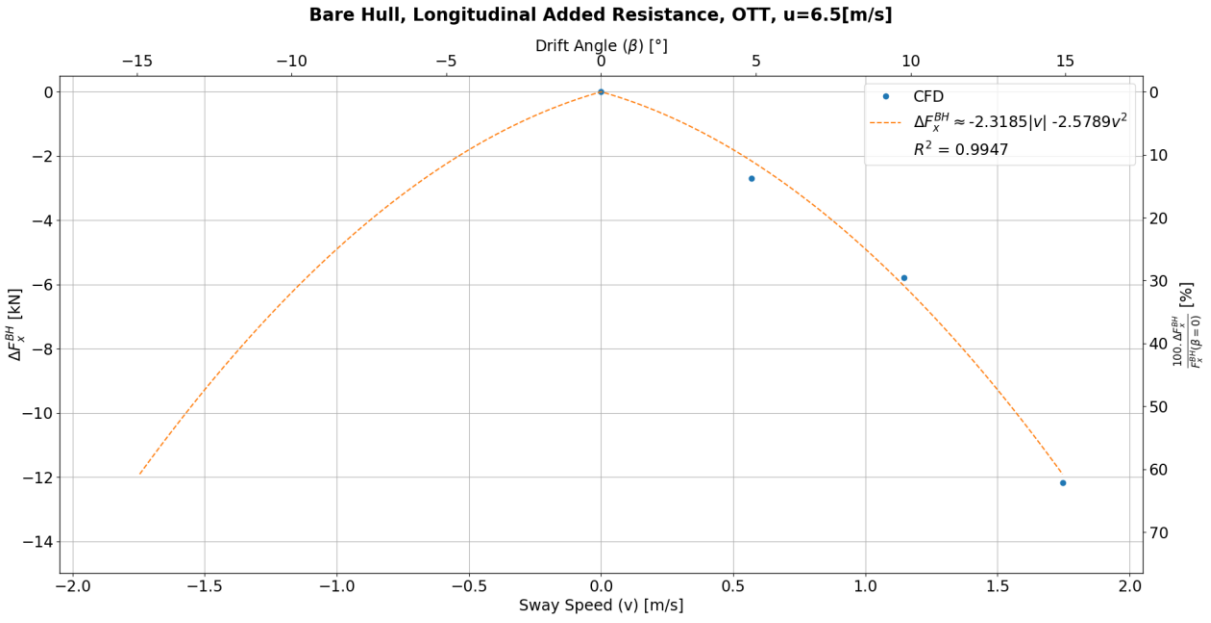

Figure 4.10: Bare hull, longitudinal added resistance due to sway speed.

The longitudinal added resistance is an even function, which means that it is not dependent on the sway direction. According to *Low Aspect Ration Wing Theory (LARWT),* presented *Section 2.10.2*, the longitudinal added resistance must be purely quadratic, since the drag of a wing is a quadratic function. However, the *LARWT* assumption is not fully applicable here since the data also shows a significant linear behaviour.

Since the *Taylor* expansion of a polynomial function is the function itself, the hydrodynamic derivatives for the added resistance in surge are given by:

- $X_{|v|}.|v| = -2.319.|v| \Rightarrow X_{|v|} = -2.319\ \left[\frac{kN.s}{m}\right] \Rightarrow X'_{|v|} = -1.1138 \times 10^{-3}\ [-]$
- $X_{vv}.v^2 = -2.579.v^2 \Rightarrow X_{vv} = -2.579\ \left[\frac{ton}{m}\right] \Rightarrow X'_{vv} = -8.0512 \times 10^{-3}\ [-]$

According to *Figure 4.10*, sway speed considerably affects the longitudinal added resistance of the vessel, reaching up to 60% of the straight-ahead resistance. The main reason for this, is an increase of pressure drag induced by flow separation and vorticity.

Together with the *Coriolis* effect ("$-v.r$" in *Eq. 2.1*) the longitudinal added resistance contributes for the speed drop phenomenon, when manoeuvring. By including the speed drop term (Δu) in *Eq. 2.48* derived in *Section 2.8,* the linear stability criteria becomes:

$$Y_v.N_r - (Y_r - m.U).N_v + m.\Delta u.N_v > 0 \qquad \textit{Eq. 4.1}$$

Note that, both the speed drop (Δu) and the *Munk* moment (N_v) are negative. Therefore, the speed drop contributes for an increase of the course stability. However, this is a very simplistic approach only useful for a conceptual understanding of the physics, after all it does not consider the entire coupling between the equation of surge (*Eq. 2.1*), sway (*Eq. 2.2*) and yaw (*Eq. 2.3*). This coupling leads to a less pronounced effect of the speed drop on the course stability, since a decrease in advance speed tends to increase the yaw rate, which decreases the sway speed leading to a decrease in yaw rate and so on. A quantitative assessment of the impact of the longitudinal added resistance on the course stability is presented in section 8.2, where a sensitivity study shows the effect of changing each hydrodynamic coefficient on the vessel's dynamic behaviour.

4.2.1.2 Hull with Hull Vane

The following plot shows the influence of the sway speed on the added resistance in surge for the hull with Hull Vane:

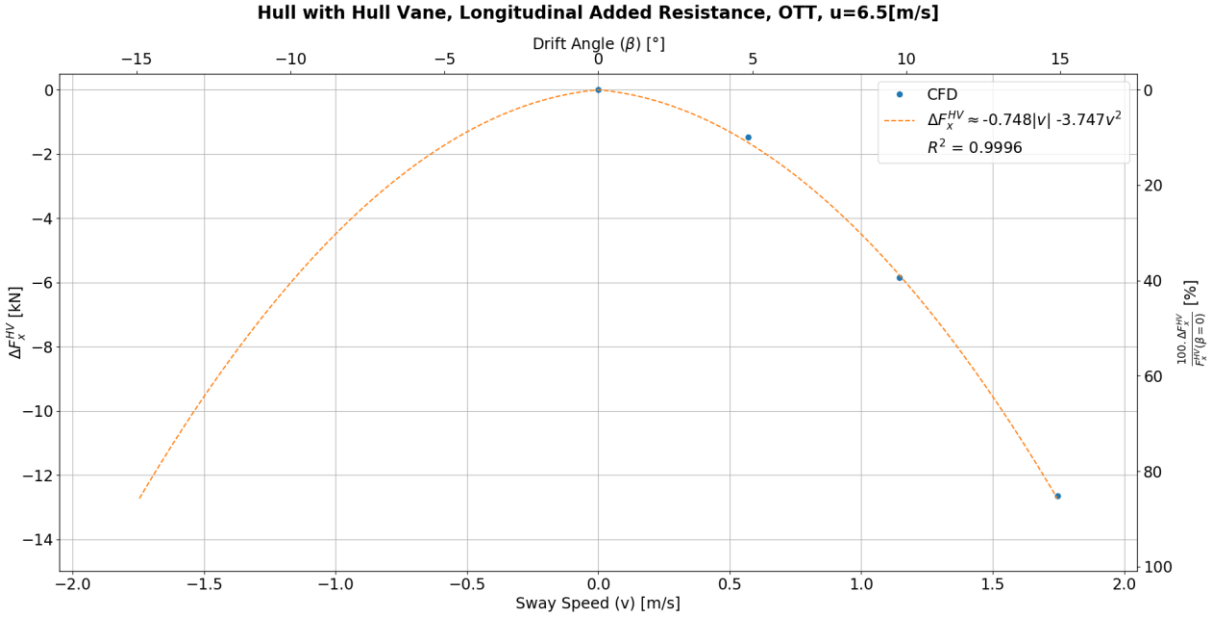

Figure 4.11: Hull with Hull Vane, longitudinal added resistance due sway speed.

A 2nd order polynomial polynomial function was also considered, according to the reasoning presented for the bare hull case. Considering this interpolation function, the hydrodynamic derivatives for the longitudinal added resistance are given by:

- $X_{|v|}.|v| = -0.748.|v| \Rightarrow X_{|v|} = -0.748\ \left[\frac{kN.s}{m}\right] \Rightarrow X'_{|v|} = -3.5926 \times 10^{-4}\ [-]$
- $X_{vv}.v^2 = -3.747.v^2 \Rightarrow X_{vv} = -3.747\ \left[\frac{ton}{m}\right] \Rightarrow X'_{vv} = -1.1698 \times 10^{-2}\ [-]$

The following plot compares the longitudinal added resistance of the vessel with and without Hull Vane:

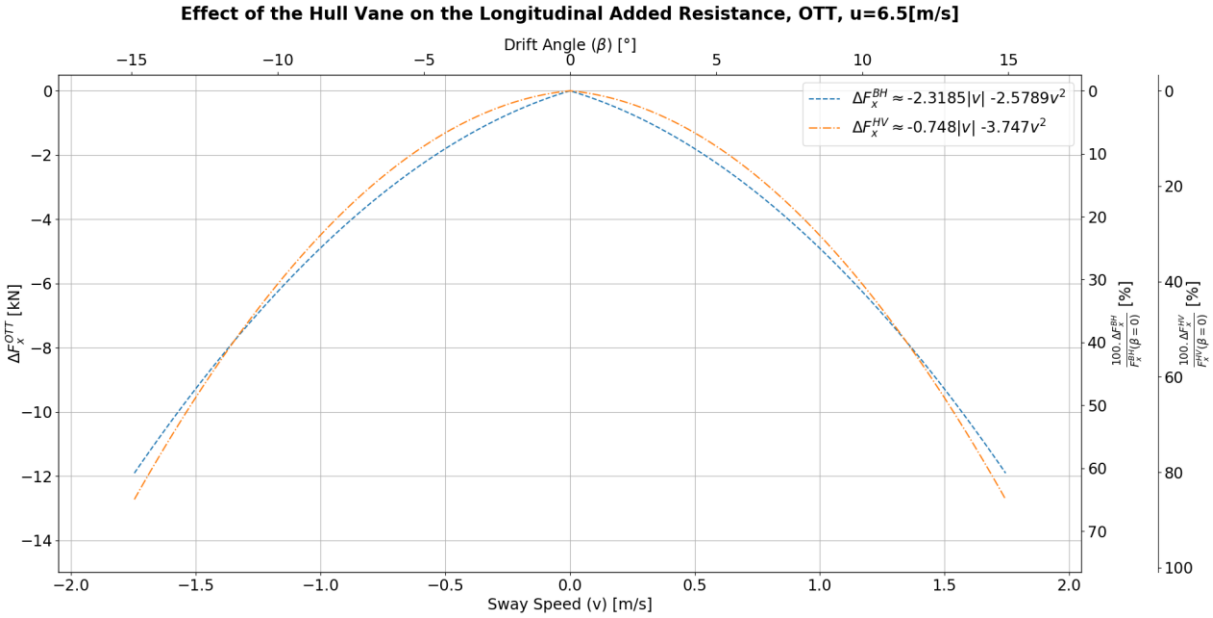

Figure 4.12: Effect of the Hull Vane on the surge added resistance due to sway speed.

Although the Hull Vane decreases the straight-ahead resistance of the vessel with 24% at 6.5 [m/s], the longitudinal added resistance. This can be explained by the fact that the increase in longitudinal resistance at drift, is caused by pressure resistance (*e.g.:* flow separation and vortex induced resistance). Since the Hull Vane does not considerably affect the upstream flow, these phenomena are practically not affected.
However, the speed drop phenomenon is more relevant than the absolute value of the longitudinal added resistance. To better understand the relation between the added resistance and the speed drop, a quadratic relation between resistance and velocity is considered:

$$\begin{cases} R_1 = c_1.u^2 \\ R_2 = c_2.u^2 \\ R_2 = R_1(1+\lambda_R) \end{cases} \qquad \textit{Eq. 4.2}$$

Note that R_1 represents the straight-ahead resistance, R_2 the resistance at drift and λ_R represents a relative increase in resistance. Assuming constant thrust during the manoeuvre, the relation between the speed drop and the added resistance is given by:

$$\Delta u = u_1.\left(\sqrt{\frac{1}{1+\lambda_R}} - 1\right) \qquad \textit{Eq. 4.3}$$

Here u_1 represents the initial speed, assuming this one constant, it is possible to see that the speed drop is related with the relative variation of resistance and not with its absolute value. According to *Figure 4.12* the relative added resistance in surge is larger for the case with the Hull Vane. However, when comparing the difference in speed drop (according to *Eq. 4.3*) for the case with and without Hull Vane at 15° drift, it is possible to conclude that the difference is about 3%, which is not expected to have a significant impact on the course stability of the vessel. Furthermore, the propulsion system tends to respond to increases in longitudinal resistance, leading to a damping of this effect on speed drop.

4.2.2 SWAY DAMPING

4.2.2.1 Bare Hull

The following plot shows the influence of the sway speed on the sway force for the bare hull:

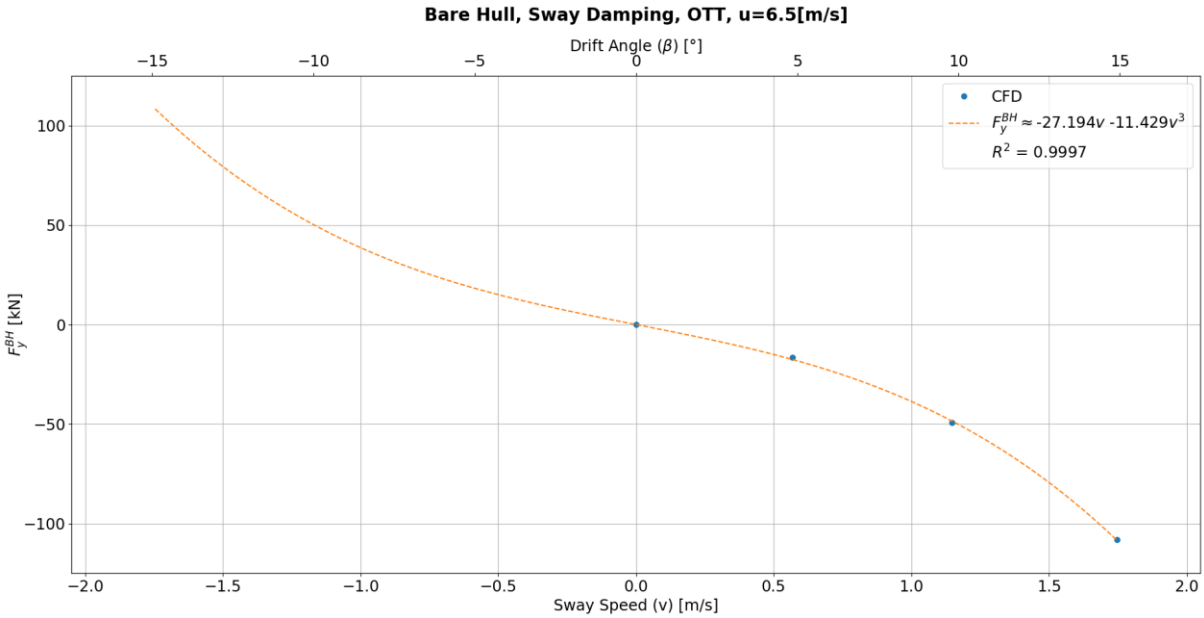

Figure 4.13: Bare hull, sway damping.

The sway force is dependent on the sway direction, so it is an odd function. A third order polynomial interpolation has a good correlation with the results ($R^2 = 0.9995$). Considering this polynomial function, the hydrodynamic coefficients for the sway force are given by:

- $Y_v.v = -27.194.v \Rightarrow Y_v = -27.194 \left[\frac{kN.s}{m}\right] \Rightarrow Y'_v = -1.3061 \times 10^{-2}[-]$
- $Y_{vvv}.v^3 = -11.429.v^3 \Rightarrow Y_{vvv} = -11.429 \left[\frac{ton}{m}\right] \Rightarrow Y'_{vvv} = -2.3193 \times 10^{-1}\ [-]$

4.2.2.2 Hull with Hull Vane

The following plot shows the influence of the sway speed on the sway force for the case of the hull with Hull Vane:

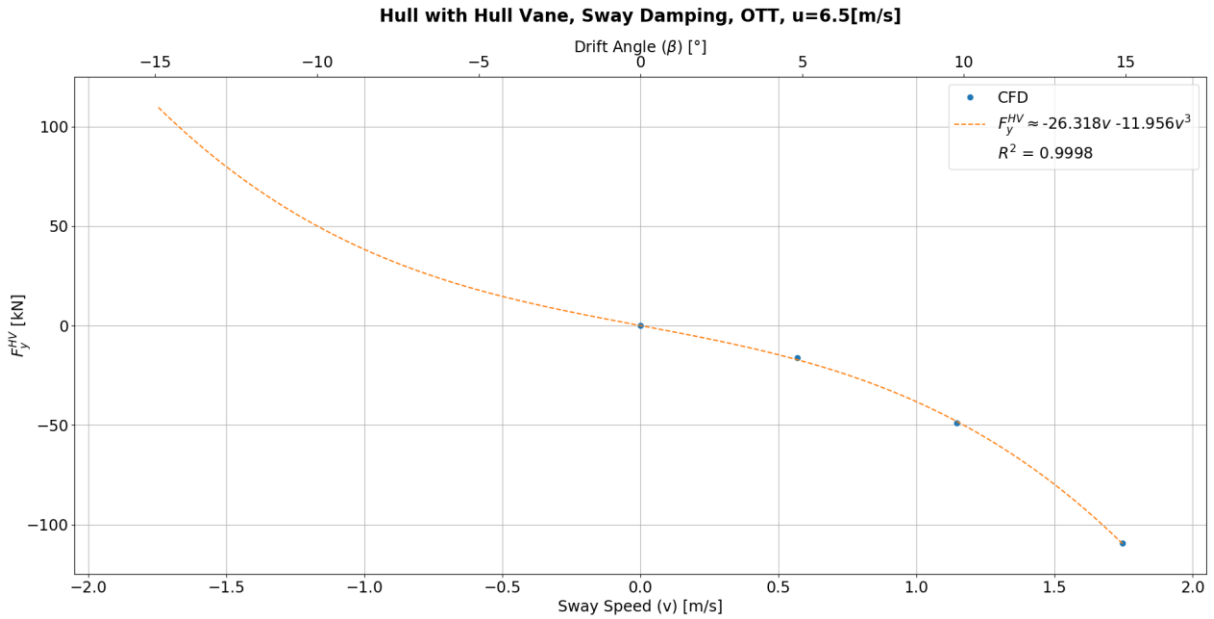

Figure 4.14: Hull with Hull Vane, sway damping.

The oblique towing tests' results are well described by a 3rd order polynomial function ($R^2 = 0.9998$), which leads to the following sway force hydrodynamic coefficients:

- $Y_v.v = -26.318.v \Rightarrow Y_v = -26.318 \left[\frac{kN.s}{m}\right] \Rightarrow Y'_v = -1.2641 \times 10^{-2}\ [-]$
- $Y_{vvv}.v^3 = -11.956.v^3 \Rightarrow Y_{vvv} = -11.956 \left[\frac{ton}{m}\right] \Rightarrow Y'_{vvv} = -2.4262 \times 10^{-1}\ [-]$

The following plot compares the regressions of the sway force due to sway speed for the case with and without Hull Vane:

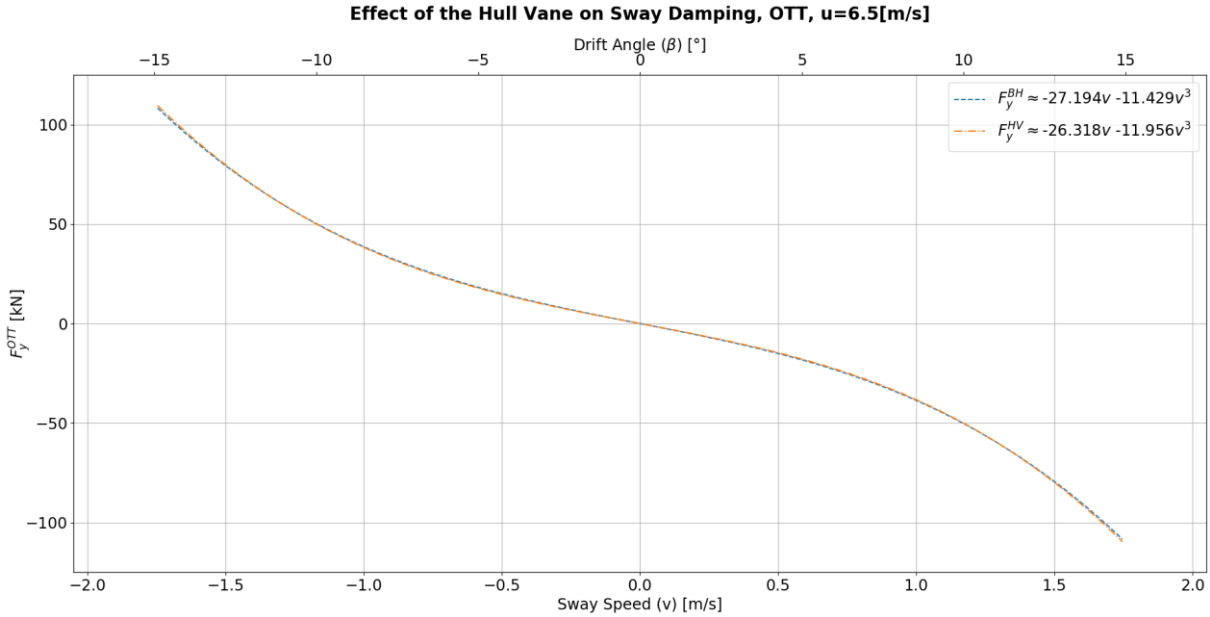

Figure 4.15: Effect of the Hull Vane on the sway force due to sway speed.

The previous plot shows that the Hull Vane practically does not affect the sway damping. This can be explained by the fact that the underwater lateral area is not significantly affects by the Hull Vane. Furthermore, the inflow angle at the struts it is expected to be straightened by the hull, which decreases their angle of attack.

4.2.3 MUNK MOMENT

4.2.3.1 Bare Hull

The following plot shows the influence of the sway speed on the yaw moment for the bare hull:

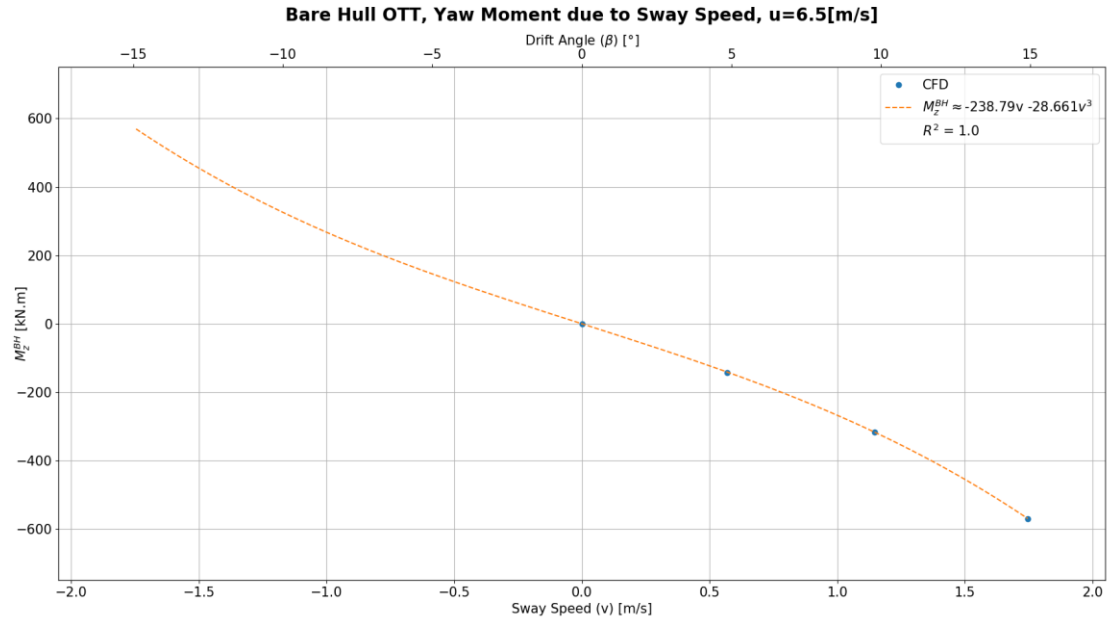

Figure 4.16: Bare hull, yaw moment due sway speed (*Munk* Moment).

A third order polynomial function was fitted through the computed points. The hydrodynamic coefficients are given by:

- $N_v.v = -238.79v \Rightarrow N_v = -238.79\ [kN.s] \Rightarrow N'_v = -4.5876 \times 10^{-3}\ [-]$
- $N_{vvv}.v^3 = -28.661.v^3 \Rightarrow N_{vvv} = -28.661\ \left[\frac{kN.s^3}{m^2}\right] \Rightarrow N'_{vvv} = -2.3264 \times 10^{-2}\ [-]$

Hull with Hull Vane

The following plot shows the influence of the sway speed on the yaw moment for hull with the Hull Vane:

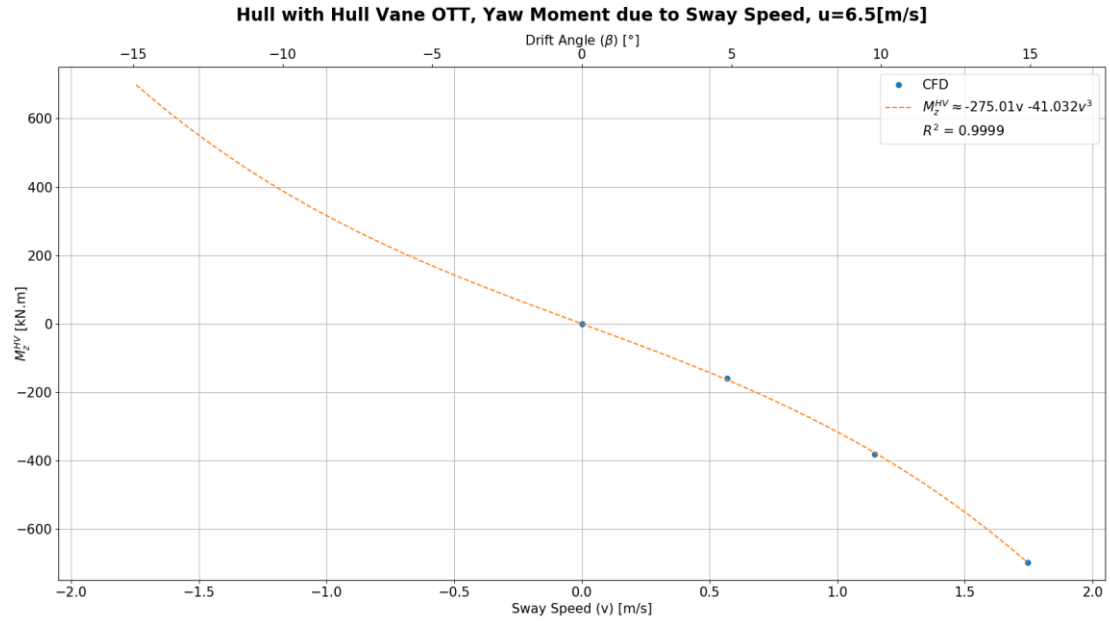

Figure 4.17: Hull with Hull Vane, yaw moment due sway speed (*Munk* Moment).

A third order polynomial function was fitted through the computed points. The hydrodynamic coefficients for the hull with Hull Vane are given by:

- $N_v.v = -275.01v \Rightarrow N_v = -275.01\ [kN.s] \Rightarrow N'_v = -5.2835 \times 10^{-3}\ [-]$
- $N_{vvv}.v^3 = -41.032.v^3 \Rightarrow N_{vvv} = -41.032\ [ton] \Rightarrow N'_{vvv} = -3.3306 \times 10^{-2}[-]$

The following plot compares the regressions for the case with and without Hull Vane:

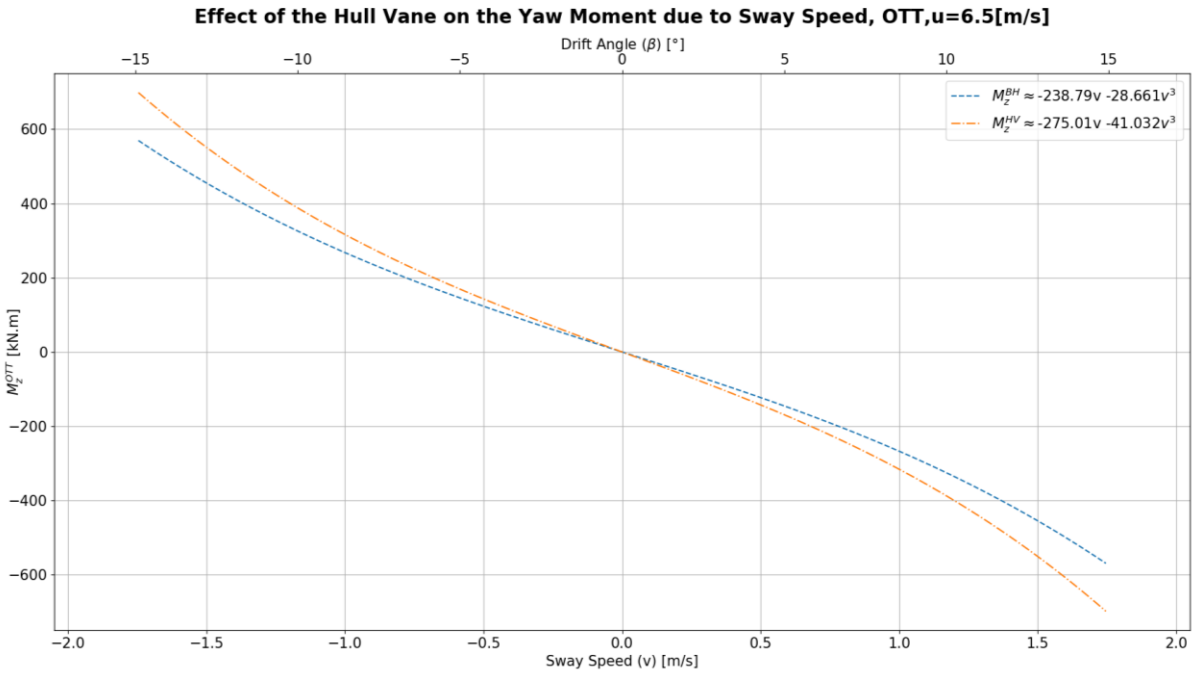

Figure 4.18: Comparison of the yaw moment due to sway speed regression with and without the Hull Vane, based on the *OTT* results.

The previous plot shows that the Hull Vane increases the *Munk* moment, contributing for a decrease in the course stability of the vessel, see *Eq. 2.51*. However, it is important to note that this difference is lower than the reference uncertainty (uncertainty of *t2G1.5*). Therefore, it is not possible to conclude that the Hull Vane increases the yaw moment due to sway speed. But it is possible to say that there is a higher chance that it increases than decreases.

This result might seem surprising since the Hull Vane struts add extra lateral area at the stern, which must lead to a decrease of the yaw moment due to sway speed (or *Munk* moment). However, the Hull Vane also affects the trim of the vessel, which increases the lateral area at the bow, leading to a decrease of the course stability, see Figure 2.8.

4.2.4 ROLL MOMENT DUE TO SWAY SPEED

4.2.4.1 Bare Hull

The following plot shows the influence of the sway speed on the roll moment:

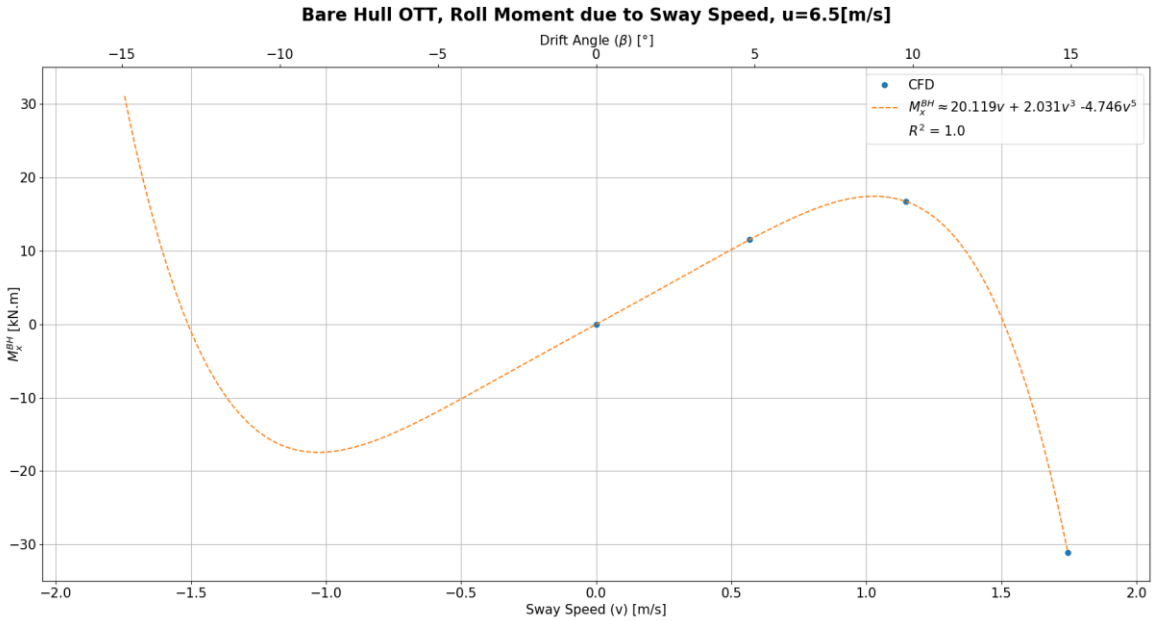

Figure 4.19: Bare hull, roll moment due sway speed.

Although the use of a 5th order polynomial fit arises concerns about an eventual over-definition of the data set, there is no physical evidence to justify the use of a 3rd order regression instead, which can be a source of modeling errors cause by the under-definition. In further research it is recommended to compute more data points in order to mitigate modeling errors.

As can be seen, in the previous figure, the roll moment has strong non-monotonic behavior. At lower sway speeds, the vessel tends to roll in one direction while at higher sway speeds it tends to roll in the opposite direction. This behavior is caused by the fact that at higher drift angles, the low pressure in the suction side of the hull (considering a hull a low aspect ratio wing, see *Section 2.10.2*) creates a roll moment greater and opposite to the one created by the skeg and pressure side. The pictures below show the static pressure (relative to atmospheric and hydrostatic) plotted in a transverse cutting plane at 5 meters from the stern, for 10° and 15° drift:

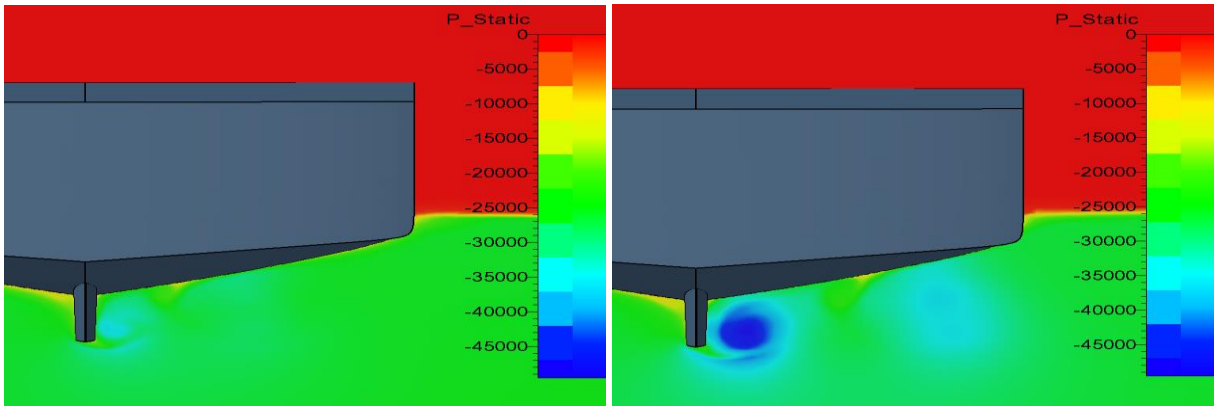

Figure 4.20: Relative static pressure plotted in a transverse cutting plane at 5 [m] from the stern. **Left:** 10° drift. **Right:** 15° drift.

As can be seen in the previous figure, the fore and aft-body vortices significantly affect the pressure field. Although at 15° drift the aft-body vortex also contributes for an increase of the skeg's roll moment, this is just a local effect which does not compensate opposite roll moment caused by the generalized decrease in pressure on the suction side of the vessel (see *Figure 4.8*).
The roll moment hydrodynamic coefficients for bare hull are:

- $K_v.v = 20.119.v \Rightarrow K_v = 20.119\ [kN.s] \Rightarrow K'_v = 3.8653 \times 10^{-4}\ [-]$
- $K_{vvv}.v^3 = 2.031.v^3 \Rightarrow K_{vvv} = 2.031\left[\frac{kN.s^3}{m^2}\right] \Rightarrow K'_{vvv} = 1.6486 \times 10^{-3}[-]$
- $K_{vvvvv}.v^5 = -4.746.v^5 \Rightarrow K_{vvvvv} = -4.746\left[\frac{kN.s^5}{m^4}\right] \Rightarrow K'_{vvvvv} = -1.6276 \times 10^{-1}\ [-]$

4.2.4.2 Hull with Hull Vane

The following plot shows the influence of the sway speed on the roll moment for the hull with Hull Vane:

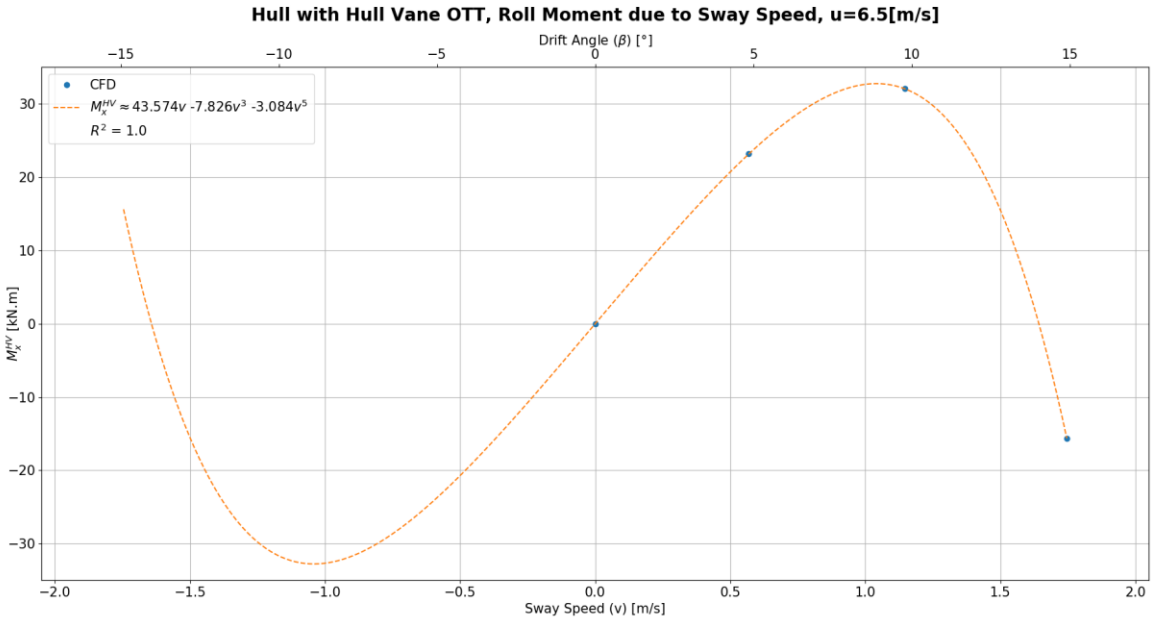

Figure 4.21: Hull with Hull Vane, roll moment due sway speed.

Similarly, to the bare hull case, a 5th order polynomial function was fit the data set. Furthermore, a non-monotonic behaviour of the roll moment is also present, a more detailed analysis of this behaviour can be found in the previous section. For the case of the hull with Hull Vane, the roll moment hydrodynamic coefficients are the following:

- $K_v.v = -20.119.v \Rightarrow K_v = 43.574\ [kN.s] \Rightarrow K'_v = 8.3714 \times 10^{-4}\ [-]$
- $K_{vvv}.v^3 = -2.031.v^3 \Rightarrow K_{vvv} = -7.826\left[\frac{kN.s^3}{m^2}\right] \Rightarrow K'_{vvv} = -6.3524 \times 10^{-3}\ [-]$
- $K_{vvvvv}.v^5 = 4.746.v^5 \Rightarrow K_{vvvvv} = -3.084\left[\frac{kN.s^5}{m^4}\right] \Rightarrow K'_{vvvvv} = -1.0576 \times 10^{-1}\ [-]$

The following plot compares the roll moment regressions for the case with and without Hull Vane:

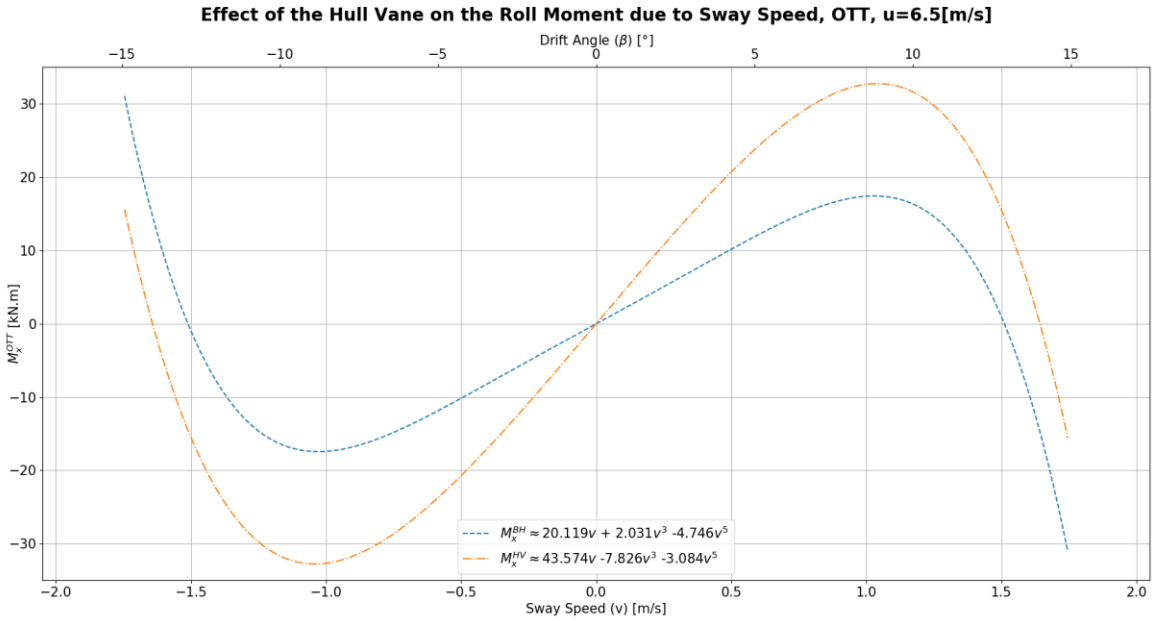

Figure 4.22 Effect of the Hull Vane on the roll moment due to sway speed.

According to these results, the Hull Vane significantly affects the roll moment due to sway speed. *Figure 4.15* shows that the contribution of the Hull Vane to the sway force is not relevant. Therefore, this effect is expected to be mainly caused by the lift distribution on the horizontal part of the Hull Vane and not by its struts. Although the free stream flow does not have a vertical velocity component, this one is induced by the vessel one the Hull Vane (*e.g.:* upwash, fore and aft body vortices) as can be seen in the following picture:

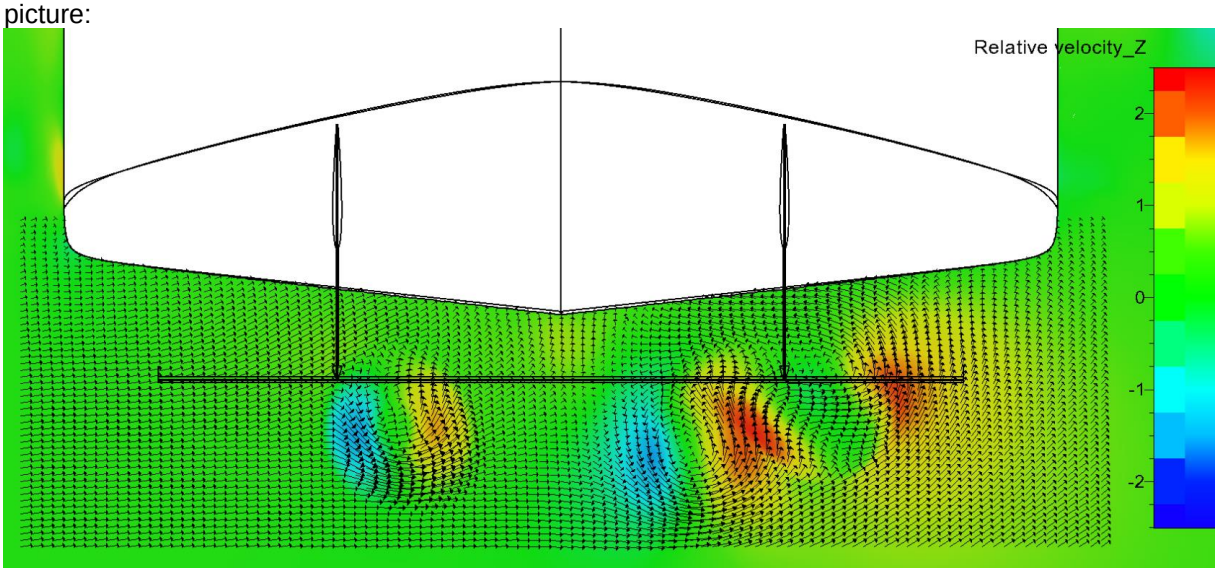

Figure 4.23: Transverse cutting plane 0.25 m forward the Hull Vane at 10° drift. The colour distribution represents the vertical component of the flow speed, the vectors represent the velocity direction and magnitude.

In the previous figure the flow is going from left to right (from portside to starboard). Due to hydrodynamic interference from the hull and actuator disks, a vertical velocity component is induced on the right (starboard) tip of the Hull Vane, contributing for a roll moment in the same direction as the skeg one, as can be verified in *Figure 4.22*. This and others interaction phenomena are analysed in more detail in *Chapter 5.*

4.2.5 SUMMARY OF THE OTT RESULTS

- **Longitudinal Added Resistance due to Sway Speed:** The added resistance in surge due to sway speed is not significantly affected by the Hull Vane. However, since in straight-ahead condition the Hull Vane decreases the resistance with 24%, this causes an increase of the relative added resistance, which contributes for an increase of the speed drop, and consequently the course stability. Nonetheless, the effect of the longitudinal added resistance in surge is damped by the coupling between motions and the propulsion system. Therefore, this the longitudinal added resistance is not expected to play an important role on course stability.

- **Sway Damping:** The sway damping is practically not affected by the Hull Vane.

- ***Munk* Moment:** The Hull Vane increases the *Munk* moment of *RPA8*, contributing for a reduction of the course stability. As previously mentioned, the Hull Vane does not affect the sway damping. Therefore, the increase in *Munk* moment is caused by the fact that the Hull Vane trims the vessel bow down.

- **Roll Moment due to Sway Speed:** The roll moment due to sway speed has a strong non-monotonic behavior, caused by the presence of fore and aft-body vortices. These vortices also interact with the Hull Vane leading to a significant impact of the Hull Vane on the roll moment due to sway speed. Due to the strong non-monotonic behavior observed, for future research, it is recommended to model the roll moment using more data points to avoid modeling errors.

These results are not enough to draw valid conclusions about the impact of the Hull Vane on the course stability of *RPA8*. To do so, it is necessary to have information about forces/moments due to yaw motion. These ones are assessed in *Section 4.5*, using data from pure-yaw *PMM* tests.

4.3 A DISCRETE SPECTRAL METHOD FOR PMM ANALYSIS

The *PMM* analysis is based on measuring the towing forces/moments and determining the in-phase part of the measured forces/moments with the accelerations and the in-phase part with the velocities. Similarly, to what is done by *Journée et al.* in [51] for the determination of the added mass and damping coefficients of a buoy in heave. *Triantafyllou* and *Hover* in [20] use this method to derive linear hydrodynamic coefficients from *PMM* tests, as the following example for sway:

$$\begin{cases} (\Delta - Y_{\dot{v}}).\dot{v} - Y_v.v = F_y \\ v = \omega.y_a.\cos(\omega.t) \\ \dot{v} = -\omega^2.y_a.\sin(\omega.t) \\ F_y = F_{y_a}.\sin(\omega.t + \epsilon) \end{cases} \qquad \textit{Eq. 4.4}$$

Here v and $\dot{v}$ are imposed and F_y is the measured force, which is assumed to have a phase angle ϵ relatively to the vessel motion. By solving this system of equations with the help of the trigonometric properties of $\sin(\omega t + \epsilon)$, it is possible to determine the added mass coefficient ($Y_{\dot{v}}$) and the damping coefficient (Y_v). However, this formulation only allows to determine linear hydrodynamic coefficients. To overcome this limitation, a discrete spectral method has been developed and implemented for the analysis of *PMM* tests in this research.

Assuming F_y to be a continuous periodic function, according to *Fourier,* this one can be represented using *Fourier Series,* see *Adams* and *Essex* in [24]:

$$F_y(t) = \frac{a_0}{2} + \sum_{n=1}^{\infty} a_n.\cos(n\omega t) + b_n.\sin(n\omega t)\,, n \in \mathbb{N} \qquad \textit{Eq. 4.5}$$

Where ω represents the fundamental frequency of the function, usually the smallest frequency present in the original function. a_0 represents a constant, a_n and b_n are the *Fourier* coefficients. These two last terms do not only define the amplitude of the different harmonics of $F_y(t)$ but also the phase angles of these ones. Therefore, *Eq. 4.*5 can be rewritten in the following form:

$$F_y(t) = \frac{a_0}{2} + \sum_{n=1}^{\infty} F_{y_a}^n . \sin(n\omega t + \epsilon_n) , n \, \epsilon \, \mathbb{N} \qquad \textit{Eq. 4.}6$$

Where $F_{y_a}^n$ represents the amplitude of the harmonic n, $n\omega$ the frequency and ϵ_n the phase angle.$F_{y_a}^n$ and ϵ_n are given by (see *Journée et al.* [51]):

$$F_{y_a}^n = \sqrt{a_n^2 + b_n^2} \qquad \textit{Eq. 4.7}$$

$$\epsilon_n = \operatorname{atan}\left(\frac{b_n}{a_n}\right) \qquad \textit{Eq. 4.8}$$

Since in *CFD* the time is discretized, $F_y(t)$ represents a discrete function which only has a solution at every time-step of the virtual *PMM* test. Therefore, to determine $F_{y_a}^n$ and ϵ_n of every wave component of $F_y(t)$, it is necessary to use a *Discrete Fourier Transform (DFT).* This is performed using a *Fast Fourier Transform (FFT)* algorithm. The mathematical details behind this algorithm are not in the scope of this research, more information about *DFT* and *FFT* can be found in chapter 11.9 of [23] (*Kreyszig, 2011*). In the end a *DFT* decomposes $F_y(t)$ in a spectrum of discrete frequencies, allowing a frequency domain analysis of this function, $F_y(\omega)$, as illustrated in the following figure:

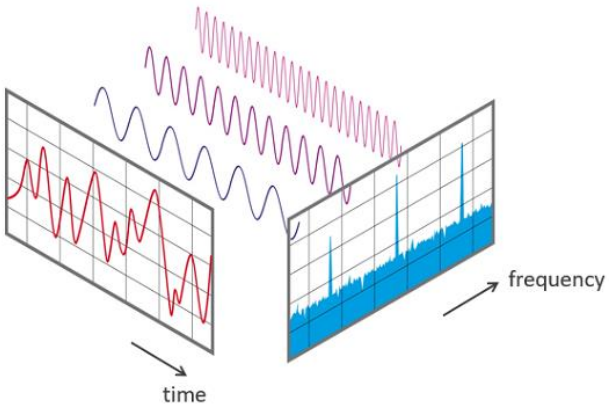

Figure 4.24: Fourier transform, time domain to frequency domain. The vertical axis represents the amplitude, *[72]*.

The frequency domain analysis allows to determine which harmonics are the most important ones to describe $F_y(t)$. These ones are related with the order of the required polynomial to describe $F_y(t)$. An example of a second order approximation for the motion equation in sway is:

$$(\Delta - Y_{\dot{v}}).\dot{v} - Y_{\dot{v}\dot{v}}\,\dot{v}^2 \;\; - Y_v \,.\, v - Y_{vv}.v^2 = \frac{a_0}{2} + F_{y_a}^1.\sin(\omega t + \epsilon_1) + \; F_{y_a}^2.\sin(2\omega t + \epsilon_2) \qquad \textit{Eq. 4.9}$$

Note that the superscript of $F_{y_a}^1$ and $F_{y_a}^2$ the harmonic number and not a power. Considering the previous example, the sway force can be rewritten in the following way, according to classical trigonometric formulations, see *Addams* and *Essex* in [24]:

$$F_{y_a}^n.\sin(n\omega t + \epsilon_n) = F_{y_a}^n.(\sin(n\omega t)\,.\cos(\epsilon_n) + \cos(n\omega t)\,.\sin(\epsilon_n)) \qquad \textit{Eq. 4.}10$$

Assuming that the sway motion is described by:

$$y = y_a.\sin(\omega t) \qquad \textit{Eq. 4.}11$$

It is then possible to split the force in two components, an unsteady component (F^u, in-phase with acceleration) and a steady component (F^s, in-phase with speed):

$$F_y{}^{u,n} = F_{y_a}^n.\sin(n\omega t).\cos(\epsilon_n) \qquad \textit{Eq. 4.}12$$

$$F_y^{s,n} = F_{y_a}^n.\cos(n\omega t).\sin(\epsilon_n) \qquad \textit{Eq. 4.}13$$

The amplitude of each one of these two components is then given by:

$$F_{y_a}^{u,n} = F_{y_a}^n.\cos(\epsilon_n) \qquad \textit{Eq. 4.}14$$

$$F_{y_a}^{s,n} = F_{y_a}^n.\sin(\epsilon_n) \qquad \textit{Eq. 4.}15$$

By representing these amplitudes in the frequency domain, it is then possible to make a preliminary assessment of the required hydrodynamic coefficients.

The following example shows how to use the *Discrete Spectral Method* to derive hydrodynamic coefficients from *PMM* tests. Although, the example here presented is for the sway force in a pure-sway test, the procedure is the same for all the remaining hydrodynamic coefficients derived from *PMM* tests:

The first step is to define the equation of motion, including the relevant force components, which are determined using the frequency domain analysis. For demonstrative purposes, the following equation of motion is considered:

$$-Y_{\dot{v}}\,\dot{v}\; - Y_{vvv}.v^3 - Y_v.v\; = F_{y_a}^1.\sin(\omega t + \epsilon_1) + F_{y_a}^3.\sin(3\omega t + \epsilon_3) \qquad \textit{Eq. 4.}16$$

Note that the previous equation only considers hydrodynamic forces. Therefore, all the inertial terms in the left-hand side are not included.

It is known that the *PMM* pure-sway motion is described by:

$$\begin{cases} v = -y_a.\omega.\cos(\omega.t) \\ \dot{v} = y_a.\omega^2.\sin(\omega.t) \end{cases} \qquad \textit{Eq. 4.}17$$

Since the *PMM* motion starts with a negative sway speed, and the phase angle is defined relative to this one, $F_{y_a}^1, F_{y_a}^3 < 0$. However, since $F_{y_a}^1, F_{y_a}^3$ represent the force amplitudes, they are positive by definition. Therefore, the motion equation becomes:

$$-Y_{\dot{v}}\,\dot{v}\; - Y_{vvv}.v^3 - Y_v.v\; = -F_{y_a}^1.\sin(\omega t + \epsilon_1) - F_{y_a}^3.\sin(3\omega t + \epsilon_3) \qquad \textit{Eq. 4.}18$$

Furthermore, according to trigonometric identities:

$$\begin{cases} \sin(\omega t + \epsilon_1) = \sin(\omega t).\cos(\epsilon_1) + \cos(\omega t).\sin(\epsilon_1) \\ \sin(3\omega t + \epsilon_3) = \sin(3\omega t).\cos(\epsilon_3) + \cos(3\omega t).\sin(\epsilon_3) \\ \cos^3(\omega t) = \dfrac{1}{4}.(3.\cos(\omega t) + \cos(3\omega t)) \end{cases} \qquad \textit{Eq. 4.}19$$

By combining *Eq. 4.*17, *Eq. 4.*18 and *Eq. 4.*19, the following expression is obtained:

$$\begin{aligned} -Y_{\dot{v}}.(y_a.\omega^2.\sin(\omega.t)) \; -\frac{1}{4}.Y_{vvv}.(-y_a.\omega)^3.(3.\cos(\omega t) + \cos(3\omega t)) - Y_v.(-y_a.\omega.\cos(\omega.t)) \\ = -F_{y_a}^1.(\sin(\omega t).\cos(\epsilon_1) + \cos(\omega t).\sin(\epsilon_1)) \\ - F_{y_a}^3.(\sin(3\omega t).\cos(\epsilon_3) + \cos(3\omega t).\sin(\epsilon_3)) \end{aligned} \qquad \textit{Eq. 4.}20$$

The previous equation can be split and simplified to obtain the following system of equations:

$$\begin{cases} Y_{\dot{v}}.\, y_a.\, \omega^2 = F_y^1.\cos(\epsilon_1) \\ Y_{vvv}.\dfrac{(y_a.\,\omega)^3}{4} = -F_y^3.\sin(\epsilon_3) \\ Y_v.\, y_a.\,\omega + \dfrac{3}{4}.\, Y_{vvv}.\,(y_a.\,\omega)^3 = -F_y^1.\sin(\epsilon_1) \end{cases} \qquad \textit{Eq. 4.21}$$

By solving this system, it is possible to reach the following solution for the hydrodynamic coefficients:

$$\begin{cases} Y_{\dot{v}} = F_{y_a}^1.\dfrac{\cos(\epsilon_1)}{y_a.\,\omega^2} \\ Y_{vvv} = -4.\, F_{y_a}^3.\dfrac{\sin(\epsilon_3)}{\left(y_a.\,\omega\right)^3} \\ Y_v = -F_{y_a}^1.\dfrac{\sin(\epsilon_1)}{y_a.\,\omega} - \dfrac{3}{4}.\, Y_{vvv}.\left(y_a.\,\omega\right)^3 \end{cases} \qquad \textit{Eq. 4.22}$$

As previously mentioned, the procedure to obtain the expressions of the remaining hydrodynamic coefficients in *Sections 4.4* and *4.5,* is equivalent to this one. Therefore it is not presented here for the sake of simplicity.

Although this method was fully developed and implemented by the author, it was later found that a similar methodology using *Fourier* transform to analyse *PMM* results have been used by *Sutulo* and *Soares* in [73].

4.4 VIRTUAL PMM RESULTS ANALYSIS – PURE SWAY

This section aims to present, analyse and discuss the results of the virtual *PMM* pure-sway test, and to determine the respective hydrodynamic coefficients. A *PMM* pure-sway test, consists in prescribing a sinusoidal motion in sway direction with constant longitudinal speed and zero-yaw rate:

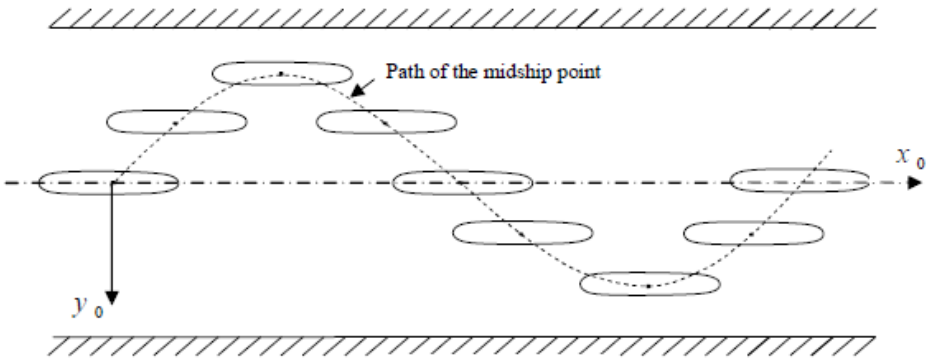

Figure 4.25: PMM, pure sway test, *[49].*

It is important to mention that the forces/moments from the virtual captive tests do not include body inertial forces, being just the result of hydrodynamic loads. According to *Eq. 3.6*, the time step for the *OTT* tests is 0.019 [s]. However, due to the highly unsteady nature of the *PMM* motion, the time step was reduced to 0.015 [s]. Further details about the settings of this virtual test can be found in *Sections 2.10.1.3* and *Chapter 3*.

4.4.1 LONGITUDINAL ADDED RESISTANCE DUE TO SWAY

4.4.1.1 Bare Hull

The following plot shows the time trace of the added resistance in surge for one period of the *PMM* motion:

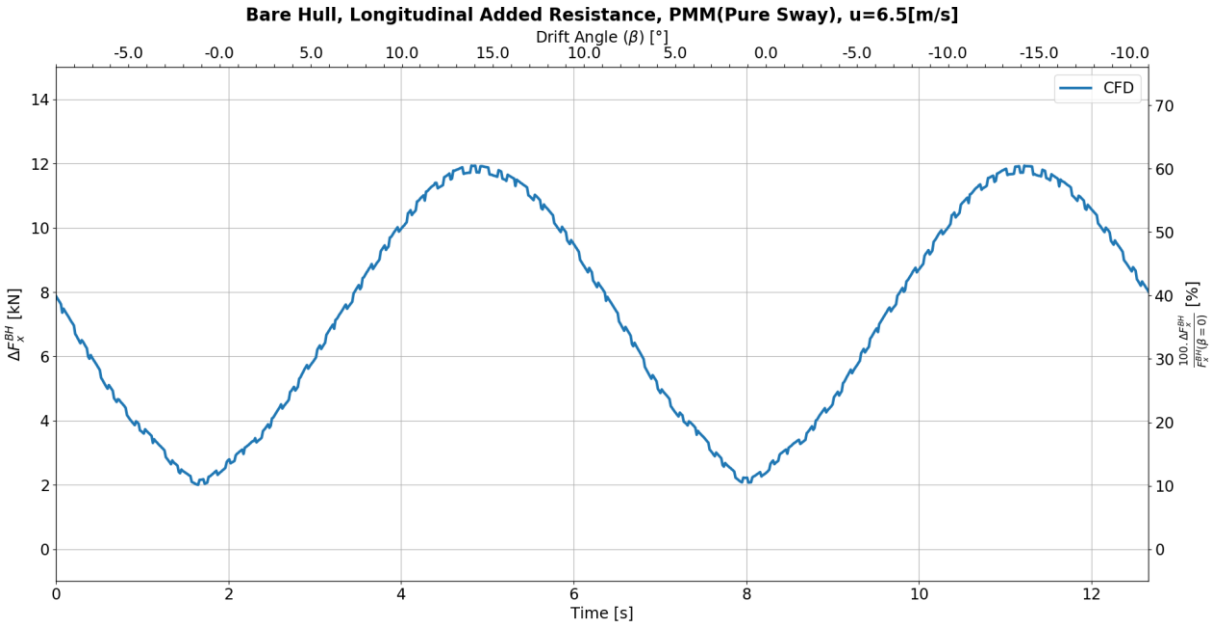

Figure 4.26: Time trace of the longitudinal added resistance of the bare hull, over a period of the pure-sway *PMM* test.

To determine the most important components of this force, a frequency domain analysis is performed:

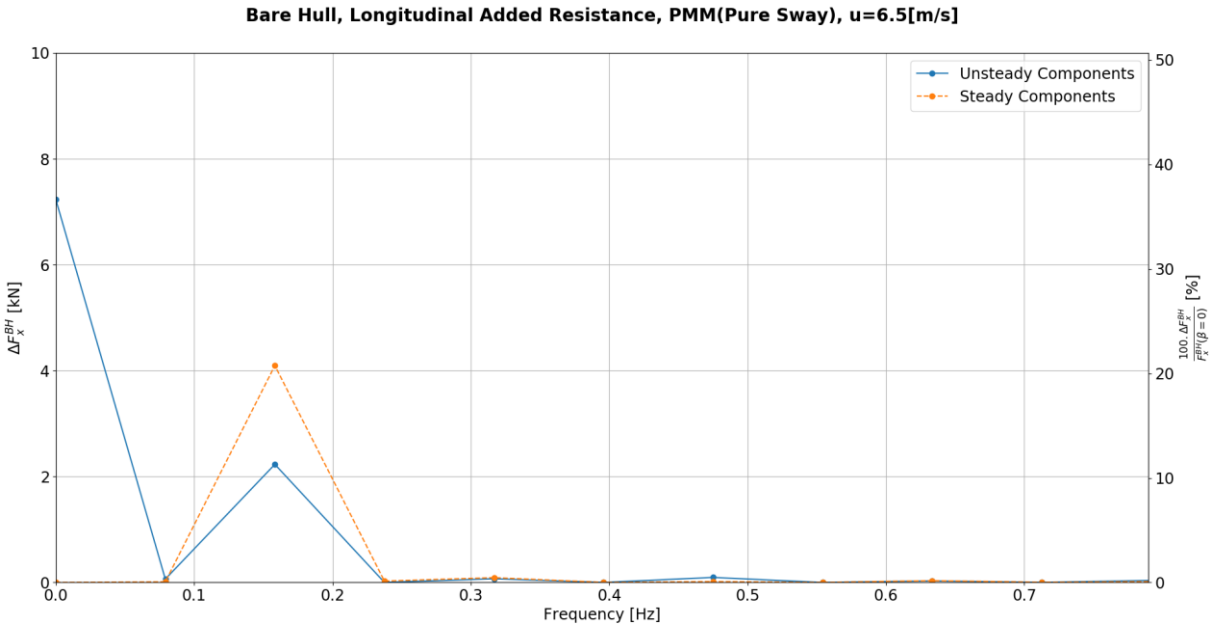

Figure 4.27: Spectrum of the absolute value of steady and unsteady longitudinal added resistance components, for the bare hull case in a *PMM* pure-sway test.

Note that frequency step of the previous plot, corresponds to the lowest possible frequency of the sample (i.e.:f_{PMM}). According to the Sampling Theorem (or *Nyquist* Theorem), to avoid aliasing effect, the maximum possible frequency corresponds to half of the sampling frequency (i.e.: $\frac{1}{2.\Delta t}$), see *Fadali* and *Visioli* in [74]. Furthermore, since manoeuvring is about the study of low frequency motions and forces (see Perez in [50]), the domain of the previous plot is restricted to 10 times the motion frequency.

According to Figure 4.27, even frequencies are the most relevant ones, this is explained by the fact that the added resistance in surge is an even function, as explained in Section 4.2.1. The peak at zero-frequency represents the shift in added resistance observed in *Figure 4.26*. However, a zero-frequency simply represents a constant signal, identifying it as an 'unsteady force' is not physically correct. This is caused by the fact that the zero-frequency component has, by definition, zero-phase angle, leading to a peak on the unsteady force since this one depends on the cosine of the phase angle. For the second harmonic it is possible to see that the steady component of the force is the most relevant one. However, the unsteady component has a comparable amplitude, meaning that it must be considered.

In Figure 4.26, it is possible to see small fluctuations in the signal. Due to their high frequency and small amplitude they are not captured in the previous plot. To understand the origin of these fluctuations the entire frequency domain is plotted:

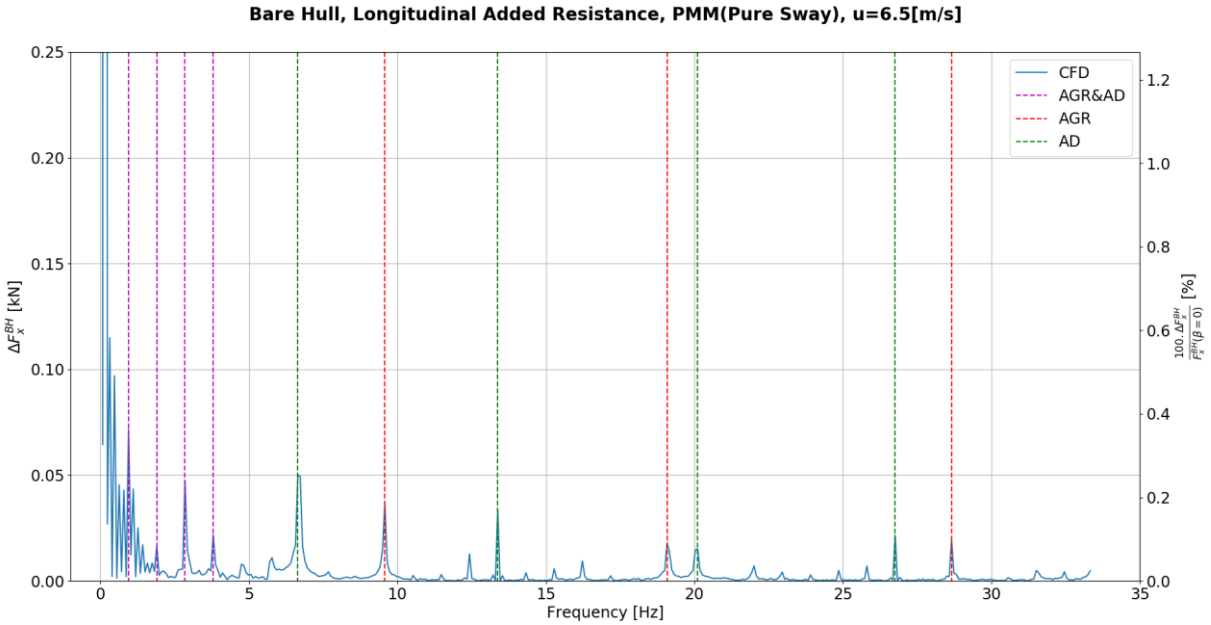

Figure 4.28: Spectrum of higher frequencies components of the longitudinal added resistance for the bare hull in a pure-sway *PMM* test.

As can be seen in the previous figure, the force amplitude is larger at lower frequencies, since these ones are closer to the *PMM* frequency and therefore more correlated to the sway motion. Thus, it is expected that the surge force amplitude decays for higher frequencies. However, in *Figure 4.28* some isolated peaks can be observed in force amplitude. A careful analysis, shows that some of these peaks correspond to harmonics of the *AGR* updating frequency (every 7 time-steps, red dashed line, $f \approx 9.56n\ Hz$), the actuator disk (AD) updating frequency (every 10 time-steps, green dashed line, $f \approx 6.6n\ Hz$) and due to the matching of the previous 2 frequencies (every 70 time-steps, magenta dashed line, $f \approx 0.95n\ Hz$). Note that for the last one only the first 4 harmonics are plotted, since these are the most relevant ones. The origin of the remaining peaks is unknown at this stage, it can be physical (*e.g.:* turbulence or vortex shedding) or numerical. Since the focus of this research is the study of low frequency forces/moments, the study of high frequency peaks is left for further research and these ones are filtered out. The following plot shows a reconstruction of the force signal using a 0 and 2nd order harmonics:

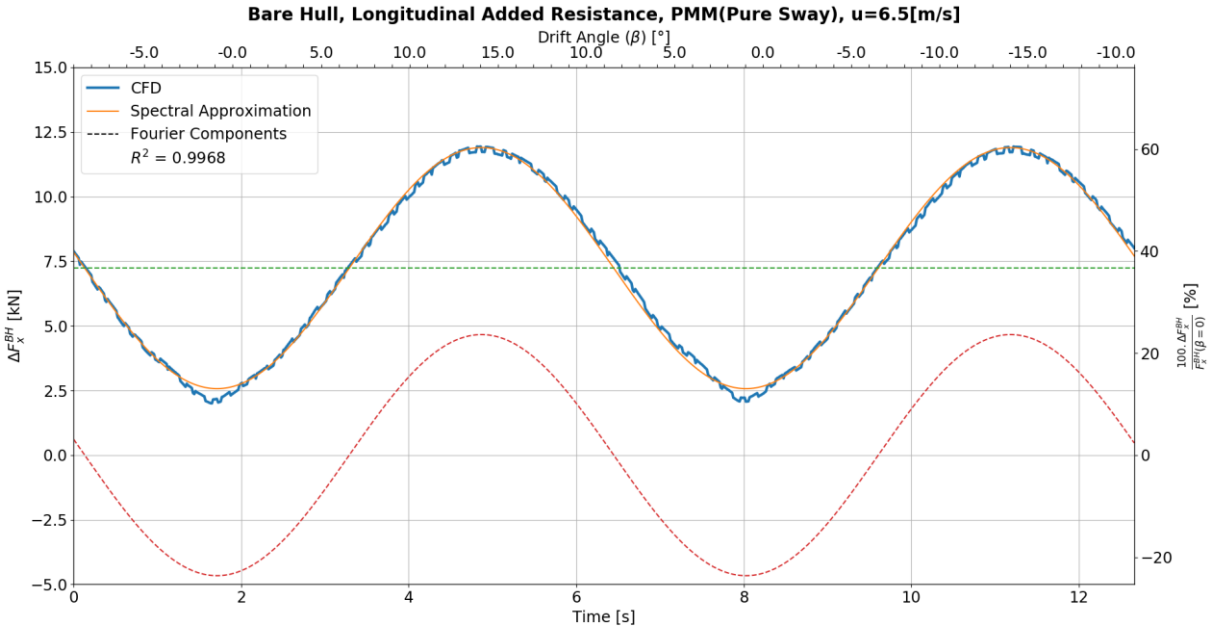

Figure 4.29: Second order reconstruction of the longitudinal added resistance over a period of the pure-sway *PMM* test.

According to the previous results, the motion equation for the longitudinal force in a pure-sway *PMM* test, is assumed to be given by:

$$-X_{\dot{v}\dot{v}}\,\dot{v}^2 - X_{vv}.v^2 = \Delta F_{x_a}^0 + \Delta F_{x_a}^2.\sin(2\omega t + \epsilon_2) \qquad \textit{Eq. 4.23}$$

Note that the superscript of ΔF_{x_a} indicates the harmonic correspondent to this force amplitude and not a power. The hydrodynamic derivatives of the surge forces due to sway speed for the bare hull are given by:

$$\begin{cases} X_{\dot{v}\dot{v}} = -\dfrac{\Delta F_{x_a}^2.\sin(\epsilon_2) + F_{x_a}^0}{y_a^2.\omega^4} \\ X_{vv} = -\dfrac{2.\Delta F_{x_a}^0}{y_a^2.\omega^2} - X_{\dot{v}\dot{v}}.\omega^4 \end{cases} \Rightarrow \begin{cases} X_{\dot{v}\dot{v}} = -4.166\left[\dfrac{ton.s^2}{m}\right] \\ X_{vv} = -3.721\left[\dfrac{ton}{m}\right] \end{cases} \Rightarrow \begin{cases} X'_{\dot{v}\dot{v}} = -8.7921\times10^{-4}[-] \\ X'_{vv} = -1.1617\times10^{-2}[-] \end{cases} \qquad \textit{Eq. 4.24}$$

The following plot compares the regressions for added resistance in surge obtained from the *OTT (Section 4.2.1.1)* and *PMM* tests for the bare hull:

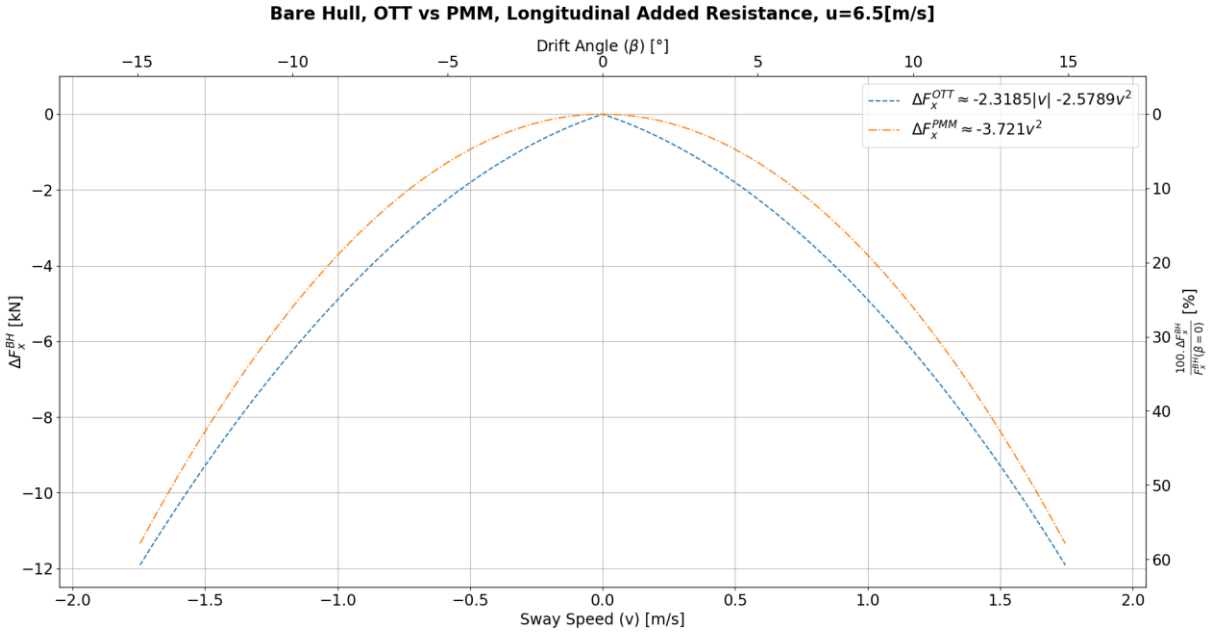

Figure 4.30: Comparison between the regression obtained from *OTT* and *PMM* tests for the longitudinal added resistance of the bare hull.

The previous figure shows that the pure-sway PMM test under-predicts the magnitude of the longitudinal added resistance, when compared to the OTT results, which contributes for an under-prediction of course stability, see *Eq. 4.1.* This difference is expected to be caused by flow memory effects due to the unsteady motion of the *PMM* test, a better convergence of the *OTTs* results and the fact that the regression from the *PMM* results is based on one point (*i.e.:* when the sway speed is equal to zero), while the *OTT* regression is based on four points.

4.4.1.2 Hull with Hull Vane

The following figure shows a second order reconstruction of the longitudinal added resistance signal, using:

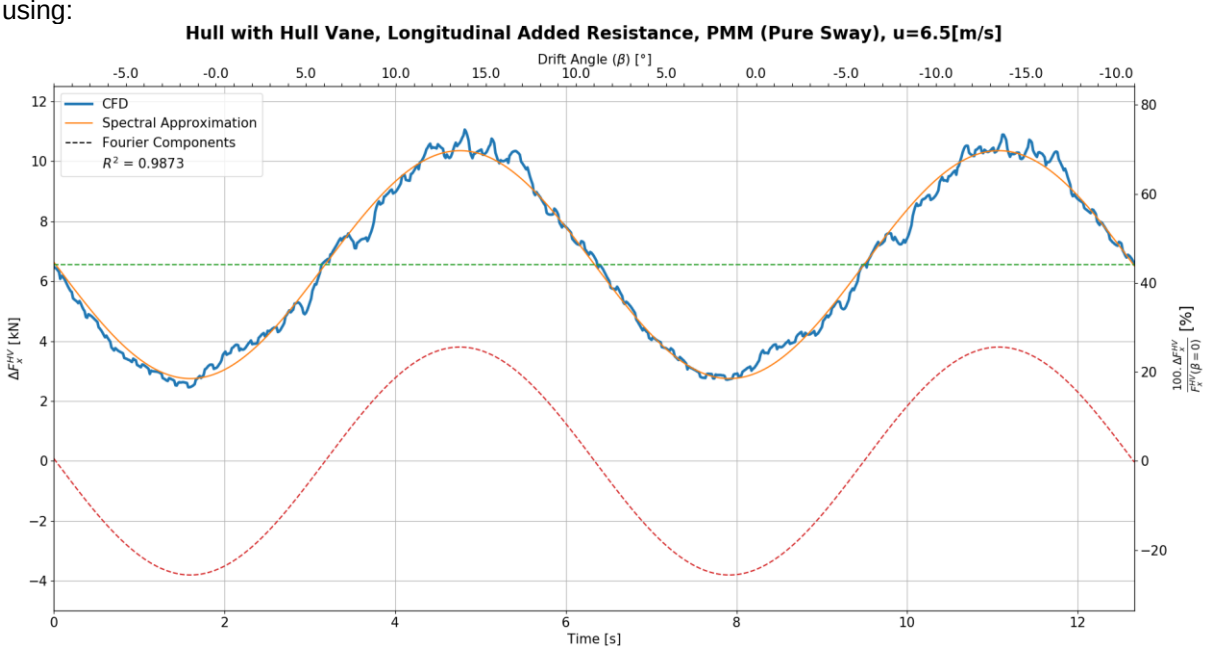

Figure 4.31: Time trace of the longitudinal added resistance in a *PMM* pure sway test for the hull with Hull Vane.

As can be seen, a good correlation is obtained with a 2nd order reconstruction ($R^2 = 0.9873$). However, it is possible to see higher amplitude fluctuations, relative to the bare-hull case. A frequency domain analysis of the force signal shows higher amplitudes of the frequencies matching the *AGR* and *AD* harmonics. This indicates that the vessel with Hull Vane is more sensitive to the *AGR* and *AD* updating frequencies. Lifting surfaces, like hydrofoils, are in general very sensitive to changes in the flow field. Therefore, since the updating of the *AGR* and *AD* (actuator disk) affects the flow field at the stern, the Hull Vane amplifies these effects.

Considering *Eq. 4.*23 and *Eq. 4.*24, the longitudinal added resistance hydrodynamic coefficients, for the hull with Hull Vane, are the following:

$$\begin{cases} X_{\dot{v}\dot{v}} = -4.008 \left[\frac{ton.s^2}{m}\right] \\ X_{vv} = -3.312 \left[\frac{ton}{m}\right] \end{cases} \Rightarrow \begin{cases} X_{\dot{v}\dot{v}} = -8.4586 \times 10^{-4}\,[-] \\ X_{vv} = -1.0340 \times 10^{-2}[-] \end{cases} \qquad \textit{Eq. 4.}25$$

The following plot compares the regressions for added resistance in surge obtained from the *OTTs (Section 4.2)* and *PMM* test for the hull with Hull Vane:

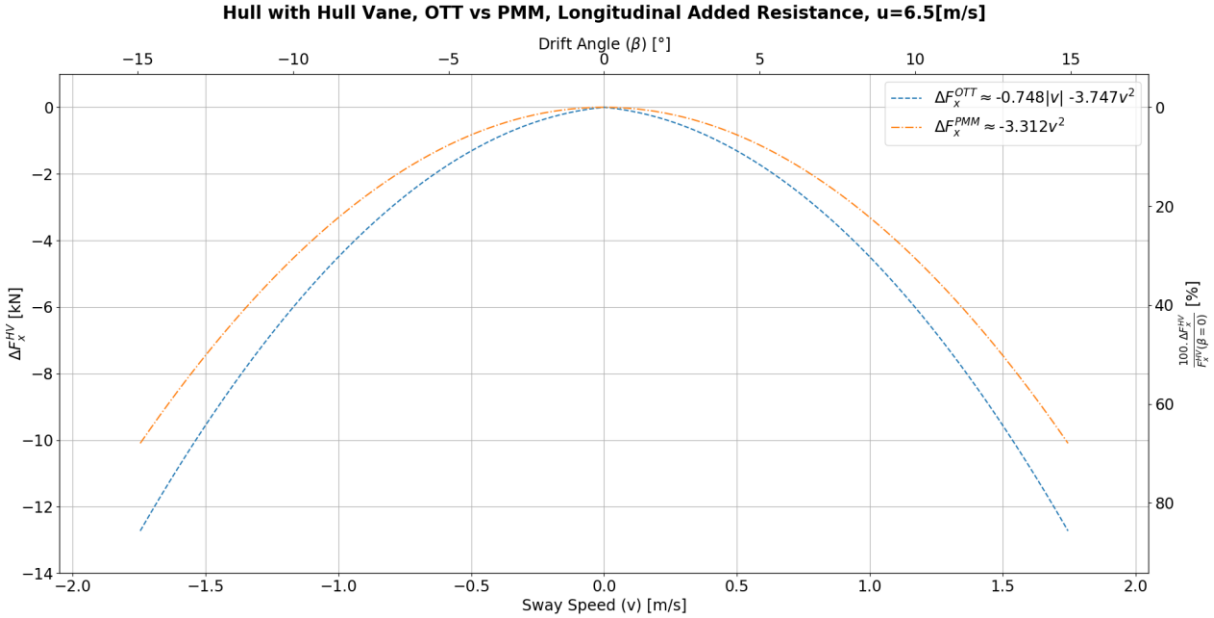

Figure 4.32: Comparison between the regression obtained from *OTT* and *PMM* tests for the longitudinal added resistance of the hull with Hull Vane.

Similarly, to what was found in the previous section, the pure-sway *PMM* test under-predicts the added resistance in surge when compared to the OTT results, which contributes for an under-estimation of course stability, see *Eq. 4.*1. The origin of this discrepancy is discussed in the previous section.

The following plot compares the regressions for the added resistance in surge due to sway speed, with and without the Hull Vane:

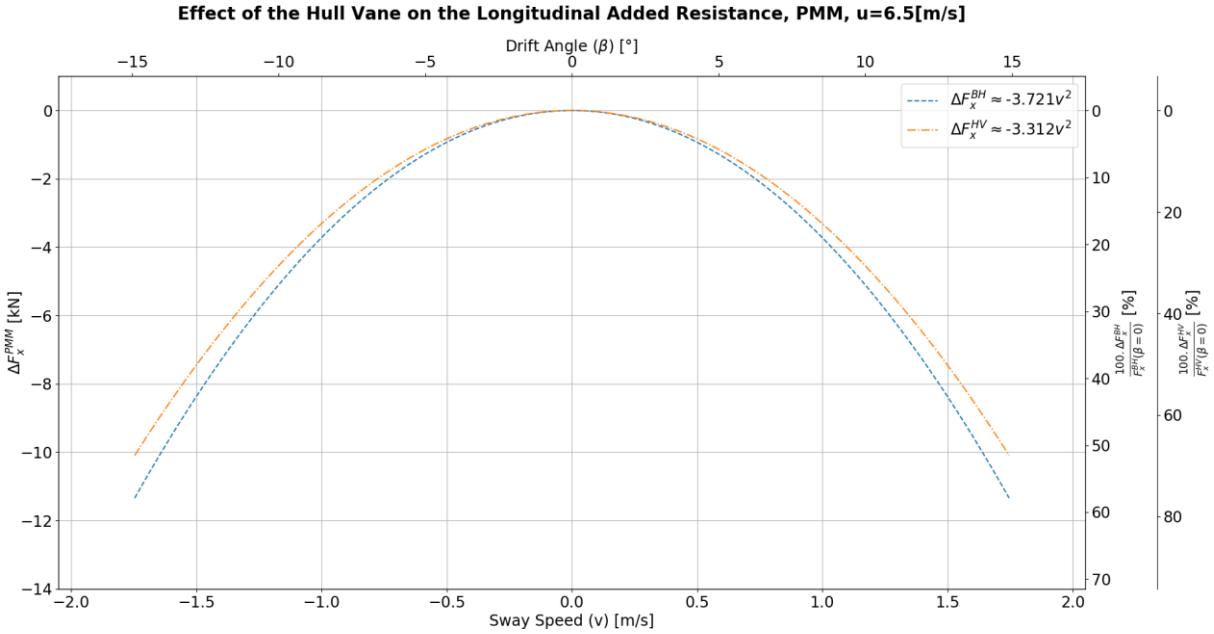

Figure 4.33: Comparison of the longitudinal added resistance, for the bare hull and Hull Vane, depending on the sway speed.

Similarly, to what was found in *Section 4.2.1*, the Hull Vane is expected to have small contribution for speed drop. Therefore, it is not expected to significantly affect course stability of the vessel. The following plot compares the added resistance in surge due to sway acceleration for the case with and without Hull Vane.

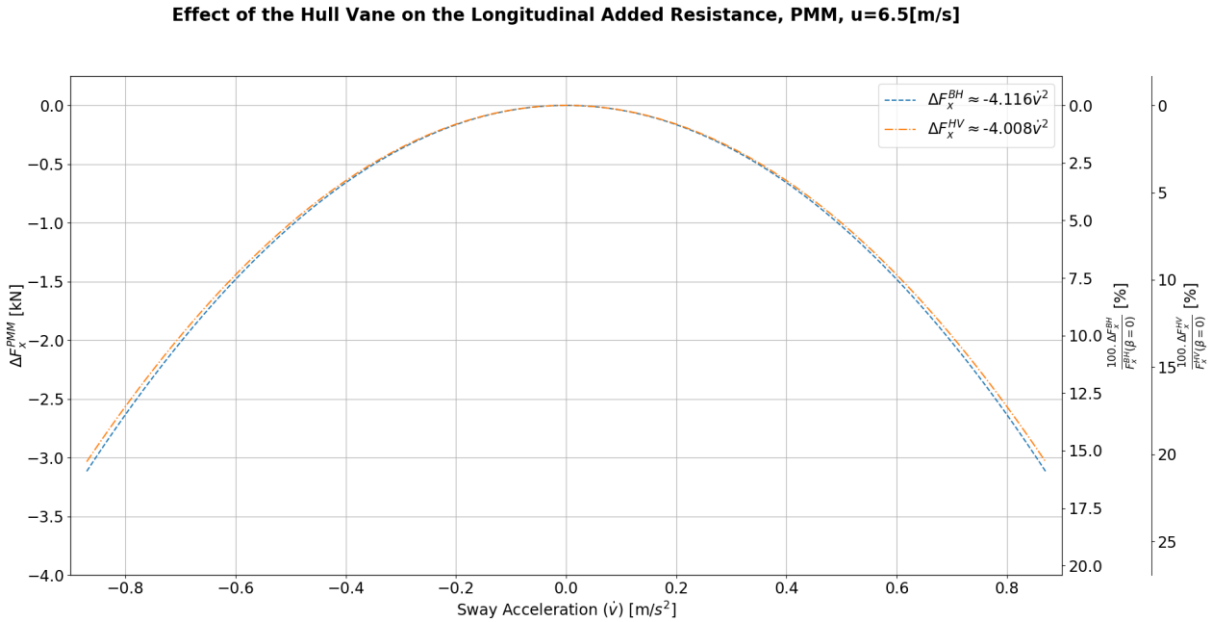

Figure 4.34: Comparison of the surge added resistance, for the bare hull and Hull Vane, depending on the sway acceleration.

According to *Figure 4.34*, the added resistance in surge due to sway acceleration, is not significantly affected by the Hull Vane.

4.4.2 SWAY DAMPING AND ADDED MASS

4.4.2.1 Bare Hull

The following plot shows the time trace of the force in sway for the bare hull, during one period of the PMM motion in a pure-sway test:

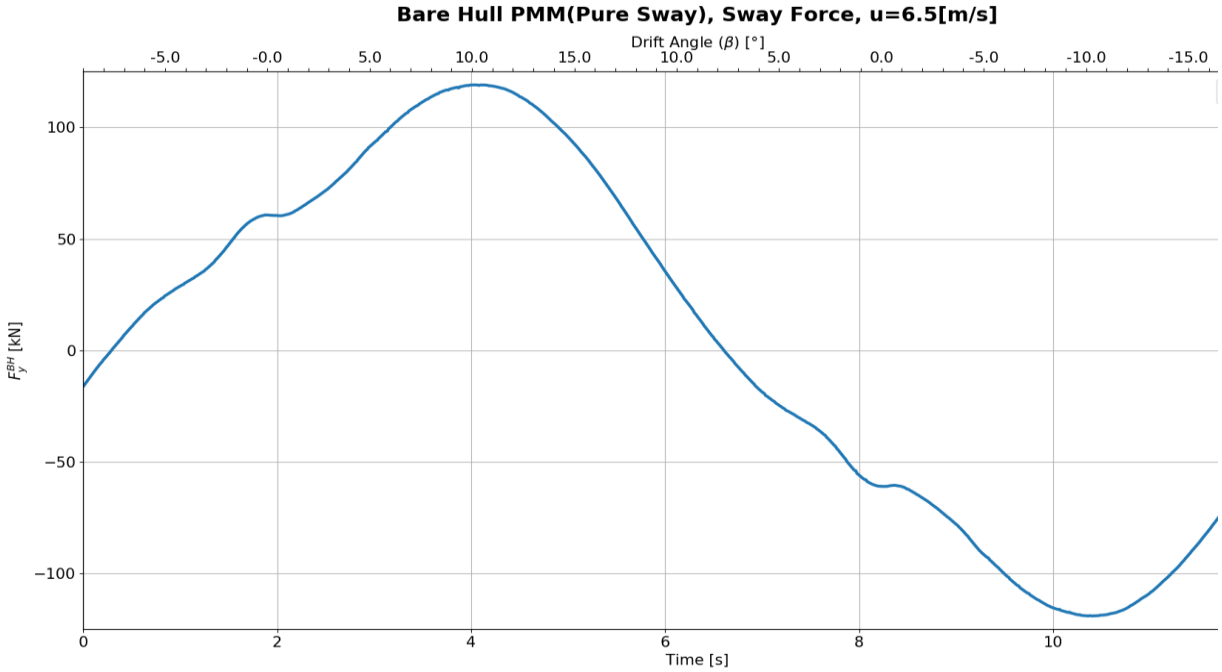

Figure 4.35: Time trace of force in sway of the bare hull, over a period of the pure-sway *PMM* test.

According to the previous plot, the sway force shows to have a non-linear relation with the sway speed, similarly to what was found in the *OTT* results, *Section 4.2.2.1.* In contrast to the longitudinal added resistance due to sway speed (*Section 4.4.1),* the signal of the sway force does not have a significant influence of noise from frequencies matching the updating frequency of actuator disk and *AGR.* This is explained by the higher amplitude of the sway force comparatively to the longitudinal added resistance (about 6 times larger). In order to determine the most significant frequencies, the magnitude of the unsteady and steady force components is plotted in the frequency domain:

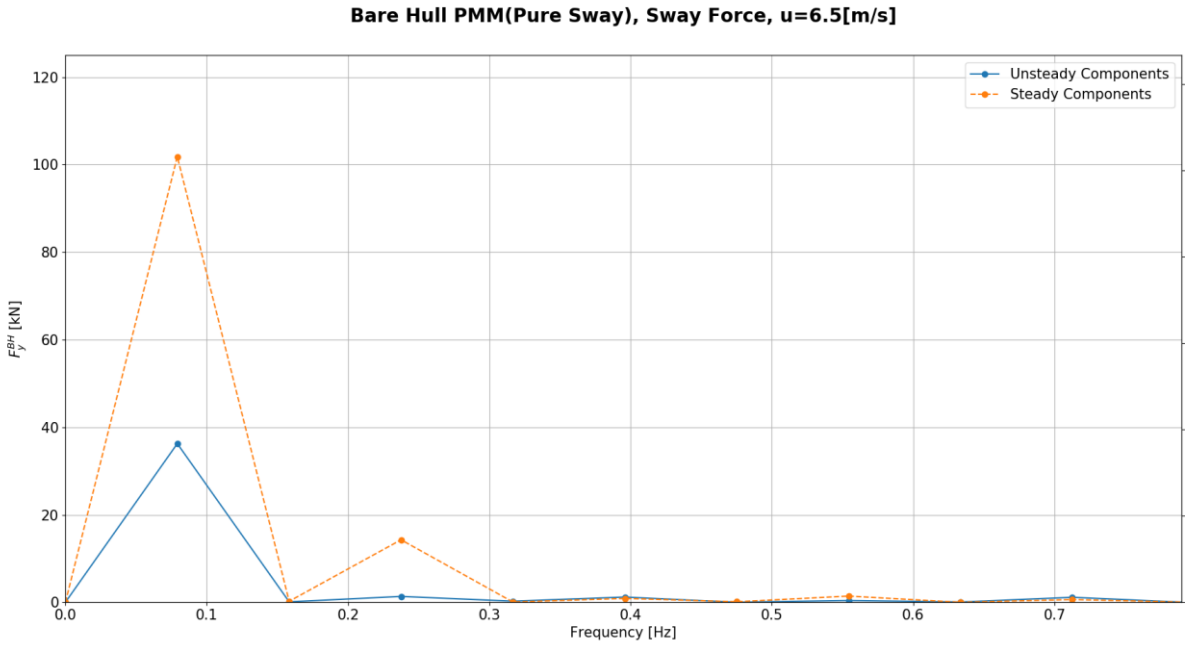

Figure 4.36: Spectrum of the magnitude of the steady and unsteady sway force components, for the bare hull case. *PMM* pure-sway test.

The previous figure shows that the sway force due to sway motion is mainly dependent on odd harmonics of the motion. This is due to the fact that the sway force is an odd function, meaning that its direction depends on the direction of the motion. The most significant frequencies correspond to the 1st and 3rd harmonics of the motion. Furthermore, for these frequencies, the steady component of the force (damping in sway) is the most significant one. The unsteady component (sway added mass) shows to be only significant for the first harmonic. The remaining frequencies are assumed to be negligible in the context of this research. The following figure shows the reconstruction of the sway force using a 1st and 3rd order motion harmonics.

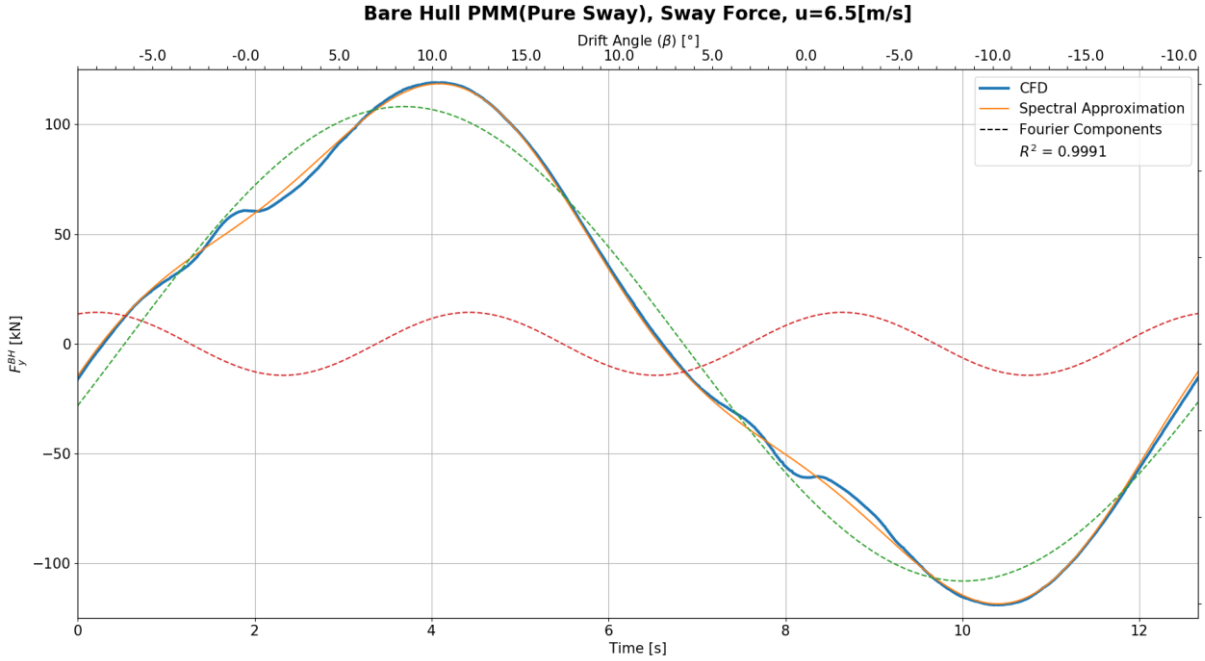

Figure 4.37: First and third order reconstruction of the added resistance in surge over a period of the pure-sway *PMM* test for the bare hull.

As can be seen in the previous plot, a 1st and 3rd order reconstruction properly captures the average behaviour of the signal ($R^2 = 0.9991$). However, it is not able to capture smaller details as the wiggles at 2 and 8 seconds. Due to the relative low frequency of these wiggles they are expected to have a physical origin. By using a 9th order reconstruction of the force it is possible to better capture them, as shown in the following picture:

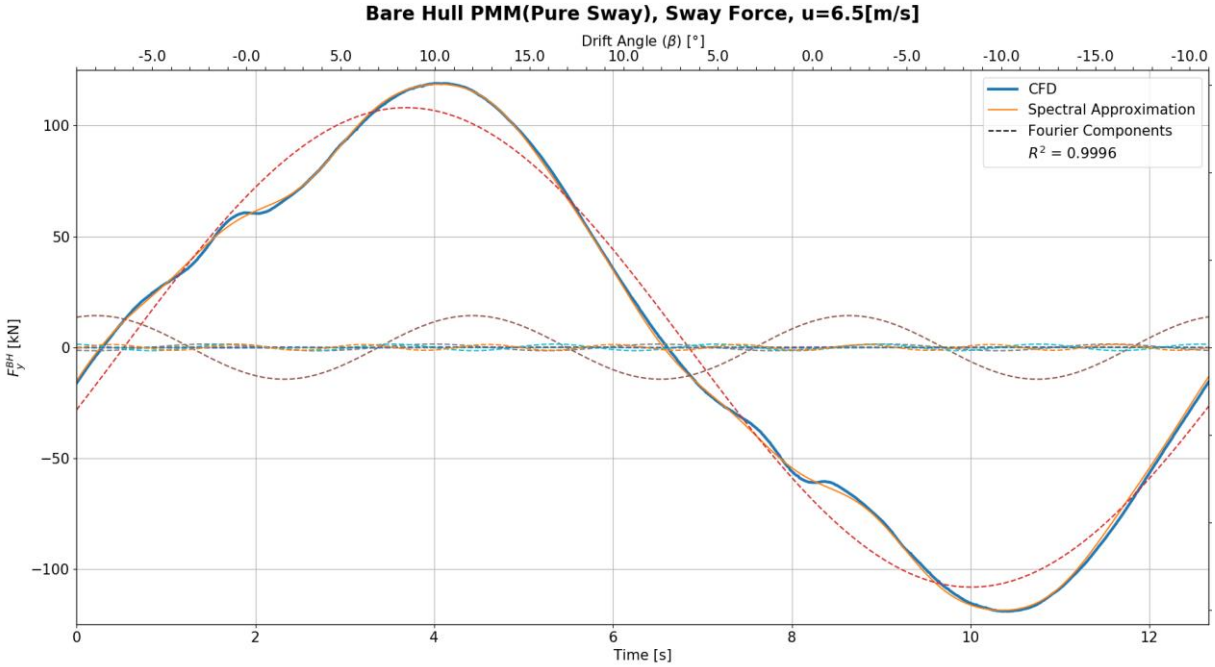

Figure 4.38: Force reconstruction using the first 9 harmonics of the motion frequency.

The origin of these wiggles is not clear at this point. As it is possible to see in the previous figure, they occur close to $\beta = 0°$. Therefore, they are related to sway acceleration (*e.g.:* flow memory effects). Due to their relatively small magnitude, these ones are neglected.

According to *Figure 4.36*, the motion equation in sway is given by:

$$-Y_{\dot{v}}\,\dot{v} \; - Y_{vvv}.v^3 - Y_v.v \; = F^1_{y_a}.\sin(\omega t + \epsilon_1) + F^3_{y_a}.\sin(3\omega t + \epsilon_3) \qquad \textit{Eq. 4.26}$$

Note that only fluid forces are being considered. Therefore, body inertial effects are not included in the measured forces. Having said this, the sway hydrodynamic coefficients are given by:

$$\begin{cases} Y_{\dot{v}} = F^1_{y_a}.\dfrac{\cos(\epsilon_1)}{y_a.\omega^2} \\ Y_{vvv} = -4.F^3_{y_a}.\dfrac{\sin(\epsilon_3)}{(y_a.\omega)^3} \\ Y_v = -F^1_{y_a}.\dfrac{\sin(\epsilon_1)}{y_a.\omega} - 3.Y_{vvv}.\dfrac{(y_a.\omega)^3}{4} \end{cases} \Rightarrow \begin{cases} Y_{\dot{v}} = -41.768\,[ton.] \\ Y_{vvv} = -10.751\left[\dfrac{kN.s^3}{m^3}\right] \\ Y_v = -33.815\left[\dfrac{kN.s}{m}\right] \end{cases} \Rightarrow \begin{cases} Y'_{\dot{v}} = -5.2159 \times 10^{-3}\,[-] \\ Y'_{vvv} = -2.1817 \times 10^{-1}\,[-] \\ Y'_v = -1.6241 \times 10^{-2}\,[-] \end{cases} \qquad \textit{Eq. 4.27}$$

The following plot compares the regressions, for the sway damping, obtained from the *OTT* tests and pure-sway *PMM* test:

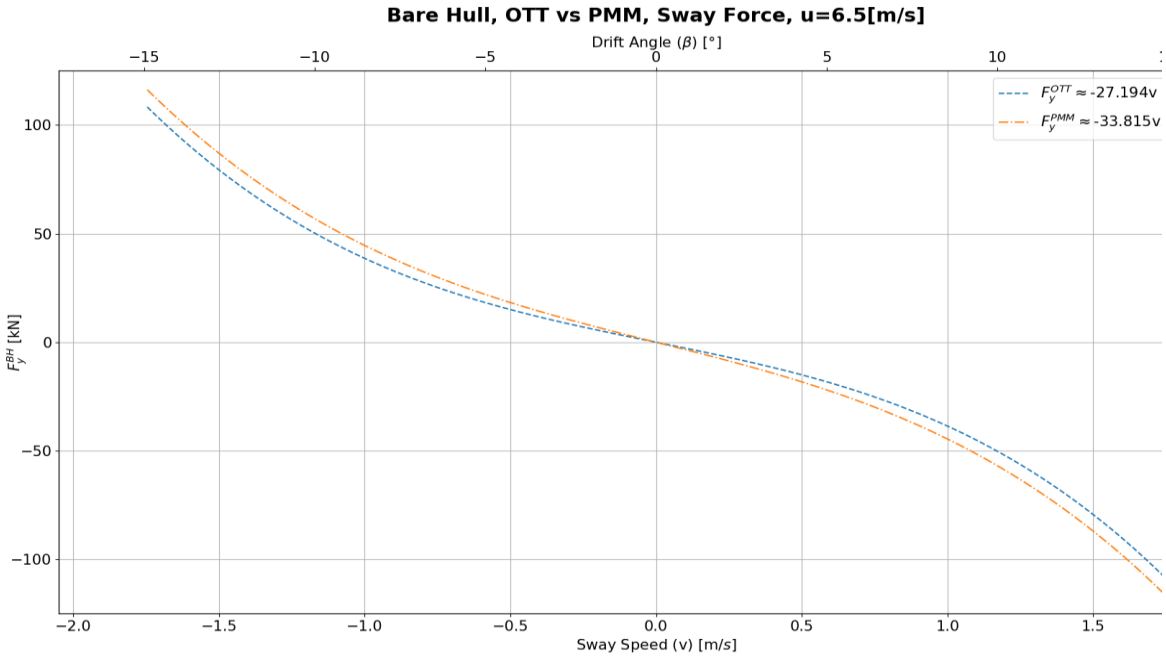

Figure 4.39: Comparison between the regression obtained from *OTT* and *PMM* tests for the bare hull sway force due to sway speed.

The previous plot shows that the pure-sway *PMM* test over-predicts the sway force due to sway speed, when compared to the OTT results. According to *Eq. 2.51*, this contributes for an over-estimation of the course stability.

4.4.2.2 Hull with Hull Vane

The time-trace of the sway force for the hull with Hull Vane, shows a similar behaviour to the bare hull case. Therefore, a 1st and 3rd harmonics were considered:

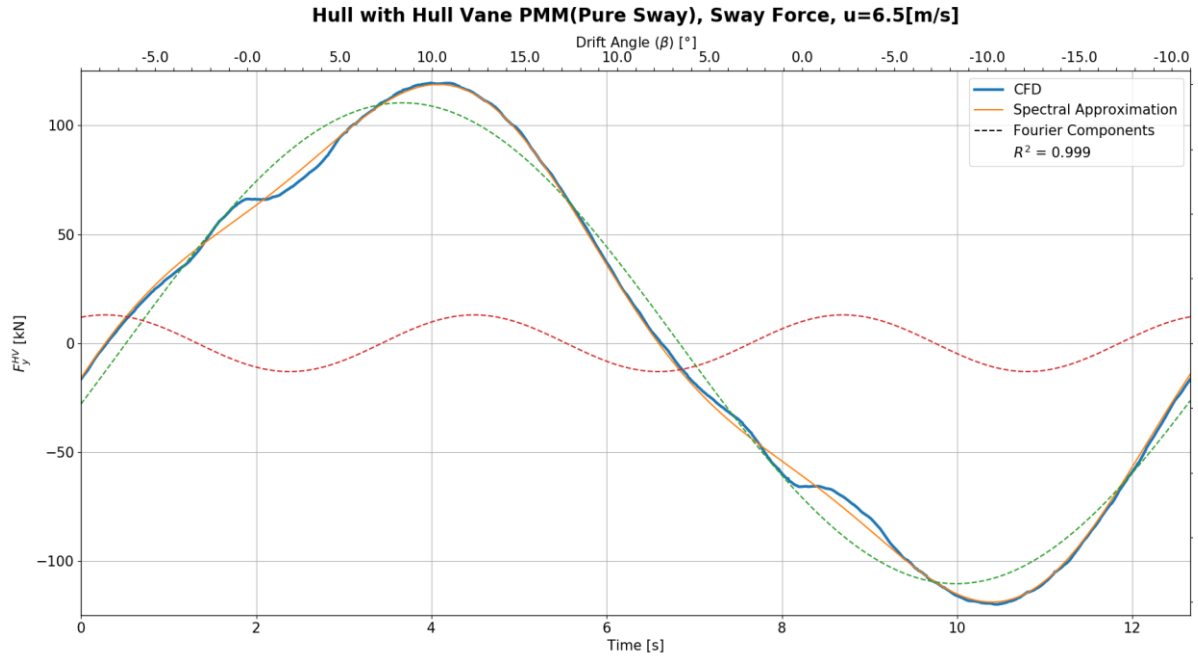

Figure 4.40: Sway force reconstruction using 1st and 3rd harmonics of the sway motion for the hull with Hull Vane.

Similarly to what was found for the bare hull case, the first and third motion harmonics have a good correlation with the sway force ($R^2 = 0.999$). The wiggles at 2 and 8 seconds require a higher order reconstruction to be captured. However due to their small amplitude, these ones are neglected, as explained for the bare hull case. Considering *Eq. 4.*26 and *Eq. 4.*14, the hydrodynamic derivatives for sway force due to sway speed are:

$$\begin{cases} Y_{\dot{v}} = -43.542\ [ton.] \\ Y_{vvv} = -9.674\ \left[\frac{kN.s^3}{m^3}\right] \\ Y_v = -37.347\ \left[\frac{kN.s}{m}\right] \end{cases} \Rightarrow \begin{cases} Y'_{\dot{v}} = -5.4374 \times 10^{-3}\ [-] \\ Y'_{vvv} = -1.9631 \times 10^{-1}\ [-] \\ Y'_v = -1.7938 \times 10^{-2}\ [-] \end{cases} \qquad \textit{Eq. 4.}28$$

The following figure compares the regression obtained from *OTT* with the one obtained from *PMM* tests, for sway damping:

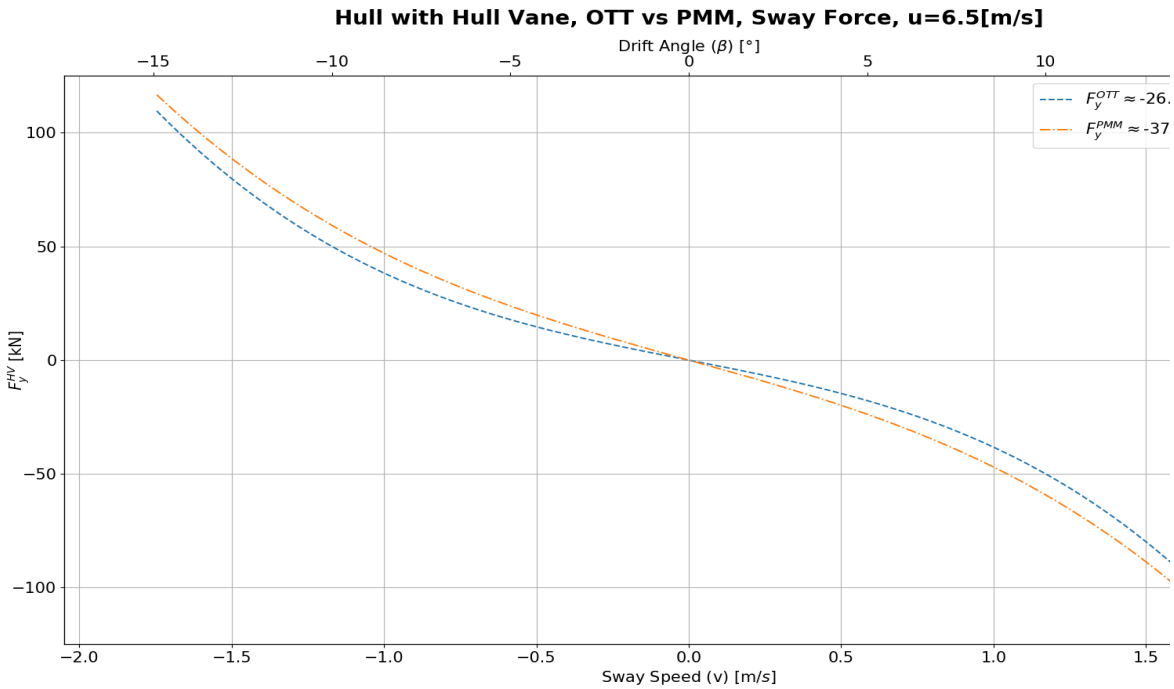

Figure 4.41: Comparison between the regression obtained from *OTT* and *PMM* tests for the sway damping for the hull with Hull Vane.

According to the previous figure, the *PMM* test also over-estimates the sway damping for the hull with Hull Vane, when compared to the oblique towing tests (*OTT*). Contributing for an over estimation of the course-stability, according to *Eq. 2.51*.

The following plot compares the sway damping of the hull with and without Hull Vane, based on the *PMM* tests' results:

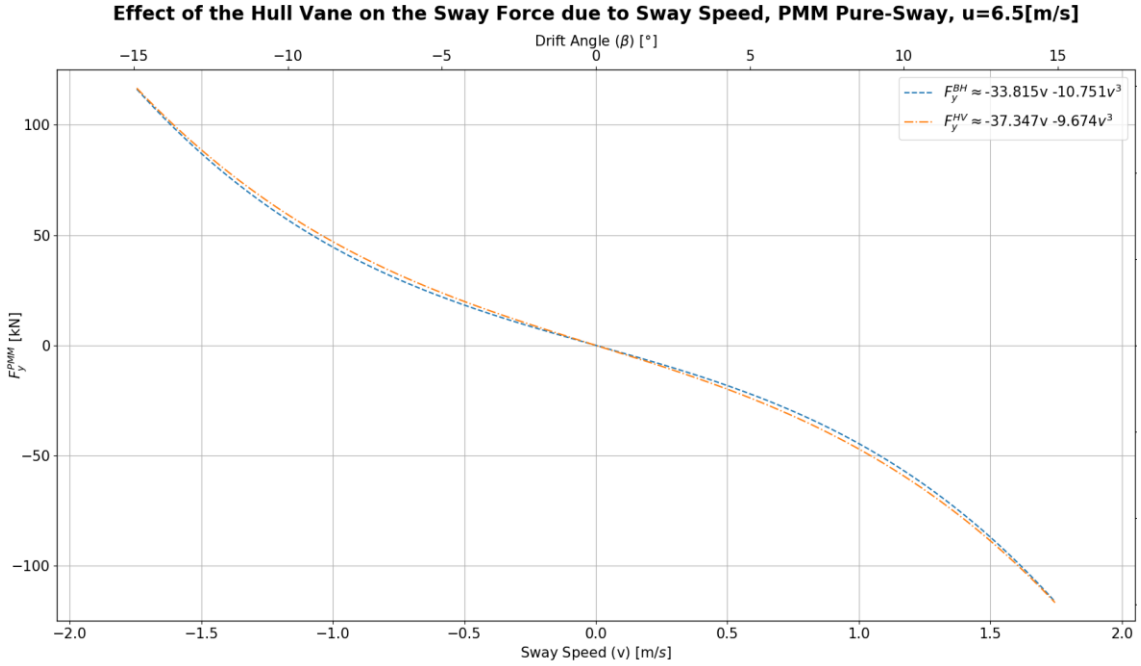

Figure 4.42: Comparison of the regressions for sway force due t sway speed, for the case with and without Hull Vane.

The previous plot shows that the sway damping is not significantly affected by the Hull Vane, which is in accordance with the *OTT* results. Furthermore, the added mass in sway is also not significantly affected by the Hull Vane. Therefore, it is possible to conclude that the Hull Vane does not significantly affect either the sway damping or added mass. This is accordance with the results from the *OTT* tests.

4.4.3 YAW MOMENT DUE TO SWAY

4.4.3.1 Bare Hull

The following plot shows the yaw moment signal in the frequency domain during a pure-sway *PMM* test:

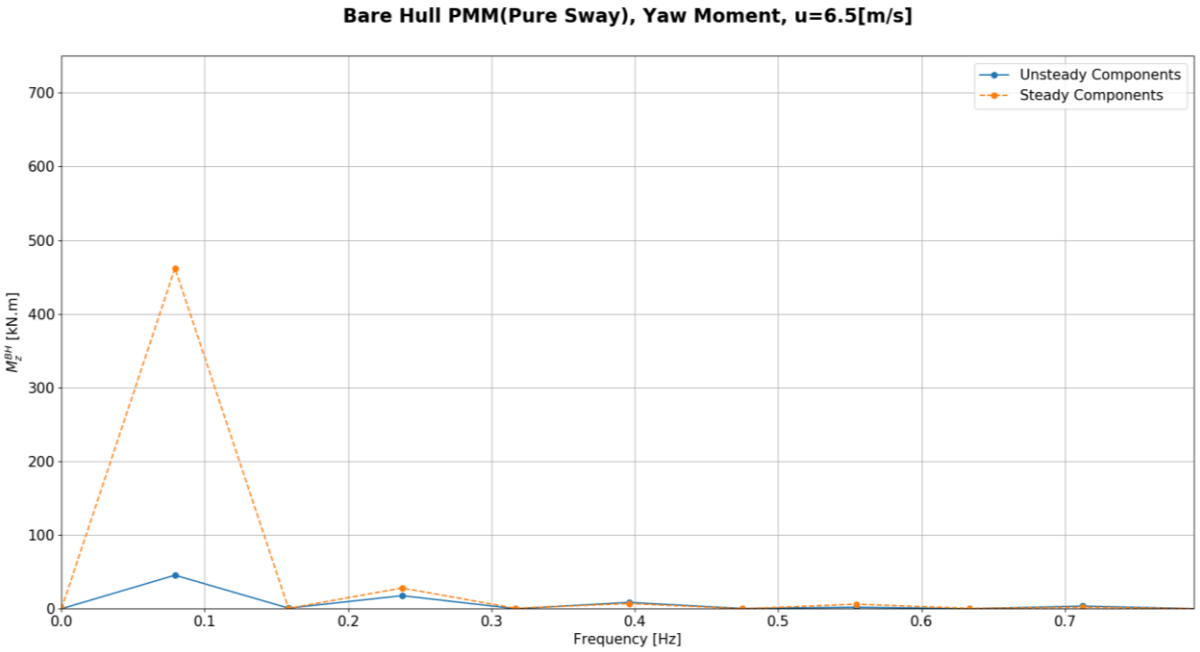

Figure 4.43: Spectrum of the amplitude of the steady and unsteady yaw moment components, for the bare hull case. *PMM* pure-sway test.

According to the previous plot, it is possible to see that the first and third harmonics are the most relevant ones. For these frequencies the steady components of the yaw moment are dominant. However, note that the unsteady component of the third harmonic has the same order of magnitude of the steady component, and therefore, it must be considered. The following plot shows the time trace of the yaw moment over a period of the pure-sway motion, and its reconstruction of using the first and third harmonics, see *Figure 4.44* in the next page:

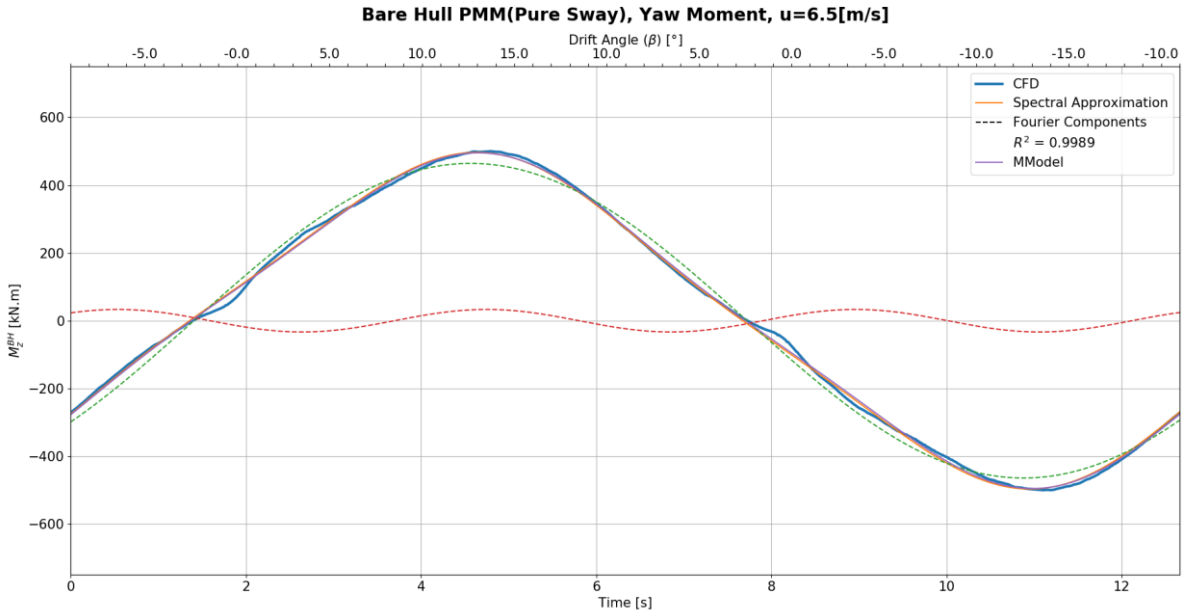

Figure 4.44: Yaw moment reconstruction using 1st and 3rd harmonics of the sway motion for the bare hull.

This reconstruction shows to adequately fit the time trace of the yaw moment ($R^2 = 0.9989$). Some details of the signal are not so well captured, especially at 2 and 8 sec, the same ones previously detected in the yaw force. Due to the small amplitude of these wiggles, they are neglected. Having said this, the equation of motion for yaw moment, in a pure-sway *PMM* test, is represented by:

$$-N_{\dot{v}\dot{v}\dot{v}}.\dot{v}^3 - N_{\dot{v}}.\dot{v} - N_{vvv}.v^3 - N_v.v = M^1_{z_a}.\sin(\omega t + \epsilon_1) + M^3_{z_a}.\sin(3\omega t + \epsilon_3) \qquad \textit{Eq. 4.}29$$

Using some mathematical manipulation, the hydrodynamic coefficients are given by:

$$\begin{cases} N_{\dot{v}\dot{v}\dot{v}} = -4.M^3_{z_a}.\dfrac{\cos(\epsilon_3)}{(y_a.\omega^2)^3} \\ N_{\dot{v}} = M^1_{z_a}.\dfrac{\cos(\epsilon_1)}{y_a.\omega^2} - 3.Y_{\dot{v}\dot{v}\dot{v}}.\dfrac{(y_a.\omega^2)^2}{4} \\ N_{vvv} = -4.M^3_{z_a}.\dfrac{\sin(\epsilon_3)}{(y_a.\omega)^3} \\ N_v = -M^1_{z_a}.\dfrac{\sin(\epsilon_1)}{y_a.\omega} - 3.N_{vvv}.\dfrac{(y_a.\omega)^2}{4} \end{cases} \Rightarrow \begin{cases} N_{\dot{v}\dot{v}\dot{v}} = -108.677\ \left[\dfrac{ton.s^4}{m}\right] \\ N_{\dot{v}} = 113.888\ [ton.m] \\ N_{vvv} = -21.182\ \left[\dfrac{ton.s}{m}\right] \\ N_v = -216.455\ [kN.s] \end{cases} \Rightarrow \begin{cases} N'_{\dot{v}\dot{v}\dot{v}} = -2.2936 \times 10^{-2}\ [-] \\ N'_{\dot{v}} = 5.6888 \times 10^{-4}\ [-] \\ N'_{vvv} = -1.7194 \times 10^{-2}\ [-] \\ N'_v = -4.1585 \times 10^{-3}\ [-] \end{cases} \qquad \textit{Eq. 4.}30$$

The following plot shows the comparison of the regressions obtained from the *OTT* and pure-sway *PMM* tests for the *Munk* moment of the bare hull:

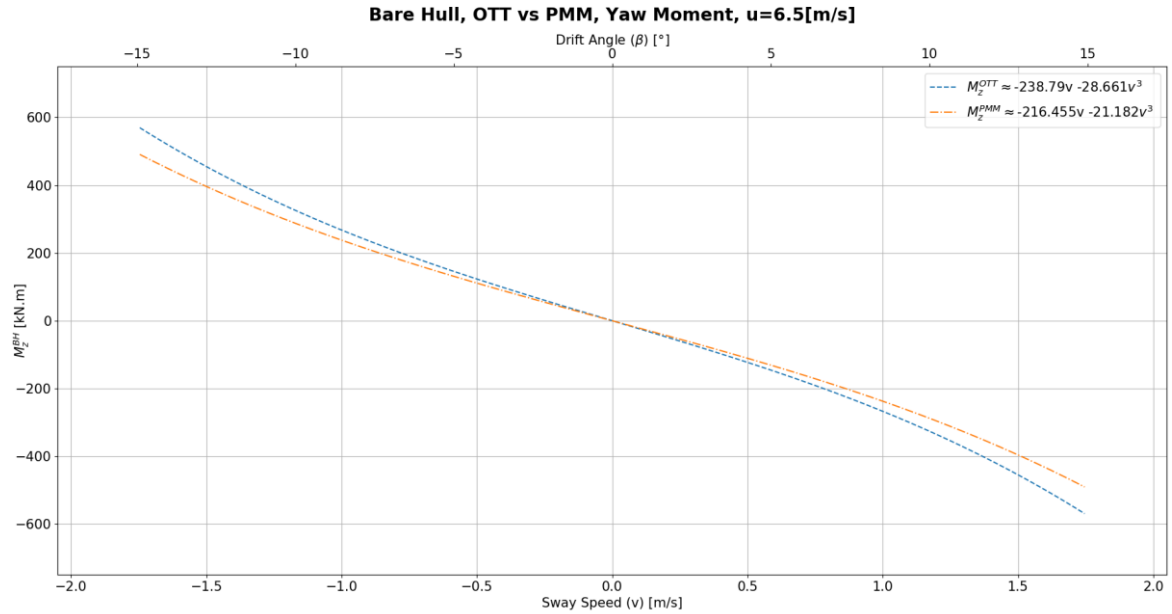

Figure 4.45: Comparison between the regression obtained from *OTT* and *PMM* tests for the yaw moment due to sway speed for the bare hull.

The previous figure shows that the pure-sway *PMM* test under-estimates the *Munk* moment (a destabilizing moment) when compared to the results from the *OTT* test. According to *Eq. 2.51*, this contributes for an over-estimation of the course stability of the vessel.

4.4.3.2 Hull with Hull Vane

The time trace of the yaw moment for the vessel with Hull Vane is similar to the bare hull one. Therefore, the same type of reconstruction is adopted, *i.e.* using the 1st and 3rd harmonics of the sway motion:

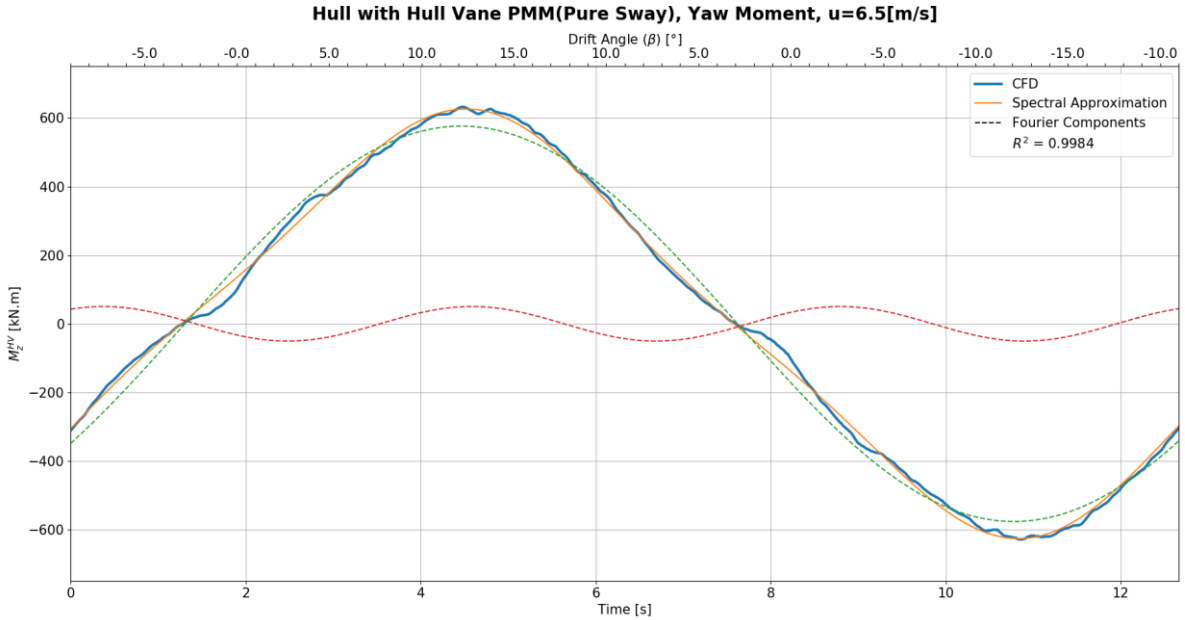

Figure 4.46: Yaw moment reconstruction using 1st and 3rd harmonics of the sway motion for the hull with Hull Vane.

Due to the similarity between the bare hull case and the hull with Hull Vane case, the same hydrodynamic coefficients are derived:

$$\begin{cases} N_{\dot{v}\dot{v}\dot{v}} = -95.983 \left[\frac{ton.s^4}{m}\right] \\ N_{\dot{v}} = 84.765\ [ton.m] \\ N_{vvv} = -36.004 \left[\frac{ton.s}{m}\right] \\ N_{v} = -247.516\ [kN.s] \end{cases} \Rightarrow \begin{cases} N'_{\dot{v}\dot{v}\dot{v}} = -2.0257 \times 10^{-2}\ [-] \\ N'_{\dot{v}} = 4.2341 \times 10^{-4}\ [-] \\ N'_{vvv} = -2.9225 \times 10^{-2}\ [-] \\ N'_{v} = -4.7553 \times 10^{-3}\ [-] \end{cases} \quad \textit{Eq. 4.}31$$

The following plot compares the *PMM* and *OTT* results for the *Munk* moment of the vessel with Hull Vane:

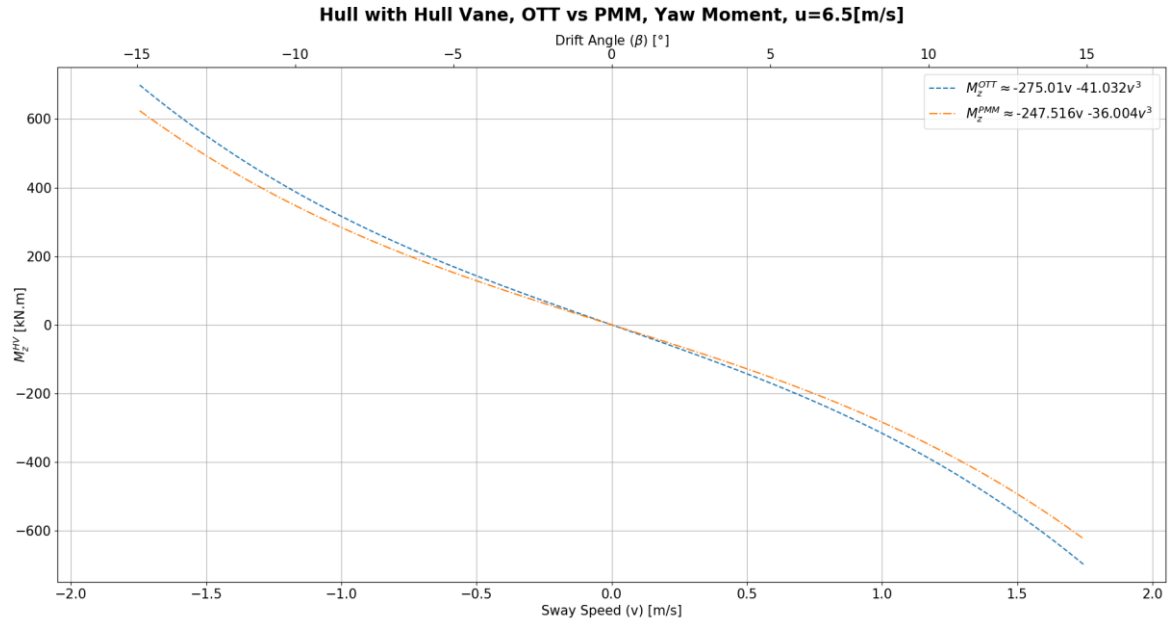

Figure 4.47: Comparison between the regression obtained from *OTT* and *PMM* tests for the yaw moment due to sway speed for the hull with Hull Vane.

In accordance to what was found for the bare hull case, the pure-sway *PMM* test under-estimates the *Munk* moment comparatively to the *OTT* test, which contributes for an over-estimation of course stability. The following plots assess the effect of the Hull Vane on the *Munk* moment and yaw moment due to sway acceleration:

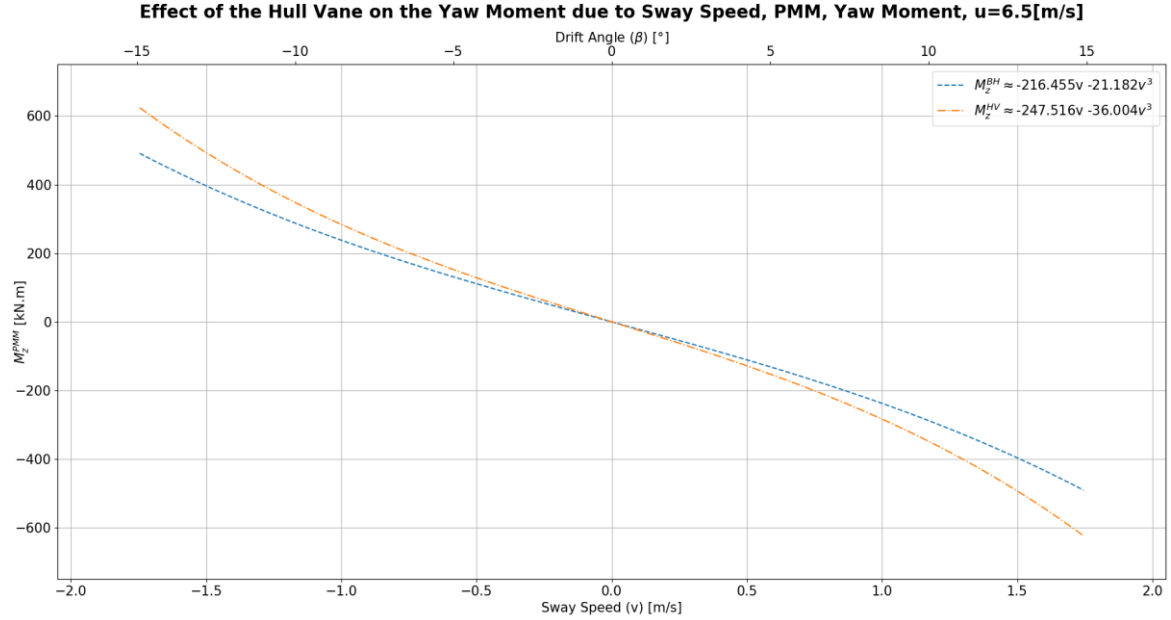

Figure 4.48: Comparison of the yaw moment due to sway speed regression with and without the Hull Vane, based on the *PMM* pure-sway results.

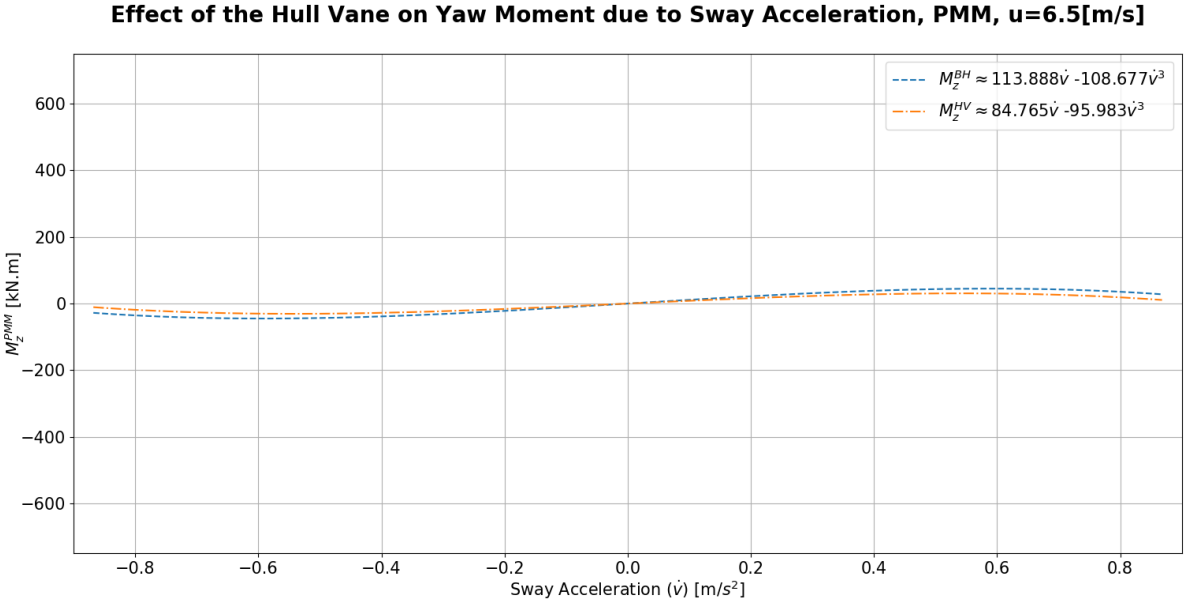

Figure 4.49: Comparison of the yaw moment due to sway acceleration regression with and without the Hull Vane, based on the *PMM* pure-sway results.

According to the previous plots, the Hull Vane increases the yaw moment due to sway speed (*Munk* moment), which contributes for a reduction of course stability (see *Eq. 2.51*). Since the Hull Vane does not affect the sway damping, this increase in *Munk* moment caused by the fact that the Hull Vane trims the vessel bow down. The yaw moment caused by a sway acceleration is practically not affected by the Hull Vane.

4.4.4 ROLL MOMENT DUE TO SWAY

4.4.4.1 Bare Hull

The following plot shows the roll moment signal in the frequency domain during a pure-sway *PMM* test:

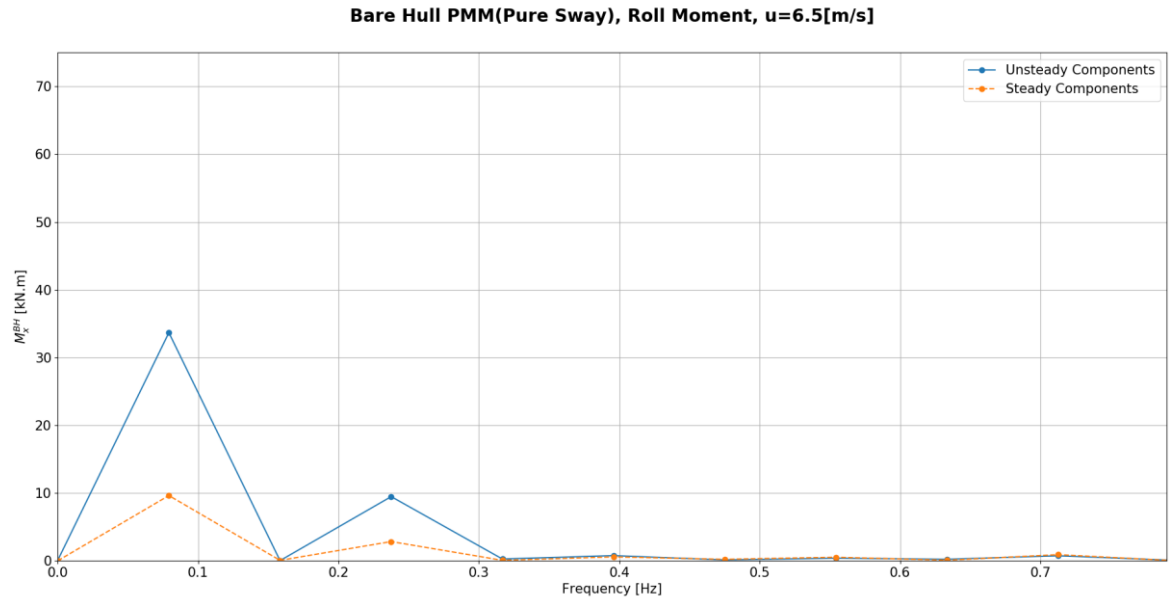

Figure 4.50: Frequency domain analysis of the bare hull roll moment over a period of the *PMM* pure-sway test. Magnitude of the steady and unsteady components of the roll moment.

In *Section 4.2.4* the roll moment due to sway speed was modelled using a 5th order polynomial, which is equivalent to use a 5th harmonic to model the roll signal from pure-sway *PMM* test. However, accordin to the previous figure, the amplitude of 5th harmonic is negligible when compared to the 1st and 3rd harmonics. Furthermore, the previous plot shows that the roll moment in the pure-sway PMM test is mainly driven by unsteady phenomena, which can be caused by strong flow memory effects.

The following figure shows a reconstruction of the roll moment signal using the 1st and 3rd harmonics of the sway motion:

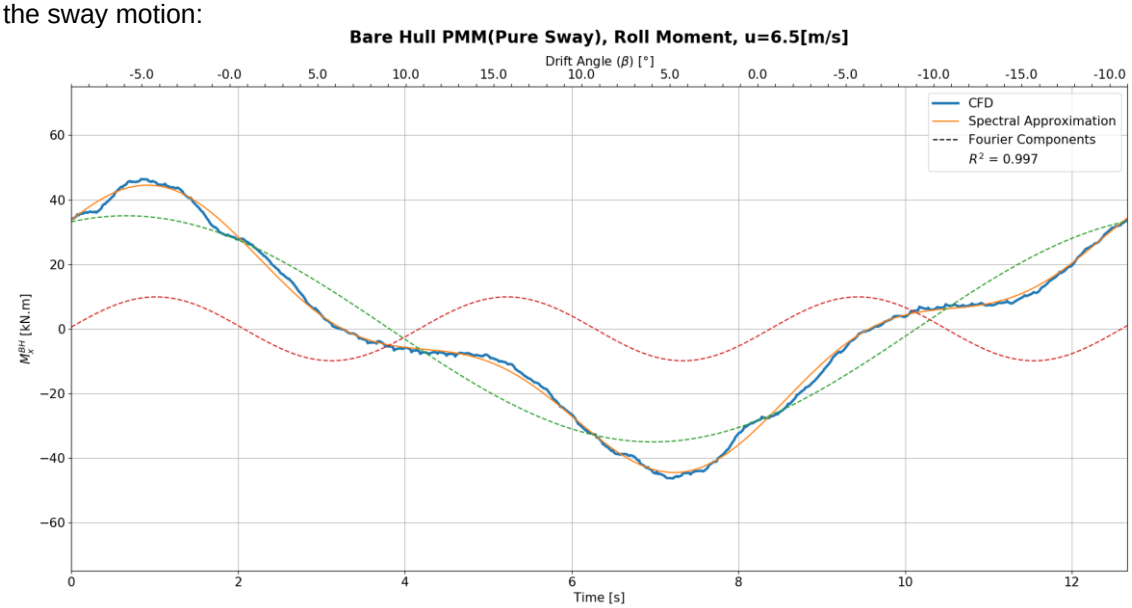

Figure 4.51: 1st and 3rd order reconstruction of the time trace of the roll moment for the bare hull in a *PMM* pure-sway test.

The previous picture shows that the maximum roll moment occurs at approximately 5° drift. Therefore, this is in accordance with the frequency domain results. Considering the results of this analysis the following equation of motion for roll during a pure-sway *PMM* test is considered:

$$-K_{\dot{v}\dot{v}\dot{v}}.\dot{v}^3 - K_{\dot{v}}.\dot{v} - K_{vvv}.v^3 - K_v.v = M^1_{x_a}.\sin(\omega t + \epsilon_1) + M^3_{x_a}.\sin(3\omega t + \epsilon_3) \qquad \textit{Eq. 4.}32$$

Using some mathematical manipulation, it is possible to derive the following formulations for the roll moment due to sway hydrodynamic coefficients (see *Section 4.3*):

$$\begin{cases} K_{\dot{v}\dot{v}\dot{v}} = -4.M^3_{x_a}.\dfrac{\cos(\epsilon_3)}{(y_a.\omega^2)^3} \\ K_{\dot{v}} = M^1_{x_a}.\dfrac{\cos(\epsilon_1)}{y_a.\omega^2} - 3.K_{\dot{v}\dot{v}\dot{v}}.\dfrac{(y_a.\omega^2)^2}{4} \\ K_{vvv} = -4.M^3_{x_a}.\dfrac{\sin(\epsilon_3)}{(y_a.\omega)^3} \\ K_v = -M^1_{x_a}.\dfrac{\sin(\epsilon_1)}{y_a.\omega} - 3.K_{vvv}.\dfrac{(y_a.\omega)^2}{4} \end{cases} \Rightarrow \begin{cases} K_{\dot{v}\dot{v}\dot{v}} = -57.935\left[\dfrac{ton.s^4}{m}\right] \\ K_{\dot{v}} = -6.045\,[ton.m] \\ K_{vvv} = -2.137\left[\dfrac{ton.s}{m}\right] \\ K_v = 10.398\ [kN.s] \end{cases} \Rightarrow \begin{cases} K'_{\dot{v}\dot{v}\dot{v}} = -1.2227\times10^{-2}[-] \\ K'_{\dot{v}} = -3.0196\times10^{-5}\ [-] \\ K'_{vvv} = -1.7346\times10^{-3}\ [-] \\ K'_v = 1.9977\times10^{-4}\ [-] \end{cases} \qquad \textit{Eq. 4.}33$$

The following plot compares the results of the *OTTs* with the results of the pure-sway *PMM* test:

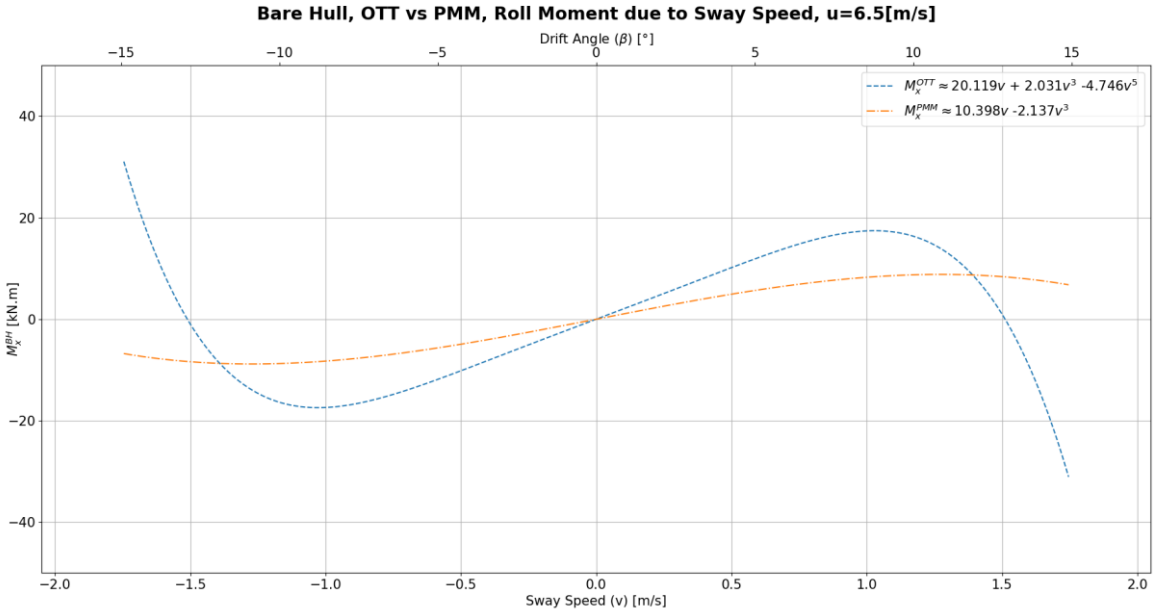

Figure 4.52: Comparison of the regression from *OTTs* and pure-sway *PMM* tests for the roll moment due to sway speed for the bare hull.

The previous plot shows a considerable mismatch between the regression obtained from OTTs and the one obtained from PMM. According to Yasukawa and Yoshimura in [35], the PMM results are dependent on the motion frequency and amplitude, which penalizes the accuracy. Since the skeg is in the bottom of the vessel and it is responsible for the generation of side force, this one strongly contributes for the roll moment. However, due to the frequency of the motion, flow memory effects influence the steady force component since it creates a link between previous motion conditions and the motion condition at certain time instant. This last phenomenon together with higher numerical residuals (comparative to OTT due to the unsteady motion), are expected to be the main sources of errors when assessing steady hydrodynamic coefficients using PMM tests. Therefore, the OTT results are expected to be more reliable since these ones are not subjected to flow memory effects.

4.4.4.2 Hull with Hull Vane

The following plot shows the roll moment signal in the frequency domain for the hull with Hull Vane, during a pure-sway *PMM* test:

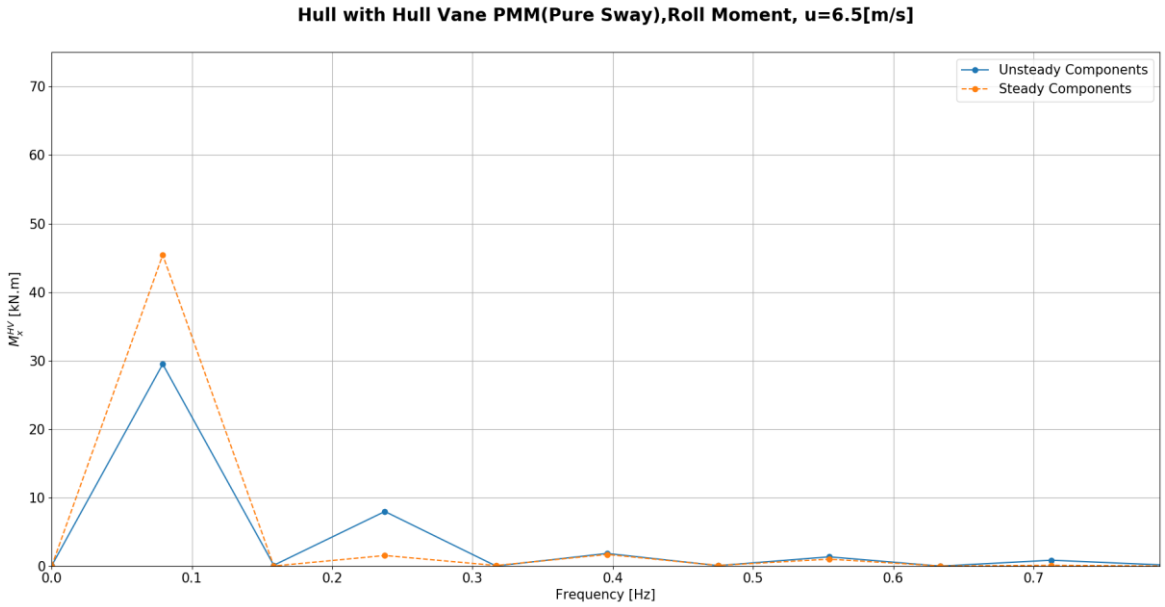

Figure 4.53: Frequency domain analysis of the roll moment of the hull with Hull Vane, over a period of the *PMM* pure-sway test. Magnitude of the steady and unsteady components of the roll moment.

Similarly, to what was found for the bare hull case, the 1st and 3rd harmonics are the most relevant ones. However, in this case, it is possible to see that the Hull Vane causes a significant increase of the steady roll moment component of the first harmonic. In *Section 4.2.4,* it is shown that most of the roll moment developed by the Hull Vane is generated by its horizontal part and not by the struts. In contrast to the skeg, when the sway direction is changed, the Hull Vane is not subjected to additional forces to revert vortices previously created (*i.e.:* flow memory effects), they tend to simply vanish due to the unloading of one side of the Hull Vane. Therefore, it is expected that the Hull Vane mostly affects the steady forces/moments components than the unsteady ones. As can be seen, the unsteady moment components are not significantly affected by the Hull Vane, while the steady component of the 1st harmonic increases significantly.

According to this, a 1st and 3rd order reconstruction of the roll moment is considered:

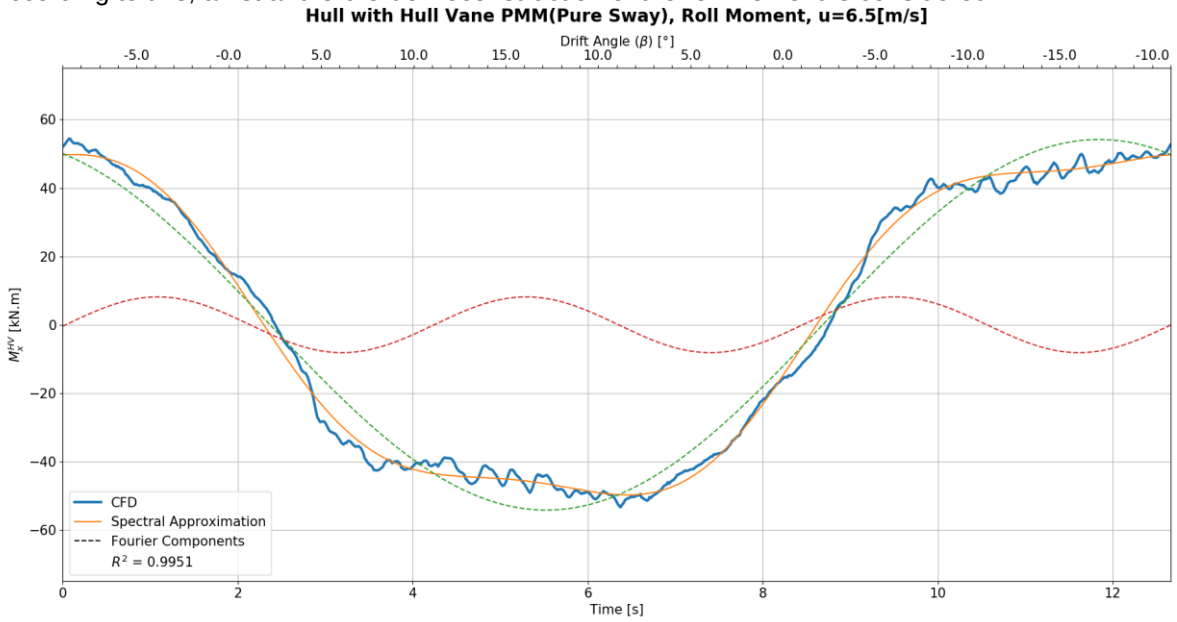

Figure 4.54: 1st and 3rd order reconstruction of the time trace of the roll moment for the hull with Hull Vane in a *PMM* pure-sway test.

The fluctuations of the roll moment signal are disregarded due to their small amplitude and high frequency. These ones are caused by an amplification of the noise from by the Hull Vane, as previously explained.
Since the roll moment is reconstructed in the same way for the hull with and without Hull Vane, *Eq. 4.*32 and *Eq. 4.*33 are considered:

$$\begin{cases} K_{\dot{v}\dot{v}\dot{v}} = -49.039\left[\frac{ton.s^4}{m}\right] \\ K_{\dot{v}} = -6.266\ [ton.m] \\ K_{vvv} = -1.093\left[\frac{ton.s}{m}\right] \\ K_{v} = 28.533\ [kN.s] \end{cases} \Rightarrow \begin{cases} K'_{\dot{v}\dot{v}\dot{v}} = -1.0349 \times 10^{-2}[-] \\ K'_{\dot{v}} = -3.1299 \times 10^{-5}[-] \\ K'_{vvv} = -8.8720 \times 10^{-4}[-] \\ K'_{v} = 5.4818 \times 10^{-4}[-] \end{cases} \qquad \textit{Eq. 4.}34$$

The following plot compares the *OTT* results with the *PMM* test results:

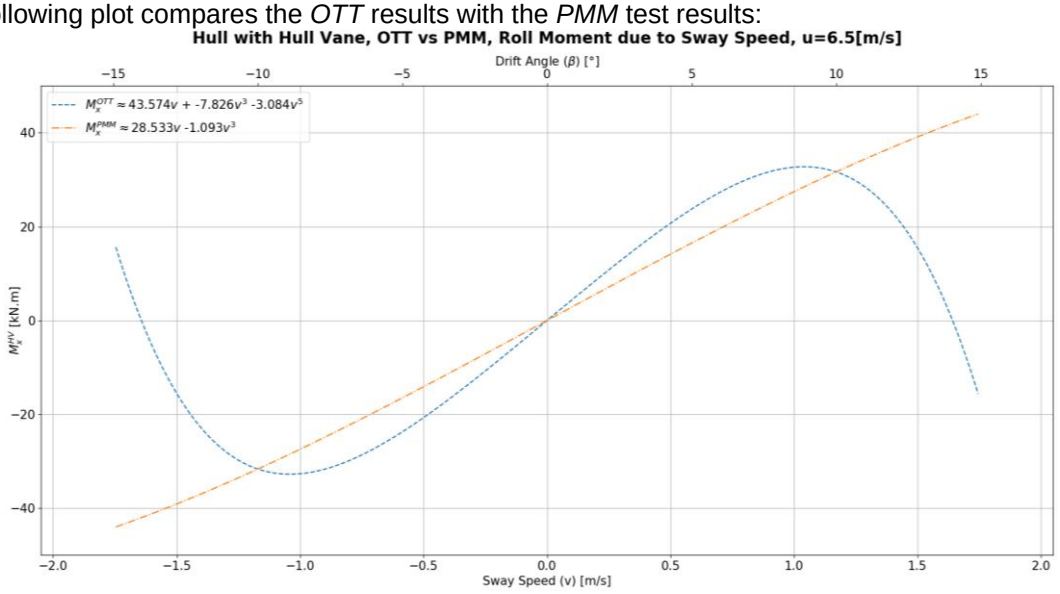

Figure 4.55: Comparison of the regression from *OTTs* and pure-sway *PMM* tests for the roll moment due to sway speed for the hull with Hull Vane.

For the hull with Hull Vane case, there is also considerable discrepancy between the *PMM* and *OTT* results. This discrepancy is expected to be mainly caused by the unsteady motion of the *PMM* tests and higher numerical residuals, a more detailed explanation can be found in the previous section (*Section 4.4.4.1)*. The following plots, compare the steady and unsteady components of the roll moment for the case with and without Hull Vane:

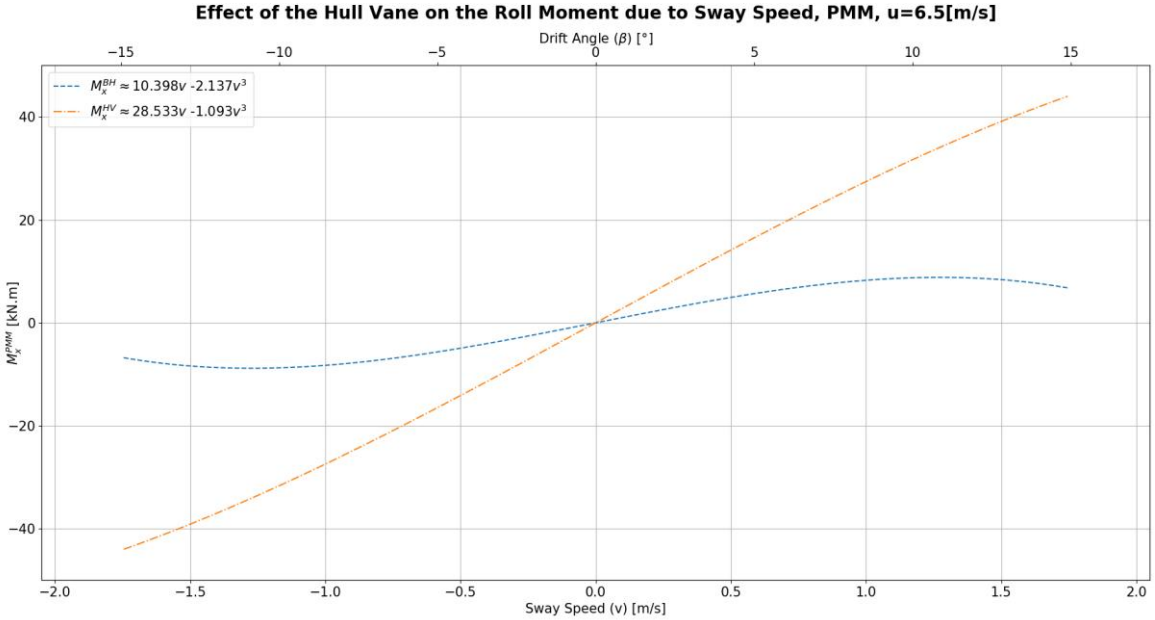

Figure 4.56: Comparison of the yaw moment due to sway speed regression with and without the Hull Vane, based on the *PMM* results.

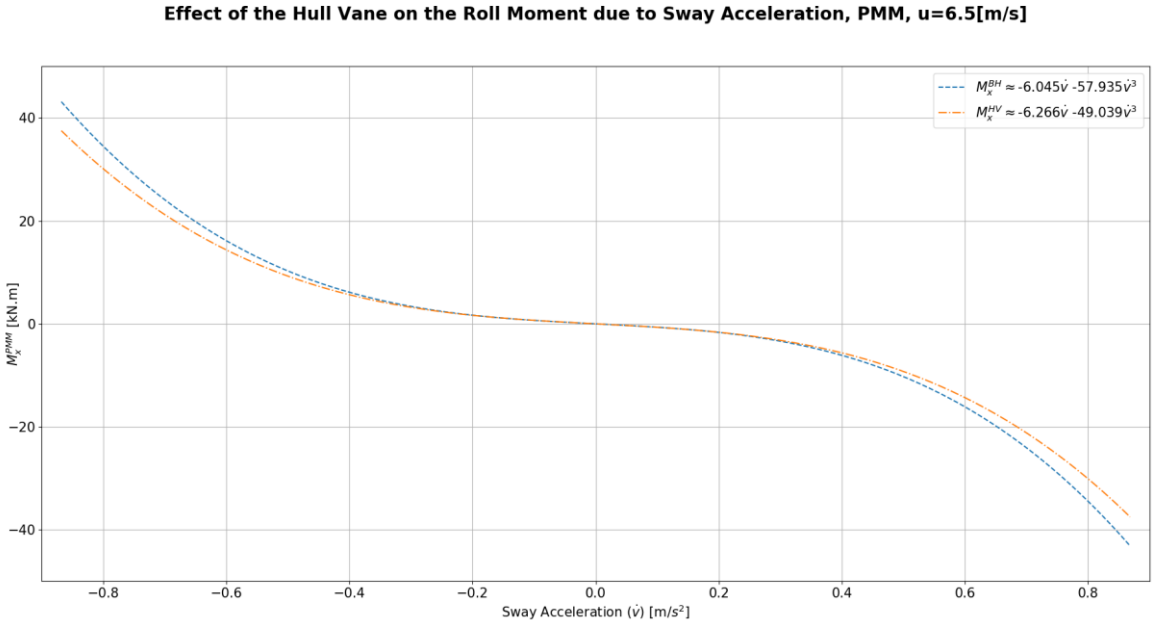

Figure 4.57: Comparison of the yaw moment due to sway acceleration regression with and without the Hull Vane, based on the *PMM* results.

According to the previous plots, the Hull Vane significantly increases the roll moment due to sway speed, which is in accordance with the phenomena described in *Section 4.2.4.2.* Regarding the roll moment due to sway acceleration, this one shows not to be significantly affected by the Hull Vane, which is in

line with the fact that the Hull Vane is not subjected to considerable flow memory effects, as previously explained.

4.4.5 SUMMARY OF THE PMM PURE-SWAY TEST RESULTS

- **Longitudinal Added Resistance due to Sway:** In comparison with the *OTT* results, the *PMM* test under-predicts the longitudinal added resistance due to sway speed. According to *Eq. 4.1*, this contributes for an under-prediction of course stability. Furthermore, the *PMM* results also show that the Hull Vane does not significantly affect the longitudinal added resistance sue to sway acceleration.

- **Sway Damping and Added Mass:** The *PMM* test over-estimates the sway damping, when compared with the *OTT* results. According to *Eq. 2.48*, this contributes for an over-estimation of course stability. In accordance with the *OTT* results, the *PMM* test also shows that the damping in sway and added mass are barely affected by the Hull Vane. This is caused by a small contribution for the total underwater lateral area of the vessel and a flow straightening effect caused by hull to Hull Vane interaction.

- **Yaw Moment due to Sway:** A comparison between the *PMM* test and *OTT* results, shows that the *PMM* test under-estimates the magnitude of the *Munk* moment. This is a destabilizing moment. Thus, an under-estimation of this one tends to increase the course stability. The *PMM* test results show that the Hull Vane increases the *Munk* moment and practically does not affect the yaw moment due to sway acceleration. Since the sway damping is not affected by the Hull Vane, the increase in *Munk* moment is mainly caused by the fact that the Hull Vane trims the vessel bow down, which is in accordance with the *OTT* results. This causes a transfer of the centre of lateral pressure forward, contributing for a decrease in course stability, see Figure 2.8.

- **Roll Moment due to Sway:** A comparison between the roll moments determined from the *PMM* test and the ones determined from *OTT* tests, show a significant discrepancy. This is mainly caused by a too high *Strouhal* number *(St_n)* of the *PMM* test, which leads to strong flow memory effects (*e.g.:* flow/vortices reversion). Furthermore, the regression obtained from *OTTs* is based on 4 data points while the one obtained from the *Discrete Spectral Method* is based on 2 points, since the 5^{th} and 7^{th} harmonics showed to be negligible. In general, it was observed that unsteady roll moment components are greater than the steady ones, which can be an indication of the presence of strong flow memory effects. The Hull Vane increases the steady components, which is in accordance with the previous hypothesis, since it is less subjected to flow memory effects than the skeg.

Discrepancies were found between the *OTTs* and *PMM* test results, for the determination of sway speed dependent hydrodynamic coefficients. The most significant discrepancy is observed for roll moment, which it is expected to be caused by flow memory effects. In the end, the pure-sway *PMM* test results tend to cause an over-estimation of course stability. Since the *PMM* tests are subjected to flow memory effects and higher numerical residuals, due to their unsteady nature, in this research, the sway speed dependent hydrodynamic coefficients derived from *OTTs* are considered.

4.5 VIRTUAL PMM RESULTS ANALYSIS– PURE YAW

This section aims to present, analyse and discuss the results of the virtual *PMM* pure-yaw test, and to determine the respective hydrodynamic coefficients. A *PMM* pure-yaw test, consists in combining a constant advance speed with a sinusoidal motion in sway and yaw in order to guarantee zero-drift angle:

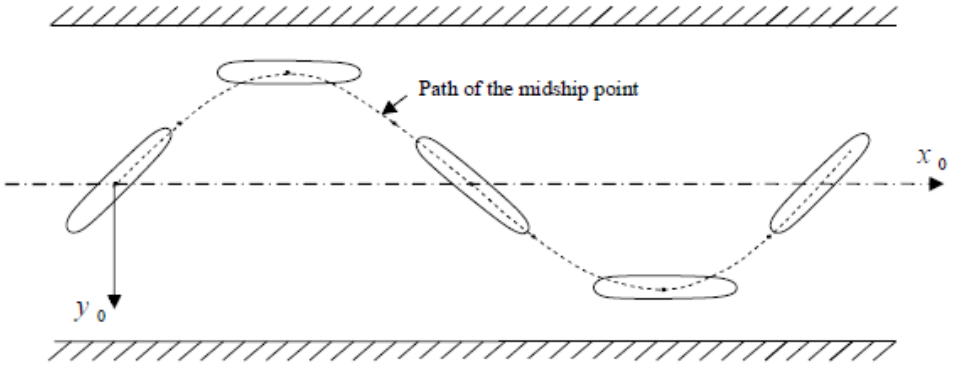

Figure 4.58: PMM, pure yaw test, [49].

It is important to mention also here, that the forces/moments from the virtual captive tests do not include body inertial forces, being just the result of hydrodynamic loads. According to *Eq. 3.6*, the time step for the *OTT* tests is 0.019 [s]. However, due to the highly unsteady nature of the *PMM* motion, the time step was reduced to 0.015 [s]. Further details about the settings of this virtual test can be found in *Section 2.10.1.3* and *Chapter 3*.

4.5.1 LONGITUDINAL ADDED RESISTANCE DUE TO YAW

4.5.1.1 Bare Hull

The following figure shows a second order reconstruction of the longitudinal added resistance over a period of a pure-yaw *PMM* test, for the Bare Hull:

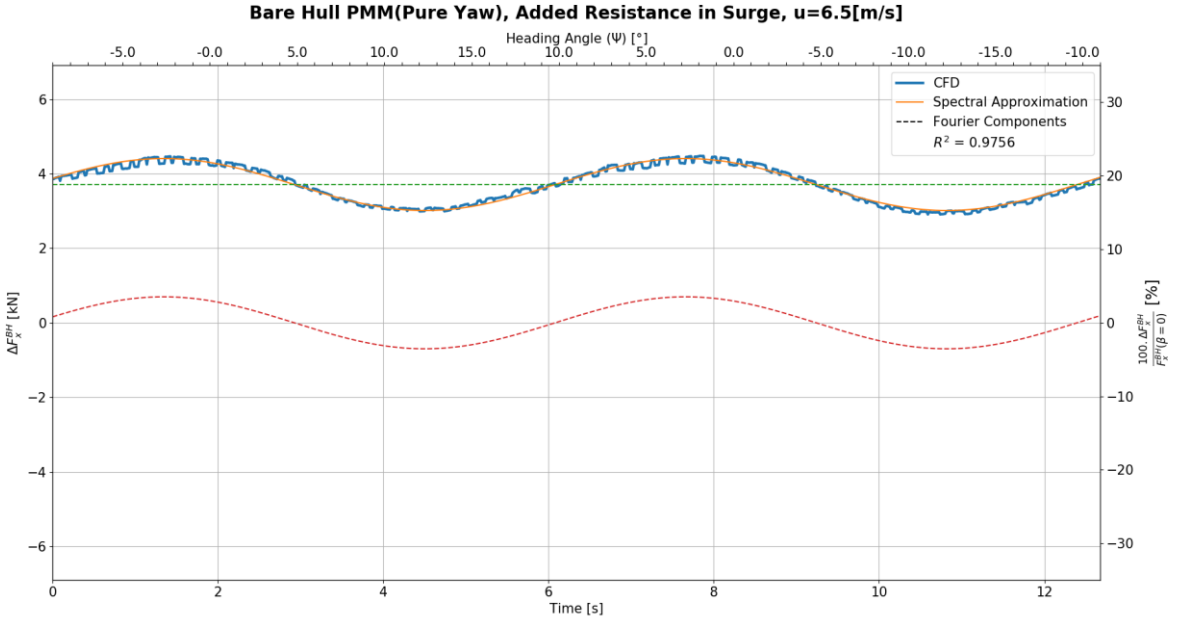

Figure 4.59: Reconstruction of the time trace of the longitudinal added resistance (ΔF_x), in a pure-yaw motion for the bare hull, using a 0 and 2nd order harmonics of the yaw motion.

According to the previous figure, the time trace of this force shows to have small fluctuations. Due to the small amplitude and high frequency of these fluctuations, they are neglected in the context of this research. A second order motion equation for surge in a *PMM* pure-yaw test is given by:

$$-X_{\dot{r}\dot{r}}\,\dot{r}^2 - X_{rr}.r^2 = \Delta F_{x_a}^0 + \Delta F_{x_a}^2.\cos(2\omega t + \epsilon_2) \qquad \textit{Eq. 4.35}$$

The hydrodynamic coefficients for surge added resistance are given by:

$$\begin{cases} X_{\dot{r}\dot{r}} = \dfrac{\Delta F_{x_a}^2.\cos(\epsilon_2) - F_{x_a}^0}{\psi_a^2.\omega^4} \\ X_{rr} = -\dfrac{\Delta F_{x_a}^2.\cos(\epsilon_2) + F_{x_a}^0}{\psi_a^2.\omega^2} \end{cases} \Rightarrow \begin{cases} X_{\dot{r}\dot{r}} = -719.094\ [kN.s^4] \\ X_{rr} = -259.567\ [kN.s^2] \end{cases} \Rightarrow \begin{cases} X'_{\dot{r}\dot{r}} = -2.4282 \times 10^{-4}\ [-] \\ X'_{rr} = -1.2966 \times 10^{-3}\ [-] \end{cases} \qquad \textit{Eq. 4.36}$$

4.5.1.2 Hull with Hull Vane

The following figure shows a second order reconstruction of the longitudinal added resistance over a period of a pure-yaw *PMM* test, for the hull with Hull Vane:

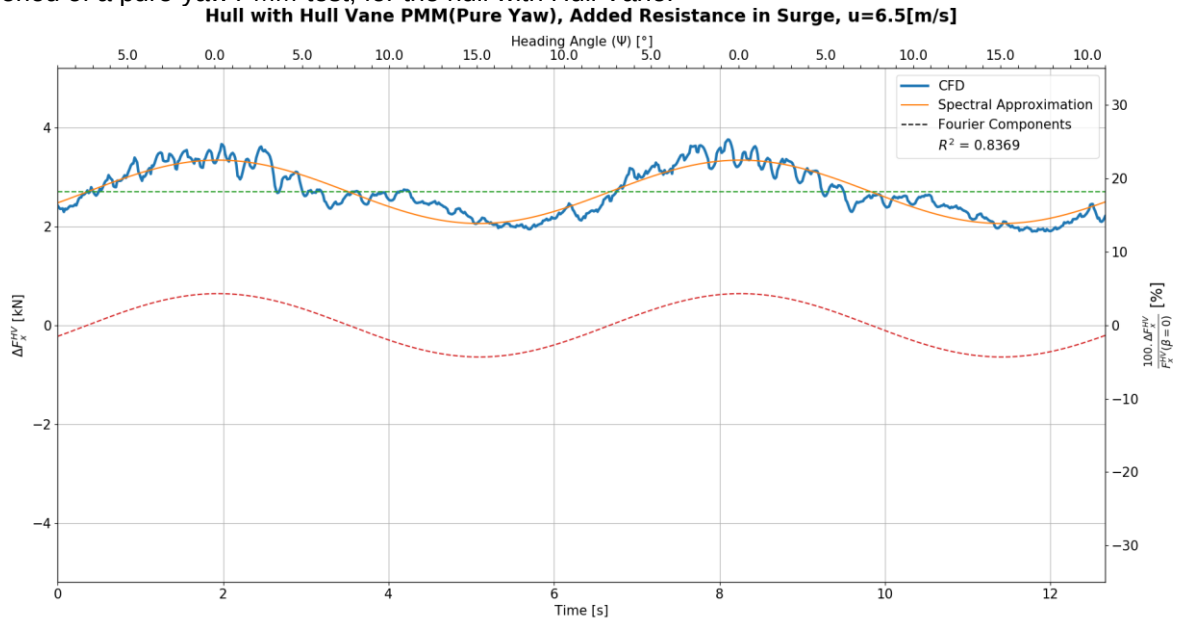

Figure 4.60: Time trace of the added resistance in surge (ΔF_x) in a pure-yaw motion for the hull with Hull Vane, using a 0 and 2nd order harmonics of the yaw motion.

Similarly to what was previously found, from the pure-sway test results, the Hull Vane amplifies the noise in the signal, an explanation of this phenomenon can be found in *Section 4.4.1*. As can be seen, a second order reconstruction does not fit the force signal as well as for the bare hull case. To improve this, a higher order reconstruction is required. However, the second order reconstruction is considered to be accurate enough for the purpose of this research, due to the relatively small amplitude of this force (in comparison with the pure-sway case. Considering this, the hydrodynamic coefficients for the longitudinal added resistance are, see *Eq. 4.36*:

$$\begin{cases} X_{\dot{r}\dot{r}} = -528.725\ [kN.s^4] \\ X_{rr} = -187.543\ [kN.s^2] \end{cases} \Rightarrow \begin{cases} X'_{\dot{r}\dot{r}} = -1.7853 \times 10^{-4}\ [-] \\ X'_{rr} = -9.3680 \times 10^{-4}\ [-] \end{cases} \qquad \textit{Eq. 4.37}$$

By comparing the hydrodynamic coefficients and the time-traces of the surge added resistance for the case with and without Hull Vane it is possible to see that the Hull Vane slightly decreases the longitudinal added resistance due to yaw motion. This difference is expected to be caused by hull-Hull Vane interaction, which increases the thrust generated by the Hull Vane. Although the Hull Vane decreases the absolute value of the added resistance in surge due to yaw motion, this one contributes for an increase in course stability, since the relative added resistance is larger for the Hull Vane case.

4.5.2 SWAY FORCE DUE TO YAW

4.5.2.1 Bare Hull

The following figure shows a third order reconstruction of the sway force over a period of a pure-yaw *PMM* test, for the Bare Hull:

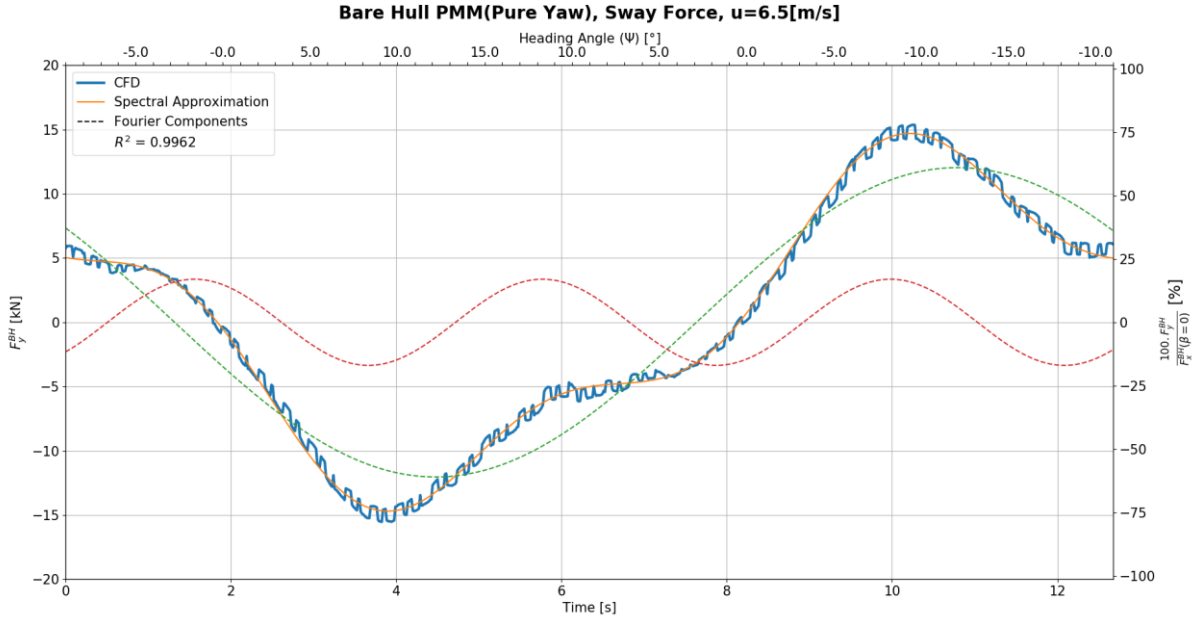

Figure 4.61: Sway force reconstruction using 1st and 3rd harmonics of the yaw motion for the bare hull.

The high frequency fluctuations in the signal can be explained by the smaller amplitude of the sway force due to yaw when compared to the pure-sway test. Due to their high frequency and small amplitude, these fluctuations are disregarded in the context of this research.

To assess which are the most relevant force components, a frequency domain analysis is performed:

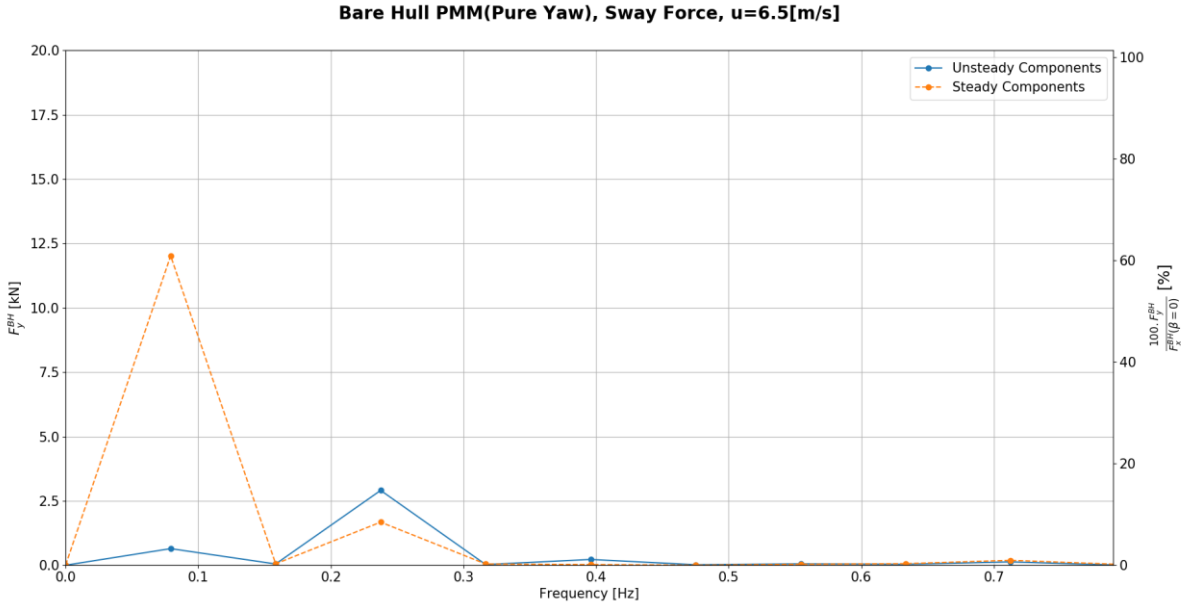

Figure 4.62: Spectrum of the magnitude of the steady and unsteady sway force components, for the bare hull case in a *PMM* pure-yaw test.

According to the previous plot, the steady force component of the first harmonic is the most relevant. For the third harmonic, the unsteady force component dominates, but the steady one is comparable. Considering this, the motion equation for the sway force in a pure-yaw *PMM* test is given by:

$$-Y_{\dot{r}\dot{r}\dot{r}}\,\dot{r}^3 - Y_{\dot{r}}\,\dot{r} - Y_{rrr}.r^3 + Y_r.r = F^1_{y_a}.\cos(\omega t + \epsilon_1) + F^3_{y_a}.\cos(3\omega t + \epsilon_3) \qquad \textit{Eq. 4.}38$$

Note that the heading in this test is described by cosine function. The sway hydrodynamic coefficients of the previous equation are given by:

$$\begin{cases} Y_{\dot{r}\dot{r}\dot{r}} = -4.F^3_{\psi_a}.\dfrac{\cos(\epsilon_3)}{(\psi_a.\omega^2)^3} \\ Y_{\dot{r}} = F^1_{\psi_a}.\dfrac{\cos(\epsilon_1)}{\psi_a.\omega^2} - 3.Y_{\dot{r}\dot{r}\dot{r}}.\dfrac{(\psi_a.\omega^2)^2}{4} \\ Y_{rrr} = 4.F^3_{\psi_a}.\dfrac{\sin(\epsilon_3)}{(\psi_a.\omega)^3} \\ Y_r = -F^1_{\psi_a}.\dfrac{\sin(\epsilon_1)}{\psi_a.\omega} - 3.Y_{rrr}.\dfrac{(\psi_a.\omega)^2}{4} \end{cases} \Rightarrow \begin{cases} Y_{\dot{r}\dot{r}\dot{r}} = -24603.974[kN.s^6] \\ Y_{\dot{r}} = -108.049[kN.s^2] \\ Y_{rrr} = -5261.914\,[kN.s^3] \\ Y_r = 62.001\,[kN.s] \end{cases} \Rightarrow \begin{cases} Y'_{\dot{r}\dot{r}\dot{r}} = -5.6162\times10^{-4}[-] \\ Y'_{\dot{r}} = -5.3972\times10^{-4}[-] \\ Y'_{rrr} = -6.8338\times10^{-3}\,[-] \\ Y'_r = 1.1912\times10^{-3}\,[-] \end{cases} \qquad \textit{Eq. 4.}39$$

4.5.2.2 Hull with Hull Vane

The time trace of the sway force in the pure yaw *PMM* test, shows to be significantly affected by the Hull Vane, when compared to the bare hull one. However, the first and third harmonics of the motion frequency are still the most significant frequencies:

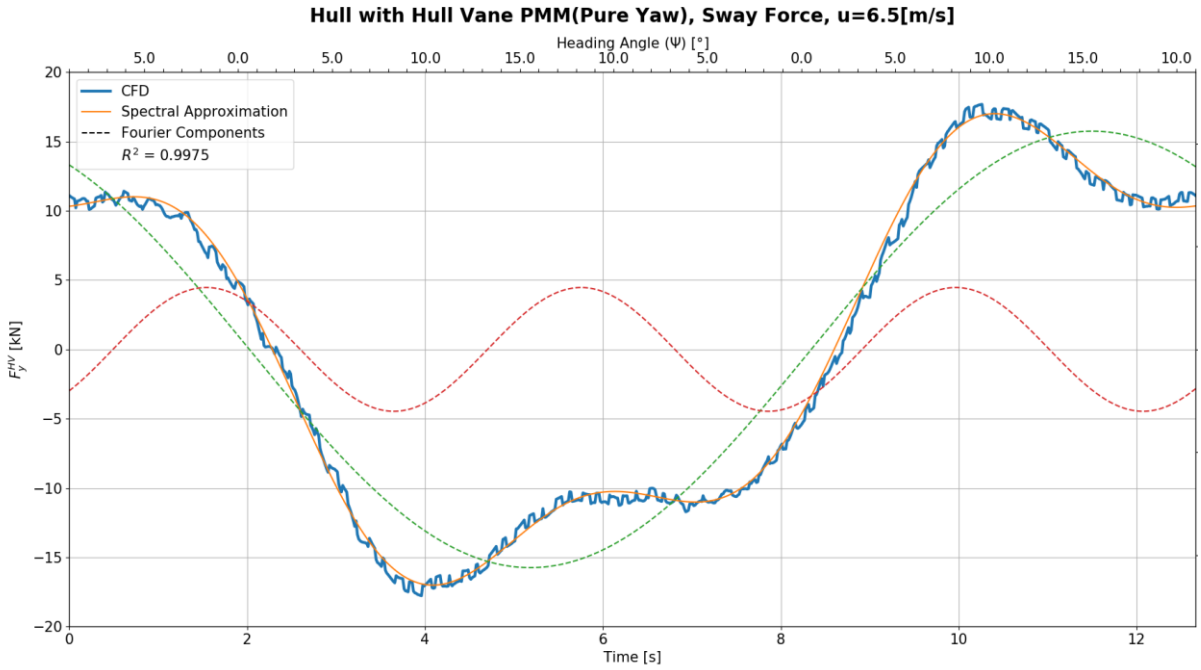

Figure 4.63: Sway force reconstruction using 1st and 3rd harmonics of the yaw motion for the hull with Hull Vane.

A good correlation is obtained using the 1st and 3rd harmonics of the motion ($R^2 = 0.9975$). Considering the same conditions as of the bare hull case, the hydrodynamic coefficients for sway force depending on yaw rate are:

$$\begin{cases} Y_{\dot{r}\dot{r}\dot{r}} = -31478.768[kN.s^6] \\ Y_{\dot{r}} = -124.325[kN.s^2] \\ Y_{rrr} = -7094.906\,[kN.s^3] \\ Y_r = 42.713\,[kN.s] \end{cases} \Rightarrow \begin{cases} Y_{\dot{r}\dot{r}\dot{r}} = -7.1855\times10^{-4}[kN.s^6] \\ Y_{\dot{r}} = -6.2102\times10^{-4}[kN.s^2] \\ Y_{rrr} = -9.2144\times10^{-3}\,[kN.s^3] \\ Y_r = 8.2060\times10^{-4}[kN.s] \end{cases} \qquad \textit{Eq. 4.}40$$

The following plots assess the effect of the Hull Vane on the sway force due to yaw:

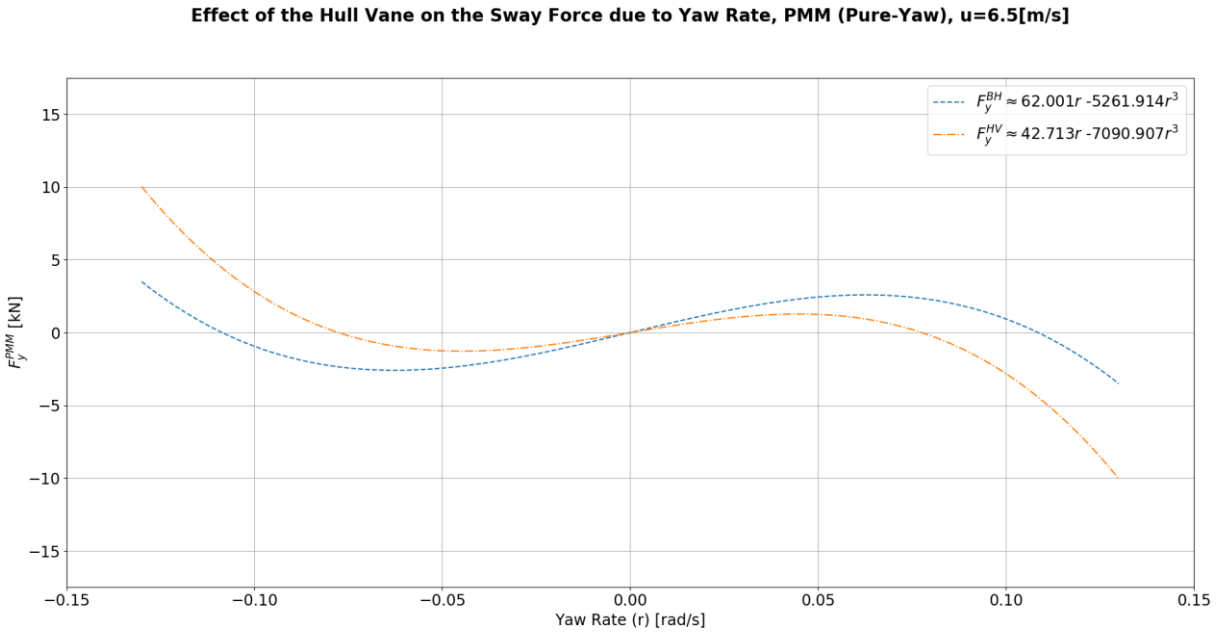

Figure 4.64: Comparison of the regressions for sway force dependent on yaw rate, for the case with and without Hull Vane. Regressions from a *PMM* pure-yaw test.

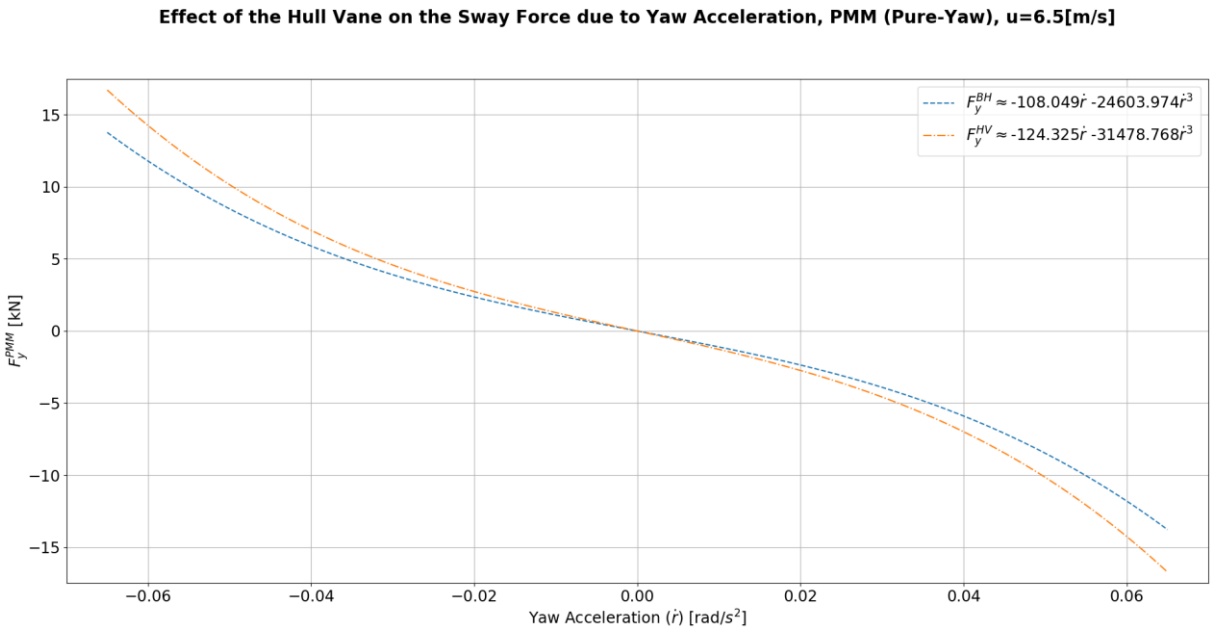

Figure 4.65: Comparison of the regressions for sway force dependent on yaw acceleration, for the case with and without Hull Vane. Regressions from a *PMM* pure-yaw test.

As can be seen in the previous plot, the sway force due to yaw rate is significantly affected by the Hull Vane. This can be explained by the fact that in pure-yaw, the side force developed by the hull is considerably smaller than the one in pure-sway, which makes the forces produced by the Hull Vane struts more relevant. Regarding the impact of the Hull Vane on the sway force due to yaw acceleration, this one is not affected as significantly as the sway force due to yaw rate, the difference caused by the Hull Vane is comparable with the numerical uncertainties (see *Section 4.1*).

4.5.3 YAW DAMPING AND ADDED MOMENT OF INERTIA

4.5.3.1 Bare Hull

In order to determine which are the most relevant frequencies of the yaw moment due to yaw motion, the magnitude of its steady and unsteady components is plotted in the frequency domain:

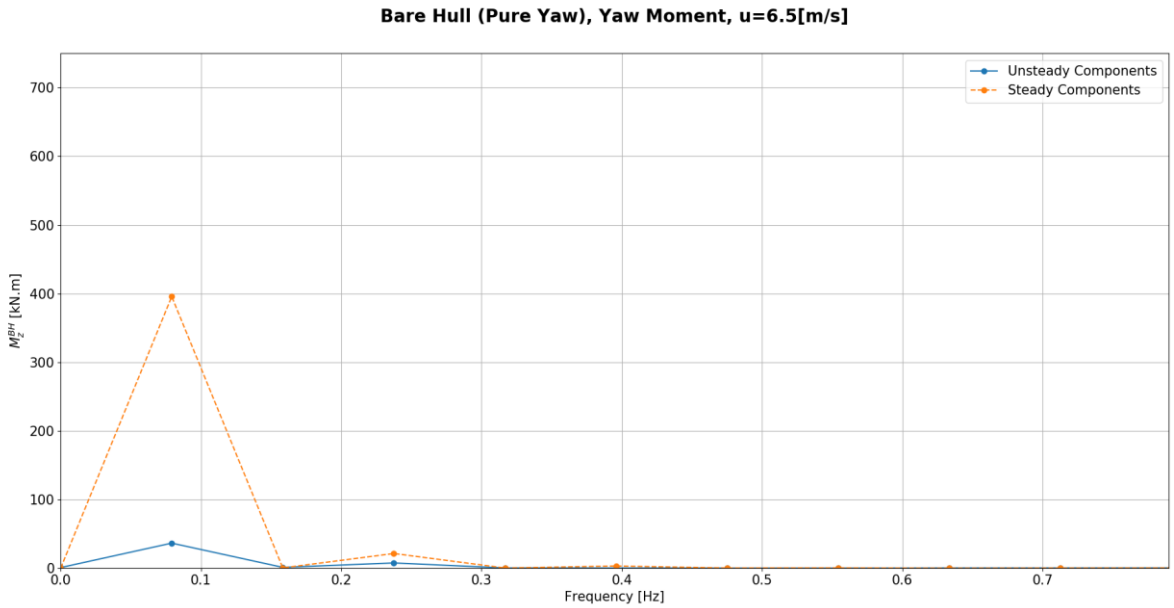

Figure 4.66: Spectrum of the magnitude of the steady and unsteady yaw moment components, for the bare hull case in a *PMM* pure-yaw test.

The previous plot shows that the first and third harmonics of the yaw motion are the most relevant ones. Furthermore, it also shows that for these frequencies, the steady component of the yaw moment is dominant. Furthermore, the unsteady component of the 3rd harmonic (non-linear added moment of inertia) is not significant, which is in accordance to what is often assumed in the literature (*i.e.:* $N_{rrr} = 0$), see *Teeuwen* in [75]. As can be seen in the figure below, a reconstruction using the 1st and 3rd harmonics is accurate enough to capture the behaviour of the yaw moment ($R^2 = 0.9994$).

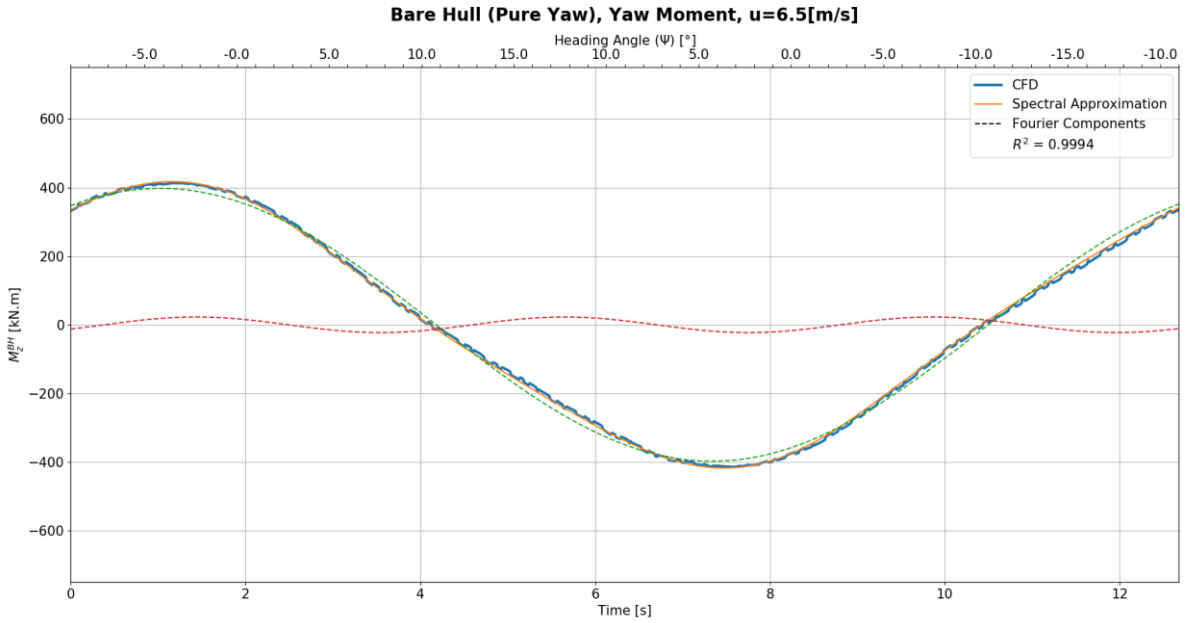

Figure 4.67: Yaw moment reconstruction using 1st and 3rd harmonics of the yaw motion for the bare hull.

For the purpose of this research, the high frequency fluctuations are neglected. Considering this, the yaw equation of motion for the pure-yaw *PMM* test is given by:

$$-N_{\dot{v}\dot{v}\dot{v}}.\dot{v}^3 - N_{\dot{v}}.\dot{v} - N_{vvv}.v^3 - N_v.v = M^1_{z_a}.\cos(\omega t + \epsilon_1) + M^3_{z_a}.\cos(3\omega t + \epsilon_3) \qquad \textit{Eq. 4.41}$$

Using some mathematical manipulation, it is possible to derive the following formulations for the hydrodynamic coefficients, see *Section 4.3*:

$$\begin{cases} N_{\dot{r}} = M^1_{z_a}.\dfrac{\cos(\epsilon_1)}{\psi_a.\omega^2} \\ N_{rrr} = 4.M^3_{z_a}.\dfrac{\sin(\epsilon_3)}{(\psi_a.\omega)^3} \\ N_r = -M^1_{z_a}.\dfrac{\sin(\epsilon_1)}{\psi_a.\omega} - N_{rrr}.\dfrac{3.(\psi_a.\omega)^2}{4} \end{cases} \Rightarrow \begin{cases} N_{\dot{r}} = -563.779\ [ton.m^2] \\ N_{rrr} = -38777.625\ [kN.s^3] \\ N_r = -2545.519\ [kN.s] \end{cases} \Rightarrow \begin{cases} N'_{\dot{r}} = -1.1265 \times 10^{-4}\ [-] \\ N'_{rrr} = -2.0145 \times 10^{-3}\ [-] \\ N'_r = -1.9562 \times 10^{-3}\ [-] \end{cases} \qquad \textit{Eq. 4.42}$$

4.5.3.2 Hull with Hull Vane

The time trace of the yaw moment for the vessel with Hull Vane is similar to the bare hull one. Therefore, the same type of reconstruction is adopted, *i.e.* using the 1st and 3rd harmonics of the yaw motion:

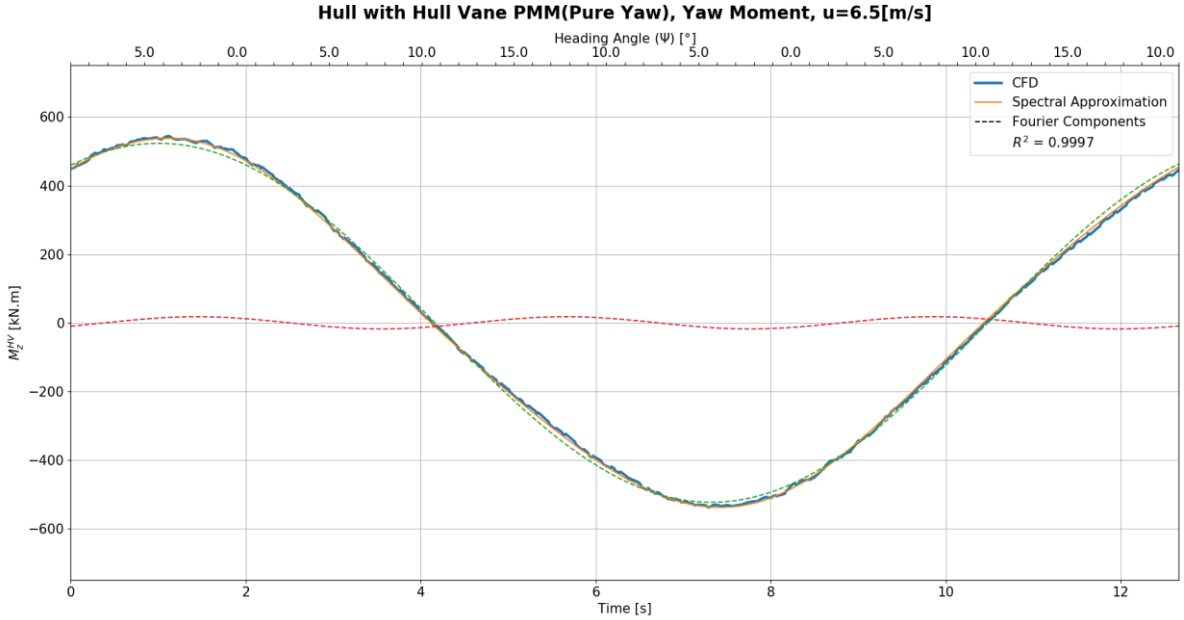

Figure 4.68: Yaw moment reconstruction using 1st and 3rd harmonics of the yaw motion for the Hull with Hull Vane.

According to *Eq. 4.*41 and *Eq. 4.*42, the hydrodynamic coefficients which describe the yaw moment due to sway speed for the hull with Hull Vane are:

$$\begin{cases} N_{\dot{r}} = -801.791\ [ton.m^2] \\ N_{rrr} = -30280.710\ [kN.s^3] \\ N_r = -3610.489\ [kN.s] \end{cases} \Rightarrow \begin{cases} N'_{\dot{r}} = -1.6020 \times 10^{-4}\ [-] \\ N'_{rrr} = -1.5731 \times 10^{-3}\ [-] \\ N'_r = -2.7746 \times 10^{-3} [-] \end{cases} \qquad \textit{Eq. 4.}43$$

By comparing the added moment of inertia ($N_{\dot{r}}$), it is possible to see that the magnitude of this one increases in about 40% with Hull Vane. Furthermore, the Hull Vane also causes an increase of the damping in yaw (N_r, N_{rrr}), as can be seen in *Figure 4.69*, see next page.

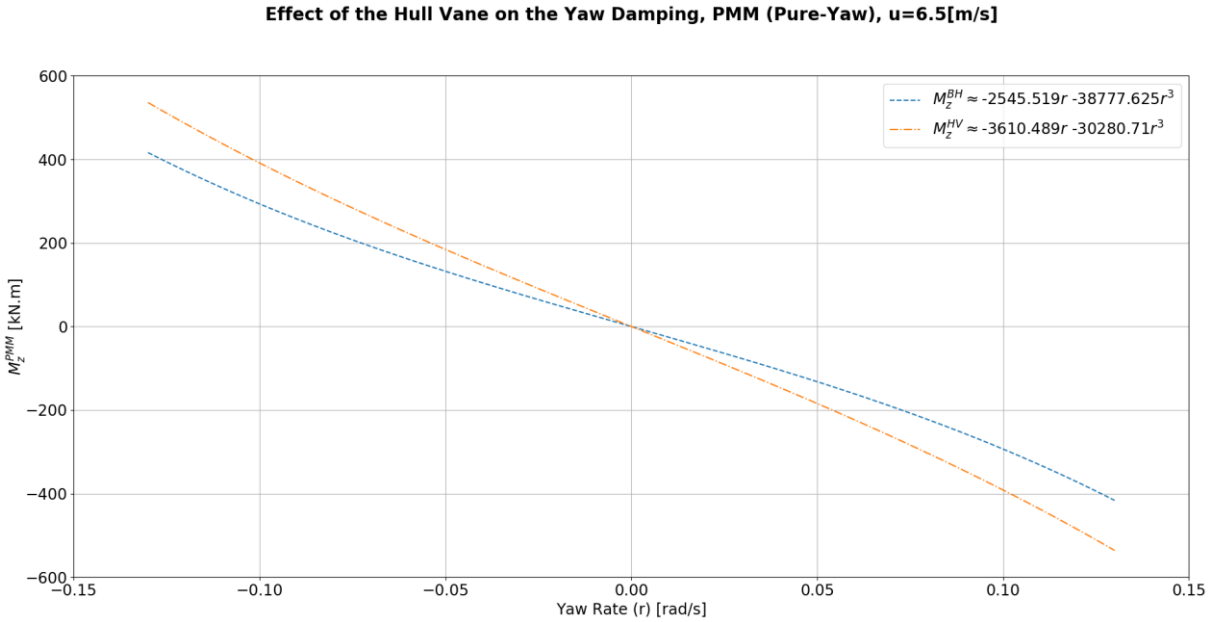

Figure 4.69: Comparison between the yaw damping for the bare hull and Hull Vane.

4.5.4 ROLL MOMENT DUE TO YAW

4.5.4.1 Bare Hull

In order to determine which are the most relevant harmonics of the roll moment due to yaw motion, the magnitude of its steady and unsteady components is plotted in the frequency domain:

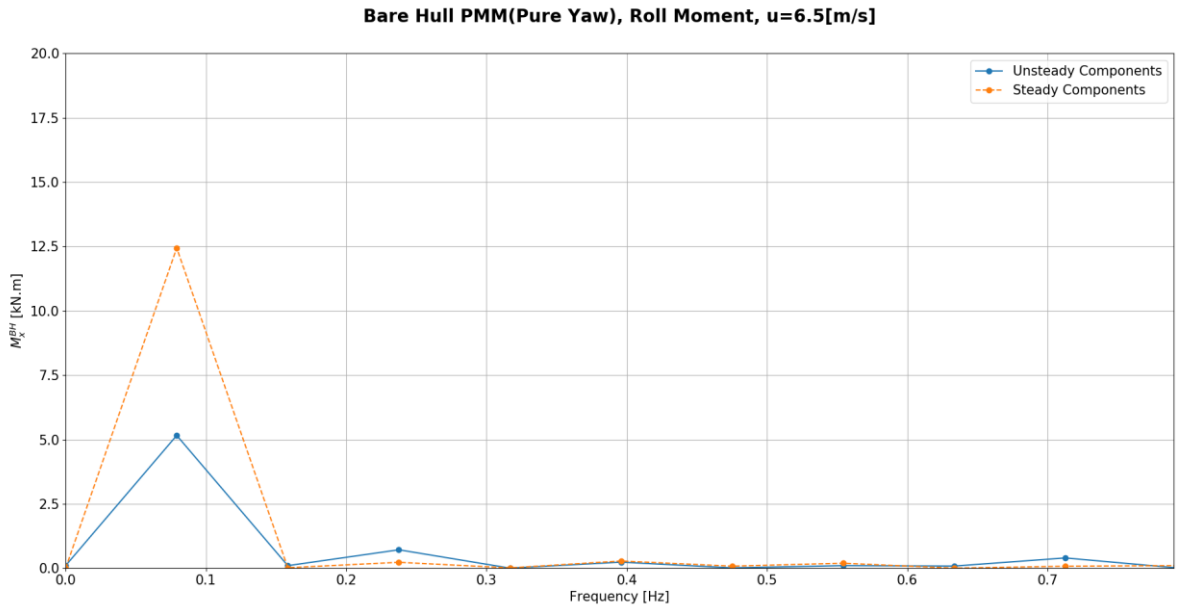

Figure 4.70: Frequency domain analysis of the bare hull roll moment, over a period of the *PMM* pure-yaw test. Magnitude of the steady and unsteady components of the roll moment.

According to the previous figure, the 1st harmonic of the yaw motion is the most significant one, showing a strong linear relation between the yaw rate and the roll moment. Furthermore, at this frequency the steady component dominates. The following plot shows the reconstruction of the roll moment signal in the time domain using the first harmonic of the yaw motion:

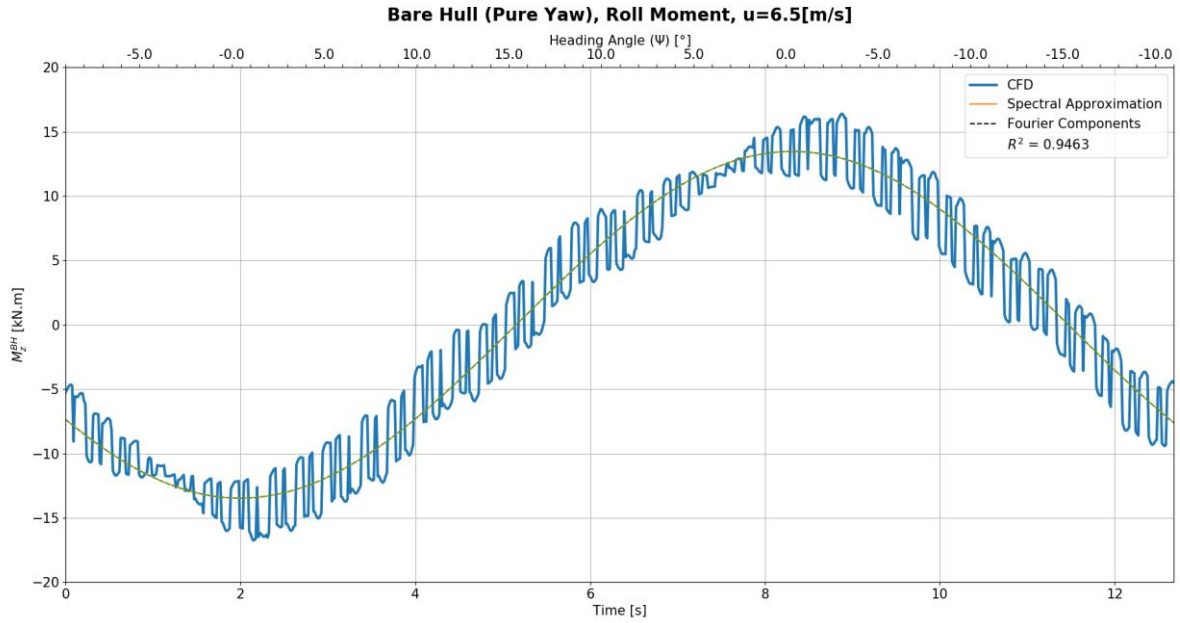

Figure 4.71: 1st order reconstruction of the time trace of the roll moment for the bare hull *PMM* pure-yaw test.

As can be seen, a linear relation shows to be able to capture the averaged behaviour of the roll moment signal. However, this one contains fluctuations, which are not captured by the first order reconstruction. Due to the considerable amplitude these fluctuations, a first order reconstruction including the *AGR* and *AD* harmonics is plotted in the following picture, to access their eventual impact on the signal:

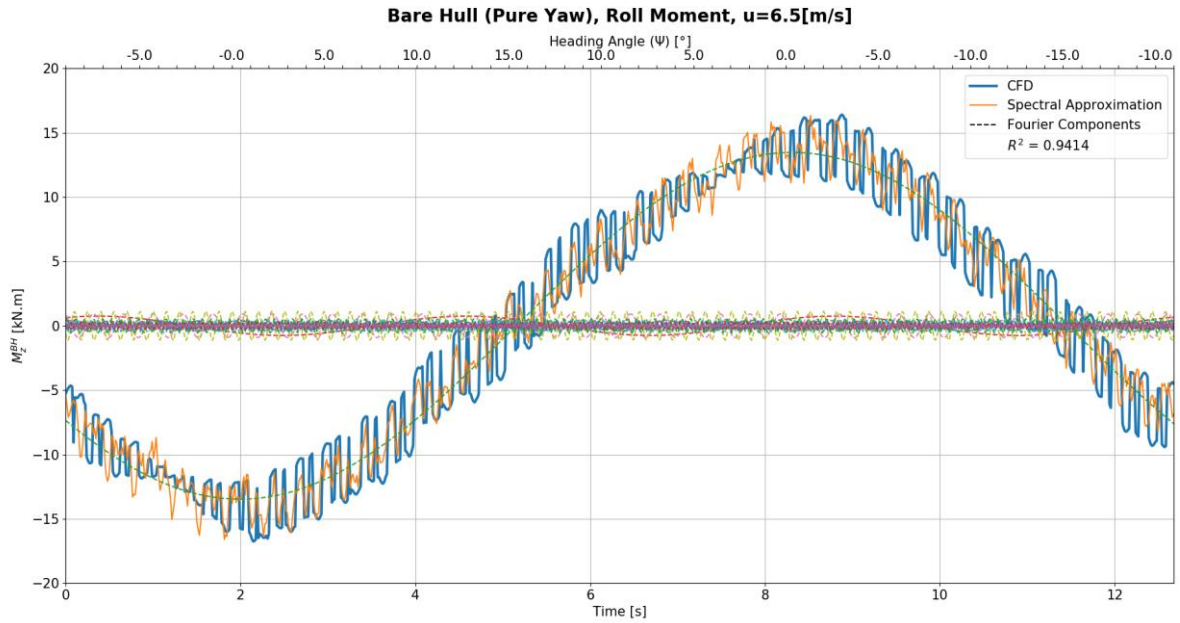

Figure 4.72: 1st order reconstruction of the time trace of the roll moment for the bare hull in a PMM pure-yaw test, including effects of the *AD and AGR* updating frequencies.

The fluctuations from the *AGR* and *AD* updating frequencies significantly affect the time trace of the roll moment. This more evident in this case since the magnitude of the moment is considerably smaller than the other moments previously studied. Since the study of manoeuvring is focused on low frequency phenomena (see *Perez* in [50]), these fluctuations are disregarded.

To assess whether the amplitude of this roll moment is significant in the context of this research, metacentric theory is used to estimate the maximum roll angle induced by yaw motion. The roll angle is given by (see *Barrass* and *Derrett* in [76]):

$$\phi = \operatorname{asin}\left(\frac{K}{\Delta.\overline{GM_t}.g}\right) = \operatorname{asin}\left(\frac{20}{58.9 \times 1.98 \times 9.81}\right) \approx 1° \qquad \textit{Eq. 4.44}$$

Since the roll motion is not the focus of this research and the maximum roll angle caused by yaw motion is about 1°, this roll moment is disregarded.

4.5.4.2 Hull with Hull Vane

The following plot shows the time-trace of the roll moment for the hull with Hull Vane, over one period of the *PMM* pure-yaw test:

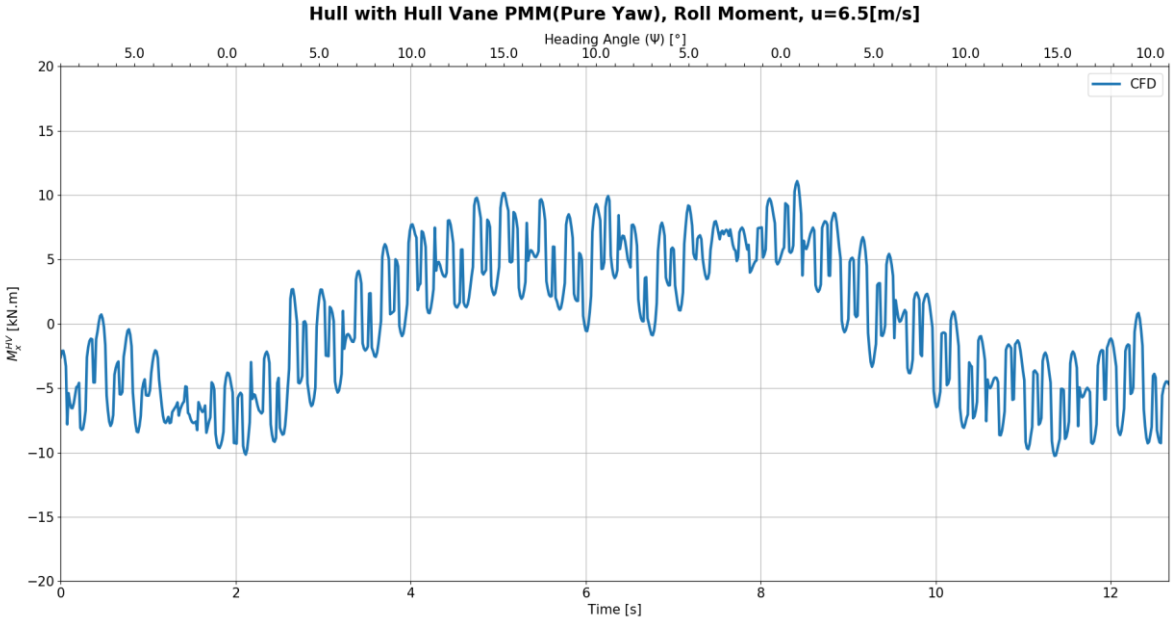

Figure 4.73: Time trace of the roll moment for the hull with Hull Vane in a PMM pure-yaw test.

Similarly to what was found in the previous sections, the hull with Hull Vane is more subjected to high frequency oscillations, this phenomena is expected to be caused by the Hull Vane since this one is sensitive to changes in the inflow conditions.
In accordance to the previous section, the roll moment due to yaw is neglected, due to its small amplitude. The validity of this and other assumptions is assessed in *Chapter 8,* when validating the mathematical model.

4.5.5 SUMMARY OF THE PMM PURE-YAW TEST RESULTS

- **Longitudinal Added Resistance due to Yaw:** The longitudinal added resistance due to yaw is about four times smaller than due to sway. Due to the small amplitude of the force, and the damping effect of the propulsion system (see *Section 4.2.1*), the longitudinal added resistance due to yaw is not expected to have a significant influence on the speed drop phenomena and consequently on course stability.

- **Sway Force due to Yaw:** The sway force due to yaw exhibits a highly non-linear behavior and due to its smaller amplitude is more subjected to noise than the sway force due to sway. The Hull Vane significantly affects the steady component of the force and increases the unsteady one (*i.e.:* sway force depending on yaw acceleration). However, for the last one the difference is comparable to the numerical uncertainties. The unsteady component of the sway force due to yaw is expected to be more relevant for zig-zag manoeuvres, where yaw accelerations are present during the entire manoeuvre.

- **Yaw Damping and Added Moment of Inertia:** The Hull Vane significantly increases the yaw damping and the yaw added moment of inertia. Therefore, this effect contributes for increase in course stability.

- **Roll Moment due to Yaw:** The amplitude of the roll moment due to yaw motion is about half of the amplitude due to sway. The maximum roll angle that can be reached due to pure-yaw is about 1°. Therefore, the roll moment due to yaw is disregarded in the context of this research. In future research this moment must be assessed using rotating arm tests, to avoid flow memory effects, which were observed in the pure-sway *PMM* test results (see *Section 4.4.4*).

The Hull Vane significantly affects the sway force due to yaw motion, the yaw damping and yaw added moment of inertia. The two last ones are stabilizing effects. However, due to the strong non-monotonic behavior of the sway force due to yaw rate, the effect of the Hull Vane can be either destabilizing or stabilizing, see *Eq. 2.48*. In one hand, the Hull Vane contributes for a decrease in course stability by trimming the vessel bow down, in another hand the Hull Vane contributes for an increase in course stability, since it increases the yaw damping. In this context and considering the strong non-linearity of the forces/moments, it is not trivial to draw general conclusions about the effect of the Hull Vane on course stability. Therefore, this is assessed from the manoeuvring prediction results in *Section 8.4.*

4.6 CONCLUSIONS

- **Solution Verification:** Two mesh topologies and an *AGR* algorithm were tested and compared. The **first mesh topology** is characterized by a refinement box around the skeg. In contrast to the skeg vortex, the fore-body vortex is poorly captured by this topology, leading to a non-converging solution. Therefore, a **second mesh topology** was developed to better capture the fore-body vortex. For this, a refinement box was placed around the entire hull. Although the solution of this mesh topology converges, leading to considerably smaller discretization uncertainties (but not satisfactory, particularly for yaw moment), the number of cells is prohibitive, in the context of this research (>22M+). In order combine a better capturing of vortices with lower computational cost, an ***AGR*** algorithm was tested. This one showed to be able to capture vortices with more detail than the finest mesh of the second topology (*t2G2,* 33M) and to reduce the computational cost by 60%. The difference in results between the *AGR* and *t2G2* is less than 1%, and therefore the *AGR* is used to perform the *virtual captive tests*. Since the method for the estimation of discretization uncertainties considered in this research requires geometrically similar grids between refinements (*see Eça* and *Hoekstra* in [47]), this one is not applicable to *AGR.* Therefore, the *AGR* discretization uncertainties are assumed to be equal to the ones from *t2G1.5,* which is considered to be a conservative assumption. In future research the *AGR* discretization uncertainties must be assessed according to the procedure proposed by *Wanckers et al.* in [71].

- **Virtual Captive Tests-Results:** The discrete spectral method developed and implemented in this research, showed to give an important contribution for the analysis of *PMM* tests. This allows to study the *PMM* results in depth, providing a better understanding and mathematical modelling of the phenomena involved (*i.e.:* physical and numerical). In this research this method not only allowed to mathematically describe non-linear components of forces and moments, but also showed that the *AGR* and *AD* (actuator disk) updating frequencies can be a significant source of numerical noise.

In general, the results from virtual *PMM* tests are subjected to more sources of errors than the ones from virtual *OTT* or *rotating arm tests,* causing some discrepancies*.* The main sources of errors are: flow memory effects and higher numerical residuals. Flow memory effects showed to particularly affect the prediction of roll moment. To avoid and quantify these unsteady effects, it would be convenient to have literature available about the effect of the St_n (*Strouhal* number) on the results from *PMM* tests. In this research, the discrepancies between pure-sway *PMM* tests and *OTTs* contribute for an over-prediction of the course stability. Having said this, the steady force components considered in this research are the ones determined from *OTTs.* In future research it is recommended to perform rotating arm tests and compare the outcome with the pure-yaw *PMM* test results. An overview of the hydrodynamic coefficients derived in this chapter can be found in *Appendix A.4*

According to the results presented in this chapter, in one hand the Hull Vane increases the *Munk* moment (destabilizing effect), on the other hand, it increases the yaw damping and the yaw added moment of inertia (stabilizing effects). Furthermore, due to the highly non-monotonic behaviour of the sway force due to yaw rate, the effect of the Hull Vane on this one can be either stabilizing or destabilizing. In this context and considering the non-linearity of the forces/moments, it is not trivial to draw general conclusions about the effect of the Hull Vane on course stability. Therefore, this is assessed from the manoeuvring prediction results in *Section 8.4.*

- **Final Remarks:** Although *PMM* tests together with the *Discrete Spectral Method* allow detailed studies of unsteady effects, their setup and analysis is more complex, time-consuming, vulnerable to errors and less reliable than *OTT* and *RAT* (rotating arm tests). Therefore, this type of *PMM* tests only represent an advantage for physical experiments (*i.e.:* reduces the experimental time and avoids the need of rotating arm facilities) or when required to perform a more detailed study of unsteady phenomena (*e.g.:* added masse/moments of inertia). However, according to *Yasukawa* and *Yoshimura* in [35], unsteady effects are often significantly less important than steady effects, and therefore they can eventually be modelled using semi-empirical models, this hypothesis is assessed in *Section 8.2* .

  In future research, the uncertainties of the *AGR* setup must be assessed, together with the influence of the St_n on the results of *PMM* tests. Furthermore, the results from pure-yaw *PMM* tests must be compared with the results from *rotating arm tests.*

5. INTERACTION PHENOMENA

As mentioned in *Section 2.7,* interaction effects are the physical phenomena responsible for the disturbances caused by one part of the vessel on the other and vice-versa (*e.g.:* the disturbance caused by the hull on the propeller inflow). This chapter aims to assess and mathematically describe interaction effects using *CFD*. The following illustration shows the interaction effects here considered:

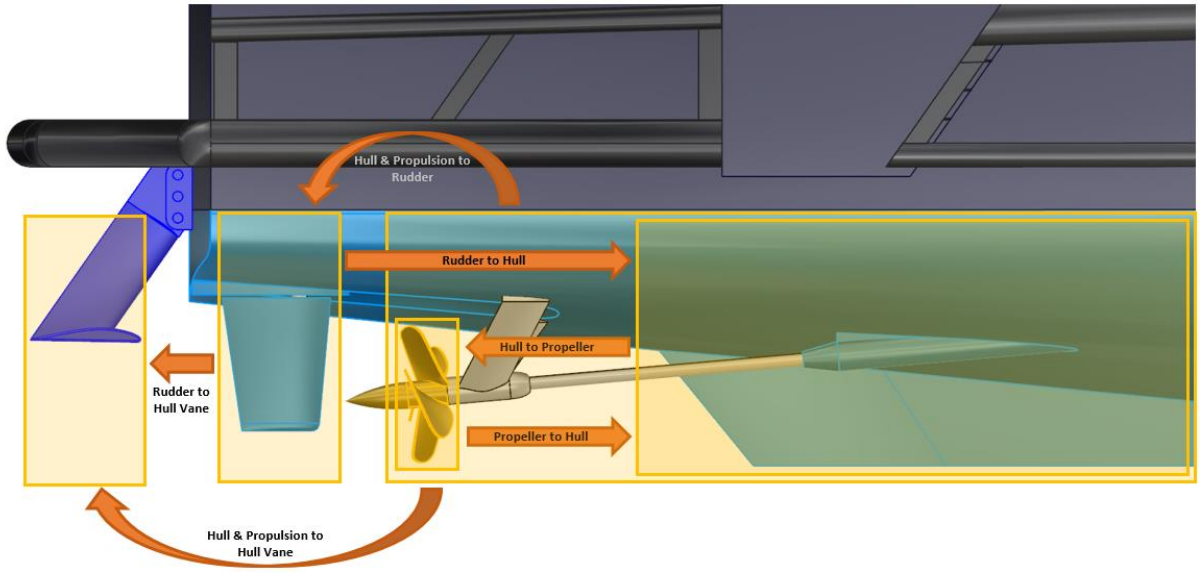

Figure 5.1: Scheme of the interaction effects studied in this chapter.

Hull Vane to hull interaction is not assessed in this chapter since this effect is automatically included in the coefficients of the integrated approach. *i.e.:* captive tests with Hull Vane. However, Hull and propulsion system to Hull Vane interaction is assessed to confirm the hypothesis that the increase of *Munk* moment, caused by the Hull Vane, is due to trimming the bow down. Hull Vane to rudder interaction is not considered relevant.

Since the *RPA8* is a symmetric twin-screw and twin-rudder vessel, for the sake of clarity, the side of the hull facing the flow is defined as the ‘outer’ side and the other one as the ‘inner’ side. In the following illustration, the starboard side is the outer one:

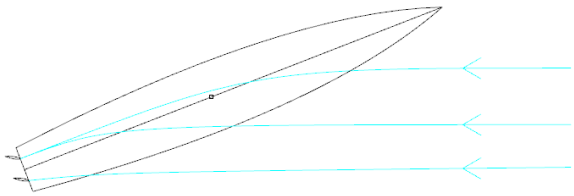

Figure 5.2: Scheme of the top view of a vessel under drift, where the starboard side is the outer side one and the portside is the inner one.

For the sake of clarity, every interaction effect is studied in a separate section, and in the end of the chapter, it is possible to find a summary of the interaction effects. A table with the interaction coefficients summarized, can be found in *Appendix A.4.3*

5.1 HULL TO PROPELLER INTERACTION

In this section the influence of drift angle on the propeller nominal wake fraction is assessed numerically. For this, the bare hull is virtually towed (without actuator disk) under multiple drift angles and the wake fraction is computed using an average of the normalized inflow speed, normal to the propeller plane.

Due to superposition of yaw and sway motions, the geometric inflow angle at the propeller plane can become considerably larger than the drift angle of the vessel. Therefore, the *OTT* were performed at drift angles ranging from 0°-20° in steps of 5° with a constant advance (surge) speed of 6.5 [m/s]. The following plot shows the effect of the drift angle on the wake fractions:

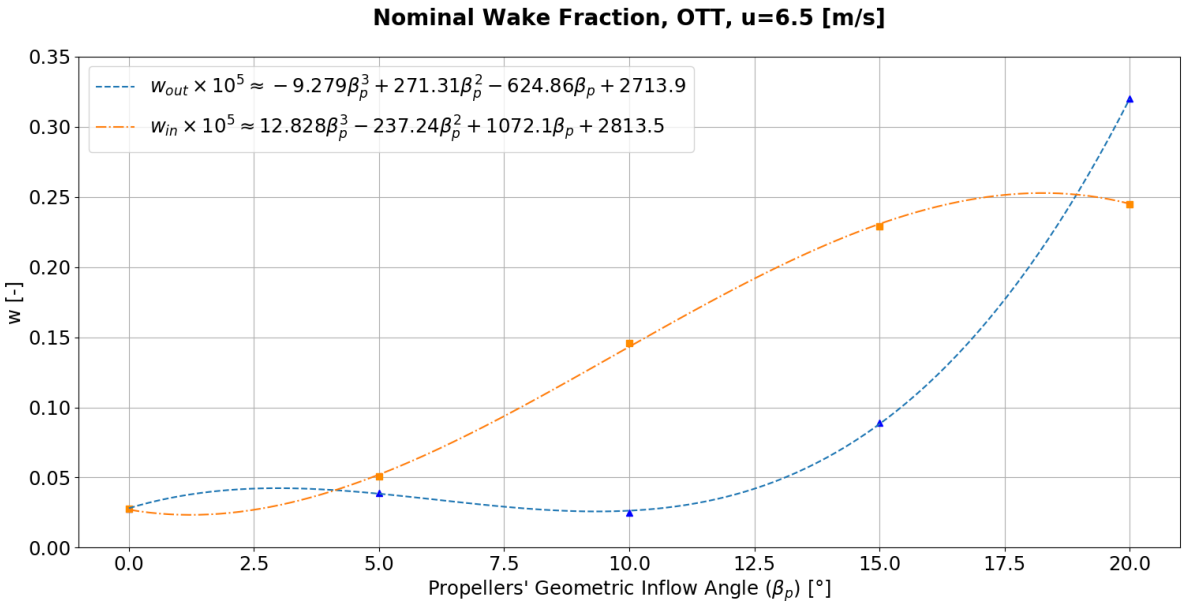

Figure 5.3: Effect of geometric inflow angle on the nominal wake fraction.

According to the *CFD* results, until 15° the inner wake fraction is larger than the outer wake fraction. This is caused by the fact that the inner propeller is in the wake of the hull, where the averaged longitudinal speed is expected to be smaller. However, it is possible to see that for 20° drift, the outside wake fraction overcomes the inside wake fraction. This is explained by the fact that the inside propeller's inflow is straightened by the hull (*Section 2.7.3*), increasing the longitudinal velocity component, relative to the outer propeller. In the hull's wake the axial flow velocity is reduced (increase of w) due to viscous effects, but the flow is also straightened (decrease of w).

5.2 PROPELLER TO HULL INTERACTION

Propeller to hull interaction is represented by the thrust deduction factor (t). According to *Sutulo* in [8], the thrust deduction factor is weakly affected by drift at moderate speed manoeuvring, and therefore is assumed constant. According to *Eq. 2.13* the thrust deduction factor is given by:

$$t = \frac{R^{SP} - R^{BH}}{R^{SP}} \qquad \textit{Eq. 5.1}$$

Here R^{SP} represents the self-propelled hull resistance and R^{BH} the bare hull resistance. The first one is determined by integrating the pressure distribution over the hull in a straight ahead *CFD* run with actuator disk. While R^{BH} is determined by towing the bare hull straight ahead (without propulsive effects). The trim change caused by the Hull Vane is assumed to be small enough to do not affect the thrust deduction factor. Therefore, this one is computed for the case without Hull Vane:

$$t = \frac{19.74 - 18.95}{19.74} = 0.04 \qquad \textit{Eq. 5.2}$$

According to numerical results, the bare hull resistance is 4% lower than the self-propelled resistance. This is caused by an increase in viscous drag and trim due to higher flow speeds at the stern.

5.3 HULL & PROPULSION TO RUDDER INTERACTION

The presence of the hull and propulsion system disturb the rudders' inflow. Thus, these effects must be considered when mathematically modeling the rudders. The first step to assess this, is to determine the lift and drag coefficients of the rudders when behind the hull and propulsion system. These coefficients are numerically determined in straight ahead sailing condition, by imposing rudder deflections and measuring the forces acting on the rudders. The following plots show the results:

Figure 5.4: Lift coefficient curves of both rudders. The dashed line represents the after-stall region.

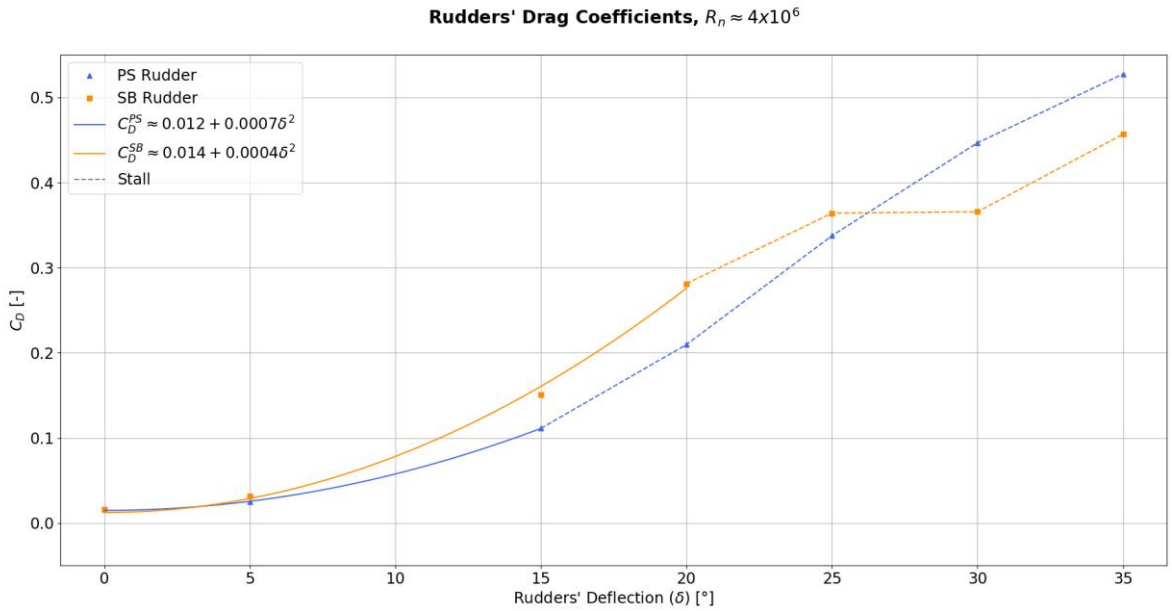

Figure 5.5: Drag coefficient curves of both rudders. The dashed line represents the after-stall region.

Note that the convention adopted in this research assumes a positive rudder deflection, a rudder deflection which causes a positive sway force (*i.e.:* from SB to PS).

As can be seen in the previous plots the lift and drag coefficients are different for the portside and starboard rudders. The difference is due to inflow disturbances caused by the presence of the hull and propulsion system. According to lifting line theory, in pre-stalling regime, the drag increases with the square of the lift coefficient (*see Eq. 2.28*), and the lift increases linearly with the angle of attack. Therefore, the pre-stalling region of both rudders is fit with first and second order polynomials for lift and drag coefficients, respectively.

In *Section* 2.7.3, the flow straightening coefficient is introduced, this one relates the geometric inflow angle of the rudders (β_R) with their hydrodynamic inflow angle (α_0). To determine flow straightening coefficients, the rudders' deflection is set to zero and multiple β_R are imposed. Then, by comparing the forces acting on the rudders with the ones previously obtained (by just deflecting the rudders in straight ahead condition), it is possible to determine hydrodynamic inflow angles.

For the determination of flow straightening coefficients, *Molland* and *Turnock* in [25], imposed geometric inflow angles at the rudders (β_R) with *OTTs* (pure-drift). Their approach assumes that flow straightening effects only depend on the geometric inflow angle (β_R) not on the type of manoeuvre (*e.g.:* pure-sway and pure-yaw). However, this method is expected to over-predict the effects of the fore and aft-body vortices, leading to an over prediction of interaction effects. To avoid this, the flow straightening effects due to pure sway and yaw must be assessed separately, as performed by *Toxopeus* in [4]. However, due to time constraints and limitations of the *CFD* software in performing rotating arm tests, *Molland's* and *Turnock's* methodology is adopted for this research.

The following plot, compares the sway forces developed by the inside and outside rudders for multiple geometric inflow angles (β_R):

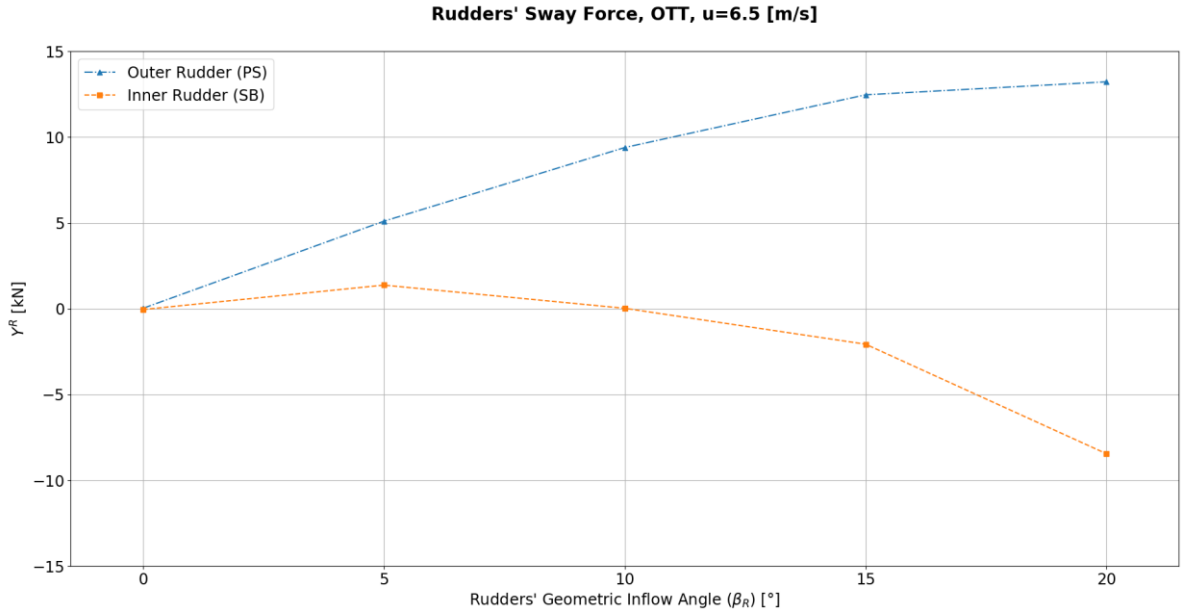

Figure 5.6: Rudders sway force for multiple geometric inflow angles with zero deflection. The dashed lines connecting the points are not meant to have a physical meaning.

According to the previous plot, the inner rudder is subjected to strong disturbances from the hull. This is caused by a local reverse flow induced by the fore and aft-body vortices, as shown in the following figure:

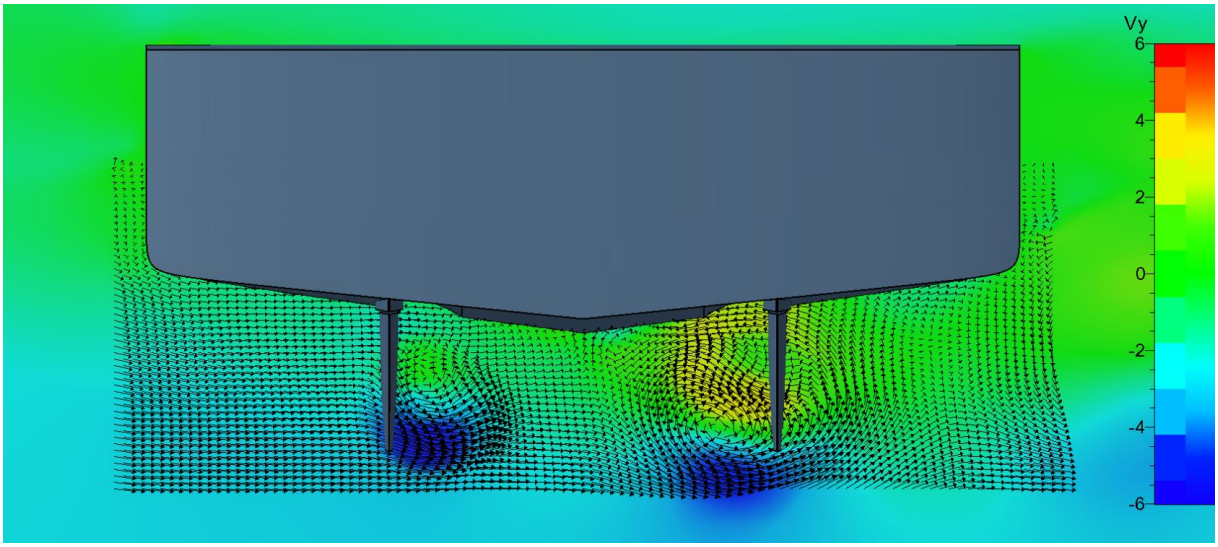

Figure 5.7: Transverse cutting plane 0.4 m forward the Rudders at 20° drift. The colour distribution represents the transverse component of the flow speed, the vectors represent the velocity direction and magnitude.

Note that the portside rotation (left in the figure) of the flow is caused by the propulsion system, which in this case is according to the 'topside-out' convention.

As previously mentioned, the flow straightening coefficients relate β_R with α_0. The last one is assessed by determining for which rudder deflection, in straight ahead condition, the rudder develops the same amount of side force as when β_R is imposed (with no rudder deflection).

The following plot relates the β_R with α_0:

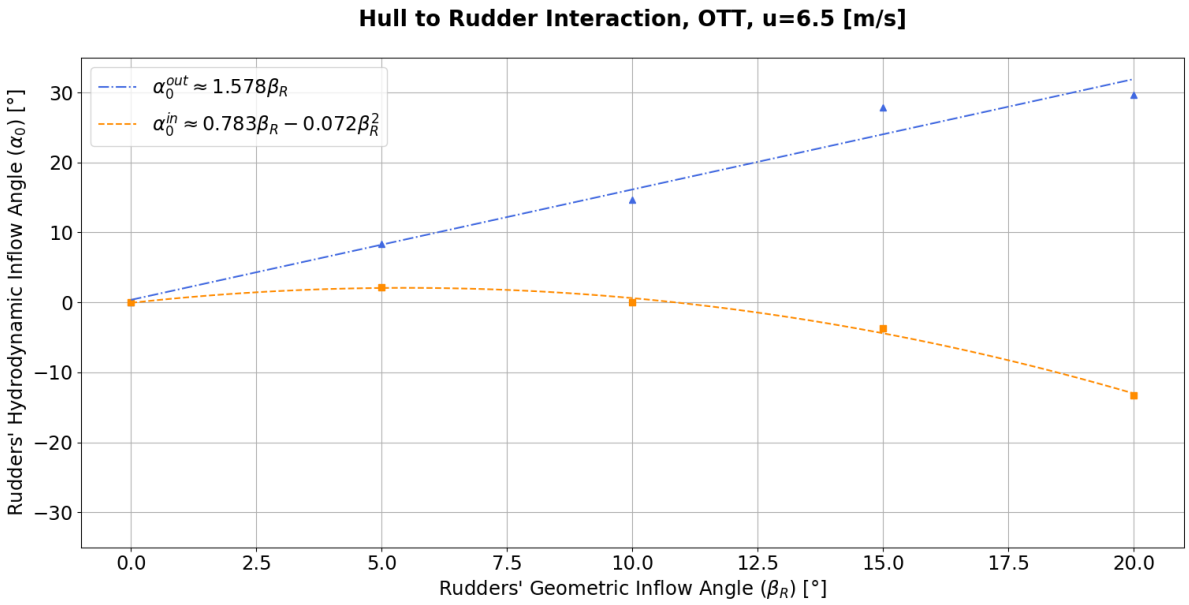

Figure 5.8: Relation between β_R and α_0 for both rudders.

These experimental results are fit with polynomial regressions, where their coefficients represent flow straightening coefficients:

$$\begin{cases} \gamma_R^{out} = 1.578\ [-] \\ \gamma_R^{in,1} = 0.783\ [-] \\ \gamma_R^{in,2} = -0.072\ [-] \end{cases} \qquad \textit{Eq. 5.3}$$

Often in the literature, β_R and α_0 are assumed to have a linear relation, see *Molland* and *Turnock* in [25] and *Eq. 2.26*. However, this assumption is not valid for the inside ruder. Its quadratic behaviour is caused by the non-linear relation between the drift angle and the intensity of the fore and aft-body vortices.

As mentioned in *Section 4.1,* the *AGR (Adaptive Grid Refinement),* specially targets wake flows and high vorticity regions. Since the outer rudder is subjected to less wake effects and vortices than the inner rudder, the inflow region of the outer rudder is less refined by the *AGR,* explaining the scatter of the outer rudder results. In further research this can be improved by fine tuning the *AGR* threshold.

The propulsion system increases the local flow speed to compensate for the longitudinal added resistance due to sway. This leads to a flow straightening coefficient for the outer rudder greater than 1.

According to these results, the inside rudder stalls earlier than the outside one, since during manoeuvring both rudders have the same deflection. Therefore, in order to improve the effectiveness of the steering system, a *Variable Rudder Angle System* was developed in parallel to this research. The aim of this system is to reduce the deflection of the inside rudder to avoid stalling, leading to an improvement of the controllability of the vessel even in sharp turns.

Note that these flow straightening coefficients include propulsive effects, which means that propeller to rudder interaction is included.

5.4 RUDDER TO HULL INTERACTION

In *Section 2.7.4* it is explained that rudder to hull interaction is a force/moment acting on the hull by the deflection of the flow caused by the rudders, similarly to flap-wing interaction. For the *RPA8* case, most of this interaction effect is developed by the skeg as can be seen in the following figure:

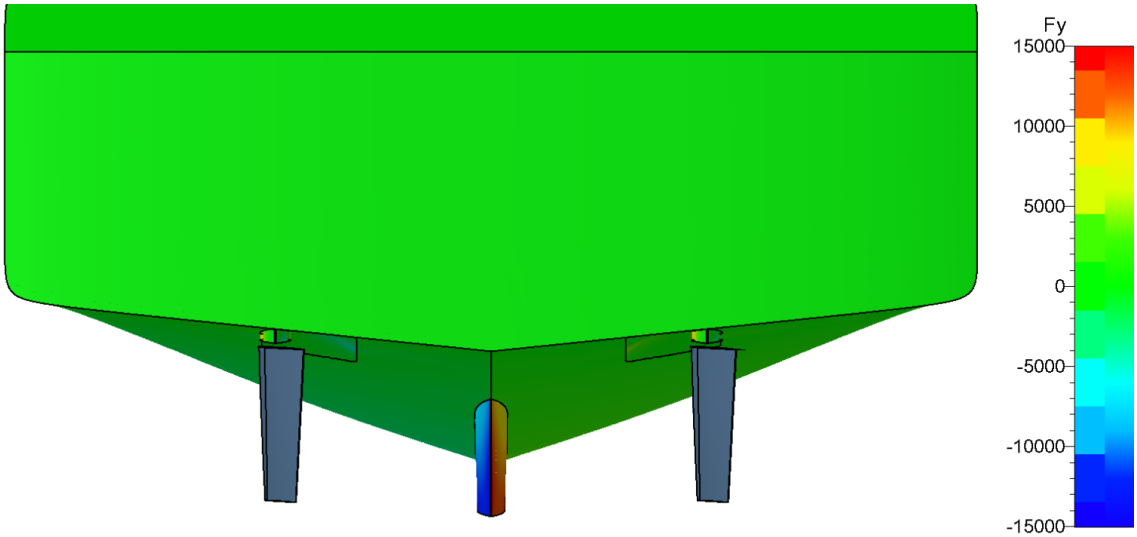

Figure 5.9: Numerical results of side force distribution on the hull (pressure) [N/m^2].

In this section, interaction coefficients are computed and compared to *Söding's* semi-empirical model (see [37] and *Section 2.7.4*). To determine rudder to hull interaction coefficients, the vessel is towed straight ahead and multiple rudder deflections are imposed ($\delta = 0, 5, 15, 20, 25, 30, 35$ [°]). Then the forces/moments acting on the hull are compared with the ones developed by the rudders. For this, the following assumptions are considered:

- Both rudders have the same deflection during manoeuvring, which is a characteristic of *RPA8;*
- The induced force/moment on the hull is only dependent on the force/moment developed by the steering system, see *Yasukawa et al. in* [35]. The bending of the flow caused by the rudders induces a change in pressure field on the hull, leading to the development of forces and moments. Since the bending of the flow is directly related to the side force developed by the rudders, this assumption is valid.

According to *Eq. 2.36* and *Eq. 2.37*, rudder to hull interaction coefficients, relate the forces/moments developed by the rudders with the ones developed by hull:

$$\begin{cases} Y^R = (1 + a_H).Y^{R0} \\ N^{R,Hull} = x_{RH}.Y^{R,Hull} \end{cases} \quad \textit{Eq. 5.4}$$

Note that $Y^{R,Hull}$ and $N^{R,Hull}$ represent the forces and moments acting on the hull due to the deflection of the rudders. The following plot relates Y^{R0} with Y^R:

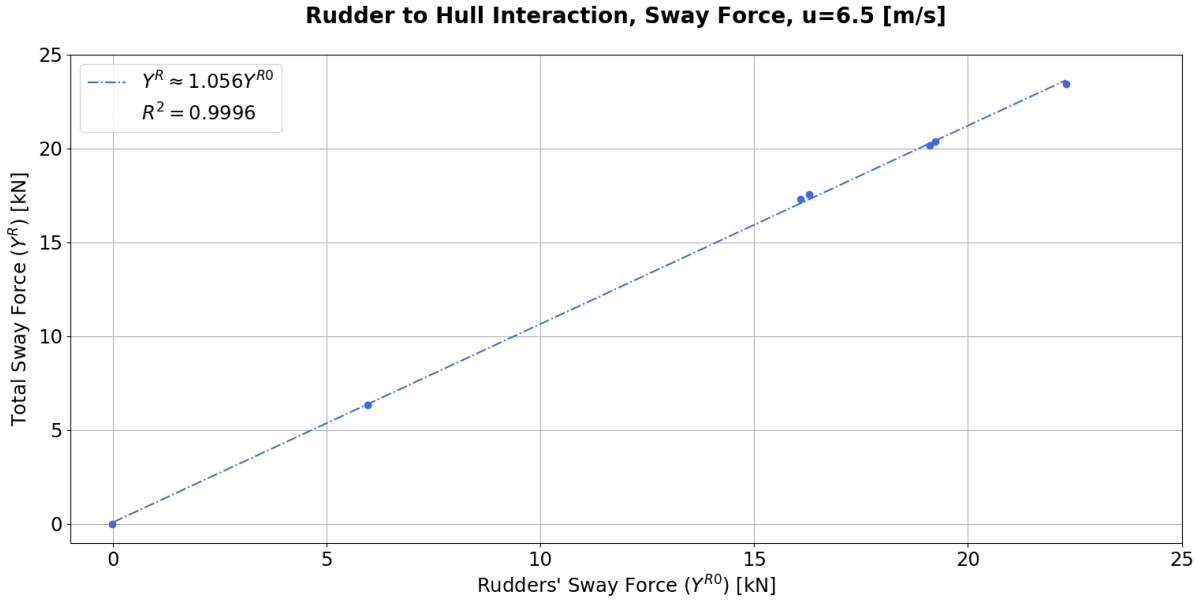

Figure 5.10: Relation between the total sway force developed by the rudders (Y^{R0}) and the total sway force acting on the vessel (Y^R).

The previous plot shows that the force acting on the hull has a linear relation with the force developed by the rudders. From *Eq. 5.4*, the slope of the linear regression is $(1 + a_H)$, which leads to:

$$a_H = 0.056\ [-] \quad \textit{Eq. 5.5}$$

Although *Söding's* semi-empirical model (*Eq. 2.40*) was developed for container vessels, this one predicts the magnitude of the interaction force ($a_H = 0.039$) relatively well.

The following plot relates the induced sway force on the hull ($Y^{R,Hull}$) with the induced yaw moment acting on it ($N^{R,Hull}$):

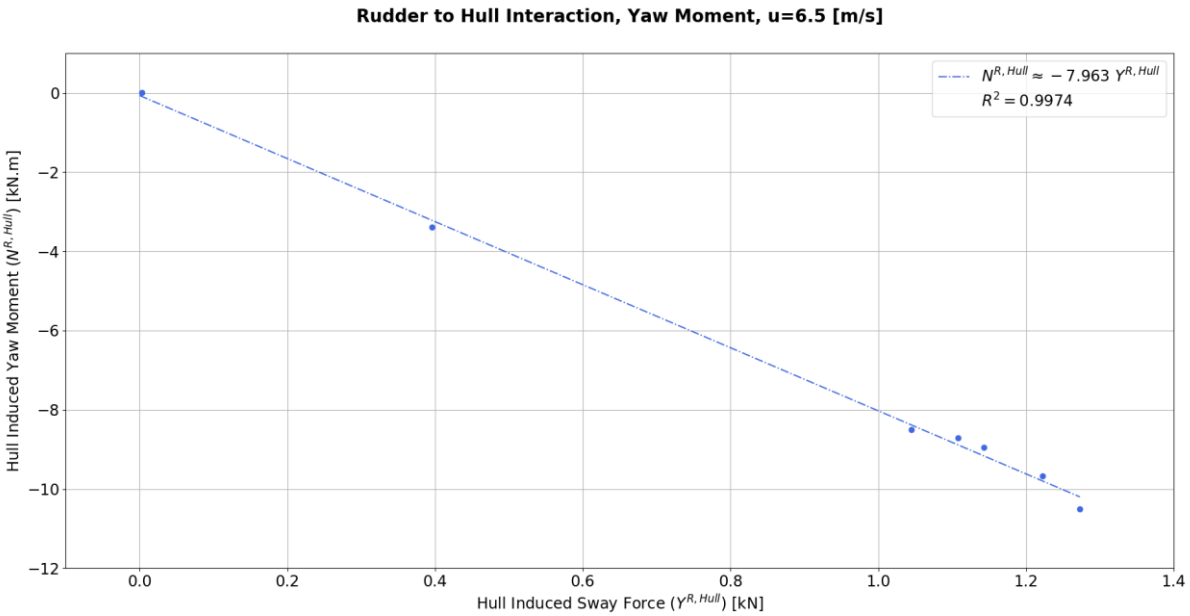

Figure 5.11: Relation between the sway force acting on the hull ($Y^{R,Hull}$) with the yaw moment developed by the hull ($N^{R,Hull}$).

The previous plot shows a linear relation between $Y^{R,Hull}$ and $N^{R,Hull}$, which is in accordance to the literature, see *Sutulo* in [8]. From *Eq. 5.4*, the slope of the linear regression is the abscissa of interaction (x_{RH}), which in this case is constant and equal to:

$$x_{RH} = -7.963\ [\mathrm{m}] \qquad \textit{Eq. 5.6}$$

This abscissa corresponds to a point between the skeg's trailing edge and the rudders. Although *Söding's* semi-empirical model (*Eq. 2.40*) predicts a_H relatively well, it is not the case anymore for x_{RH}, for which the model predicts an interaction abscissa at -1.742 [m].

When comparing these interaction forces/moments with the ones acting on the hull in the *Virtual Captive Tests* (*Chapter 4),* it is possible to conclude that this interaction phenomena has a small contribution for the overall forces/moments acting on the vessel (1-2%).

5.5 HULL & PROPULSION TO HULL VANE INTERACTION

Since the study of roll motion is not the focus of this research, as previously explained, only the sway forces developed by the Hull Vane struts are assessed in this section. According to the results of *Chapter 4*, the Hull Vane does not affect the sway damping, suggesting that the increase in *Munk* Moment caused by the Hull Vane is due to trimming the bow down. Therefore, this section aims to confirm this hypothesis and contribute for a better understanding of hull to Hull Vane interaction. The following picture shows the Hull Vane's inflow velocity field at 15° drift:

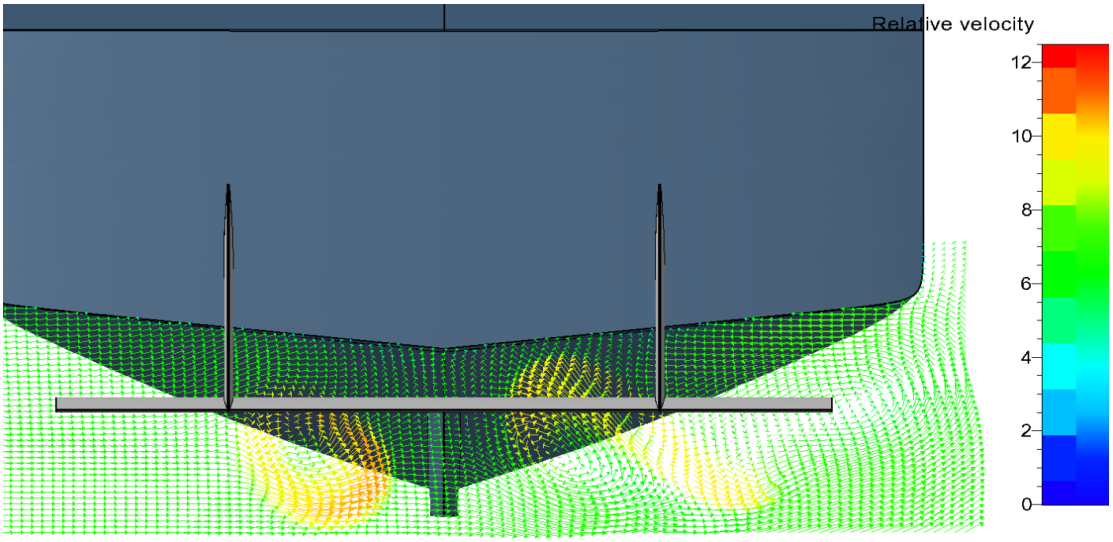

Figure 5.12: Velocity field 0.5 m forward the Hull Vane at 15° drift. The vectors' colours represent the velocity magnitude.

Note that the portside rotation (left in the figure) of the flow is caused by the propulsion system, which in this case is according to the 'topside-out' convention. On the starboard side (inside) it is possible to observe a strong counter-flow, which induces an opposite inflow angle on the inside strut (starboard), comparative to the outside one. This counter flow is caused by the fore and aft body vortices. The following plot compares the forces acting on the outside (portside) and inside (starboard) struts for multiple geometric inflow angles (β_s):

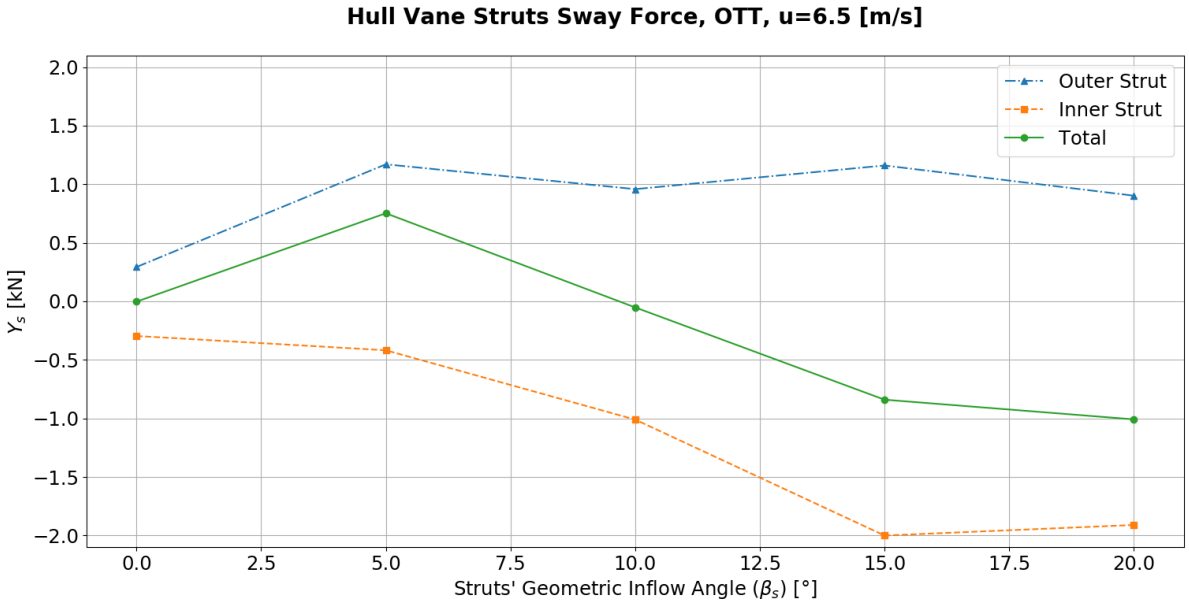

Figure 5.13: Sway force developed by the Hull Vane struts for multiple geometric inflow angles.

The previous figure shows that the sway force on the inner strut significantly increases until 15° while on the outer strut it remains relatively steady. This difference is caused by the fact that the Hull Vane is close to the hull, making the inflow of the outer strut relatively stable, due to the wake of the hull, as can be seen in the following figures:

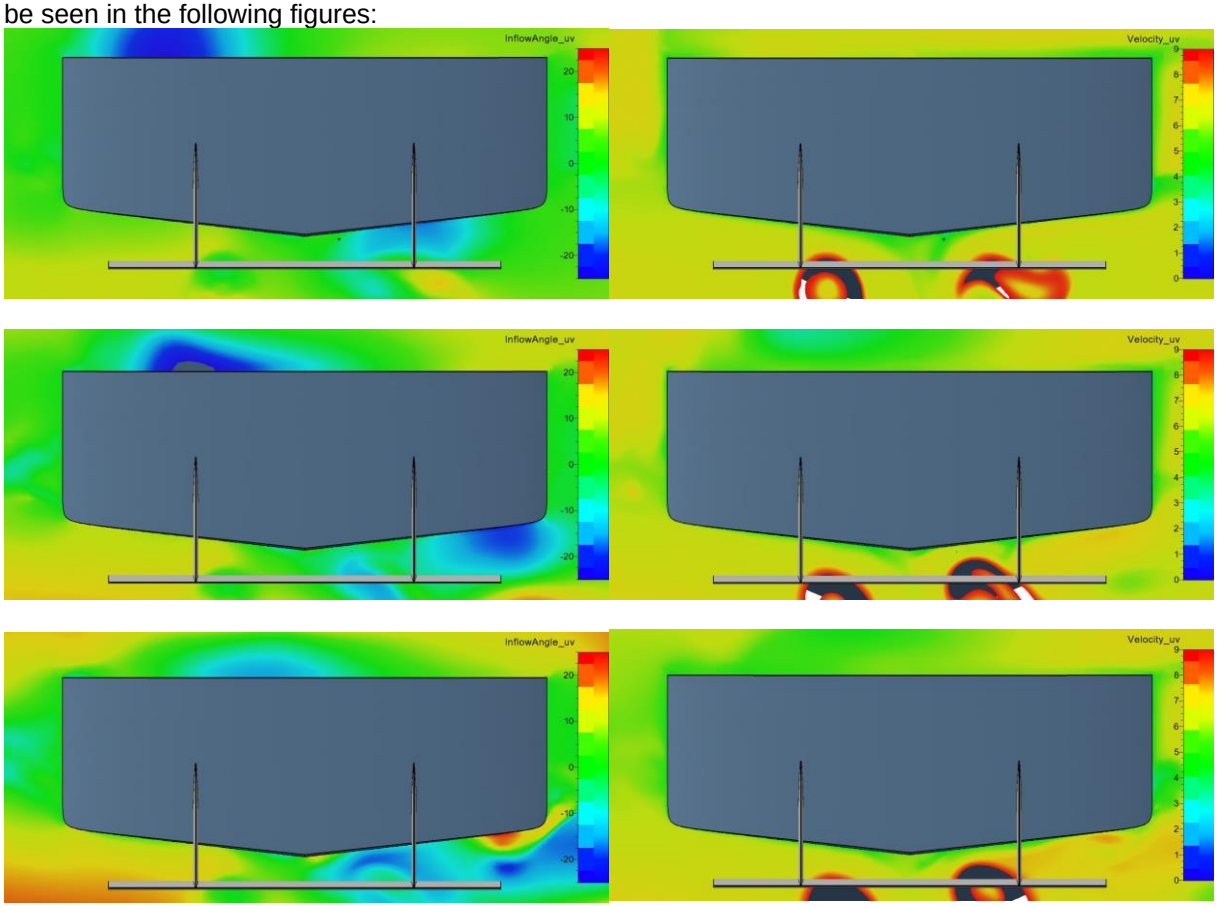

Figure 5.14: Struts horizontal inflow angle (left) and speed (right) for 10°, 15° and 20° geometric inflow angles, from top to bottom respectively. Cutting plane 0.5m forward the Hull Vane.

For the outer strut, the same does not happen, since its inflow is strongly disturbed by the fore and aft body vortices, and these ones significantly change with the drift angle. Resulting in an interesting phenomenon, which is the development of sway thrust by the Hull Vane for $\beta_s > 10°$. However, as previously explained in *Section 5.3,* pure drift to tests are expected to overestimate interaction phenomena.

When comparing the total sway forces developed by the Hull Vane with the sway forces and yaw moments of the bare hull (see *Section 4.2*), it is possible to note that the Hull Vane contribution represents about 1-2% of the total forces/moments. This explains why the Hull Vane practically does not influence the sway damping. Furthermore, it also shows that the influence of the Hull Vane on *Munk* moment is mainly due to the change in dynamic trim (see Figure 2.8) and not by the yaw moment developed by the struts. However, the side force developed by the Hull Vane struts due to yaw is expected to be more relevant than in pure-sway, since the flow reversion phenomenon is less strong. A detailed assessment of the forces developed by the Hull Vane struts due to yaw, is left for further research due to time constraints and, limitations of the *CFD* software in performing rotating arm tests. Later in *Sections 5.6* and *6.3,* the force developed by the struts in pure-yaw is modeled using *Fujii's LAR LLT* (Low Aspect Ratio Lifting Line Theory, *Eq. 2.30*).

According to these results, the sway force developed by the Hull Vane in pure drift is not relevant in the context of this research. This, confirms the hypothesis that the influence of the Hull Vane on the *Munk* moment is caused by the change in dynamic trim, see *Chapter 4*. Furthermore, the Hull Vane practically does not influence the flow upstream, since is a fixed appendage, so, Hull Vane to Hull interaction is neglected.

5.6 RUDDER TO HULL VANE INTERACTION

Since the Hull Vane struts are aligned with the rudders, rudder to strut interaction is expected. To study this, multiple rudder deflections are set in straight-ahead sailing condition. Then by using *Fujii's LAR LLT* (*Eq. 2.30*) to model the struts, it is possible to determine their hydrodynamic inflow angle (as previously done in *Section 5.3*). Assuming that the spacing between struts is sufficiently large to neglect interaction effects between *PS* and *SB* struts (or rudders), an average of the forces acting on both struts is considered. The following plot relates the hydrodynamic inflow angle of a strut, with the effective rudder angle (α_E), which is this case is approximately the same as the rudder deflection since $\beta_R = 0$.

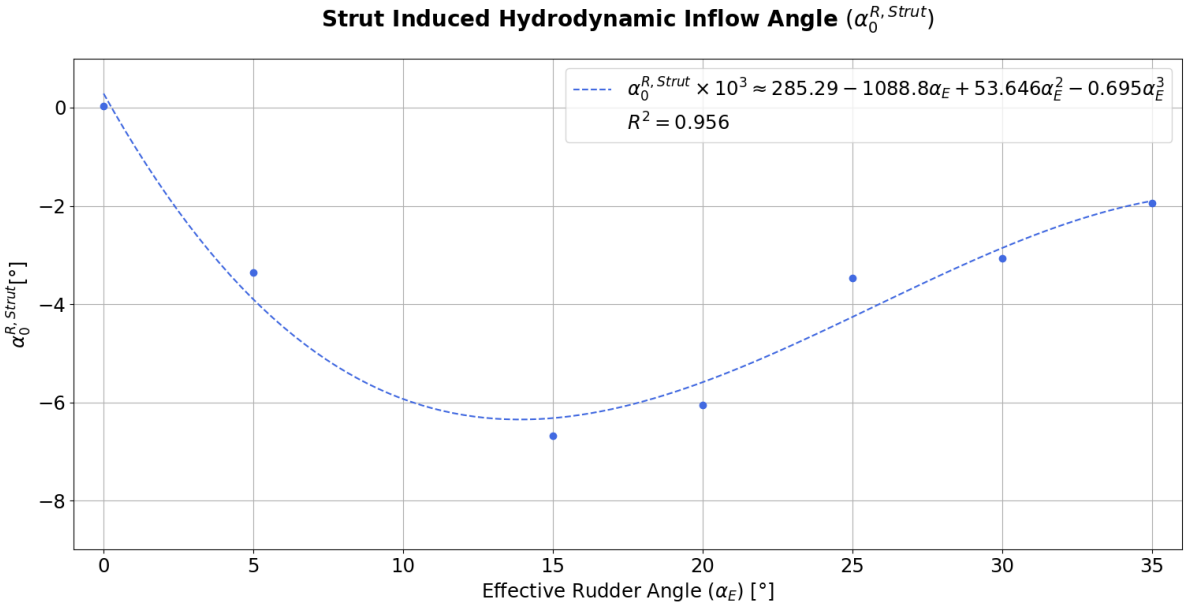

Figure 5.15: Relation between the effective rudder angle and induced hydrodynamic angle at the struts.

According to the previous plot, the maximum inflow angle induced by a rudder on a strut occurs at 15° rudder angle, corresponding to about 1 [kN] of side force acting on the strut at 6.5 [m/s], straight ahead. The non-monotonic behaviour of these results is caused by stalling of the rudder, which disturbs the strut's inflow and reduces the bending of the flow caused by the rudder. Note that $\alpha_0^{R,Strut}$ and α_E have opposite signs since the deflection of the flow caused by the rudder creates an inflow angle at the strut with an opposite sign, due to momentum conservation. The coefficients of the polynomial regression represent flow bending coefficients, denoted by $\Gamma_S^0, \Gamma_S^1, \Gamma_S^2, \Gamma_S^3$.

5.7 CONCLUSIONS

In this section it is shown that the vortices developed by the hull strongly affect propulsion system, steering system and the Hull Vane. To assess these effects, geometric inflow angles were imposed using oblique towing tests. However, this methodology is expected to over-estimate interaction effects, as discussed in *Section 5.3.* The use of alternative methods is left for future research, due to time constraints and limitations of the *CFD* software.

As previously mentioned, in free running manoeuvring, the geometric inflow angle at a certain location is the result of a superposition of sway and yaw motions, leading to large inflow angles at the stern. Therefore, the *OTTs* were performed up to 20° drift, which is larger than the drift angle used for solution verification of the *CFD* set up (*Section 4.1*). However, due to the flexibility of *AGR*, it is expected that the main flow properties are captured for 20° drift as well as for 15° drift.

- **Hull to Propeller Interaction:** The propellers' nominal wake fractions are significantly affected by the geometric inflow angle, increasing up to 10 times for certain conditions. The wake of the hull reduces the axial flow speed on the inside part of the hull (increasing w), but also straightens the flow (decreasing w). Until 15° drift, the first effect dominates. However, for 20° drift the wake fraction of the inside propeller becomes smaller than the wake of the outside one, due to flow straightening effects.

- **Propeller to Hull Interaction:** The thrust deduction factor (t), which represents a propeller to hull interaction, is assumed to be constant for moderate speed manoeuvring, according to *Sutulo* in [8]. The obtained results show that the bare hull resistance is 4% lower than the self-propelled resistance. This is caused by an increase in viscous resistance and trim due to higher flow speeds at the stern.

- **Hull & Propulsion to Rudder Interaction:** In *Section 5.3,* the lift and drag curves of the rudders were presented and flow straightening effects assessed. Due to flow reversion caused by the fore and aft-body vortices, the inside rudder has negative flow straightening coefficients for $\beta_R > 10°$, and its inflow angle (α_0) has a quadratic relation with the geometric inflow angle (β_R). Due to these interaction effects, the inside rudder is prone to stall earlier than the outside one during manoeuvring. Furthermore, the outer rudder results in pure drift show some scatter. This was caused by the *AGR* settings. In future research a fine tuning of *AGR* is recommended for the study of interaction phenomena.

- **Rudder to Hull Interaction:** The magnitude of rudder to hull interaction force is about 6% of the total side force developed by the rudders, which represents about 1-2% of the sway force/moment developed by the hull in drift. Therefore, it is not a significant interaction effect. Furthermore, *Söding's* semi-empirical model (*Eq. 2.40*), predicts the magnitude of the interaction force relatively well, but not the interaction moment (or interaction abscissa).

- **Hull & Propulsion to Hull Vane Interaction:** The side force developed by the Hull Vane Struts is significantly affected by the fore and aft-body vortices from the hull. For β_s (struts' geometric inflow angle) greater than 10°, the Hull Vane struts even developed thrust in sway. Furthermore, the magnitude of the total side force/moment developed by the struts, represents about 1-2% of the magnitude of the force/moment developed by the hull in drift. Therefore, it was concluded that the main effect of the Hull Vane on the forces/moment due to sway, is caused by the change in dynamic trim of the vessel. However, it is expected that the forces/moments developed by the Hull Vane in pure-yaw motion, are more relevant than in pure sway. Since, the hull develops weaker vortices, reducing the flow reversion effect at the inner strut. A detailed assessment of the forces developed by the struts due to yaw, is left for future research, due to time constraints and limitations of the *CFD* software in performing rotating arm tests.

- **Rudder to Hull Vane Interaction:** In *Section 5.6* rudder to Hull Vane interaction was assessed and flow bending coefficients have been determined ($\Gamma_s^{\#}$), by combining numerical results with *Fujii's LAR LLT (*Low Aspect Ratio Lifting Line Theory, *Eq. 2.30)*. This showed that the maximum induced force on a strut occurs at about 15° of effective rudder angle (α_E). For higher effective rudder angles, the inflow angle induced on the strut is reduced due to stalling of the rudder.

6. PROPULSION AND APPENDAGE MATHEMATICAL MODELS

This chapter presents the propulsion and steering systems mathematical models, including the interaction effects assessed in the *Chapter 5*. Furthermore, a mathematical model for the Hull Vane is derived, completing the 3rd and last research objective.

6.1 PROPULSION SYSTEM

The *RPA8's* propulsion system is composed by two shaft lines with fixed pitch propellers. The thrust and *rpm of the* propellers is computed using their open water diagram and the method presented in *Section 2.5.* Since the *rpm* is assumed constant (see *Section 2.5*), this can lead to non-realistic thrust values, for instance when speed drops. To avoid this, a maximum power is imposed to the propeller, P_{max}. In case this limit is reached, the maximum thrust (T_{max}) is then computed by (see *Woud* and *Stapersma* in [28]):

$$T_{max} = \frac{P_{max}.\eta_o(J)}{V_A} \quad \text{Eq. 6.1}$$

The wake fractions and thrust deduction factors were determined in the previous section
Having said this, the forces and moments developed by *RPA8's* propulsion system are given by:

$$\begin{cases} X^P = (T^{PS} + T^{SB}).\cos(\theta^S) \\ N^P = y^P.(X^{P,PS} - X^{P,SB}) \end{cases} \quad \text{Eq. 6.2}$$

Note that θ^S represents the shaft angle and y^P the y-coordinate of the propeller. Pitch moments and heave forces are not considered in the context of this research, as previously explained.

6.2 STEERING SYSTEM

In *Chapter 5* the lift and drag of the rudders has been assessed and mathematically modelled, together with the interaction effects. Once the lift and drag of each rudder are computed, it is necessary to transform their forces to the vessel's frame of reference. This is done according to the formulation presented in *Section 2.6.3*. For the *RPA8* case, the total longitudinal and side forces of the steering system are given by:

$$\begin{cases} X^{R0,PS/SB,} = -D^{PS/SB}.\cos\left(\alpha_0^{PS/SB}\right) + L^{PS/SB}.\sin\left(\alpha_0^{PS/SB}\right) \\ Y^{R0,PS/SB} = D^{PS/SB}.\sin\left(\alpha_0^{PS/SB}\right) + L^{PS/SB}.\cos\left(\alpha_0^{PS/SB}\right) \\ X^{R0} = X^{PS,R0} + X^{SB,R0} \\ Y^{R0} = (Y^{PS,R0} + Y^{SB,R0}).\cos(\phi) \end{cases} \quad \text{Eq. 6.3}$$

Note that the previous forces only represent the direct effects of the rudders, where ϕ represents the roll angle. The following formulations represent the total forces and moments induced by the propulsion system on the vessel, *i.e.:* including rudder to hull interaction effects:

$$\begin{cases} X^R = X^{R0} \\ Y^R = Y^{R0}.(1 + a_H) \\ K^R = -\dfrac{z^R.Y^{R0}}{\cos(\phi)} \\ N^R = (x^R + a_H.x_{RH}).Y^{R0} + y^R.(X^{R,PS} - X^{R,SB}) \end{cases} \quad \text{Eq. 6.4}$$

Where (x^R, y^R, z^R), represent the rudder position.

6.3 HULL VANE MATHEMATICAL MODEL -A LINEAR PRESSURE DISTRIBUTION METHOD

As mentioned in *Section 1.3.3,* one of the objectives of this research is to develop a Hull Vane mathematical model and compare it with the integrated approach. The aim of the Hull Vane mathematical model is to allow a less expensive assessment of the impact of the Hull Vane on the manoeuvring performance. According to the results of *Chapter 4,* the Hull Vane:

- Increases the *Munk* moment
- Increases the yaw damping
- Affects the sway force due to yaw rate
- Affects the Roll Moment
- Increases the yaw added moment of inertia
- Affects the sway force due to yaw acceleration

This section will only focus on the three first effects, since these are the ones which mainly affect the course stability of the vessel, see *Section 2.8*.

As shown in *Chapters 4* and *5,* the Hull Vane increases the *Munk* moment by trimming the vessel bow down. Therefore, for the mathematical modeling of the effect of the Hull Vane on the *Munk* moment, the effect of the struts is neglected and only the effect of trim and sinkage is considered. The yaw damping and sway force due to yaw rate are more dependent on the presence of the struts, since these ones are less subjected to hull to Hull Vane interaction phenomena than in pure drift. Thus, to mathematically model the impact of the Hull Vane on yaw damping and sway force due to yaw rate, the effects of trim and sinkage are considered together with the Hull Vane struts. These ones are modeled using *Fujii's LAR LLT* (*Low Aspect Ratio Lifting Line Theory*, *Eq. 2.30*).

As previously mentioned, a variation of trim can significantly affect the manoeuvring performance of a vessel, see Figure 2.8. Often, full-scale trials of ships are only performed at one load condition. However, during operation, a vessel is subjected to multiple loading conditions. With the aim of mathematically modelling the effect of trim on the manoeuvring performance of vessels, *Inoue* et al. in [53], developed a semi-empirical method for merchant ships. Since *RPA8* is out of the applicability range of the method, this one gives poor results. Furthermore, this method is not able to account for changes in draft. Therefore, an alternative methodology is developed in this section, the *Linear Pressure Distribution Method*. This method is based on three fundamental assumptions:

- Trim and sinkage do not significantly change during manoeuvring, relative to straight-ahead condition. The numerical *OTTs* results confirm this assumption, where a variation of less than 0.1° for trim and 0.02 m for sinkage are observed.
- The change in trim and sinkage is small enough to do not significantly affect the lateral pressure distribution on the Hull;
- The lateral pressure distribution can be linearized, as shown in the following picture:

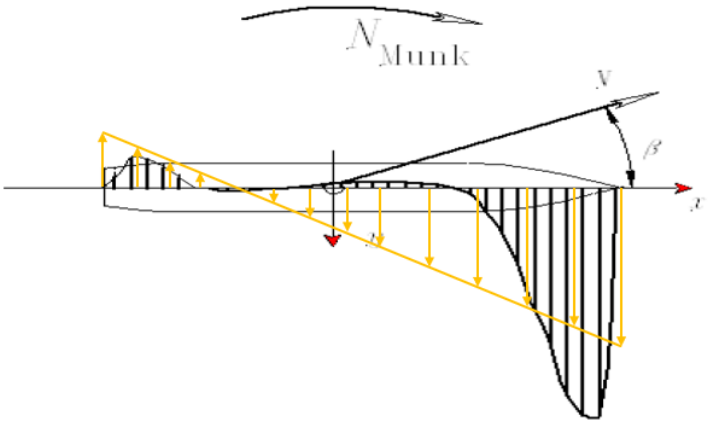

Figure 6.1: Linearization of the lateral pressure distribution (yellow load).

Since the sway forces and yaw moments are known for the bare hull, it is possible to determine the equation of the linearized lateral pressure distribution by solving the following system of equations, considering the underwater projected lateral area:

$$\begin{cases} p(x) = a.x + b \\ F_y = \int_a^b \int_0^{h(x)} p(x)\, dz\, dx \\ M_z = \int_a^b \int_0^{h(x)} p(x).x\, dz\, dx \end{cases} \qquad \textit{Eq. 6.5}$$

Once the linearized pressure distribution equation is known, this one is used for the computation of the forces and moments acting on the hull with a new load condition, by using the new underwater lateral area.

The complex underwater shape of the hull makes difficult the determination of the limits of integration in *Eq. 6.5*. Therefore, the initial lateral projected area (the one for which the forces and moments are known) is assumed to be a rectangle, with the same water line length, area and first moment of inertia of the underwater lateral projected area of the hull, as illustrated below:

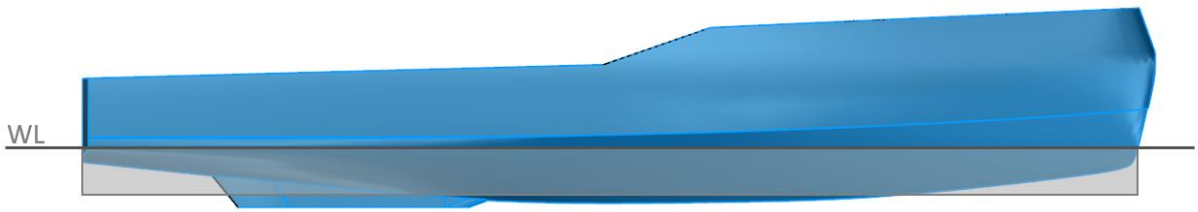

Figure 6.2: Uniform lateral area distribution in grey, for the original water line. Just a representative illustration.

The new underwater area (new load case), is assumed to be a trapezoid, in order to accommodate the change in first moment of inertia caused by trim, as illustrated below:

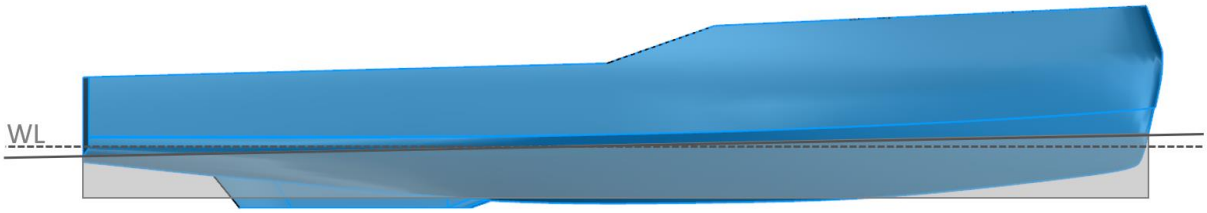

Figure 6.3: Linear lateral area distribution in grey, trimmed by the bow. Just a representative illustration.

Note that the height and slope of the trapezoid's upper edge is computed to match the first moment of inertia, area and water line length of the new underwater projected lateral area.

The following plots compare the *CFD* results with and without Hull Vane, with the results of this method:

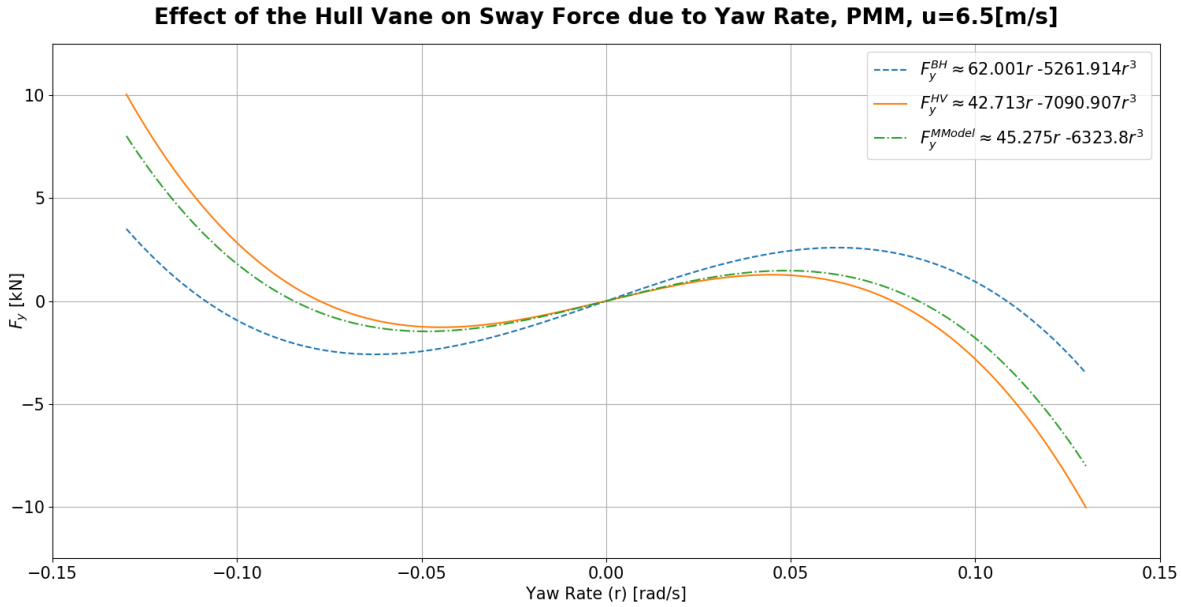

Figure 6.4: Comparison of the *CFD* results with the Hull Vane mathematical model, for the sway force due to yaw rate.

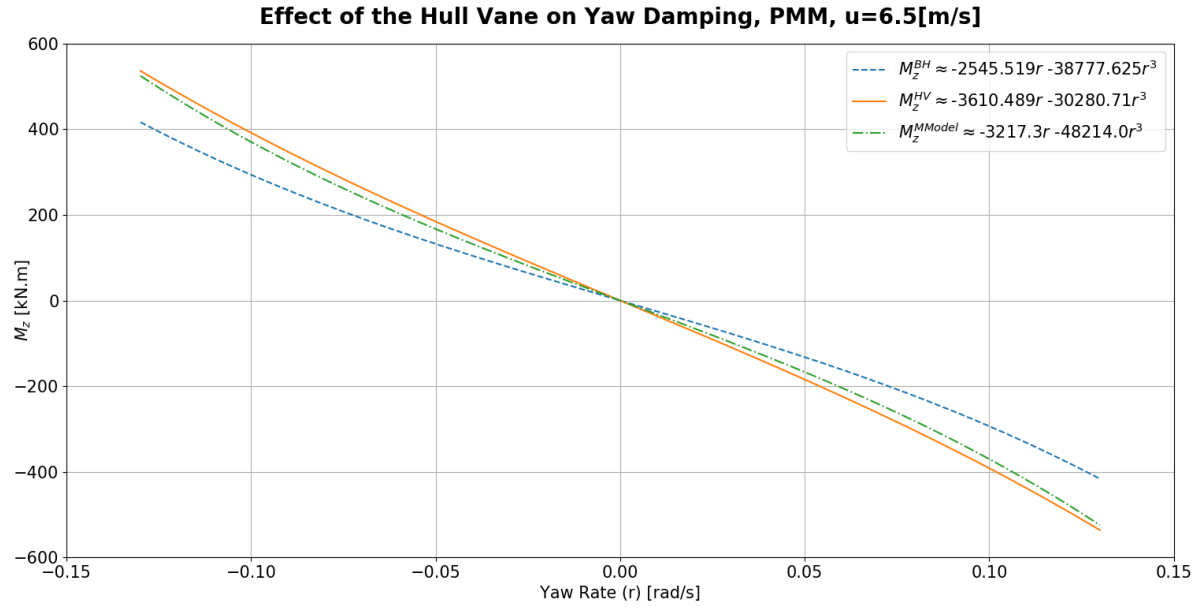

Figure 6.5: Comparison of the *CFD r*esults with the Hull Vane mathematical model, for the yaw damping.

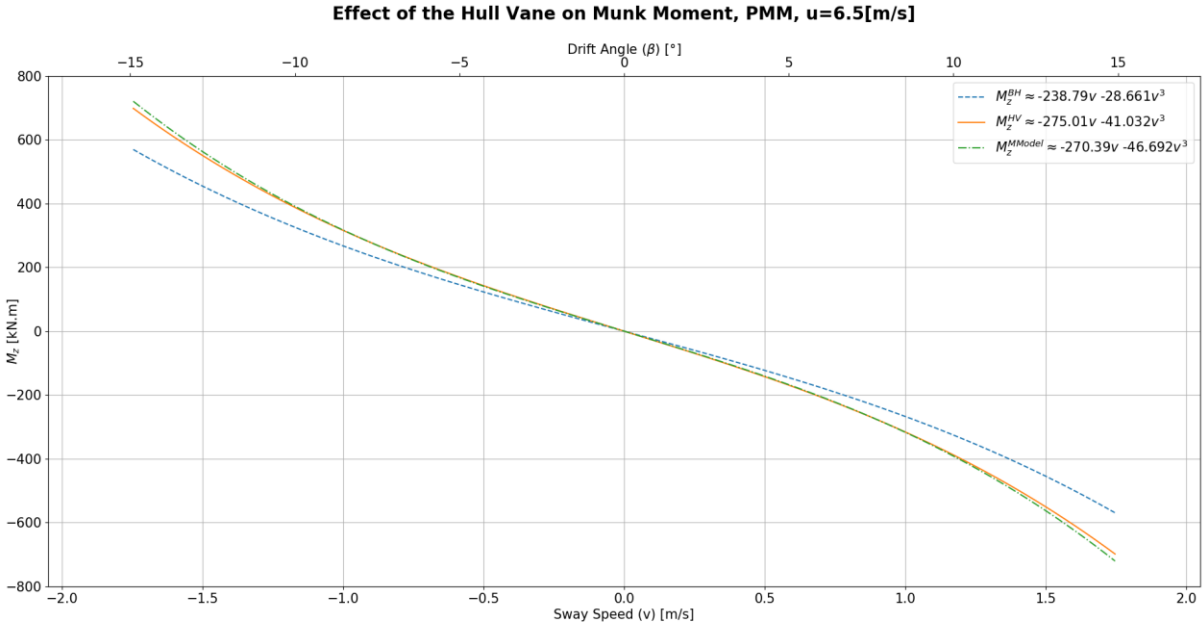

Figure 6.6: Comparison of the *CFD* results with the Hull Vane mathematical model, for the *Munk* moment.

According to the previous plots, the method presented here, predicts the effect of the Hull Vane on the forces/ moments acting on the vessel relatively well. The sway force due to yaw rate has a higher discrepancy with the numerical results. This is mainly caused by the non-linear behaviour of the pressure distribution and the modelling errors of the Hull Vane struts, for instance: free surface effects and hull to struts interaction. Improvements to this model are left for further research, where eventually a semi-empirical model can be developed for the forces acting on the Hull Vane. At this point, it is expected, that this mathematical model is useful for preliminary studies of the impact of the Hull Vane on manoeuvring. Later in *Section 8.3.4,* the manoeuvring performance using the Hull Vane model is compared to the performance using the integrated approach.

Furthermore, with the *Linear Pressure Distribution Method,* it is possible to obtain good results for *RPA8,* which is a vessel with a strong non-uniform area distribution. Due to the purely physical nature of this model, the it can be applied to a broad range of vessels' types, avoiding the need of semi-empirical formulations. Further development and validation of this method is left for future research, where can be studied: the effect of different types of underwater area distributions, prediction of roll moments, added masses and moments of inertia.

Furthermore, the hydrodynamic derivatives computed in *Chapter 4* do not include rudder to strut interaction effects. Therefore, it is necessary to include these effects on the mathematical model when considering the Hull Vane, independently on the approach to model the Hull Vane (modular or integrated). The mathematical description of this is given by:

$$\begin{cases} \alpha_{0,PS/SB}^{R,strut} \times 10^3 = 285.29 - 1088.8\,\alpha_{E,PS/SB} + 53.646\,\alpha_{E,PS/SB}^2 + 0.695\,\alpha_{E,PS/SB}^3 \\ C_{L,PS/SB}^{strut} = \dfrac{6.13\,AR\sin\left(\alpha_{0,PS/SB}^{R,strut}\right)}{2.25 + AR} \\ Y^{HV} = \left(C_{L,PS}^{strut} + C_{L,SB}^{strut}\right).\dfrac{1}{2}.\rho.(u^2 + v_{strut}^2).S^{strut} \\ N^{HV} = x^{HV}.Y^{HV} \\ K^{HV} = -z^{HV}.Y^{HV} \end{cases} \qquad \textit{Eq. 6.6}$$

The first equation corresponds the regression of Figure 5.15 and the second equation to *Fujii's LAR LLT, Eq. 2.30*.

6.4 CONCLUSIONS

In this section the final formulations for the forces and moments developed by the propulsion and steering systems are presented. Furthermore, the effect of the Hull Vane on the *Munk* moment, yaw damping and sway force due to yaw rate were modelled. Showing a good correlation with numerical results, which indicates that the assumptions made are valid. This method is expected to be useful for preliminary studies of the impact of the Hull Vane on manoeuvring. The effects of the Hull Vane on roll moment, yaw added moment of inertia and sway force due to yaw acceleration were not modelled, since these ones are not expected to significantly affect the course stability of the vessel. The validity of these assumptions is assessed in *Section 8.3.4.*

From the results obtained for *RPA8*, the *Linear Pressure Distribution Method* is expected to be robust and reliable. The physical nature of this method allows it to be applied to a broad range of vessels' types. The author strongly recommends further research, extension and validation of it.

7. MANOEUVRING MODEL OVERVIEW

For the purpose of this research, a mathematical model has been developed to study the manoeuvring behaviour of foil-assisted vessels. The focus of this section is to describe the global working principle and implementation of the mathematical model.

There is no limit for the complexity of a mathematical model. Therefore, it is important to define an applicability range and to make some assumptions. For the purpose of this research, the main assumptions and requirements of the model are:

- The vessel is assumed to be a rigid body;
- Canonic environment is considered (i.e. deep and calm water, still air, and steering by means of rudders);
- Aerodynamic forces/moments are considered negligible;
- The model should be able to simulate moderate speed manoeuvring of twin-screw vessels with two rudders, except wringing (one propeller producing positive thrust and the other negative);
- Constant propeller rpm during the manoeuvre, see *Section 2.5*;
- The model should solve the vessel's motion for surge, sway, yaw and roll. As mentioned in *Chapter 3* only one way coupling is considered for roll, *i.e.:* the roll does not affect other motions.

As mentioned in *Chapter 4,* the non-dimensionalization of the equations of motion is convenient, since it allows a more direct comparison between different hydrodynamic coefficients and physical phenomena. The equations of equations are made non-dimensional with the dynamic pressure. Therefore, the force equations are divided by $\frac{1}{2}\rho V^2 L^2$ and the moment equations by $\frac{1}{2}\rho V^2 L^3$, see *Lewis* in [14]. The non-dimensional values in this report assume $V = 6.5\ [m/s]$ (design speed) and $L = L_{pp} = 25\ [m]$. Furthermore, time also needs to be made non-dimensional using the reference speed (V) and length (L).

7.1 MOTIONS AND FORCES

In *Chapter 2,* the frames of reference were introduced together with the *Euler* equations of motion. Furthermore, in *Chapters 4, 5* and *6* hull, interaction effects and appendages were mathematically modelled. The purpose of this section is to combine all this in a mathematical model, able to solve the equations of motion and simulate the *RPA8* in free running manoeuvres.

Assuming $4DOF$ (surge, sway, yaw and roll), the *Euler* equations in a frame of reference located at the CoG are:

$$\Delta . (\dot{u} - v.r) = X \qquad \textit{Eq. 7.1}$$

$$\Delta . (\dot{v} + u.r\,) = Y \qquad \textit{Eq. 7.2}$$

$$I_{zz}.\dot{r} = N \qquad \textit{Eq. 7.3}$$

$$I_{xx}.\dot{p} = K \qquad \textit{Eq. 7.4}$$

7.1.1 SURGE MOTION

The total surge force acting on the system is assumed to be composed by a hull component (X^H), propulsion component (X^P) and steering system component (X^R):

$$X = X^H + X^P + X^R \qquad \textit{Eq. 7.5}$$

The computation of propulsive force (X^P, *Eq. 6.2*) and steering force (X^R, *Eq. 6.4*) is described in *Chapter 6.* Considering the results of the virtual captive tests, in *Chapter 4*, the hull surge force equation is given by:

$$X^H \approx X^H_u + X^H_{uu} + X^H_{\dot{u}}.\dot{u} + X^H_{|v|}.|v| + X^H_{vv}.v^2 + X^H_{\dot{v}\dot{v}}.\dot{v}^2 + X^H_{rr}.r^2 + X^H_{\dot{r}\dot{r}}.\dot{r}^2 \qquad \textit{Eq. 7.6}$$

By combining *Eq. 7.1*, *Eq. 7.5* and *Eq. 7.6* the equation for surge motion becomes:

$$\Delta.(\dot{u} - v.r) = X^H_u + X^H_{uu} + X^H_{\dot{u}}.\dot{u} + X^H_{vv}.v^2 + X^H_{\dot{v}\dot{v}}.\dot{v}^2 + X^H_{rr}.r^2 + X^H_{\dot{r}\dot{r}}.\dot{r}^2 + X^P + \mathrm{X^R} \qquad \textit{Eq. 7.7}$$

The previous equation represents a 1st order, non-linear, homogeneous *ODE.* For sake of clarity, the equation is rearranged:

$$\boldsymbol{(\Delta - X^H_{\dot{u}}).\dot{u} - \Delta.v.r - X^H_u - X^H_{uu} - X^H_{vv}.v^2 - X^H_{\dot{v}\dot{v}}.\dot{v}^2 - X^H_{rr}.r^2 - X^H_{\dot{r}\dot{r}}.\dot{r}^2 = X^P + X^R} \qquad \textit{Eq. 7.8}$$

The left-hand side of the equation contains the main characteristics of the vessel while the right hand side represents the 'external' forces (propulsion and steering system).
The added mass in surge is often neglected for manoeuvring of non-planing vessels, since small accelerations are expected. Therefore, the added mass is assumed to be constant (see *Fossen* in [13]) and is determined according to the results of *Tristan et al.* in [77], where the manoeuvrability of a patrol vessel is assessed and the following relation found:

$$X^H_{\dot{u}} \approx -0.05\Delta = -2.946\ [ton] \approx -3.7 \times 10^{-4}[-] \qquad \textit{Eq. 7.9}$$

Note that the previous result is made non-dimensional according to the definition presented in the beginning of this chapter. In *Chapter 8* the validity of the use of this coefficient in this research is assessed

7.1.2 SWAY MOTION

Since *RPA8's* propulsion system is symmetric and this research is focused on moderate speed manoeuvring, it is assumed that this one does not develop side forces. Therefore, the total sway force acting on the system is given by:

$$Y = Y^H + Y^R + Y^{HV} \qquad \textit{Eq. 7.10}$$

The computation of the steering force (Y^R, *Eq. 6.4*) and Hull Vane force (Y^{HV}, *Eq. 6.6*) is described in *Chapter 6.* Note that Y^{HV} only represents the interaction force of the rudders with the Hull Vane. The remaining effects of the Hull Vane are included in the hull hydrodynamic coefficients, as explained in *Section 6.3.* Considering the results of the virtual captive tests in *Chapter 4*, the hull sway force equation is given by:

$$Y^H \approx Y^H_v.v + Y^H_{\dot{v}}.\dot{v} + Y^H_{vvv}.v^3 + Y^H_r.r + Y^H_{\dot{r}}.\dot{r} + Y^H_{rrr}.r^3 + Y^H_{\dot{r}\dot{r}\dot{r}}.\dot{r}^3 \qquad \textit{Eq. 7.11}$$

By combining and rearranging *Eq. 7.2*, *Eq. 7.10* and *Eq. 7.11*, the sway motion equation becomes:

$$\boldsymbol{(\Delta - Y^H_{\dot{v}}).\dot{v} - Y^H_v v + (\Delta.u - Y^H_r).r - Y^H_{vvv}.v^3 - Y^H_{\dot{r}}.\dot{r} - Y^H_{rrr}.r^3 - Y^H_{\dot{r}\dot{r}\dot{r}}.\dot{r}^3 = Y^R + Y^{HV}} \qquad \textit{Eq. 7.12}$$

7.1.3 YAW MOTION

The yaw moment acting on the vessel is composed by hull, propulsion, steering and Hull Vane components:

$$N = N^H + N^P + N^R + N^{HV} \qquad \textit{Eq. 7.13}$$

The propulsion, steering and Hull Vane yaw moments are described in *Eq. 6.2*, *Eq. 6.4* and *Eq. 6.6*, respectively. Considering the results of the virtual captive tests in *Chapter 4*, the hull yaw moment equation is given by:

$$N^H \approx N^H_{\dot{r}}.\dot{r} + N^H_r.r + N^H_{rrr}.r^3 + N^H_v.v + N^H_{\dot{v}}.\dot{v} + N^H_{vvv}.v^3 + N^H_{\dot{v}\dot{v}\dot{v}}.\dot{v}^3 \qquad \textit{Eq. 7.14}$$

By combining and rearranging *Eq. 7.3*, *Eq. 7.13* and *Eq. 7.14*, the yaw motion equation becomes:

$$(\boldsymbol{I_{zz}} - \boldsymbol{N^H_{\dot{r}}}).\dot{\boldsymbol{r}} - \boldsymbol{N^H_r}.\boldsymbol{r} - \boldsymbol{N^H_{rrr}}.\boldsymbol{r^3} - \boldsymbol{N^H_v}.\boldsymbol{v} - \boldsymbol{N^H_{\dot{v}}}.\dot{\boldsymbol{v}} - \boldsymbol{N^H_{vvv}}.\boldsymbol{v^3} - \boldsymbol{N^H_{\dot{v}\dot{v}\dot{v}}}.\dot{\boldsymbol{v}}^3 - \boldsymbol{N^H_{vr}}.\boldsymbol{vr} = \boldsymbol{N^P} + \boldsymbol{N^R} + \boldsymbol{N^{HV}} \qquad \textit{Eq. 7.15}$$

7.1.4 ROLL MOTION

As previously mentioned, this research is mainly focused on the effects of the Hull Vane on the course stability of vessels. Since canonical conditions are considered, the metacentric height is assumed to be large enough to neglect the influence of roll on other motions, see *Sutulo* in [8]. Thus, the roll motion is only included for preliminary assessments. In contrast to surge, sway and yaw motions, the roll moment developed by the hull is composed by the hydrostatic (HS) and hydrodynamic (HD) components:

$$\begin{cases} K = K^H + K^R + K^{HV} \\ K^H = K^{HD} + K^{HS} \end{cases} \qquad \textit{Eq. 7.16}$$

The hydrostatic component is assumed to be independent from hydrodynamic effects.
The computation of the steering and Hull Vane roll moments are described in *Eq. 6.4* and *Eq. 6.6*, respectively. Considering the results of the virtual captive tests in *Chapter 4*, the hull roll moment equation is given by:

$$K^{HD} \approx K^{HD}_{\dot{p}}.\dot{p} + K^{HD}_p.p + K^{HD}_v.v + K^{HD}_{\dot{v}}.\dot{v} + K^{HD}_{vvv}.v^3 + K^{HD}_{\dot{v}\dot{v}\dot{v}}.\dot{v}^3 + K^{HD}_{vvvvv}.v^5 \qquad \textit{Eq. 7.17}$$

Assuming small heel angles ($\phi < 7°$), the roll moment acting on the hull due to hydrostatic forces (K^{HS}, usually referred as righting moment) can be determined using metacentric theory, see *Barrass* and *Derrett* in [76]:

$$K^{HS} = -\Delta.g.\overline{GM_t}.sin(\phi) \qquad \textit{Eq. 7.18}$$

By combining and rearranging *Eq. 7.4*, *Eq. 7.16*, *Eq. 7.17* and *Eq. 7.18*, the roll motion equation becomes:

$$(\boldsymbol{I_{xx}} - \boldsymbol{K^{HD}_{\dot{p}}}).\dot{\boldsymbol{p}} - \boldsymbol{K^{HD}_p}.\boldsymbol{p} - \boldsymbol{K^{HD}_v}.\boldsymbol{v} - \boldsymbol{K^{HD}_{\dot{v}}}.\dot{\boldsymbol{v}} - \boldsymbol{K^{HD}_{vvv}}.\boldsymbol{v^3} - \boldsymbol{K^{HD}_{\dot{v}\dot{v}\dot{v}}}.\dot{\boldsymbol{v}}^3 - \boldsymbol{K^{HD}_{vvvvv}}.\boldsymbol{v^5} + \boldsymbol{\Delta.g.\overline{GM_t}.sin(\phi)} = \boldsymbol{K^R} + \boldsymbol{K^{HV}} \qquad \textit{Eq. 7.19}$$

The roll added moment of inertia ($K^{HD}_{\dot{p}}$) and damping (K^{HD}_p) are estimated based on the results of *Tristan et al.* in [77] for a patrol vessel:

$$K^{HD}_{\dot{p}} \approx -0.2I_{xx} = -19.8\,[ton.m^2] \approx -4 \times 10^{-6} \qquad \textit{Eq. 7.20}$$

$$K^{HD}_p \approx -3.8 \times 10^{-4}[-] \qquad \textit{Eq. 7.21}$$

The previous results are mede non-dimensinaliz according to the definition presented in the beginning of this chapter.

7.2 SOLUTION METHOD

In *section 7.1* the equations of motion for the *RPA8* case were defined. In this section the solution method for this system of coupled $ODE's$ is going to be described. The system of equations is composed by *Eq. 7.*8, *Eq. 7.*12, *Eq. 7.*15 and *Eq. 7.*19, and can be represented in the matricial form as:

$$[m].\{\vec{a}\} + [b].\{\vec{u}\} + [k].\{\vec{x}\} = \{\vec{F}\} \qquad \textit{Eq. 7.22}$$

This system of equations represents a forced mass-damper-spring system. Where $[M].\{\vec{a}\}$, $[B].\{u\}$ and $[K].\{x\}$ represent the inertial, damping and spring terms, respectively. $\{\vec{\mathrm{F}}\}$ represents the external force vector.

- The inertial term is the multiplication of the mass matrix $[m]$, times the acceleration vector $\{\vec{a}\}$:

$$[m].\{\vec{a}\} = \begin{bmatrix} \Delta - X_{\dot{u}}^H & -X_{\dot{v}\dot{v}}^H.\dot{v} & -X_{\dot{r}\dot{r}}^H.\dot{r} & 0 \\ 0 & \Delta - Y_{\dot{v}}^H & -Y_{\dot{r}}^H - Y_{\dot{r}\dot{r}\dot{r}}^H.\dot{r}^2 & 0 \\ 0 & -N_{\dot{v}}^H - N_{\dot{v}\dot{v}\dot{v}}^H.\dot{v}^2 & \mathrm{I_{zz}} - N_{\dot{r}}^H & 0 \\ 0 & -K_{\dot{v}}^H - K_{\dot{v}\dot{v}\dot{v}}^H.\dot{v}^2 & 0 & \mathrm{I_{xx}} - K_{\dot{p}}^H \end{bmatrix}.\begin{Bmatrix} \dot{u} \\ \dot{v} \\ \dot{r} \\ \dot{p} \end{Bmatrix} \qquad \textit{Eq. 7.23}$$

- The damping term is given by the multiplication of the damping matrix $[b]$, by the velocity vector $\{\vec{u}\}$:

$$[b].\{\vec{u}\} = \begin{bmatrix} -X_u^H - X_{uu}^H.u & -X_{vv}^H.v - \Delta.r & -X_{rr}^H.r & 0 \\ \Delta.r & -Y_v^H - Y_{vvv}^H.v^2 & -Y_r^H - Y_{rrr}^H.r^2 & 0 \\ 0 & -N_v^H - N_{vvv}^H.v^2 & -N_r^H - N_{rrr}^H.r^2 & 0 \\ 0 & -K_v^H - K_{vvv}^H.v^2 - K_{vvvvv}^H.v^4 & 0 & -K_p^H \end{bmatrix}.\begin{Bmatrix} u \\ v \\ r \\ p \end{Bmatrix} \qquad \textit{Eq. 7.24}$$

- The spring term is given by the multiplication of the spring matrix $[k]$, by the position vector $\{\vec{\mathrm{x}}\}$:

$$[k].\{\vec{x}\} = \begin{bmatrix} 0 & 0 & 0 & 0 \\ 0 & 0 & 0 & 0 \\ 0 & 0 & 0 & 0 \\ 0 & 0 & 0 & \dfrac{\Delta.g.\overline{GM_t}.sin(\phi)}{\phi} \end{bmatrix}.\begin{Bmatrix} x \\ y \\ \psi \\ \phi \end{Bmatrix} \qquad \textit{Eq. 7.25}$$

- Last, but not least, the excitation vector $\{\vec{\mathrm{F}}\}$ is given by:

$$\{\vec{F}\} = \begin{Bmatrix} X^E \\ Y^E \\ N^E \\ K^E \end{Bmatrix} = \begin{Bmatrix} X_{|v|}^H.|v| + X^P + X^R \\ Y^R + Y^{HV} \\ N^P + N^R + N^{HV} \\ K^R + K^{HV} \end{Bmatrix} \qquad \textit{Eq. 7.26}$$

The mass, damping and spring matrices describe and characterize the system (the hull in this case). While the excitation vector describes the forces and moments applied to the system.

At this point it is possible to see that *Eq. 7.*22 represents a time-dependent system of *ODE's*. Therefore, a time marching algorithm is required to solve it. For this the following mathematical model is implemented in *Python 3.6*, its general structure is the following:

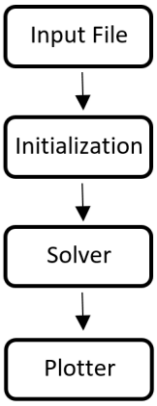

Figure 7.1: Structure of the manoeuvring model.

The **Input File** contains technical data about the manoeuvre, the vessel (*e.g.:* hull, propulsion system and appendages) and plotting options.

The **Initialization** module defines the initial conditions and initializes all the necessary variables, matrices and arrays for the solver.

The **Solver** module solves the equations of motion, using a time-marching algorithm, and stores the results. The equations of motion are solved using the *odeint* command from the *scipy* library of *Python,* which is based on the method proposed by *Hindmarsh* in [78]. The following scheme illustrates the general structure of time marching algorithm (*i.e.:* the solver block):

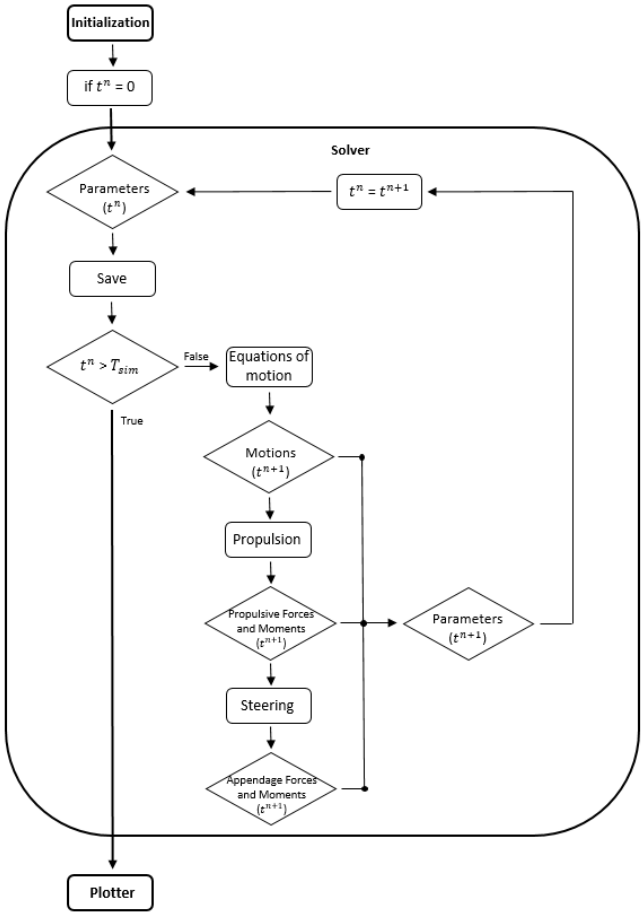

Figure 7.2: Structure of the Solver.

The **Plotter** module, plots the trajectory of the vessel, velocities, accelerations and forces acting on the vessel (hull, propulsion and steering). Also gives some additional information such as the turning circle diameter (if applicable), the maxium overshoot (if applicable), the maximum heel, drift angle, rudder position and effective rudder angles, among others, as can be seen in the following example:

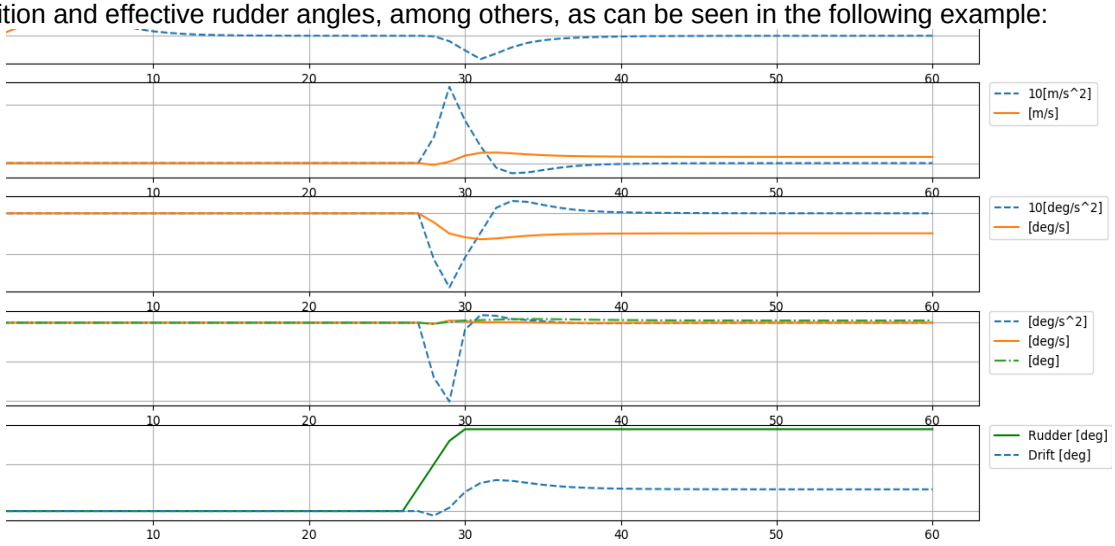

Figure 7.3: Plot of accelerations, speeds, rudder angle and drift angle.

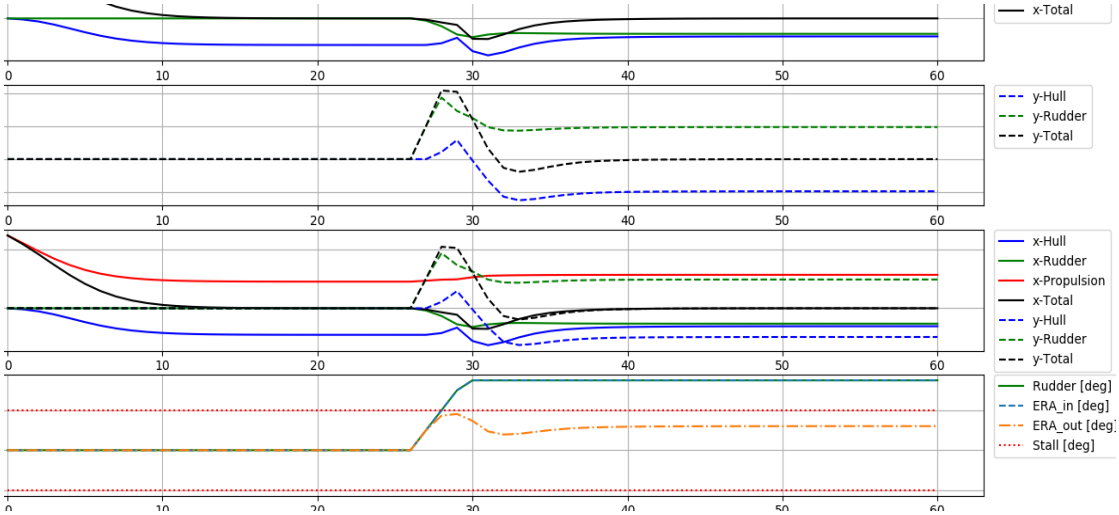

Figure 7.4: Plot of forces, rudder angle, stall angles and effective rudder angles.

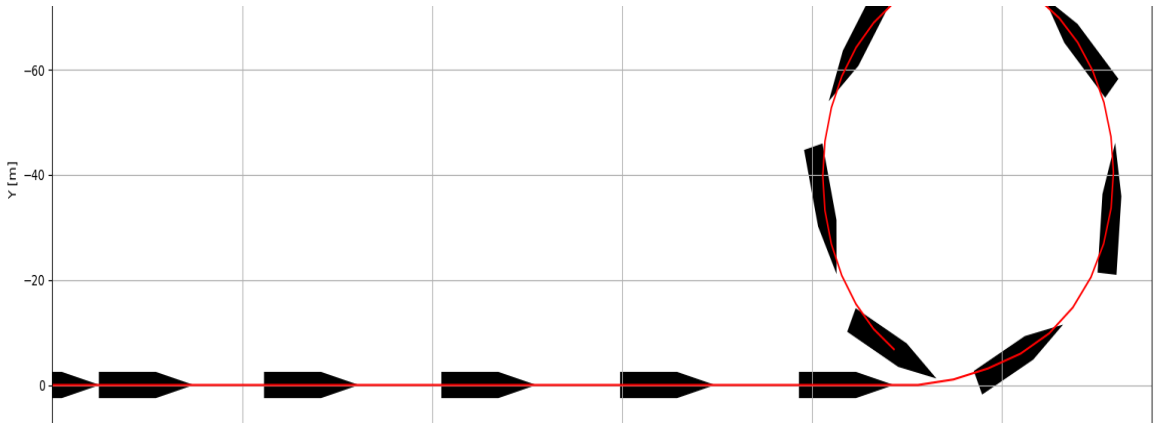

Figure 7.5: Plot of the trajectory (bird view), display of the turning circle diameter and maximum heel.

8. MANOEUVRING PREDICTION ANALYSIS

The aim of this chapter is to analyse the results of the manoeuvring prediction process developed during this research. First, the manoeuvring model is verified. Then, in *Section 8.2,* a sensitivity analysis is performed together with an assessment of the effects of *CFD* uncertainties on manoeuvring predictions. After this, the *Discrete Spectral Method*, the manoeuvring prediction process and the Hull Vane mathematical model are validated. The validation of the manoeuvring prediction process is preformed using experimental data from model and full-scale experiments. The validation of the Hull Vane mathematical model completes the 3rd research objective (see *Section 1.3.3).* In the end of this chapter, the effect of the Hull Vane on the manoeuvring performance of *RPA8* is assessed.

8.1 MANOEUVRING MODEL VERIFICATION

As previously mentioned, the verification process is a purely mathematical exercise that assesses whether a mathematical model is being properly solved, *see Roache* in [45]. To verify the the manoeuvring model, a test case with an analytical solution is used. Since the system of differential equations presented in *Section 7.2* is too complex to determine an analytical solution, this one has been simplified. Therefore, the following equivalent system is considered:

$$\begin{bmatrix} \Delta & 0 & 0 & 0 \\ 0 & \Delta & 0 & 0 \\ 0 & 0 & I_{zz} & 0 \\ 0 & 0 & 0 & I_{xx} \end{bmatrix} \cdot \begin{Bmatrix} \dot{u} \\ \dot{v} \\ \dot{r} \\ \dot{p} \end{Bmatrix} + \begin{bmatrix} -X_{uu}.|u| & -\Delta.r & 0 & 0 \\ 0 & -Y_v & 0 & 0 \\ 0 & -N_v & -N_r & 0 \\ 0 & -K_v & 0 & -K_p \end{bmatrix} \cdot \begin{Bmatrix} u \\ v \\ r \\ p \end{Bmatrix} + \begin{bmatrix} 0 & 0 & 0 & 0 \\ 0 & 0 & 0 & 0 \\ 0 & 0 & 0 & 0 \\ 0 & 0 & 0 & -K_\phi \end{bmatrix} \cdot \begin{Bmatrix} x \\ y \\ \psi \\ \phi \end{Bmatrix} = \begin{Bmatrix} 0 \\ F_y \\ 0 \\ 0 \end{Bmatrix} \quad \textit{Eq. 8.1}$$

Note that this system does not represent a vessel, it was designed just for verification purposes, *i.e.: "a purely mathematical exercise*" (*Roache*, [45]). This system assesses the performance of the solver in four main aspects:

- Capability of solving ordinary differential equations (*ODE*'s);
- Capability of dealing with couplings between equations;
- Capability of solving non-linear *ODE's.*
- Capability of solving forced mass-damper-spring systems

To assess the first capability, the sway motion equation was linearized and all the coupling terms from other motions disregarded. Furthermore, the external force (F_y) is defined as a step input. This describes a simple forced mass-damper system, which can be solved analytically in the *Laplace* domain:

$$\mathcal{L}(\Delta.\dot{v} - Y_v.v) = \mathcal{L}(F_y)$$

$$\Leftrightarrow \Delta.V(s).s - Y_v.V(s) = \frac{F_y}{s}$$

$$\Leftrightarrow V(s) = \frac{F_y}{s.(\Delta.s - Y_v)}$$

$$\Leftrightarrow \mathcal{L}^{-1}\big(V(s)\big) = \mathcal{L}^{-1}\left(\frac{F_y}{s.(\Delta.s - Y_v)}\right)$$

$$\Leftrightarrow v(t) = \frac{F_y}{-Y_v}.(1 - e^{\frac{Y_v}{m}.t}) \quad \textit{Eq. 8.2}$$

To evaluate the performance of the solver in solving systems of coupled differential equations, the *Munk* moment (N_v) is included in the yaw motion equation. Since this equation remains linear, it is possible to derive the following analytical solution also using *Laplace Transform:*

$$r(t) = \left(\frac{N_v . F_y}{m . I_{zz}}\right) . \left(\frac{I_{zz} . m}{N_r . Y_v} + \frac{I_{zz} . e^{\frac{N_r}{I_{zz}} . t}}{-N_r . \left(-\frac{N_r}{I_{zz}} + \frac{Y_v}{m}\right)} + \frac{m . e^{\frac{Y_v}{m} . t}}{-Y_v . \left(-\frac{Y_v}{m} + \frac{N_r}{I_{zz}}\right)} \right) \qquad \textit{Eq. 8.3}$$

In order to test capability of solving non-linear *ODE's,* the quadratic term of the surge resistance is included (*i.e.:* X_{uu}). Note that, for the purpose of this section, this term is multiplied by $|u|$ in *Eq. 8.*1,to allow a stable system even for negative advance speeds. Due to the non-linear nature of the equation for surge and the coupling with yaw, the derivation of an analytical expression becomes more challenging. Since the transient response is assessed with the equation of sway and yaw (for which analytical solutions are defined), for the case of surge, only the steady state solution is considered (u^{SS}). This one is given by:

$$u^{SS} = sign(\Delta . r . v) . \sqrt{\left|\frac{\Delta . r . v}{X_{uu}}\right|} \qquad \textit{Eq. 8.4}$$

Finally, to verify the capability of the solver to compute the solution of forced mass-damper-spring systems. The roll motion equation is included. For the sake of simplicity, the numerical solution is compared with the steady solution, similarly to what is performed for the advance speed. The steady solution is given by:

$$\phi^{SS} = -\frac{K_v . v}{K_{phi}} \qquad \textit{Eq. 8.5}$$

The following plot compares the analytical and steady solutions, previously derived, with the numerical solutions of the solver, considering $F_y = 20\ [kN]$ and a time-step $\Delta t = 1\ [s]$:

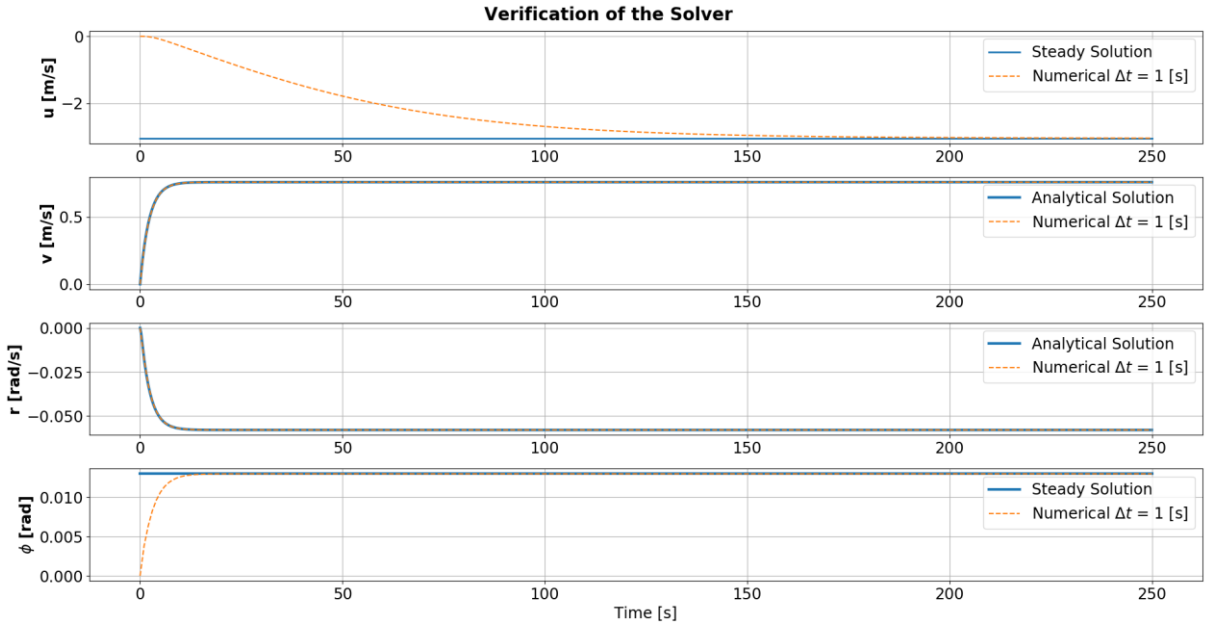

Figure 8.1: Comparison of the analytical solutions of the motions with the numerical ones from the solver. Considering a step input $F_y = 20\ [kN]$ and a time-step $\Delta t = 1\ [s]$.

The previous results show that the solution of the solver matches the analytical/steady solutions. Therefore, it is proved that the solver *"is solving the equations right" (Roache,* [45]*).* Note that these results must not be interpreted as a manoeuvre, but as a purely mathematical exercise for verification purposes, which justifies the negative advance speed (u).

8.2 SENSITIVITY STUDY

As explained in *Chapter 2,* the hydrodynamic forces and moments acting on the vessel are mathematically described using hydrodynamic coefficients. For the determination of these coefficients, specific manoeuvres were performed and the forces/moments acting on the vessel measured (*i.e.: Captive Tests, Chapter 4*). Since these are 'artificial' manoeuvres, just for the purpose of determining hydrodynamic coefficients, these ones are not representative of free running manoeuvres. Although the coefficients presented in *Chapter 4* are necessary for an adequate modeling of the forces/moments acting on the vessel during the Virtual *Captive Tests,* this does not mean that all of them (coefficients) are equally important in free running manoeuvring. A good understanding of which hydrodynamic coefficients are the most and least important ones in free running manoeuvring, allows for a better interpretation of the results and it is useful for further research. Therefore, in this section a sensitivity analysis is performed, this consists on a systematic variation of the hydrodynamic coefficients to determine their influence on the manoeuvres of interest (*i.e.:* turning circle and zig-zag tests). Furthermore, the effect of *CFD* uncertainties on the manoeuvring prediction results, is estimated using a similar method. The hydrodynamic coefficients used in the mathematical model can be found in *Appendix A.4.*

8.2.1 TURNING CIRCLE MANOEUVRE

This section aims to assess which are the most important hydrodynamic coefficients and which is the effect of *CFD* uncertainties on the manoeuvring prediction of turning circles. For this, the full scale trial turning circle manoeuvre is considered (*i.e.:* 35° rudder at 9.42 [m/s]).

First, each hydrodynamic coefficient is increased by 10%, at the time, and the influence on the turning circle characteristics is measured. The following plot shows the results:

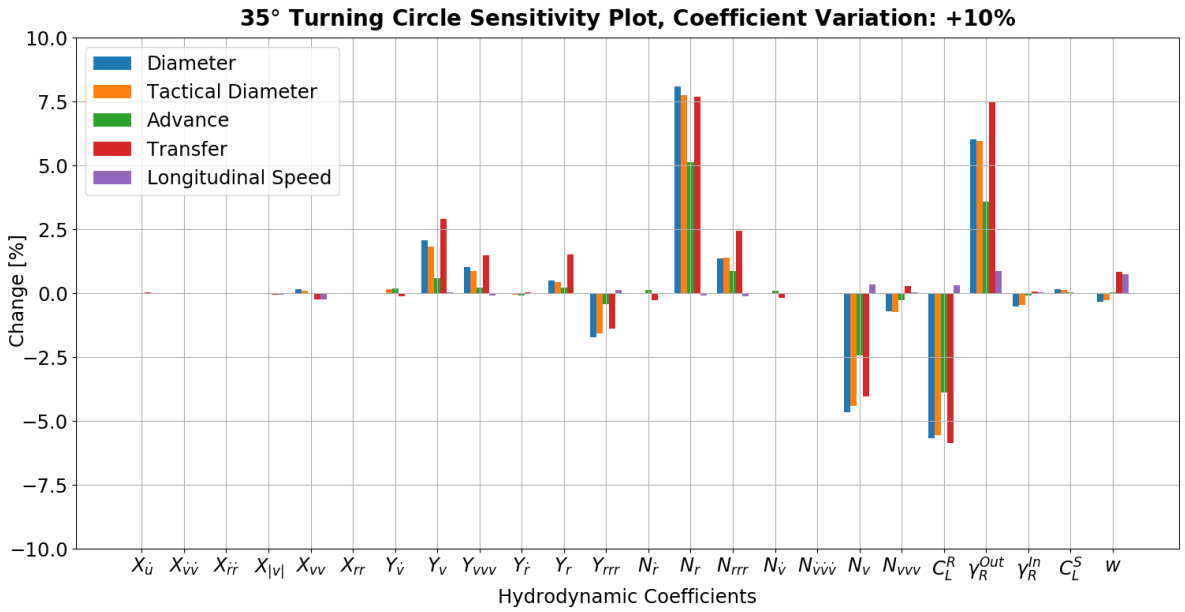

Figure 8.2: Sensitivity analysis, 35° turning circle at 9.42 [m/s]. Note that the longitudinal speed refers to the steady state longitudinal speed.

According to the previous results, it is possible to observe that the unsteady coefficients practically do not affect the turning circle properties. This is caused by the fact that the accelerations during this manoeuvre are not significant. In contrast to this, it is possible to observe that the yaw damping (N_r), *Munk* moment (N_v), rudders lift (C_L^R) and the outer rudder flow straightening coefficient (γ_R^{Out}) are particularly important. Note that the contrast in the effect of the inner and outer flow straightening coefficients is caused by the stalling of the inner rudder. Furthermore, it is possible to observe that the surge coefficients do not significantly affect the turning circle characteristics, which it is explained by the fact that the propulsion system damps (*i.e.:* partially compensates) changes in surge added resistance. A simple example is: if the longitudinal added resistance increases → decreases the longitudinal speed→ decreases the propellers' advance speed→decreases the advance ratio (since n_p is fixed) →increases the thrust factor (K_T) →increases longitudinal speed.

In *Chapter 4,* the uncertainties of the virtual captive tests were assessed. In order to estimate their influence on the manoeuvring prediction, the sway and yaw uncertainties were applied to the sway and yaw coefficients, respectively, with the aim of increasing the course stability (*i.e.:* stabilizing forces/moments were increased and vice-versa). The following figure shows the results:

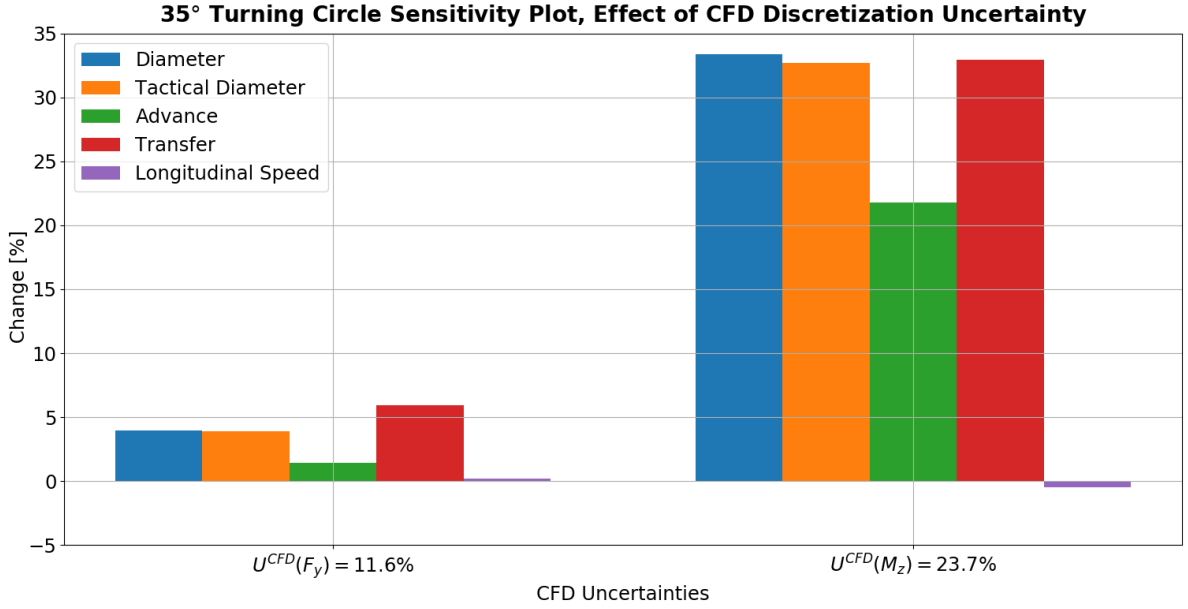

Figure 8.3: Effect of *CFD* discretization uncertainties on turning circle prediction. Note that the longitudinal speed refers to the steady state longitudinal speed.

As can be seen in the previous plot, the *CFD* discretization uncertainties of the *Virtual Captive Tests,* can have a significant influence on the manoeuvring prediction results. Especially the yaw moment uncertainty, since this one is greater than the sway force uncertainty and the yaw moments play the most important role on course stability (*see* Figure 8.2).

8.2.2 ZIG-ZAG MANOEUVRE

This section aims to assess which are the most relevant hydrodynamic coefficients and which is the effect of *CFD* uncertainties on the manoeuvring prediction of zig-zag manoeuvres. For this, the zig-zag manoeuvres performed at model scale are considered (*i.e.:* 3°-3° at 6.41 [m/s]).

To determine which are the most relevant coefficients for zig-zag manoeuvres, every hydrodynamic coefficient is increased by 10%, at the time, and the influence of these changes on the on the zig-zag characteristics are measured. The following plot shows the results:

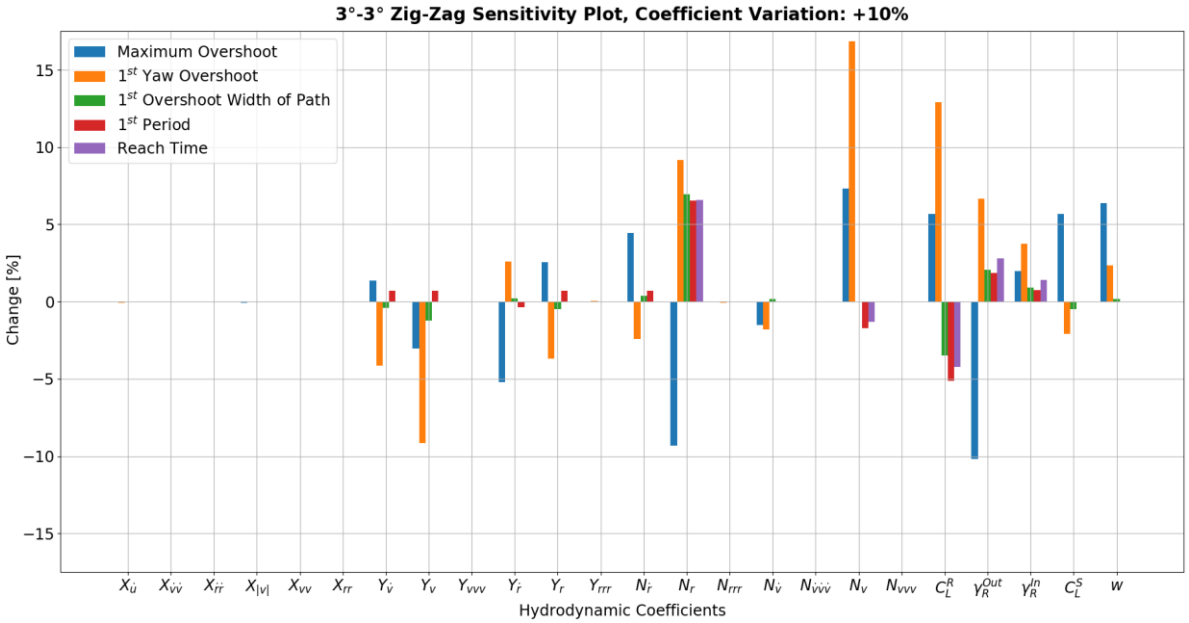

Figure 8.4: Sensitivity analysis, 3°-3° Zig-Zag at 6.41 [m/s].

In comparison to the turning circle results, unsteady phenomena play a more relevant role in zig-zag, since it is by definition an unsteady manoeuvre. While for the turning circle the most important coefficient corresponds to the yaw damping, for the zig-zag corresponds to the *Munk* moment (sway dependent). Also, the propeller wake fraction and the lift coefficient of the struts are more important for the zigzag manoeuvre. This last one is caused by the fact that the rudders do not stall, amplifying the interaction effect with the struts, see *Figure 5.15*. Furthermore, the non-linear coefficients are less important for the zig-zag manoeuvre than for the turning circle. This is caused by the fact that the drift angles and yaw rates are smaller in a zig-zag manoeuvre than in a turning circle. The variation of surge force coefficients practically does not affect the zig-zag motion, since small sway speeds and yaw rates are present, and as previously explained, the propulsion system also tends to damp changes in longitudinal resistance.

To assess the influence of the *CFD* discretization uncertainties on the zig-zag manoeuvre, the same procedure as for the turning circle is adopted, but with the aim of increasing the overshoot. The results can be found in the following plot:

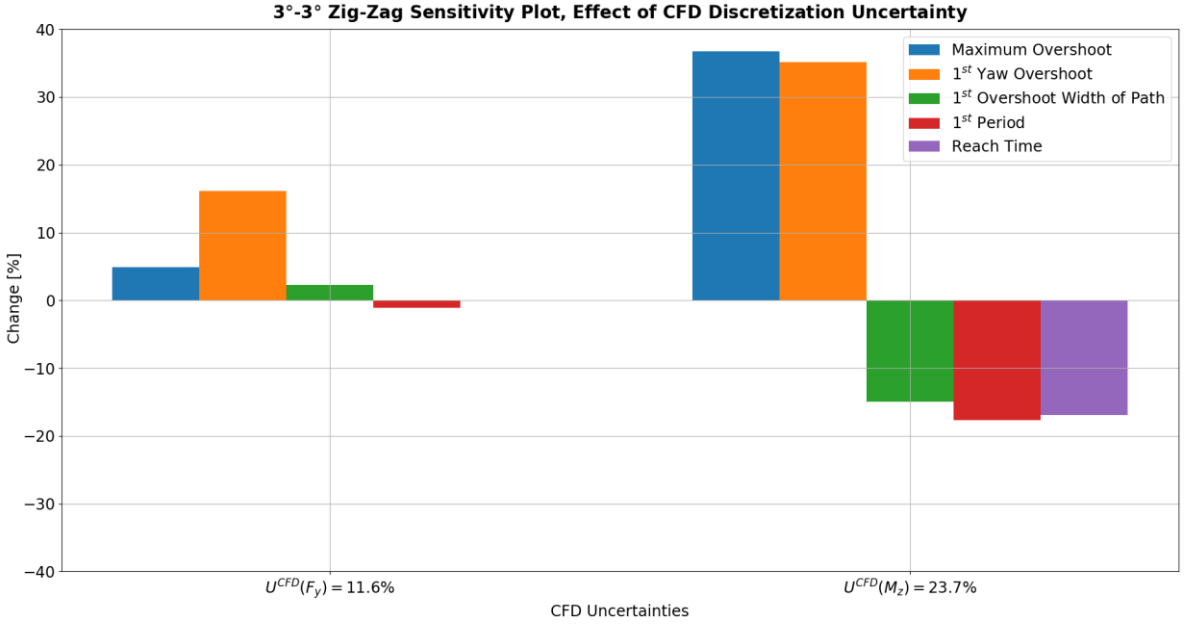

Figure 8.5: Effect of *CFD* discretization uncertainties on zig-zag prediction.

Similarly, to what was found for the turning circle, the zig-zag manoeuvre is mainly affected by yaw moments rather than sway forces. Since the yaw moments also have big uncertainties, this can lead to a strong influence of the *CFD* uncertainties on the characteristics of the zig-zag manoeuvre.

8.2.3 RESULTS DISCUSSION

According to the results presented in this chapter, the most important hydrodynamic coefficients are:

- Yaw damping (N_r);
- *Munk* moment (N_v);
- Rudders' lift coefficients (C_L^R);
- Flow straightening coefficient of the outside rudder (γ_R^{Out}).

Therefore, it is important that these hydrodynamic coefficients are well determined for an adequate manoeuvring prediction. The flow straightening coefficient of the outside rudder is especially important in comparison to the inside flow straightening coefficient, since the outside rudder is not subjected to stalling, as explained in *Section 5.3.* The sensitivity analysis also showed that a good estimation of the propeller wake fraction and struts lift coefficient is more important for the prediction of the zig-zag manoeuvre than the turning circle. Having said this, it is recommended to adopt *Toxopeus'* methodology for the determination of interaction coefficients, see *Section 5.3.*

Due to the unsteady nature of the zig-zag manoeuvre, unsteady forces/moments are more relevant than in the turning circle manoeuvre. However, due to small accelerations, their influence is rather limited. Therefore, the advantages of performing *PMM* tests for a good assessment of unsteady forces/moments is partially lost, since these effects are not significant. Instead semi-empirical models might be suitable for this purpose. Furthermore, the surge added resistance coefficients do not significantly affect the motions of the vessel, including the speed drop. This is caused by a damping of small variations in longitudinal (surge) resistance, caused by the propulsion system.

The manoeuvring prediction results can be significantly affected by *CFD* discretization uncertainties, especially in yaw moment. Therefore, more accurate manoeuvring predictions require to reduce the uncertainties of the *Virtual Captive Tests*. For this it is recommended to start by performing an adequate solution verification of the *AGR* setup and use rotating arm tests to derive rotational hydrodynamic derivatives instead of *PMM* tests. However, it is important to refer that the results of the impact of *CFD* uncertainties on the manoeuvring prediction, are considered conservative, since the regressions for the determination of hydrodynamic coefficients tend to "damp" numerical uncertainties, by imposing a more physical behavior on the *CFD* solutions. Furthermore, the uncertainties of the *AGR* setup are also considered conservative, as explained in *Section 4.1.*

8.3 VALIDATION

This section brings together the results of the research performed until this point. Here the *Discrete Spectral Method* is validated and the hydrodynamic coefficients previously obtained in *Chapters 4 and 5* are implemented in the manoeuvring model described in *Chapter 7.* With this, it is then possible to proceed to the validation of the manoeuvring prediction process. First, the results of the Hull Vane integrated approach are compared with experimental data. Then the Hull Vane mathematical model results are compared with the integrated approach. This assesses the validity of the assumptions made to model the Hull Vane effect on manoeuvrability, *Section 6.3*, completing the third and last research objective, see *Section 1.3.3*.

The uncertainties of the experimental data, used for validation purposes in this section, are unknown. The hydrodynamic coefficients considered in the mathematical model can be found in *Appendix A.4.*

First, the method to obtain mathematical models from the *PMM* tests using *Discrete Spectral Method* (*Section 4.3*), is verified by comparing the results (of the mathematical models) with the virtual *PMM* tests' results.

8.3.1 DISCRETE SPECTRAL METHOD

In *Section 4.3,* several mathematical models were derived to describe the forces and moments acting on the vessel during *PMM* tests. Using the *Discrete Spectral Method*, forces/moments were filtered and represented by simplified polynomial expressions, which aim to describe the main characteristics of the measured forces/moments. This section aims to validate the polynomial expression obtained according to the *Discrete Spectral Method* results. For the sake of simplicity, this section only presents the validation of the sway force due to yaw rate for the bare Hull, since this force presents a highly non-linear behavior. The validation of the remaining forces and moments can be found in *Appendix A.3.* According to *Section 4.5.2.1*, the sway force due to yaw rate is described by:

$$Y^{BH}(r) = -Y_{\dot{r}\dot{r}\dot{r}}\,\dot{r}^3 - Y_{\dot{r}}\,\dot{r} - Y_{rrr}.r^3 + Y_r.r \qquad \textit{Eq. 8.}6$$

The values of the hydrodynamic coefficients can be found in *Eq. 4.*39. The following plot compares the *CFD* results with the polynomial expression obtained using the *Discrete Spectral Method*:

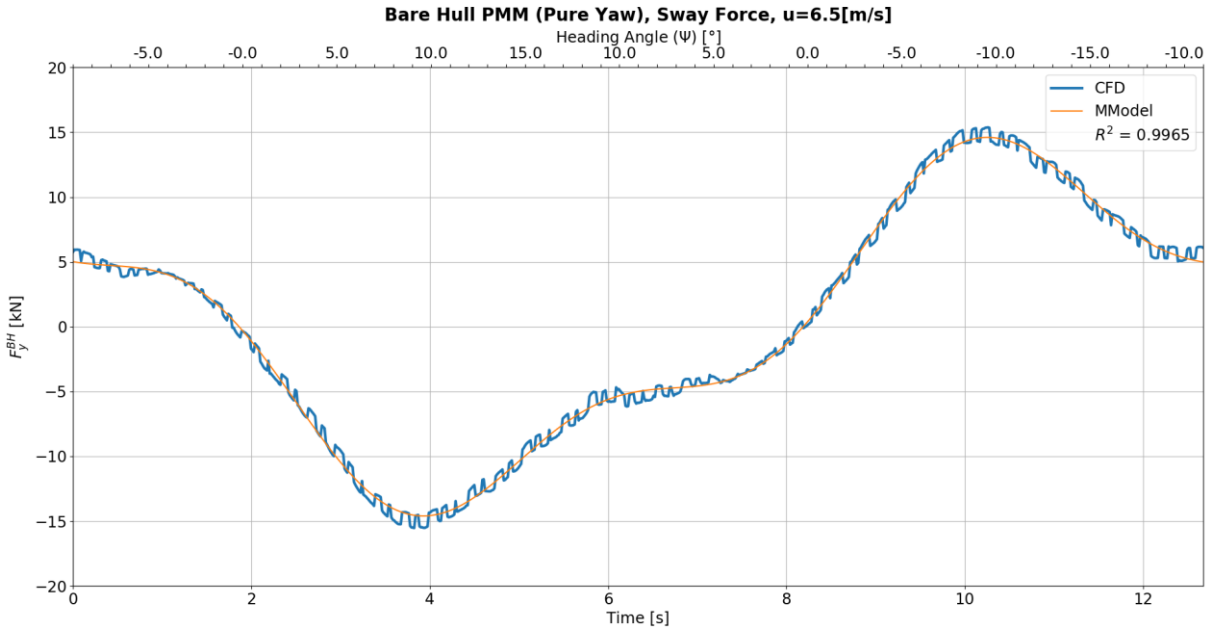

Figure 8.6: Sway force due to yaw motion: CFD vs Mathematical model.

This shows that the polynomial model obtained using the *Discrete Spectral Method* is valid, *i.e.:* solving the right equation, see *Roache* in [45]. The surge forces are not modelled as well as the remaining forces/moments, see *Appendix* A.3. However, according to the results of the sensitivity analysis, these modelling errors are not expected to have any relevant influence on the manoeuvring prediction results.

8.3.2 TURNING CIRCLE PREDICTION

In this section, the results of the manoeuvring prediction process, are compared with the full-scale 35° turning circle manoeuvre. The following figure, compares the full-scale result with the manoeuvring prediction:

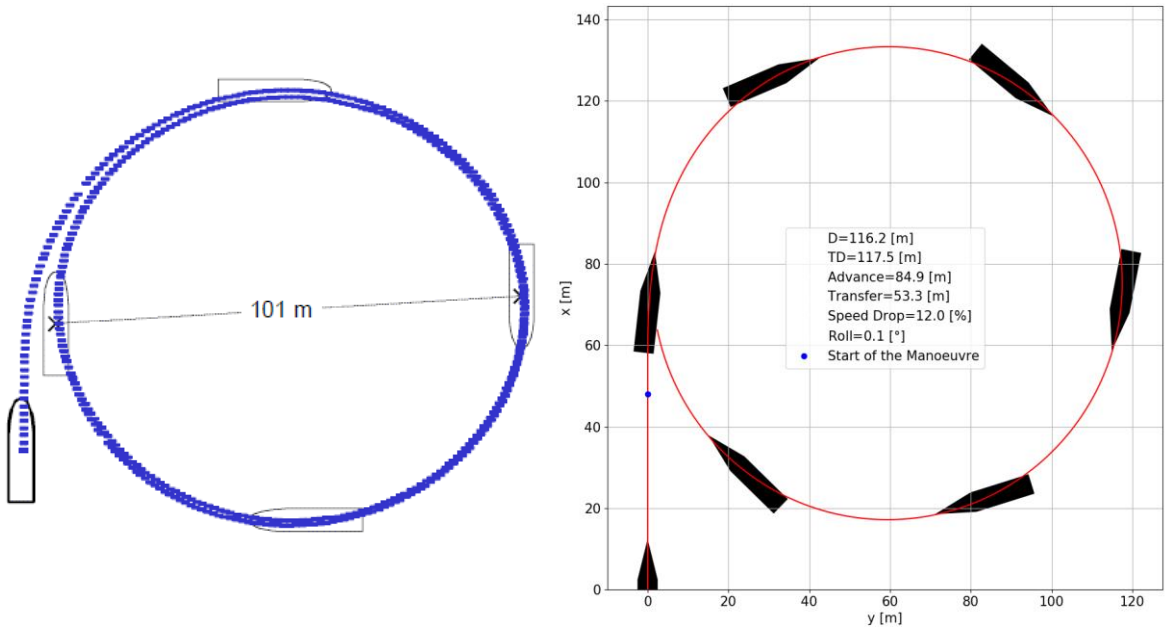

Figure 8.7: Turning circle manoeuvre, 35° rudder deflection, 9.42 [m/s] initial speed. **Left:** Full-scale trial result, **Right:** Manoeuvring prediction process result.

The following table makes a quantitative comparison of the results:

Table 8.1: Quantitative comparison of the full-scale trials results with the manoeuvring prediction.

Characteristic	Full-Scale (Average)	Manoeuvring Prediction	Prediction Error
Diameter (D)	$3.88\ L_{pp}$	$4.65\ L_{pp}$	20%
Tactical Diameter	$4.20\ L_{pp}$ **or** $1.08\ D$	$4.7\ L_{pp}$ **or** $1.01\ D$	12% **or** -7%
Advance	$3.44\ L_{pp}$**or** $0.89\ D$	$3.40\ L_{pp}$ **or** $0.73\ D$	-1% **or** -17%
Transfer	$2.16\ L_{pp}$**or** $0.56\ D$	$2.13\ L_{pp}$**or** $0.46\ D$	-1% **or** -18%
Steady Longitudinal Speed [m/s]	6.88	8.29	$21\ \%$
Roll	$4°$ (out)	$0.1°$ (in)	-103%

According to these results, it is possible to observe some discrepancies between the full-scale trials and the manoeuvring prediction. Except for the speed drop and roll, the remaining turning circle characteristics are in the range of uncertainties caused by *CFD (*see *Figure 8.3).* Since the roll motion is not the focus of this research the *CFD* uncertainties of the roll moment are unknown. Therefore, the discrepancy in roll prediction can be caused by:

- *CFD* uncertainties in the determination of hydrodynamic coefficients;
- Roll moment due to yaw motion was neglected (*Section 4.2.4*);
- Error in the estimation of the $\overline{GM_t}$.

The origin of the speed drop error can be:

- Errors of the full-scale measurements;
- *CFD* uncertainties in the determination of hydrodynamic coefficients;
- Assumption of constant propeller rate (n_p);
- The method of determining propeller wake fractions (just pure drift, see *Section 5.3*);
- Neglecting the added resistance due to sway and yaw motions (X_{vr})
- Neglecting effects of roll on other motions.

In the end, the manoeuvring prediction over-estimates turning circle size, which indicates an overestimation of the course stability or an under-estimation of the rudders' effectiveness (*see Section 2.3.1*). Furthermore, it is important to note that the initial speed of these manoeuvres corresponds to $F_n \approx 0.6$. At this F_n, the effect of dynamic pressure on the hull can significantly affect the trim and sinkage, effect which is neglected by the manoeuvring model.

Due to too high *CFD* uncertainties, unknown experimental uncertainties and the significant under-estimation of speed drop, it is not possible to validate the manoeuvring prediction of turning circles in this research. Further research is required for the validation of the turning circle prediction, with especial focus on reducing the *CFD* discretization uncertainties. Since the manoeuvring model has been verified and it includes the main physical aspects of ship manoeuvring, this one is considered suitable for qualitative/comparative assessments of manoeuvring performance.

8.3.3 ZIG-ZAG PREDICTION

As mentioned in *Section 2.12,* 3°-3° Zig-Zag manoeuvres were performed at model scale. The following pictures compare the experimental results, with the manoeuvring prediction:

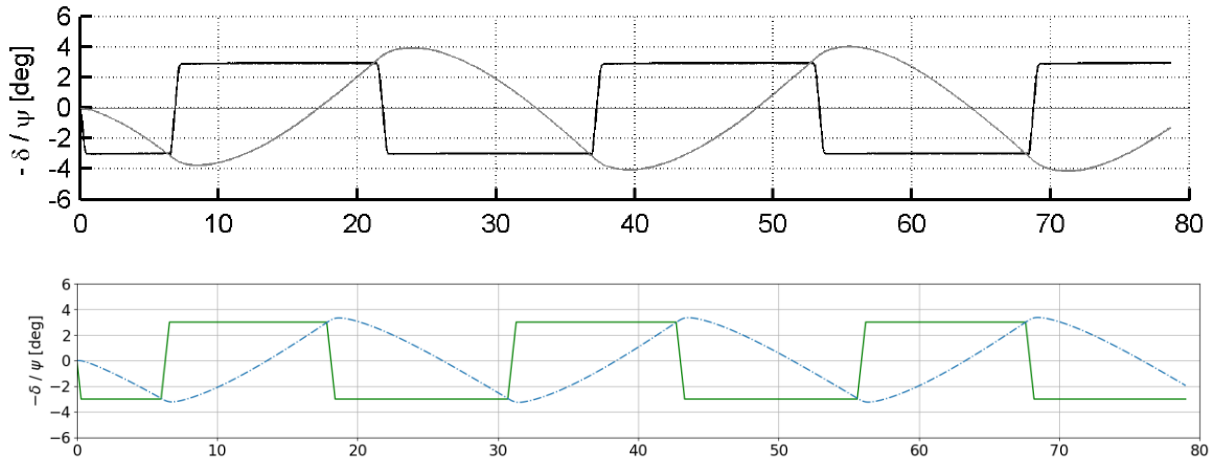

Figure 8.8: Rudder deflection (continuous green line in the bottom figure, δ) and heading (dot-dashed blue line in the bottom figure, ψ) during a 3°-3° Zig-Zag manoeuvre. **Top:** Extrapolated model scale results. **Bottom:** Manoeuvring prediction. The horizontal axis represents time in seconds.

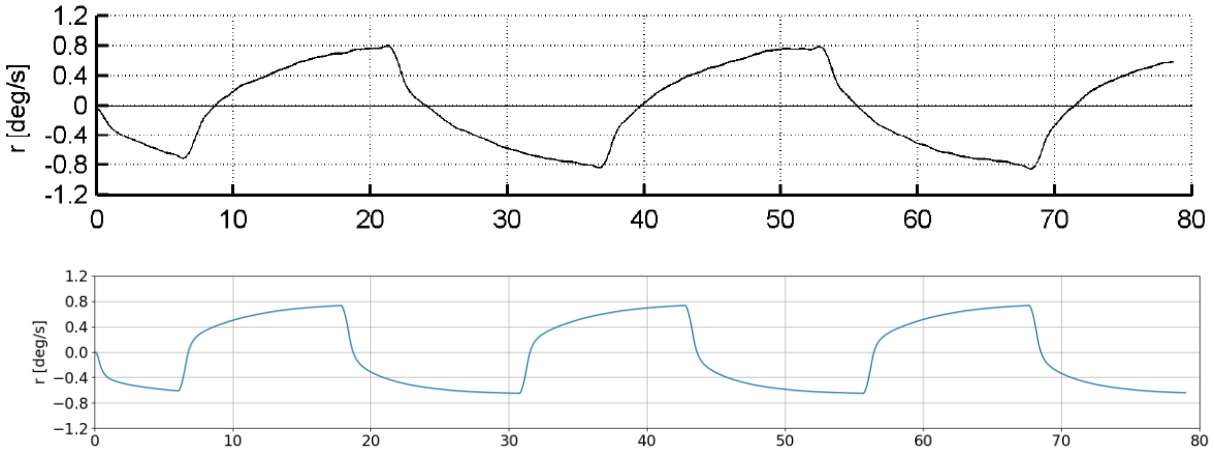

Figure 8.9: Yaw rate during a 3°-3° zig-zag manoeuvre. **Top:** Extrapolated model scale results. **Bottom:** Manoeuvring prediction. The horizontal axis represents time in seconds.

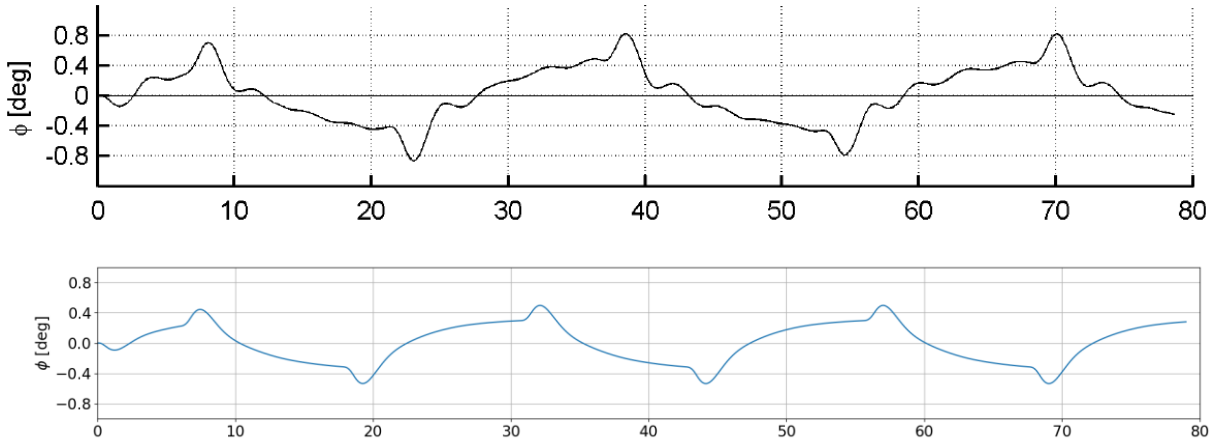

Figure 8.10: Roll amplitude during a 3°-3° zig-zag manoeuvre. **Top:** Extrapolated model scale results. **Bottom:** Manoeuvring prediction. The horizontal axis represents time in seconds.

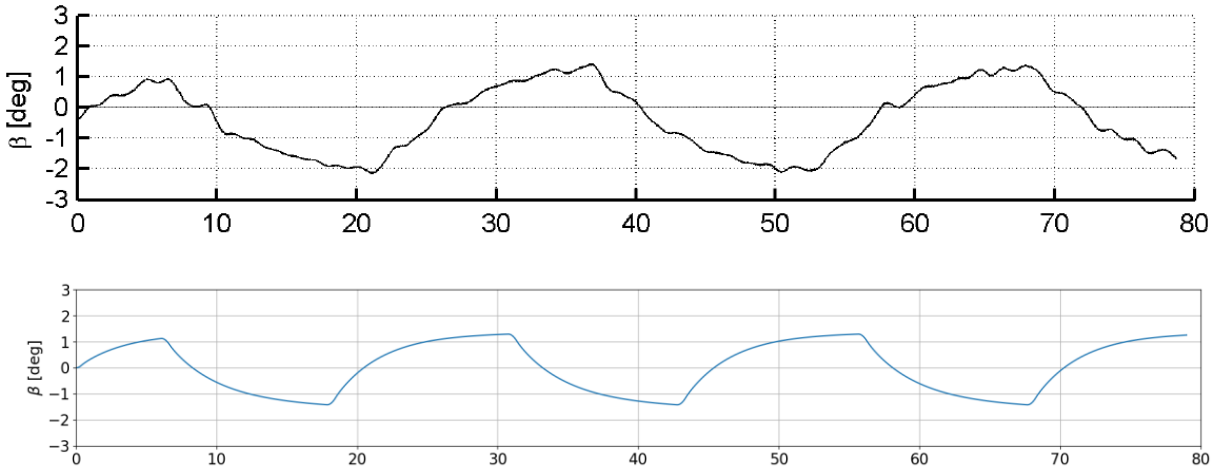

Figure 8.11: Drift angle during a 3°-3° zig-zag manoeuvre. **Top:** Extrapolated model scale results. **Bottom:** Manoeuvring prediction. The horizontal axis represents time in seconds.

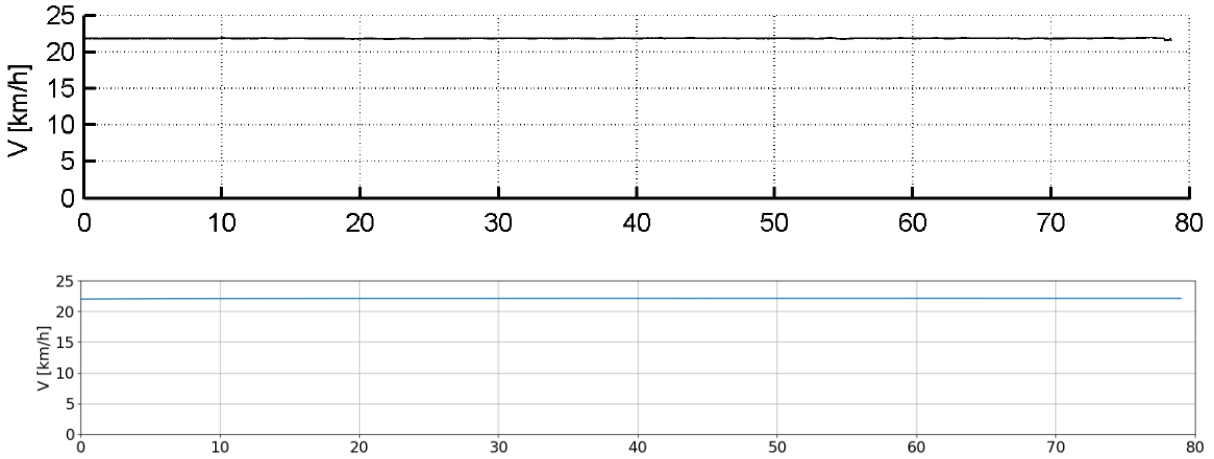

Figure 8.12: Advance speed during a 3°-3° zig-zag manoeuvre. Here V represents u according to the convention of the author of the model scale experiments. **Top:** Extrapolated model scale results. **Bottom:** Manoeuvring prediction. The horizontal axis represents time in seconds.

Note that the advance speed remains practically constant, since it is a $3° - 3°$ zig-zag manoeuvre.

The following table compares the yaw overshoot of the model scale experiments with the manoeuvring prediction. Since in the experiments, zig-zag manoeuvres were performed for both sides (PS and SB), the following table considers the average of these results:

Table 8.2: Quantitative comparison of the model scale results with the manoeuvring prediction for a 3°-3° zig-zag manoeuvre.

Yaw Overshoot	Measured Model Scale	Manoeuvring Prediction	Prediction Error (ϵ)
1st	0.6° ± 0.1°	0.3°	-57% $< \epsilon <$ -40%\
2nd	0.8° ± 0.1°	0.4°	-56% $< \epsilon <$ -43%
3rd	0.8° ± 0.1°	0.4°	-56% $< \epsilon <$ -43%
4th	0.9° ± 0.1°	0.4°	-60% $< \epsilon <$ -50%

The previous results show that the manoeuvring prediction under-estimates the yaw overshoot. Since the yaw overshoots in question are small ($\psi < 1°$), the prediction error should be put in perspective.

This under-estimation of yaw overshoot can be caused by:

- Experimental errors in the setup, measurements and extrapolation of the results from model to full scale;
- Over-prediction of course stability by the mathematical model (see *Section 2.3.2*);
- Under-prediction of the rudders' effectiveness (see *Section 2.3.2*).
- Under-prediction of yaw added moment of inertia ($N_{\dot{r}}$)

Looking at *Figure 8.9* and *Figure 8.11,* it is possible to observe that the predicted yaw rate and sway speed magnitudes are close to the ones measured in the experiments. Therefore, this indicates a good estimation of sway damping, yaw damping and rudder forces. However, the period of the zig-zag manoeuvre and the transient phase of the yaw motion are under-predicted by the manoeuvring model. This indicates that the source of error is a possible mismatch of the total yaw moment of inertia ($I_{zz} + N_{\dot{r}}$) between the manoeuvring model and the experimental setup. This difference can be caused by scaling errors and/or numerical errors of the *Virtual Captive Tests* in the estimation of $N_{\dot{r}}$.

Due to the too high numerical uncertainties and the discrepancy in zig-zag period, it is not possible to validate the manoeuvring prediction results in this research. For this, further research is required, particular attention must be given to the *CFD* settings and *Virtual Captive Tests* setup to reduce numerical uncertainties. Since the manoeuvring model has been verified and it includes the main physical aspects of ship manoeuvring, this one is considered suitable for qualitative/comparative assessments of manoeuvring performance.

8.3.4 HULL VANE MATHEMATICAL MODEL

In *Section 6.3* a mathematical model for the Hull Vane is developed with the purpose of allowing a less expensive estimation of the Hull Vane effects on the manoeuvring performance, which is particularly useful at early design stages. For this, the *Linear Pressure Distribution Method* was used together with *Fujii's LAR LLT.* One of the main assumptions of this model is that the Hull Vane only affects the sway force due to yaw rate, yaw damping and *Munk* moment. To assess the validity of the Hull Vane mathematical model, in this section turning circle and zig-zag manoeuvres are performed. Then the results of the Hull Vane mathematical model are compared to the ones from the integrated approach, completing the 3rd and last research objective.

8.3.4.1 Turning Circle Manoeuvre

The following figure compares turning circle manoeuvres at 9.42 [m/s] with 35° rudder deflection, obtained using the integrated approach and the Hull Vane mathematical model:

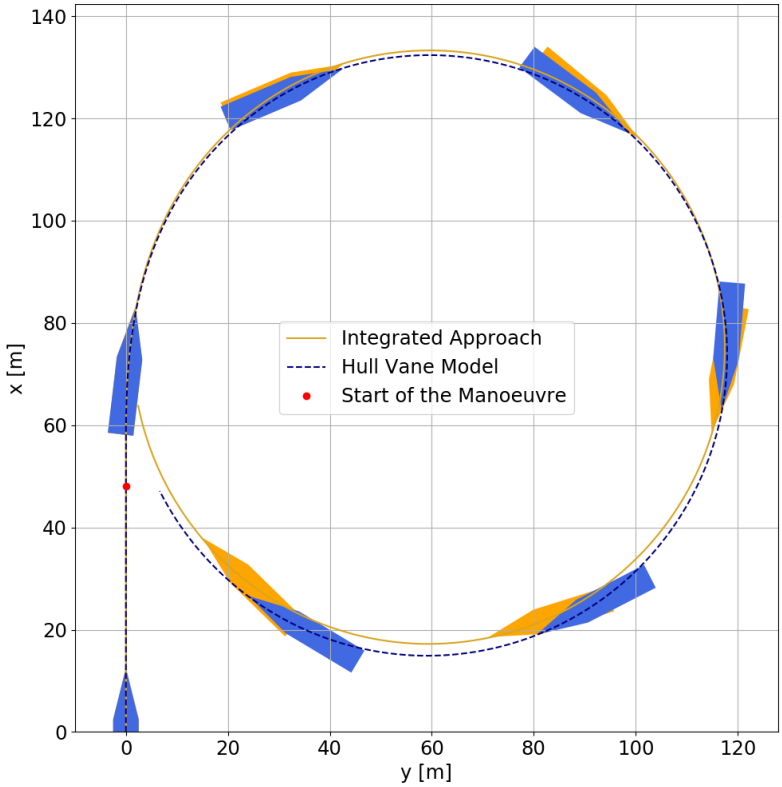

Figure 8.13: Comparison of the Hull Vane mathematical and the integrated approach. Turning circle, 35° at 9.42[m/s].

The following table compares the different characteristics of the turning circles presented in the previous figure:

Table 8.3: Quantitative comparison of the Hull Vane mathematical and the integrated approach. Turning circle, 35° at 9.42[m/s].

	Integrated Approach	Hull Vane Model	Hull Vane Model Error
Diameter [m]	116.2	117.6	1.2%
Tactical Diameter [m]	117.5	117.9	0.3%
Advance [m]	84.9	84	-1.1%
Transfer [m]	53.3	53.3	0.0%
Steady Longitudinal Speed [m/s]	8.29	7.91	-4.6%
Roll [deg]	0.1	0.8	87.5%

Considering the aim for which the mathematical modeling of the Hull Vane was developed, it is possible to observe a satisfactory matching between the integrated approach results and the Hull Vane mathematical model. The Hull Vane Model over-estimates the speed drop. This is caused by the fact that the Hull Vane model considers the bare-hull resistance of the vessel. Thus, the required propulsive power during the manoeuvre reaches the limit of the installed power, which by *Eq. 6.*1 reduces the generated thrust. As explained in *Section 6.3,* the effects of the Hull Vane on roll are not included in the mathematical model of the Hull Vane, which justifies the discrepancy in roll.

8.3.4.2 Zig-Zag Manoeuvre

For the validation of the Hull Vane mathematical model in predicting a zig-zag manoeuvre, a 10°-10° zig-zag is performed at 9.42 [m/s] (0.97 V_{max}), since it is the most common test case in full scale trials. The figure below compares the results of the Hull Vane mathematical model with the integrated approach results:

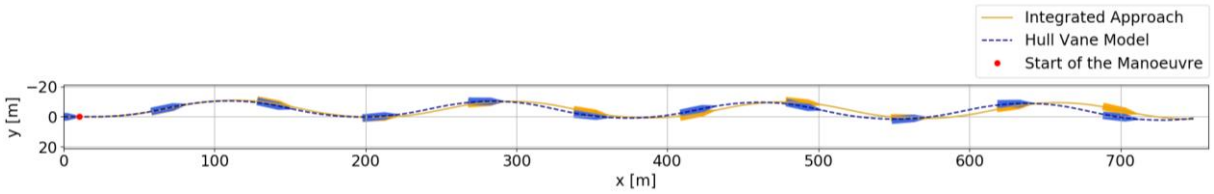

Figure 8.14: Comparison of the Hull Vane mathematical and the integrated approach. Zig-zag, 10°- 10°at 9.42[m/s].

The following table compares the different characteristics of the zig-zag manoeuvres presented in the previous figure:

Table 8.4: Quantitative comparison of the Hull Vane mathematical and the integrated approach. Zig-zag, 10°-10°at 9.42[m/s].

	Integrated Approach	**Hull Vane Model**	**Hull Vane Model Error**
Maximum Yaw Overshoot [deg]	2.8	3.1	11%
1st Yaw Overshoot [deg]	2.2	2.3	5%
1st Overshoot Width of Path [m]	8.4	8.3	-1%
1st Period [s]	19.6	18.7	-5%
Reach Time [s]	10.5	10.1	-4%
Maximum Roll [deg]	1.1	1.3	18%

As explained in *Section 8.2.2,* zig-zag manoeuvres are more dependent on unsteady phenomena than turning circle manoeuvres. According to the results of *Chapter 4,* it is possible to conclude that the Hull Vane affects the sway force due to yaw acceleration and increases the yaw added moment of inertia. However, in *Section 6.3,* when mathematically modeling the Hull Vane, it was assumed that these unsteady effects are of secondary importance and therefore neglected. Which contributes for higher relative errors, of the Hull Vane mathematical model, in the prediction of zig-zag manoeuvres than turning circles. In the end the Hull Vane mathematical model:

- Over-estimates of yaw overshoot;
- Under-estimates of zig-zag period;
- Under-predicts of roll amplitude.

The modeling errors observed in

Figure 6.4, *Figure 6.5* and *Figure 6.6* decrease the course stability of the vessel, contributing for the over-estimation of the yaw overshoot by the Hull Vane mathematical model. For a 20°-20° zig-zag test the under-estimation of the course stability increases since the modeling errors increase. The discrepancy in the prediction of the roll motion is caused by having neglected effect of the Hull Vane on roll (*Section 6.3*).

In the end the Hull Vane mathematical model provides satisfactory results of zig-zag manoeuvres, which is valid for early design stage studies of the impact of the Hull Vane on the manoeuvring performance.

8.3.5 RESULTS DISCUSSION

In this section the manoeuvring prediction results were compared with experimental data for validation purposes. This comparison shows that the turning circle diameter is over-predicted with about 20% and the yaw overshoot under-predicted with about 50% (0.4°), indicating an over-estimation of the course stability. It is also observed that the roll motion is not predicted as well as the other motions (especially for turning circle), the steady longitudinal turning speed is over-predicted with about 5% and the zig-zag period under-predicted. In the end, due to too high *CFD* uncertainties, and unknown uncertainties of the experimental data, further research is required to validate the manoeuvring prediction results. With special focus in reducing the numerical uncertainties of the *Virtual Captive Tests.* Although it is not possible to validate the results of the manoeuvring prediction, this one has been successfully verified and it contains the main physical aspects of ship manoeuvring. Therefore, it is considered to be suitable for qualitative/comparative assessments of ship manoeuvring.

The Hull Vane model derived in *Section 6.3,* was compared with the integrated approach, showing to be valid for initial manoeuvring performance assessments. Since the Hull Vane mathematical model does not include the effects of the Hull Vane on roll, this one is less well predicted. The Hull Vane model under-estimates by 5% the steady longitudinal turning speed, which is caused by an overload of the propulsion system, since the bare hull resistance is considered. Regarding the zig-zag manoeuvre, the Hull Vane model over-estimates the yaw overshoot by 11% (0.3°) and under-estimates the zig-zag period with about 5% (0.9 [s]). Modelling errors of the Hull Vane contribute for an under-estimation of the course stability, which is in accordance with the results. In the end the Hull Vane model allows simple, practical and quick assessments of the impact of the Hull Vane on the manoeuvring performance, and its accuracy is adequate for preliminary studies. However, further validation is recommended with other vessels before adopting this model as a standard.

In the end it is possible to conclude that the setup of the captive tests was adequate, *i.e.:* the drift angles, inflow angles and yaw rates of the manoeuvring predictions are in the range of the virtual captive tests. It is important to note that, cross terms such as Y_{vu}, Y_{vr}, N_{rv}, were neglected, which contributes for discrepancies in the results. Particularly the two last ones, can be relevant for the dynamic behaviour of vessels, see *Wang et al.* in [79].

8.4 EFFECT OF THE HULL VANE ON THE MANOEUVRING PERFORMANCE

In the course of this research, the most natural question is “what is the effect of the Hull Vane on the manoeuvring performance?”. To answer to this question, turning circle and zig-zag manoeuvres with and without Hull Vane are compared. According to *Chapters 4, 5* and 6*,* the Hull Vane:

- Increases the *Munk* moment (N_v, N_{vvv}) due to trimming the vessel bow down, **destabilizing contribution**;
- Increases the yaw damping (N_r, N_{rrr}) and yaw added moment of inertia ($N_{\dot{r}}$) due to the presence of the struts, **stabilizing contribution**;
- Affects the sway force due to yaw rate (Y_r, Y_{rrr}) and sway force due to yaw acceleration ($Y_{\dot{r}}, Y_{\dot{r}\dot{r}\dot{r}}$) due to trimming the vessel bow down and the presence of the struts, **either destabilizing or stabilizing contribution**;
- Affects the Roll Moment (K_v, K_{vvv}, K_{vvvvv}) due to Hull to Hull Vane interaction;
- Decreases the steering force due to the interaction between rudders and struts (Γ_S).

The combination of these effects makes challenging to draw general conclusions about the effect of the Hull Vane on the manoeuvring performance, as mentioned in *Section 4.6*. Therefore, the following results are only representative of the *RPA8* case. The figure below, compares a 35° turning circle at 9.42 [m/s] (0.97 V_{max}) performed with and without Hull Vane:

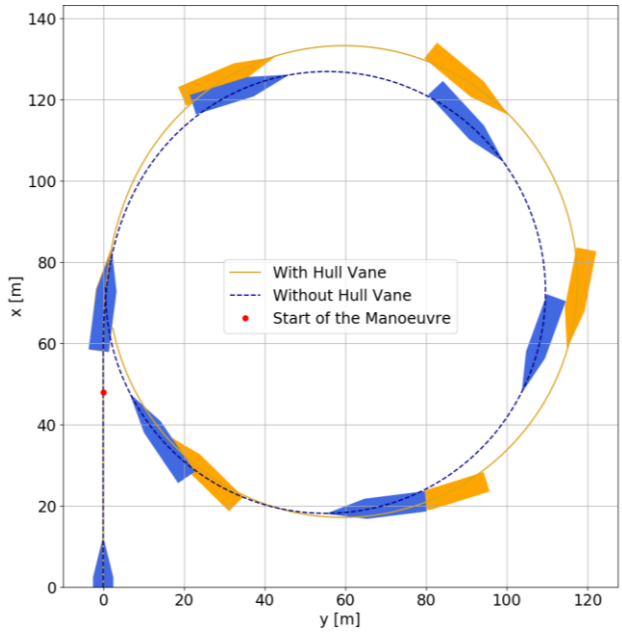

Figure 8.15: Effect of the Hull Vane on a 35° turning circle at 9.42[m/s].

The following table compares multiple parameters of the turning circle manoeuvres in the previous figure:

Table 8.5: Quantitative comparison of the effect of the Hull Vane on a 35° turning circle at 9.42[m/s].

	Without Hull Vane	With Hull Vane	Relative Difference
Diameter [m]	109.0	116.2	7%
Tactical Diameter [m]	109.6	117.5	7%
Advance [m]	78.6	84.9	8%
Transfer [m]	49.9	53.3	7%
Steady Longitudinal Speed [m/s]	7.9	8.3	5%
Roll [deg]	0.8	0.1	-88%

Based on 20° full speed, turning circle manoeuvres, performed at full scale with an offshore supply vessel, *K.Uithof et al.* in [12] found about 4% increase of the turning circle diameter when a Hull Vane was installed. According to the results presented here, the Hull Vane increases the turning circle diameter in about 7%, which indicates an increase of course stability. The speed drop decreases with the Hull Vane since without the Hull Vane the resistance increases, leading to an overload of the propulsion system. However, assuming the same propellers, no power limitations and constant propeller rate (n_p), the speed drop of the vessel without Hull Vane would be smaller than the one with Hull Vane, since n_p is bigger. According to *Eq. 4.*1, this would decrease the course stability of the vessel without Hull Vane, leading to a smaller turning circle diameter than the one in the table. Furthermore, as expected from the results of *Chapter 4,* the Hull Vane significantly contributes for an 'outward' roll moment.

The following figure compares the results of a 10°-10° zig-zag manoeuvre at 9.42 [m/s] (0.97 V_{max}) with and without Hull Vane:

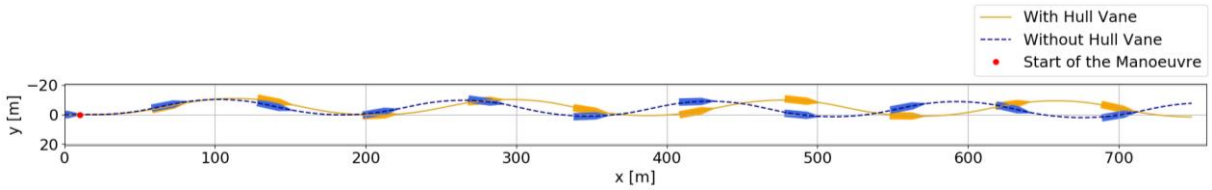

Figure 8.16: Effect of the Hull Vane on a 10°- 10° zig-zag at 9.42 [m/s].

The following table compares multiple parameters of the zig-zag manoeuvres in the previous figure:

Table 8.6: Quantitative comparison of the effect of the Hull Vane on 10°- 10° zig-zag at 9.42[m/s].

	Without Hull Vane	With Hull Vane	Relative Difference
Maximum Yaw Overshoot [deg]	3.4	2.8	-18%
1st Yaw Overshoot [deg]	2.6	2.2	-15%
1st Overshoot Width of Path [m]	8	8.4	5%
1st Period [s]	17.4	19.6	13%
Reach Time [s]	9.5	10.5	11%
Maximum Roll [deg]	1.6	1.5	0%

According to the previous results, the Hull Vane decreases the yaw overshoot and period and increases the overshoot width of path and reach time. This suggests an increase in course stability caused by the Hull Vane, which is in accordance with the turning circle results.

In the end, it is possible to conclude that the Hull Vane increases the course stability of *RPA8,* which is in accordance with the results presented by *K.Uithof et al.* in [12]. This increase in course stability leads to an increase of the turning circle diameter by 7% and a decrease of the maximum yaw overshoot by 18%. Therefore, for this case, it is possible to verify that the increase of destabilizing effects (*e.g.: Munk* moment) caused by the Hull Vane, is not dominant over the increase in stabilizing effects. However, this is not necessarily truth for any case, particularly when the Hull Vane causes a significant change in trim.

8.5 CONCLUSIONS

In this section the main conclusions of this chapter are presented. For the sake of clarity, the conclusions are split in multiple parts:

- **Manoeuvring Model Verification:** The manoeuvring model was verified using a test case, for which it was possible to derive an analytical solution. The numerical results of the manoeuvring model showed a perfect match with the analytical solution, which verifies the manoeuvring model, *i.e.:* it solves the equations right, according to *Roache* in [45].

- **Sensitivity Analysis:** A sensitivity analysis of the manoeuvring model was performed for turning circle and zig-zag manoeuvres. The results showed that unsteady forces and moments have a small influence on turning circle and zig-zag manoeuvres. Therefore, the gain in accuracy in the determination of unsteady forces/moments, provided by *PMM* tests, hardly compensates the cost and loss in accuracy caused by flow memory effects and numerical uncertainties. The use of semi-empirical models for the determination of unsteady forces and the use of rotating arm tests instead of pure-yaw *PMM* tests, must be assessed in future research, since this can considerably decrease the cost of manoeuvring predictions. Furthermore, it is also shown, that the *CFD* discretization uncertainties are amplified by the manoeuvring model, which can lead to manoeuvring prediction uncertainties over 30%, particularly caused by the yaw moment uncertainties. Thus, future research must be focused on reducing the numerical uncertainties of *Virtual Captive Tests*.

- **Manoeuvring Prediction Validation:** The *Discrete Spectral Method (DSM)* was successfully validated, showing a good match between the *CFD* results and the polynomial regressions obtained with the *DSM.* Furthermore, the manoeuvring predictions results show to be in the range of the characteristics of the *Virtual Captive Tests* (*e.g.:* drift angles, yaw rates). In the end it is possible to conclude that the manoeuvring prediction process over-estimates the course stability, leading to an over-estimation of the turning circle diameter of about 20% and an under-estimation of the overshoot of about 50% (0.4°). It is also possible to observe that roll motion is not predicted as well as the other motions. Furthermore, the speed drop in the turning circle manoeuvre is under-estimated. Due to the significant uncertainty of the *Virtual Captive Tests,* further research is required to validate the manoeuvring prediction process. With special focus on reducing numerical uncertainties and using rotating arm tests instead of *PMM* pure-yaw tests. However, the manoeuvring model is considered to be valid for qualitative/comparative purposes.

- **Hull Vane Mathematical Model Validation:** According to the obtained results, the Hull Vane mathematical model is considered valid for initial manoeuvring estimations. Relatively to the integrated approach results, the Hull Vane model predicts the turning circle dimensions with about 1% difference from the integrated approach, about 5% difference for the 1st zig-zag yaw overshoot and 11% for the maximum yaw overshoot. The speed drop is over-estimated since the Hull Vane model is considering the resistance of the hull without Hull Vane, which leads to an overload of the propulsion system during the manoeuvre. At the end, this model allows, simple, practical and quick estimations of the effect of the Hull Vane on manoeuvring. In future work, this model must be further validated for different types of vessels and the effects of the Hull Vane on roll motion included.

- **Effect of the Hull Vane on the Manoeuvring Performance:** To assess the effect of the Hull Vane on the manoeuvring performance, a 35° turning circle and a 10°-10° zig-zag manoeuvres were performed at 9.42 [m/s] (0.97 V_{max}) with the manoeuvring model, with and without the Hull Vane. For the case of the vessel with Hull Vane, the turning circle diameter increased with about 7% and the maximum overshoot decreased with 18%. This shows that the Hull Vane causes an increase in course stability, which is in accordance with the results presented by *K.Uithof et al.* in [12]. However, this is not necessarily true for every case, particularly when the Hull Vane causes a significant change in trim.

9. CONCLUSIONS

The competitiveness of the maritime sector together with energetic and environmental challenges have promoted a demand for more efficient marine vehicles. In response to this, research campaigns have been conducted with the aim of developing new technologies. One of these technologies is the application of hydrofoils to marine vehicles. Although they provide a significant increase in efficiency, challenges and concerns arise due to their influence on seakeeping and manoeuvring performance. As a starting point, to better understand the impact of hydrofoils on the dynamic behaviour of seagoing vessels, this research focused on calm water manoeuvring prediction of foil-assisted vessels. For this, a 25 m patrol vessel (*RPA8*) equipped with a Hull Vane was considered, for which experimental data is available. The following figure illustrates the manoeuvring prediction process developed in this research:

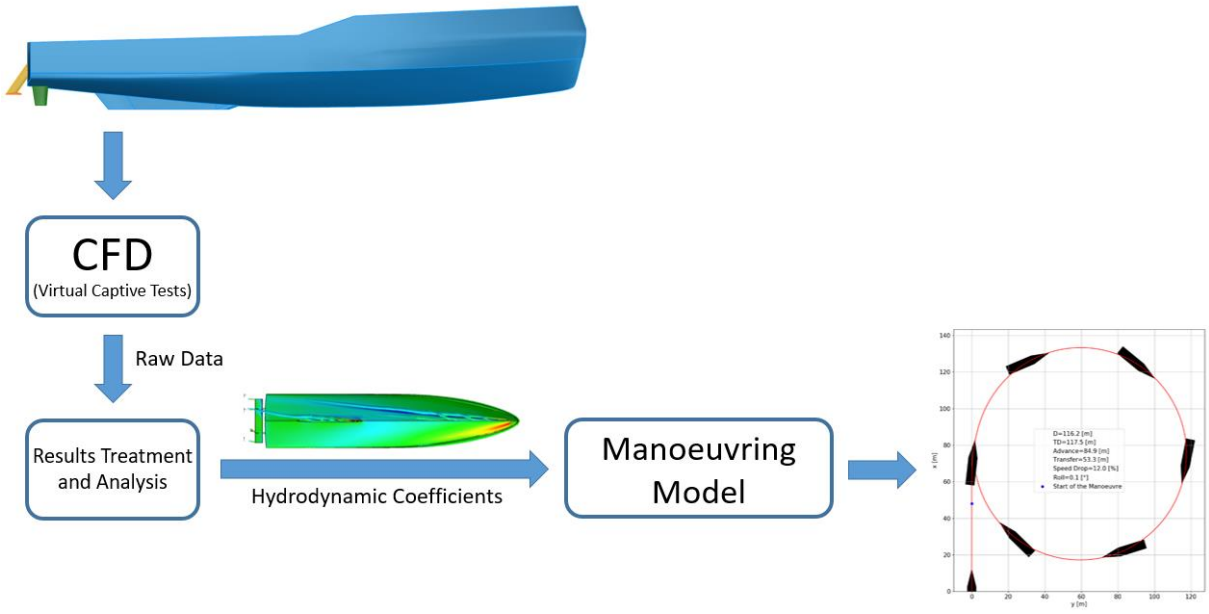

*Figure 9.1:*Manoeuvring prediction process.

The manoeuvring prediction process starts with a *3D* geometry and inertial properties of a vessel. With this, *Virtual Captive Tests (VCT)* are performed and analysed to determine hydrodynamic coefficients. These coefficients are then the input of a manoeuvring model, which simulates free running manoeuvres based on the inertial and hydrodynamic characteristics of the vessel.

In the end, this research developed knowledge, methodologies and tools which allow to perform manoeuvring simulations of vessels equipped with a Hull Vane, without the need of performing expensive physical experiments (*e.g.:* model scale tests).

9.1 VIRTUAL CAPTIVE TESTS: SETUP AND ANALYSIS

The first step to perform *VCT*, was to define a mesh for the numerical computations (*CFD*). This was done by conducting a solution verification study of a 15°-Oblique Towing Test (*OTT*). Reaching a solution convergence showed to be a challenging task, due to the presence of complex flow features (*e.g.*: fore and aft-body vortices), which is in accordance with the conclusions of *Hochbaum* in [3] and *Toxopeus* in [4]. In the end, an Adaptive Grid Refinement (*AGR*) algorithm was used, to allow an equilibrium between computational cost and the capturing of complex flow features.

Two types of *VCT* were performed and compared: *OTT's* and Planar Motion Mechanism (*PMM)* tests. Relatively to *OTT's, PMM* tests require a more complex setup and analysis of the results. Due to the strong non-linear nature of hydrodynamic forces and moments, a *Discrete Spectral Method* was developed and implemented for the analysis of *PMM* tests. This approach uses *Fourier* transform to decompose the measured forces and moments in multiple sinusoidal components. This does not only allow to mathematically describe the non-linear behaviour of forces and moments, but also to identify sources of noise, *e.g.:* noise caused by the actuator disk and *AGR* updating frequencies.

According to a sensitivity analysis, the gain in accuracy that the *PMM* tests provide, in the determination of unsteady effects (*e.g.:* Added masses and moments of inertia), hardly compensates the loss in accuracy in the determination of steady effects (*e.g.:* damping effects). This loss in accuracy is caused by flow memory effects and higher numerical residuals. In general, *PMM* tests are convenient in the context of physical experiments, since they reduce the experimental time and avoid the need of rotating arm test facilities. However, when performing *VCT* this is often not the case. Instead, it is recommended to use *OTTs* and *rotating arm tests* for the determination of steady forces/moments, and semi-empirical models to estimate unsteady forces. This allows a less time-consuming and a better assessment of steady hydrodynamic coefficients, which are more relevant than unsteady ones (see *Section 8.2*).

9.2 VIRTUAL CAPTIVE TESTS: RESULTS

The *VCT* were performed with and without Hull Vane. The results showed that the Hull Vane causes an increase in yaw damping which is a stabilizing effect, but at the same time also increases the *Munk* moment (since it trims the vessel bow down), which is a destabilizing effect. Thus, it is not trivial to draw general conclusions about the impact of the Hull Vane on the manoeuvring performance. Furthermore, dedicated *VCT* for the determination of interaction effects, showed that the vortices developed by the hull, cause a strong reversion of the flow at the stern. This leads to a significant increase of the angle of attack of the inner rudder and a symmetric angle of attack between Hull Vane struts. The consequence of this, is an early stalling of the inside rudder and a weak contribution of the Hull Vane for sway damping, which is a stabilizing effect. Furthermore, rudder to strut interaction tends to reduce the steering ability and hull to Hull Vane interaction can strongly affect the roll motion.

9.3 MANOEUVRING MODEL

As previously mentioned, a manoeuvring model was developed and implemented to assess the manoeuvring performance of *RPA8*. This manoeuvring model solves the *Euler* equations of motion. It uses mathematical models of forces, moments and interaction effects (previously derived from *VCT)* to predict the manoeuvrability of vessels. Although in this research *VCT* were performed with (Integrated Approach) and without Hull Vane, for practical purposes, it is significantly expensive to perform the *VCT* twice to assess the influence of the Hull Vane on manoeuvring. Therefore, one of the goals of this research, was to develop and implement a mathematical model to allow the assessment of the effect of the Hull Vane, without the need of performing *VCT* twice. As mentioned before, the Hull Vane does not affect the sway damping and increases the *Munk* moment, which is caused by trimming the vessel bow down, (see *Figure 2.8*). *Inoue* et al. in [53] proposed a method to model the effect of trim on hydrodynamic forces and moments. However, it provides poor results for *RPA8* since it was developed for merchant ships. In alternative to this, a *Linear Pressure Distribution Method (LPDM)* was developed. This method assumes a linear side pressure distribution over the length of the hull. By using *Fujii's Low Aspect Ratio Lifting Line Theory (Fujii's LAR LLT, Eq. 2.30),* to model the effect of the Hull Vane struts in yaw, and the *LPDM*, a mathematical model for the Hull Vane was successfully developed and validated. The comparison of this method with the integrated approach showed about 1% difference in predicting the dimensions of a 35° turning circle, about 5% difference for the 1st yaw overshoot and 11% for the maximum yaw overshoot in a 10°-10° zig-zag. These results are satisfactory and show that the model allows simple and quick estimations of the effect of the Hull Vane on manoeuvring, which is useful for preliminary calculations. However, further validation of this model is recommended for other types of vessels.

9.4 MANOEUVRING PREDICTION

In this research the impact of *CFD* uncertainties on manoeuvring predictions was assessed. It was demonstrated that the mathematical model amplifies the *CFD* uncertainties, leading to manoeuvring prediction uncertainties over 30%. Although the experimental uncertainties are unknown, the manoeuvring prediction over-estimates the course stability relatively to experimental data. This leads to an over-estimation of the $35°$ turning circle diameter with about 20 [m] (≈20%) and under-estimation of the $3°$-$3°$ zig-zag overshoot with about $0.4°$ (≈50%). Further research is required to validate the manoeuvring prediction process, especially in reducing the uncertainties of *VCT.* However, since the manoeuvring model was successfully verified and it contains all the main physical aspects of ship manoeuvring, the manoeuvring prediction is considered adequate for comparative/qualitative manoeuvring assessments. In addition to this, the Hull Vane causes an increase of the course stability of *RPA8,* by increasing the 35° turning circle diameter in 7% and reducing the 10°-10° zig-zag yaw overshoot in about 18%. Although the results here presented are in accordance with *K.Uithof et al.* in [12], it is important to note that an increase in course stability due to the Hull Vane, is not a trivial conclusion. Particularly when the dynamic trim is strongly affected by the Hull Vane. Therefore, this result must not be generalized for every case.

9.5 SUMMARY AND FINAL CONSIDERATIONS

The aim of this research was to:

- *"Establish methodologies for the determination of hydrodynamic coefficients using virtual captive tests, including free surface effects."*
- *"Develop a Hull Vane mathematical model and assess its impact on the overall manoeuvring prediction process."*
- *"Develop a Hull Vane mathematical model and assess its impact on the overall manoeuvring prediction process."*

All the research objectives were successfully reached. The **first research objective** was completed by testing multiple mesh setups and *Virtual Captive Tests*, assessing their discretization uncertainties and the impact of these ones on the manoeuvring prediction. Furthermore, a *Discrete Spectral Method* was developed and implemented for the analysis of *PMM* results. The **second** objective was accomplished by mathematically describing forces, moments and interaction effects based on the *Virtual Captive Tests* results and implementing these ones in a manoeuvring model. Finally, the **third** and last research objective was accomplished by performing a careful analysis of the *Virtual Captive Tests* results, and by developing the *Linear Pressure Distribution Method.* This led to the development of a Hull Vane mathematical model, which allows quick estimations of the impact of the Hull Vane on the manoeuvring performance. Being particularly suitable for early stage manoeuvring assessments.

In the end, this research developed knowledge, tools and methodologies which provide a better understanding of the dynamic behaviour of foil-assisted vessels, particularly vessels equipped with a Hull Vane. Besides the contribution for the scientific community, *Van Oossanen* is now able to perform manoeuvring predictions of vessels and has a solid foundation for further research and development in this field.

As previously mentioned, this research is a starting point for a better understanding of the impact of hydrofoils on the dynamic behaviour of seagoing vessels. Further research must be carried out towards this goal, eventually at *PhD.* level (see *Chapter 10*). This eventually would result in the development of seaworthy and manoeuvrable offshore high-speed crafts with hydrofoils. This would not only increase the efficiency and efficacy of high-speed vessels (*e.g.:* offshore supply vessels) but also fill a gap in the transportation sector, between expensive and quick air transports, and slow and relatively cheap maritime transports, especially for small to medium distances.

10. RECOMMENDATIONS AND FUTURE WORK

10.1 VIRTUAL CAPTIVE TESTS

For a successful validation of manoeuvring predictions, it is necessary to reduce the numerical uncertainties of *Virtual Captive Tests (VCT).* For this, it is recommended the use of an *Adaptive Grid Refinement* (*AGR*) algorithm, since it allows to combine a reasonable computational cost with the capturing of complex flow features. For the purpose of *VCT*, a solution verification analysis must be performed specifically for *AGR,* with the aim of properly capturing the fore and aft-body vortices, see *Wackers* et al. in [71]. This one must include all the forces and moments which are relevant for manoeuvring prediction purposes, *e.g.:* surge force, sway force, yaw moment, roll moment. In this research the boundary layer was modelled using a wall function. Although, this significantly reduces the computational cost, it can be a significant source of uncertainty in the prediction of separation, see *Wilcox* in [65]. Therefore, it is recommended to perform a comparative study between using a wall function and solving the boundary layer, for the prediction of forces/moments. A step further, could be an assessment of the effect different turbulence models, iterative errors and using other methods such as Detached Eddy Simulation (*DES*). Furthermore, the use of a turbulence model rotational correction, for the prediction of forces in *Virtual Captive Tests* must be assessed, see *Deng* and *Visonneau* in [80].

Performing virtual Planar Motion Mechanism (*PMM*) tests, in general, does not represent an advantage from the computational cost, accuracy and simplicity point of view. However, to reduce the uncertainties of this method, it is strongly recommended to perform a study of the effects of the *Strouhal* number (St_n) on the results. This would allow to quantify and avoid undesirable flow memory effects. In alternative to *PMM* tests, it is recommended to perform *oblique towing tests* and *rotating arm tests* to determine steady forces/moments. Due to the relatively small relevance of unsteady forces/moments in turning circles and zig-zag manoeuvres, these ones can eventually be estimated using semi-empirical models. However, if *PMM* tests are performed, it is recommended to make use of the *Discrete Spectral Method*, to analyze the results and determine hydrodynamic coefficients. Furthermore, the *AGR* settings must be fine-tuned to assess interaction effects, and these ones must not only be assessed using *oblique towing tests* but also with *rotating arm tests*.

10.2 MANOEUVRING MODEL

In future research, the effect of couplings between surge, sway and yaw must be assessed (*e.g.:* Y_{vu}, Y_{rv}, N_{rv}), especially if the aim is to be able to predict a broad range of manoeuvres. In this research, significant discrepancies were found in the prediction of roll. To improve this, it is recommended to perform a solution verification study of roll, and to use more than 4 data points to mitigate modeling errors, see *Section 4.2.4*. For the study of planing crafts, is particularly important to properly model roll motions and the effects of roll on other forces/moments, *e.g.:* $Y_{v\phi}, N_{r\phi}$, see *Tavakoli* et al. in [81]. According to the results of this research, the Hull Vane significantly affects the roll motion. Therefore, it would be convenient to extend the Hull Vane mathematical model to consider this effect. For this it is also recommended to include the virtual impact of the Hull Vane on the metacentric height of the vessel, see *Pierre et al.* in [60].

The *Linear Pressure Distribution Method (LPDM),* presented in this research, showed to provide satisfactory results for the influence of trim and sinkage on the manoeuvring performance. This method is expected to be valid for different types of vessels, which can represent a good alternative to semi-empirical formulations (*e.g.: Inoue* et al. [53]). Therefore, further validation studies must be performed for different types of vessels, and to better defined the range of applicability of the *LPDM.*

10.3 MANOEUVRING PREDICTION

The use of systems identification for the determination of parameters for ship manoeuvring, can significantly decrease the cost of manoeuvring predictions. According to *Bonci* in [26], systems identification allows an optimal compromise between accuracy and cost of manoeuvring predictions. In general, this method requires free running data, which can be obtained from physical experiments or numerical simulations. Although numerical simulations are less expensive, and therefore more attractive, this requires complex free running *CFD* simulations. However, according to *Bonci et al.* in [5], the latter still need to be improved. Therefore, in order to combine systems identification with *CFD,* it is required to perform extensive solution verification and validation studies of free running manoeuvres in *CFD.* Which can be a challenging task due to the coupling between forces/moments and motions. The data and results presented in this research can be used for the development of a system identification algorithm, without the need of having free running data from *CFD* (or physical experiments) beforehand. For more information see *Bonci et al.* in [5].

From a more global perspective, this research must be continued, for instance at a *PhD.* level*,* with topics such as:

- Control and dynamic stability of foiling vessels in stern-quartering waves and following seas, see *Faltinsen* in [6].
- Limiting criteria and control of transverse accelerations in foiling vessels.
- Simulation, mitigation and control of ventilation and cavitation effects on the dynamic behaviour of foiling vessels, see *Faltinsen* in [6].

This will contribute for the development of knowledge, methodologies and tools, which can eventually result in a new generation of seagoing vessels.

11. REFERENCES

[1] P. van Oossanen, J. Heimann, J. Henrichs and K. Hochkirch, “Motor Yacht Hull Form Design for the Displacement to Semi-Displacement speed Range,” 2009.

[2] “Wikipedia,” [Online]. Available: https://en.wikipedia.org/wiki/Hydrofoil#History. [Accessed 09 2018].

[3] A. Cura-Hochbaum, “Virtual PMM Tests for Manoeuvring Prediction,” Berlin, 2006.

[4] S. Toxopeus, Pratical application of viscous-flow calculations for the simulation of manoeuvring ships, Delft: Marine Research Institute Netherlands (MARIN), 2011.

[5] M. Bonci, M. Viviani, R. Broglia and G. Dubbioso, “Method for Estimating Parameters of Practical Ship Manoeuvring Models Based on the Combination of RANSE Computations and System Identification,” Applied Ocean Research, 2015, 52, 274-294.

[6] O. M. Faltinsen, “Hydrodynamics of High-Speed Vessels,” Cambrige University Press, New York, 2005.

[7] J. P. Hackett, J. S. P. Pierre, C. Bigler, T. J. Peltzer, F. Quadvlieg and F. v. Walree, “Computational Predictions vs. Model Testing for a High Speed Vessel with Lifting Bodies,” November 2007.

[8] S. Sutulo, Basics of Ship Manoeuvrability, Lisbon, 2013.

[9] E. J. Kerwin and B. J. Handler, The Principles of Naval Architecture Series: Propulsion, New Jersey: The Society of Naval Architects and Marine Engineers, 2010.

[10] K. Uithof, P. van Oossanen, N. Moerke, P. van Oossanen and K. Zaaijer, “An update in the development of the Hull Vane,” 2014.

[11] M. P. de Jonge, “Dynamic Hull Vane,” 2017.

[12] K. Uithof, B. Bouckaert, P. G. van Oossanen and N. Moerke, “The Effects of the Hull Vane on Ship Motions of Ferries and Ropax Vessels,” May 2016.

[13] T. I. Fossen, Handbook of Marine Craft Hydrodynamics and Motion Control, Trondheim: Wiley, 2011.

[14] E. V. Lewis, Principles of Naval Architecture: Motions in Waves and Controllability, Jersey: The Society of Naval Architects and Marine Engineers, 1989.

[15] G. F. Franklin, J. D. Powell and A. Emami-Naeini, Feedback Control of Dynamic Systems, New Jersey: Prentice Hall, 2002.

[16] International Maritime Organization, “Standards for Ship Manoeuvrability,” IMO, 2002.

[17] G. Kempf, “Maňoveriernorm f̆ur Schiffe,” Hansa, Deutsche Schiffahrs-zeitschrift, 1944.

[18] E. S. Arentzen and P. Mandel, “Naval Architecture Aspects of submarine Design,” SNAME, 1960.

[19] J. Dieudonne, “Collected French Papers on Stability of Route of Ships at Sea,” 1953.

[20] S. M. Triantafyllou and S. F. Hover, Manoeuvring and Control of Marine Vehicles, Cambridge: Massachusetts Institute of Technology , 2003.

[21] E. M. Lewandowski, “The Dynamics of Marine Craft, Manoeuvering and Seakeeping,” World Scientific Publishing Co. Pte. Ltd., Singapore, 2004.

[22] N. Kornev, “Lectures on Ship Manouvrability,” Rostock University, Rostock, 2013.

[23] E. Kreyszig, H. Kreyszig and J. E. Norminton, Advanced Engineering Mathematics, Ohio: John Wiley & Sons, Inc., 2006.

[24] R. A. Adams and C. Essex, Calculus, A Complete Course, Toronto: Pearson, 2010.

[25] F. A. Molland and R. S. Turnock, Marine Rudders and Control Surfaces, Oxford : Elsevier, 2007.

[26] M. Bonci, “Application of System Identification Methods for the Evaluation of Manoeuvrability Hydrodynamic Coefficients from Numerical Free Running Tests,” Genova, 2014.

[27] P. K. Kundo, I. M. Cohen and D. R. Dowling, Fluid Mechanics, London: Elsevier, 2016.

[28] H. K. Woud and D. Stapersma, Design of Propulsion and Electric Power Generation Systems, London: IMarEST, 2003.

[29] G. Dubbioso and M. Viviani, “Aspects of twin screw ships semi-empirical manoeuvring models,” Elsevier, Rome, 2012.

[30] J. D. Anderson, Fundamentals of Aerodynamics, Singapore: McGraw-Hill, 2001.

[31] “Air Foil Tools,” [Online]. Available: http://airfoiltools.com/. [Accessed 2018].

[32] H. Fujii and T. Tuda, “Experimental Research on Rudder Performance,” J Soc Naval Architects Jpn, 1961.

[33] L. Larsson and H. C. Raven, “Principles of Naval Architecture: Ship Resistance and Flow,” The Society of Naval Architects and Marine Engineers , New Jersey, 2010.

[34] S. Inoue, M. Hirano, K. Kijima and J. Takashima, “Pratical Calculation Method of Ship Maneuvring Motion,” 1981.

[35] H. Yasukawa and Y. Yoshimura, “Introduciton of MMG standard method for ship manoeuvring predictions,” 2014.

[36] K. Kose, A. Yumuro and Y. Yoshimura, “Concrete of Mathematical Model for ship Manoeuvring,” Society of Naval Architects, 1981.

[37] H. Söding, “Manoeuvring Technical Manual,” Hamburg, 1993.

[38] L. F. Richardson, “Weather Prediction by Numerical Process,” Cambridge Mathematical Library, Washington, 1922.

[39] S. Hickel, “CFD for Aerospace Engineers,” Delft University of Technology, Delft, 2017.

[40] J. H. Ferziger and M. Perić, “Computational Methods for Fluid Dynamics,” Springer, London, 2002.

[41] M. H. Sadd, “Elasticity: Theory, Applications and Numerics,” ELSEVIER, Kingston, 2005.

[42] G. K. Batchelow, “An Introduction to Fluid Dynamics,” Cambridge University Press, Cambridge , 2000.

[43] S. Hickel and S. Hulshoff, “CFD3 - Large Eddy Simulatoin,” Delft University of Technology, Delft, 2017.

[44] D. F. Domingos and L. J. Lagendijk, “Numerical Simulation of a Lid Driven Cavity,” Delft University of Technology, Delft, 2018.

[45] P. J. Roache, “Verification and Validation in Computer Science and Engineering,” Hermosa Publishers, Albuquerque, 1998.

[46] H. W. Coleman and W. G. Steele, “Experimentation, Validation and Uncertainty Analysis for Engineers,” John Wiley & Sons, Inc., 2009.

[47] L. Eça and M. Hoekstra, “A procedure for the estimation of the numerical uncertainty of CFD calculations based on grid refinement studies,” ELSEVIER, Lisbon, 2014.

[48] T. Xing and F. Stern, “Comment on "A procedure for the estimation of the numerical uncertainty of CFD calculations based on grid refinement studies"(L.Eça and M. Hoekstra),” ELSEVIER, Moscow(US), 2015.

[49] Z. Zaojian, Ship Manoeuvring and Seakeeping, Shanghai: Shanghai Jiao Tong University, 2006.

[50] T. Perez, Ship Motion Control, Trondheim: Springer, 2005.

[51] J. M. Journée, W. W. Massie and R. H. Huijsmans, Offshore Hydromechanics, Delft: Delft University of Technology, 2015.

[52] S. Tsakonas, “Effect of Appendage and Hull Form on the Hydrodynamic Coefficients of Surface Ships,” Davidson Laboratory, 1959.

[53] S. Inoue, M. Hirano and K. Kijima, “Hydrodynamic derivatives on Ship Manoeuvring,” International Shipbuilding Progress, 1981.

[54] V. Ankudinov, “Assessment and Principal Structure of the Modular Mathematical Model for Ship Manoeuvrability Prediction and Real Time Manoeuvring Simulation,” MARSIM, 1993.

[55] T. Ohmori, M. Fujino and H. Hiyata, “A study on flow field around full ship forms in manoeuvring motion,” Journal of Marine Science and Technology, 1998.

[56] B. Alessandrini and G. Delhommeau, “Viscous free surface flow past a ship in drift and in rotating motion,” 22nd Symposium on Naval Hydrodynamics, Fukuoka, 1998.

[57] A. Cura Hochbaum, “Computation of the turbulent flow arround a ship model in steady turn and in steady oblique motion,” 22nd Symposium on Naval Hydrodynamics, Fukuoka, 1998.

[58] A. Cura Hochbaum, “Virtual PMM tests for manoeuvring prediction,” 26th Symposium on Naval Hydrodynamics, Rome, 2006.

[59] L. Ljung, “Perspectives on system identification,” ELSEVIER, Korea, 2010.

[60] J. C. St. Pierre, J. P. Hackett, C. Bilgler and F. H. Quadvlieg, “Controllability of High-Speed Craft,” 10th International Symposium on Practical Design of Ships and Other Floating Structures, Texas, 2007.

[61] R. Tonelli and C. Boers, “Patrol Vessel (25 m); Free Running Manoeuvring Model Tests,” MARIN, Wageningen, 2016.

[62] F. M. White, Viscous Fluid Flow, New York: Mc Graw Hill, 2006.

[63] L. Larsson, R. E. Eliasson and M. Orych, Principles of Yacht Design, London: Adlard Coles Nautical, 2014.

[64] B. Vink, “A Verification & Validation Study of CFD Simulations for the Flow Around the RSD Tug 2513,” Delft University of Technology, Delft, 2017.

[65] D. C. Wilcox, “Wall Matching, A rational Alternative to Wall Functions,” 27th Aerospace Sciences Meeting, Reno, Nevada, 1989.

[66] t. S. Pas, “The Influence of y+ in Wall Funcitons Applied in Ship Viscous Flows,” MARIN, Wageningen, 2016.

[67] NUMECA, “Fine/Marine User Guide,” NUMECA, Nantes, 2018.

[68] C. Fureby, S. L. Toxopeus, M. Johansson, M. Tormalm and K. Petterson, A Computational Study of the Flow around KVLCC2 Model Hull at Straight Ahead and Conditions and at Drift, Stokholm: ELSEVIER, 2016.

[69] S. B. Pope, “Turbulent Flows,” Cambridge University Press, Cambridge, 2013.

[70] M. Visonneau, G. B. Deng, P. Queutey, J. Wackers and B. Mallol, “Anisotropic Grid Adaptation for RANS Simulation of a Fast Manoeuvring Catamaran,” Auckland, 2012.

[71] J. Wackers, G. Deng, E. Guilmineau, A. Leroyer, P. Queutey, M. Visonneau, A. Palmieri and A. Liverani, “Can Adaptive Grid Refinement Produce Grid-Independent Solutions for Incompressible Flows?,” Journal of Computational Physics, 2017.

[72] Wikipedia, “Fast Fourier transform,” [Online]. Available: https://en.wikipedia.org/wiki/Fast_Fourier_transform. [Accessed 2018].

[73] S. Sutulo and C. G. Soares, “Contribution of Higher-Order Harmonics for Estimating Manoeuvring Derivatives from Oscillatory Tests,” International Shipbuilding Progress, Lisbon, 2007.

[74] M. S. Fadali and A. Visioli, “Digital Control Engineering,” ELSEVER, Oxford, 2013.

[75] N. W. Teeuwen , “On the Determination of the Hydrodynamic Coefficients for Real Time Ship Manoeuvring Simulaiton,” Delft University of Technology, Delft, 2018.

[76] C. B. Barrass and D. R. Derrett, Ship Stability for Masters and Mates, Oxford: Elsevier, Ltd., 2006.

[77] T. Perez, A. Ross and T. I. Fossen, “A 4-DOF Simulink Model of a Coastal Patrol Vessel for Manoeuvring in Waves,” Norges Teknisk-Naturvitenskapelige Universitet (NTNU), Trondheim, 2006.

[78] C. A. Hindmarsh, “ODEPACK, A Systematized Collection of ODE Solvers,” Scientific Computing, Amsterdam, 1982.

[79] X.-g. Wang, Z.-j. Zou, Z.-l. Yang and F. Xu, “Sensitivity Analysis of teh Hydrodynamic Coefficients in 4 Degrees of Freedom Ship Manoeuvring Mathematical Model,” Journal of Shanghai Jiaotong University, Shanghai, 2015.

[80] M. Visonneau and G. Deng, “On the Predictoin of Swirling Induced Recirculatoin,” 3rd International Symposium on Turbulence and Shear Flow Phenomena, Sendai, 2003.

[81] S. Tavakoli, S. Mancini and A. Dashtimanesh, “A theoretical method to explore influence of free roll motion on behavior of a high speed planing vessel through steady yawed motion,” 2017.

APPENDIX

A.1 *RPA8* EXPERIMENTAL RESULTS

Table 11.1: Results from model scale tests, after extrapolation to full-scale, *[61]*. 3°-3° Zig-Zag, 6.11 [m/s] initial speed.

Side	Characteristic	Result
PS	1st Overshoot	0.6°
	2nd Overshoot	0.7°
	3rd Overshoot	0.8°
	4th Overshoot	0.8°
SB	1st Overshoot	0.5°
	2nd Overshoot	0.9°
	3rd Overshoot	0.8°
	4th Overshoot	0.9°

Table 11.2 Sea trials results, turning circle, 9.42 [m/s] initial speed, rudder deflection 35° .

Side	Characteristic	Result
PS	Advance	86 m
	Transfer	53 m
	Tactical Diameter	101 m
	Diameter	92 m
	Roll	4°
	Speed Drop	26%
SB	Advance	85 m
	Transfer	55 m
	Tactical Diameter	109 m
	Diameter	101 m
	Roll	-4°
	Speed Drop	28%

A.2 CFD SOLUTION VERIFICATION

A.2.1 Topology 1

A.2.1.1 Uncertainty Analysis

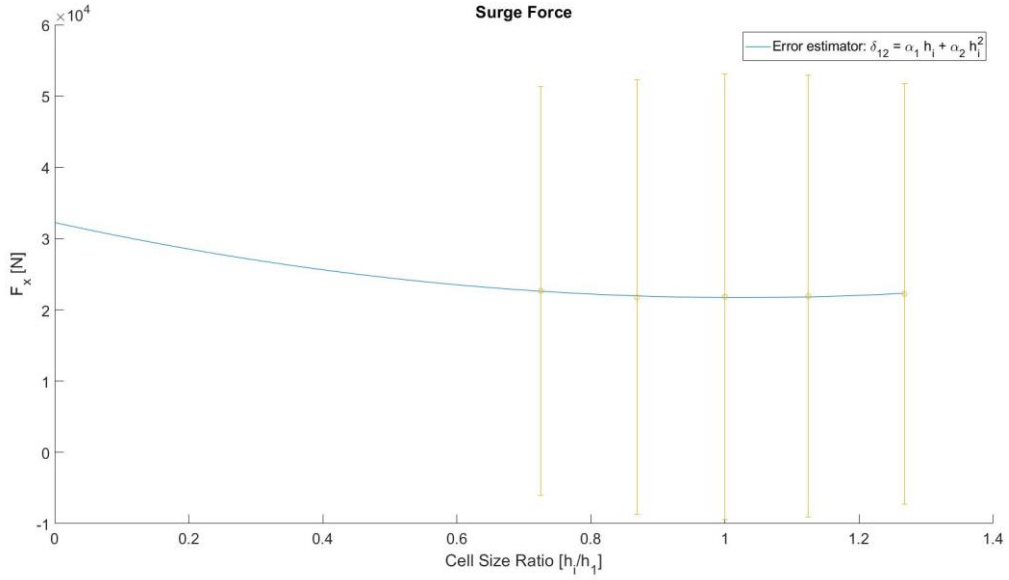

Figure 11.1: Surge force solutions with the respective uncertainties for each grid of topology 1.

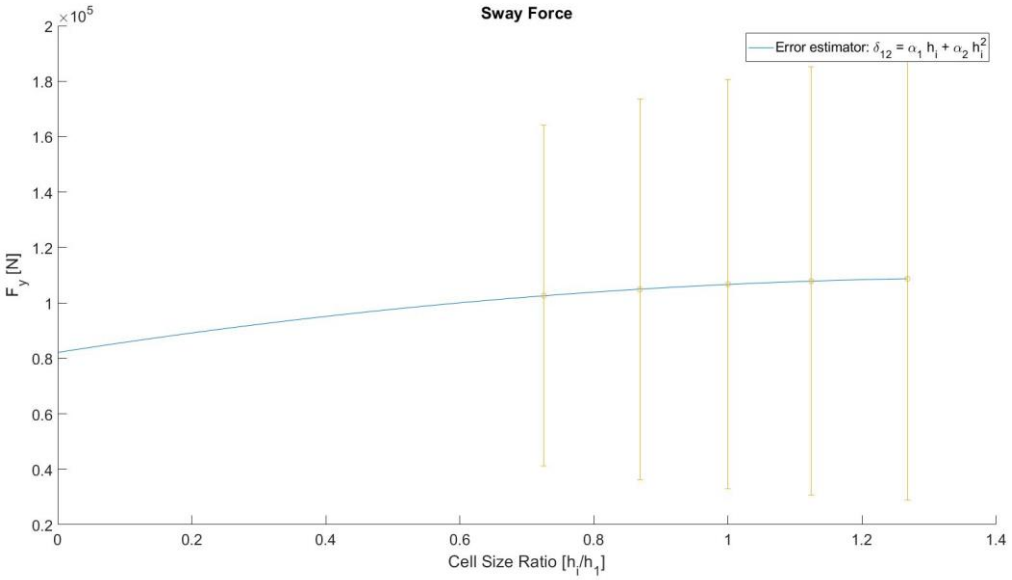

Figure 11.2: Sway force solutions with the respective uncertainties for each grid of topology 1.

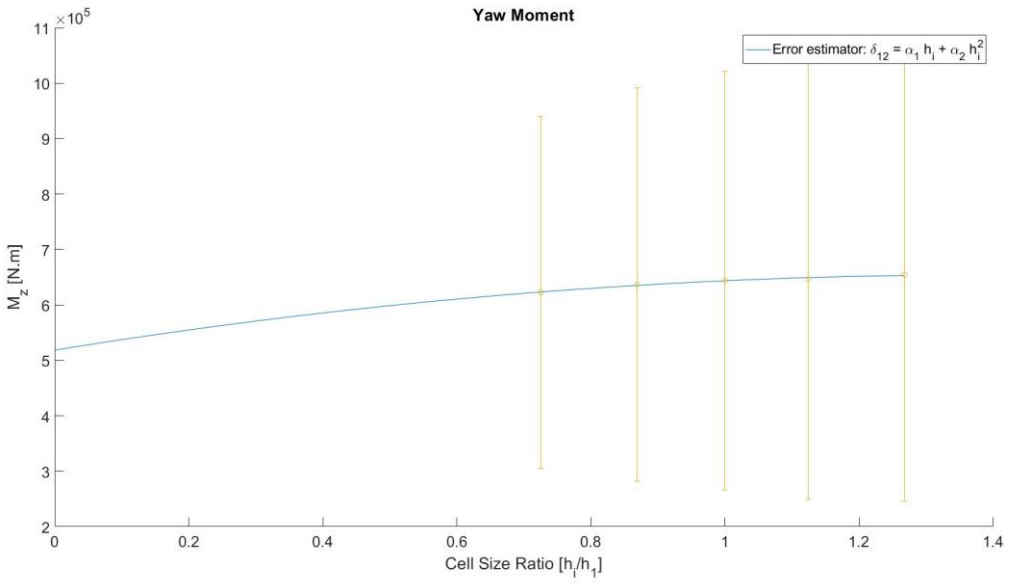

Figure 11.3: Yaw moment solutions with the respective uncertainties for each grid of topology 1.

A.2.1.2 Post-Process

The following figures show the hydrodynamic pressure distribution on the hull surface. The vortices correspond to iso-surfaces of Q=100 and they are coloured with the magnitude of the curl of the velocity field (blue-close to 0 [1/s], red close to 75 [1/s]).

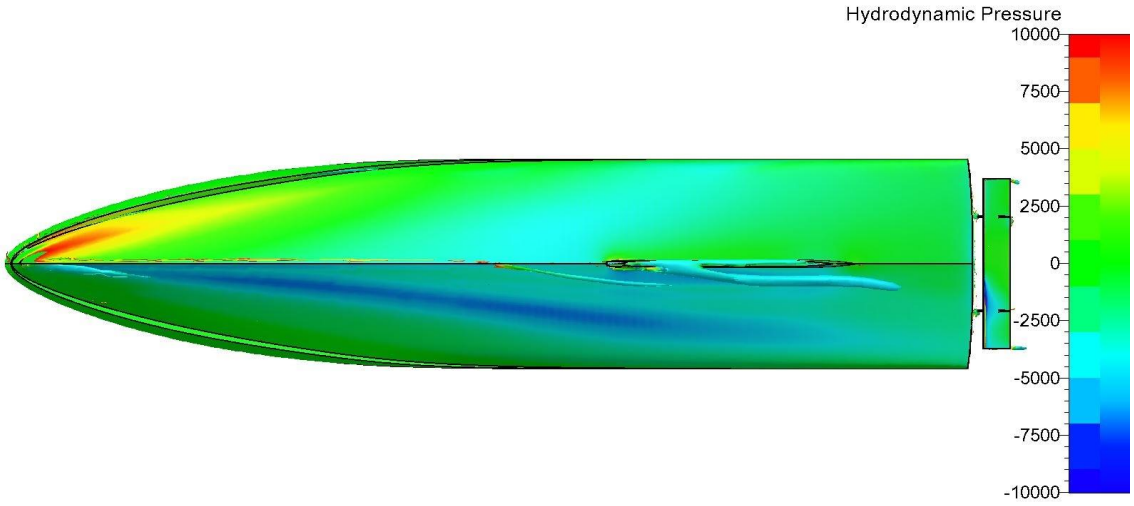

Figure 11.4: Mesh G0.5, topology 1.

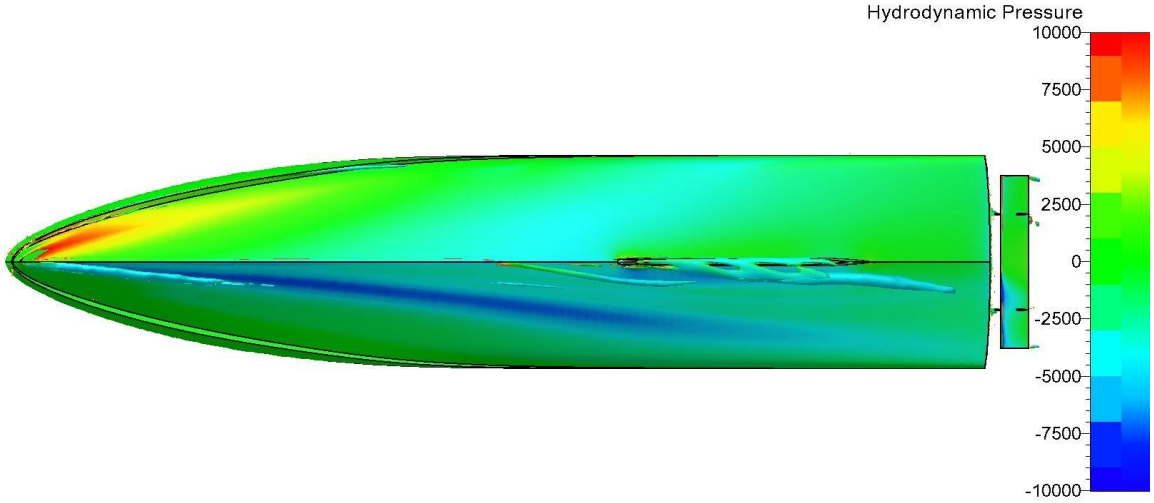

Figure 11.5: Mesh G0.75, topology 1.

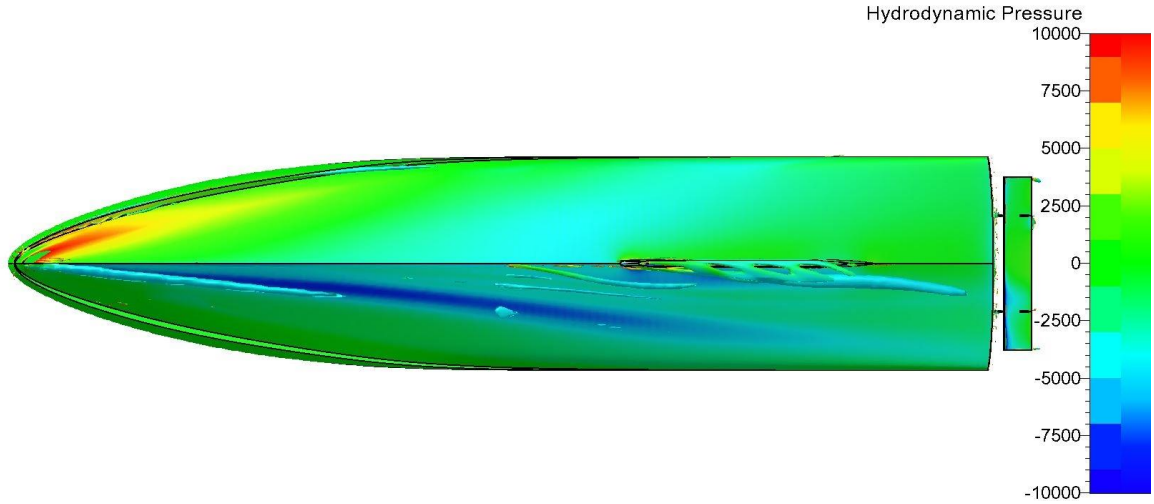

Figure 11.6: Mesh G1, topology 1.

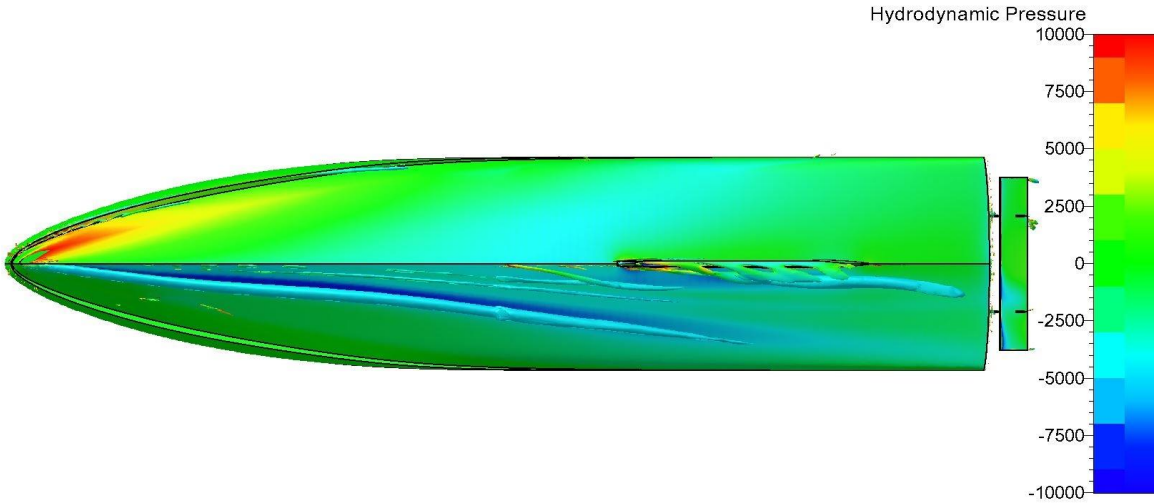

Figure 11.7: Mesh G1.5, topology 1.

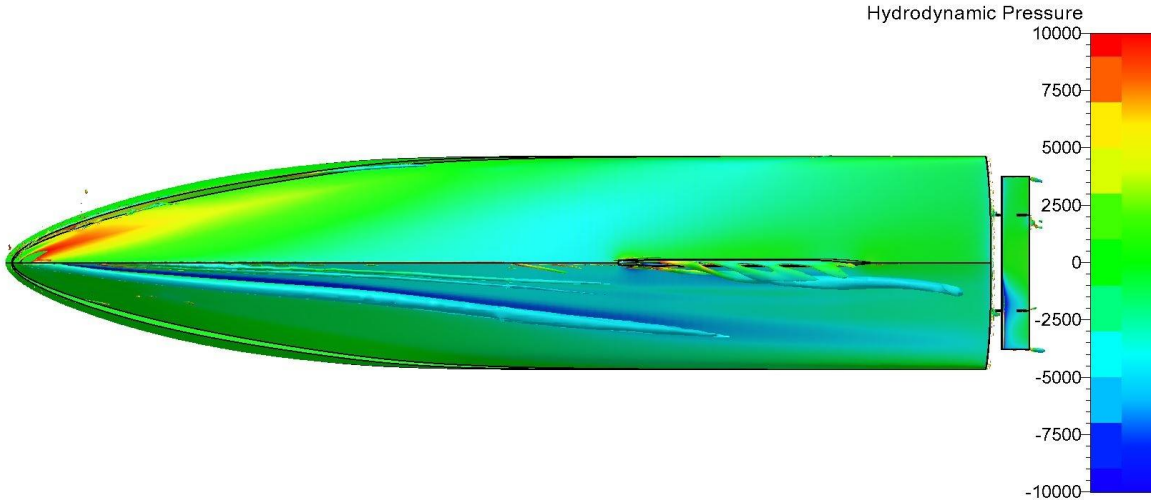

Figure 11.8: Mesh G2.75, topology 1.

Table 11.3: Error of each grid relative to G1, for surge force, sway force and yaw moment.

Forces	F_x_Hull_PS	F_x_Hull_SB	F_y_Hull_PS	F_y_Hull_SB	M_z_Hull_PS	M_z_Hull_SB
G0.5	-2.4%	-16.1%	-0.2%	-4.9%	-1.7%	-7.1%
G0.75	0.5%	2.0%	0.4%	-0.7%	0.2%	-0.3%
G1	**0.0%**	**0.0%**	**0.0%**	**0.0%**	**0.0%**	**0.0%**
G1.5	-0.5%	0.0%	-0.4%	0.7%	-0.1%	1.1%
G2.75	0.1%	23.6%	0.0%	1.4%	-1.0%	0.5%
Abs. Average	**0.7%**	**8.3%**	**0.2%**	**1.5%**	**0.6%**	**1.8%**

A.2.2 Topology 2

A.2.2.1 Uncertainty Analysis

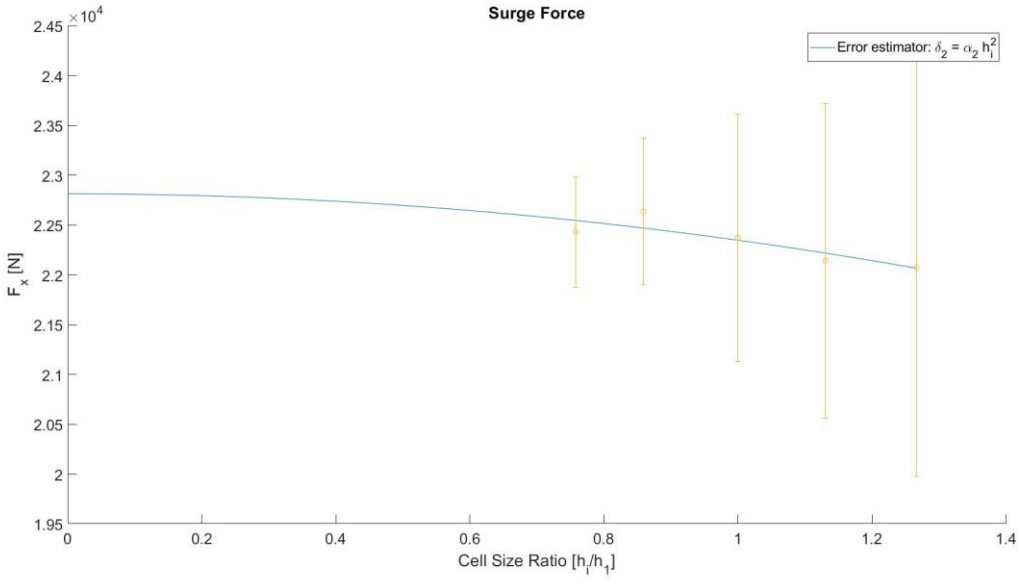

Figure 11.9: Surge force solutions with the respective uncertainties for each grid of topology 2.

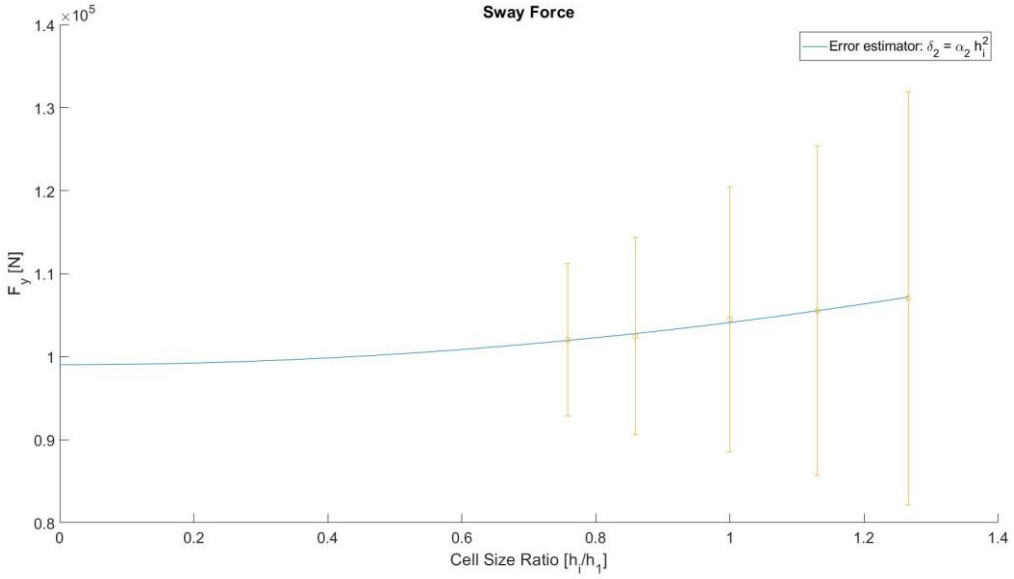

Figure 11.10: Sway force solutions with the respective uncertainties for each grid of topology 2.

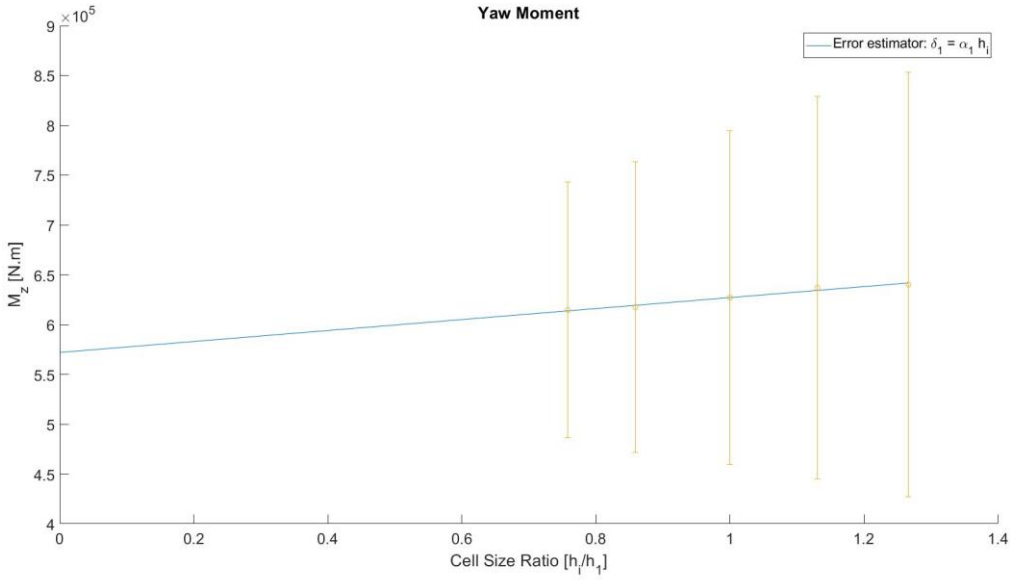

Figure 11.11: Yaw moment solutions with the respective uncertainties for each grid of topology 2.

A.2.2.2 Post-Process

The following figures show the hydrodynamic pressure distribution on the hull surface. The vortices correspond to iso-surfaces of Q=100 and they are coloured with the magnitude of the curl of the velocity field (blue-close to 0 [1/s], red close to 75 [1/s]).

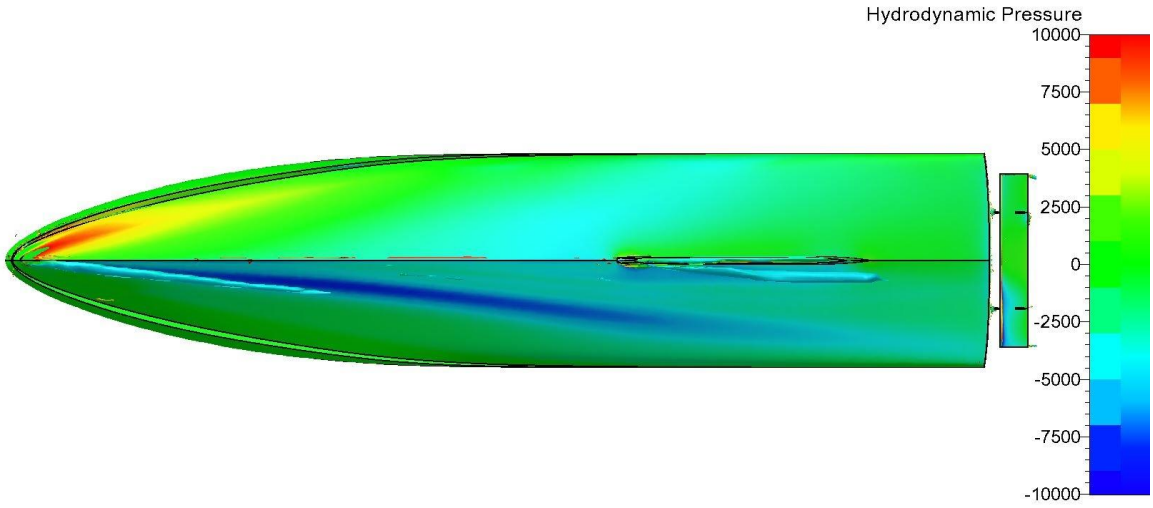

Figure 11.12: Mesh G0.5, topology 2.

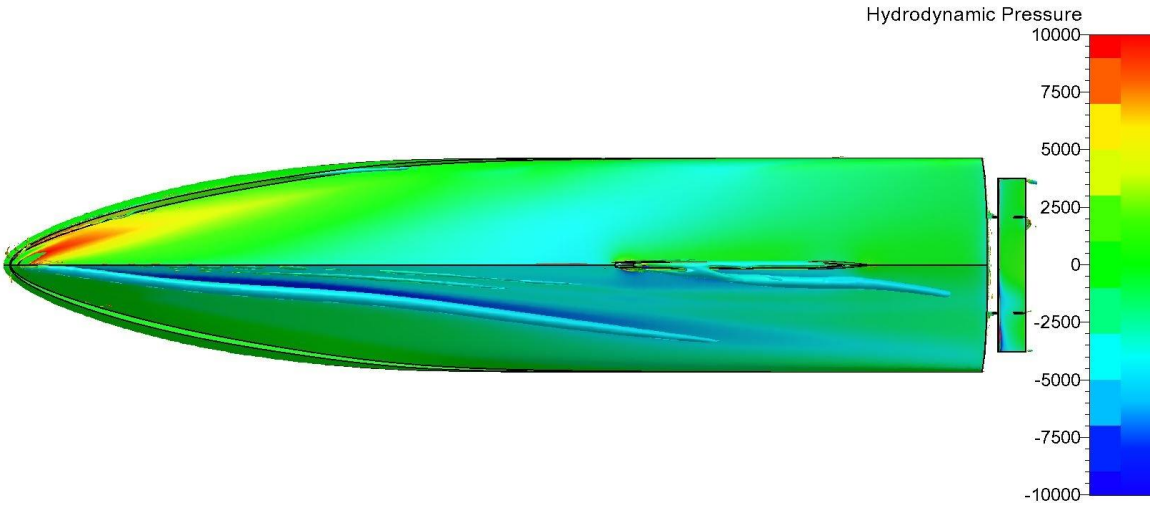

Figure 11.13: Mesh G0.75, topology 2.

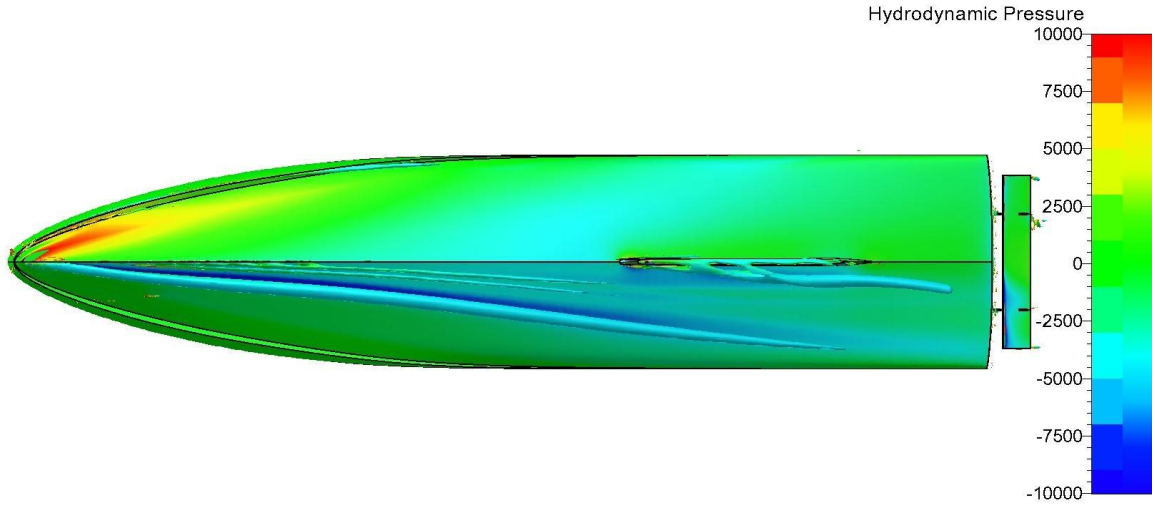

Figure 11.14: Mesh G1, topology 2.

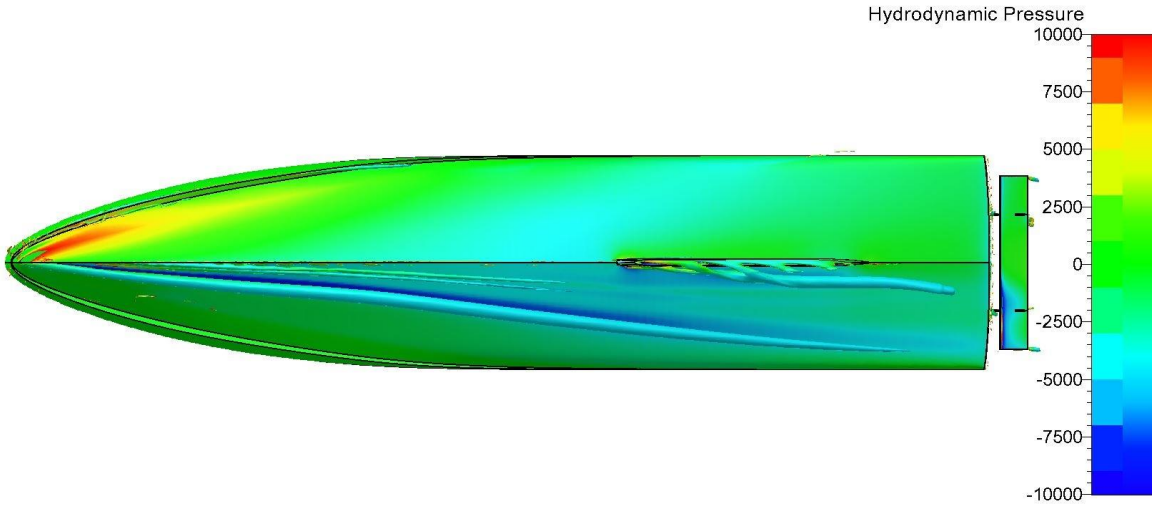

Figure 11.15: Mesh G1.5, topology 2.

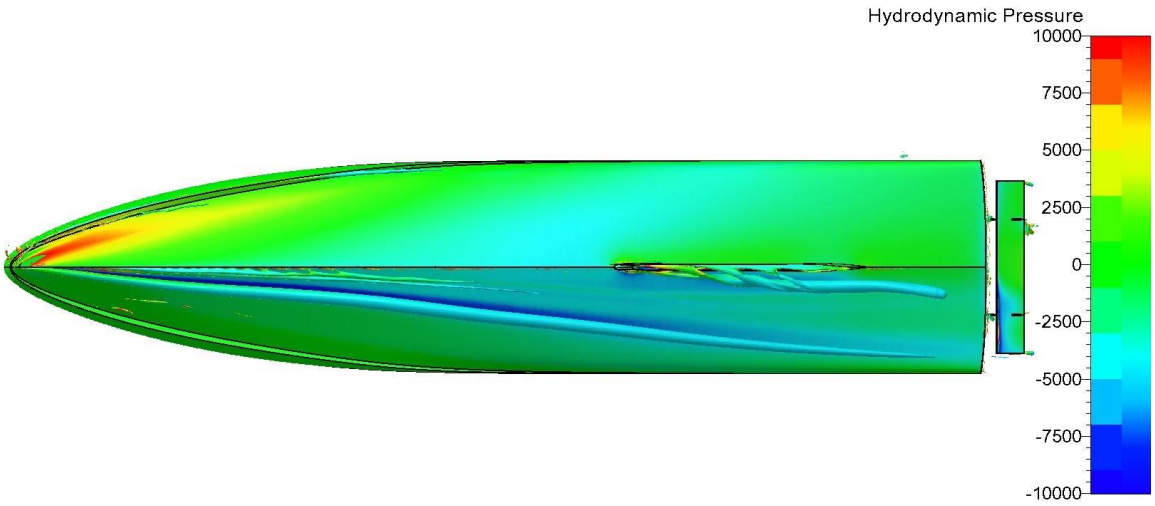

Figure 11.16: Mesh G2, topology 2.

A.3 DISCRETE SPECTRAL METHOD-VALIDATION

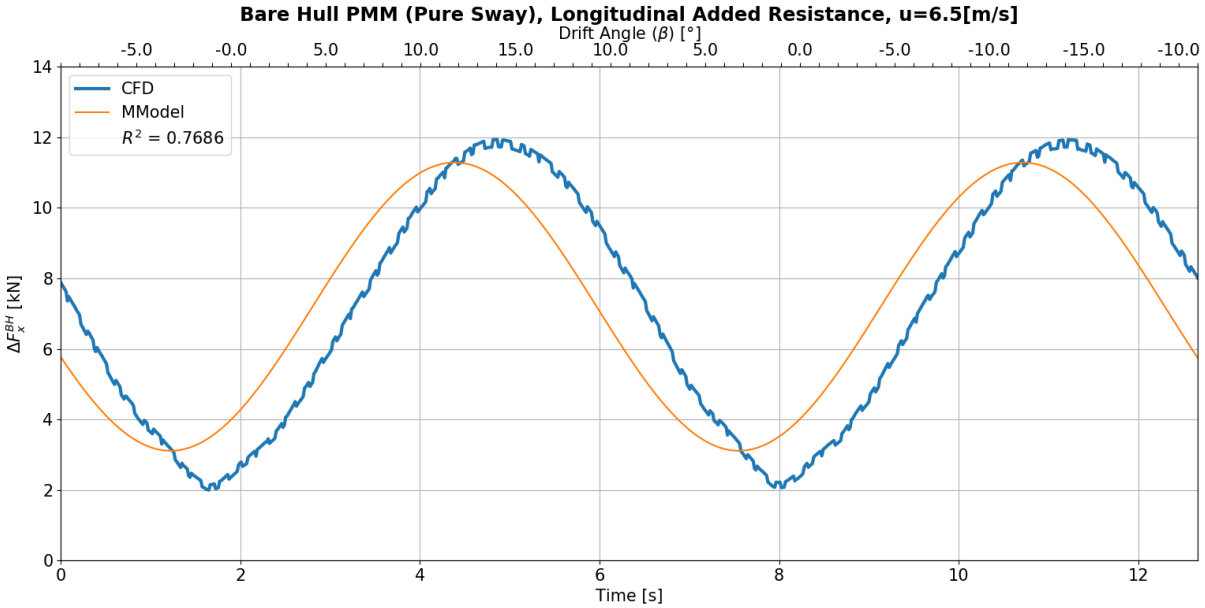

Figure 11.17: Bare hull longitudinal added resistance due to sway motion: CFD vs Mathematical model.

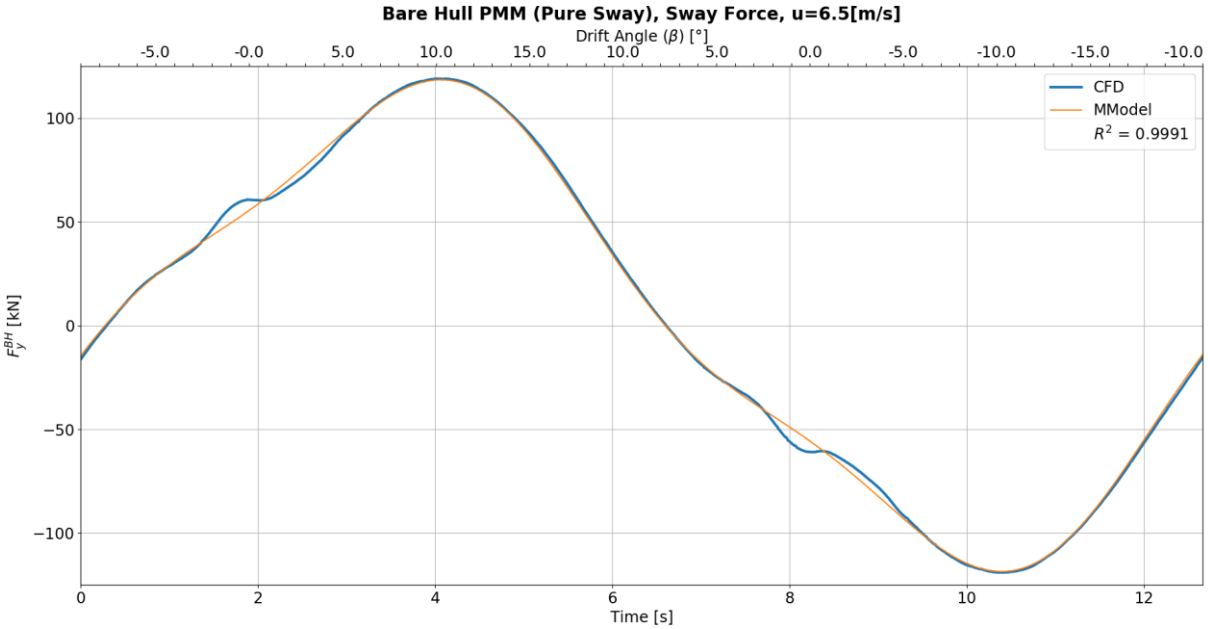

Figure 11.18: Bare hull sway force due to sway motion: CFD vs Mathematical model.

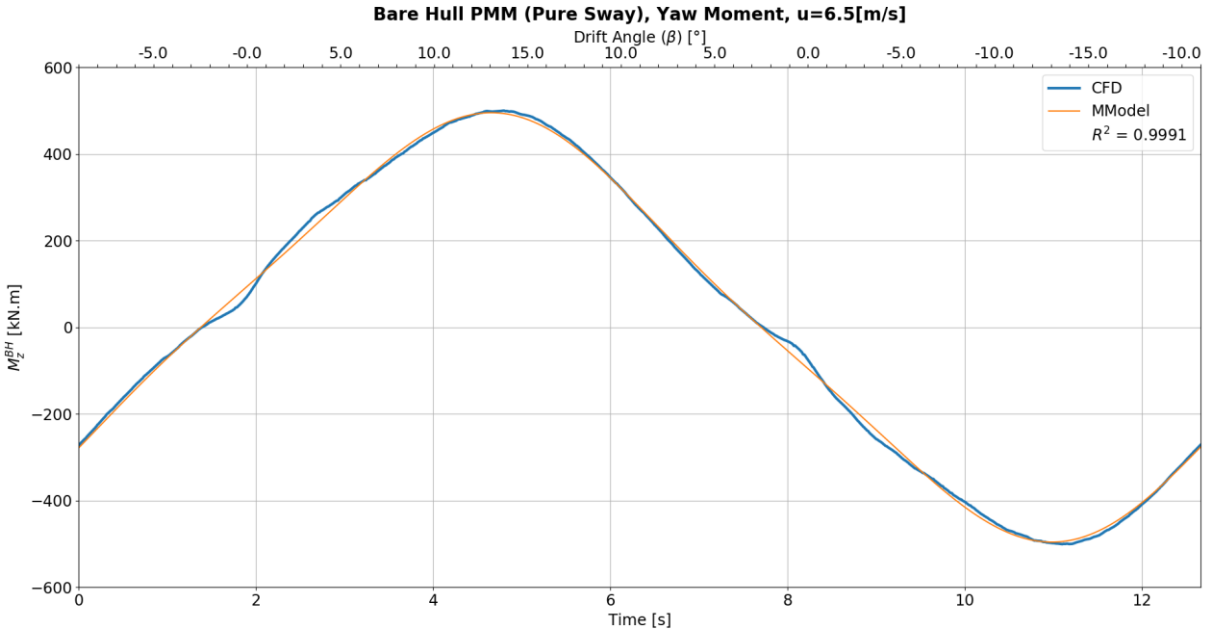

Figure 11.19: Bare hull yaw moment due to sway motion: CFD vs Mathematical model.

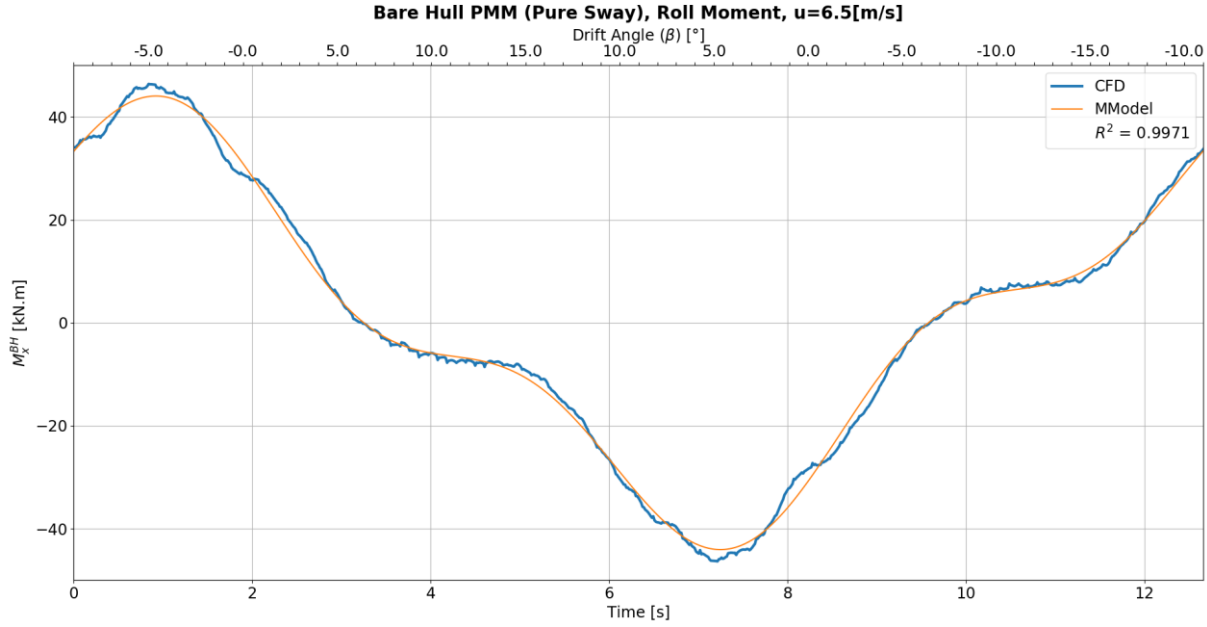

Figure 11.20: Bare hull roll moment due to sway motion: CFD vs Mathematical model.

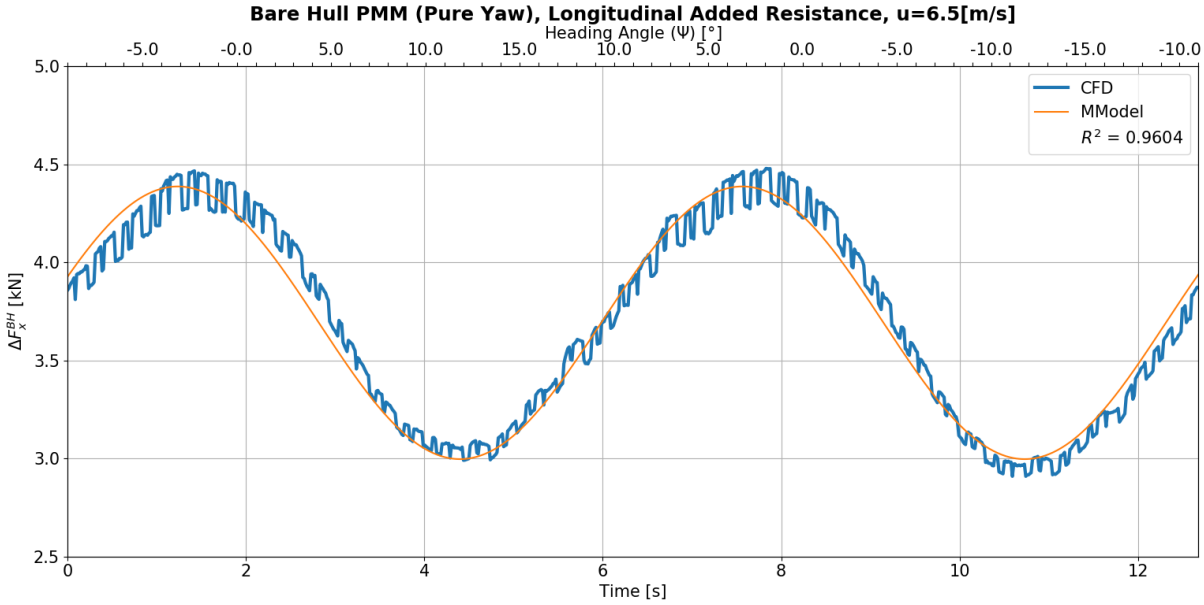

Figure 11.21: Bare hull longitudinal added resistance due to yaw motion: CFD vs Mathematical model.

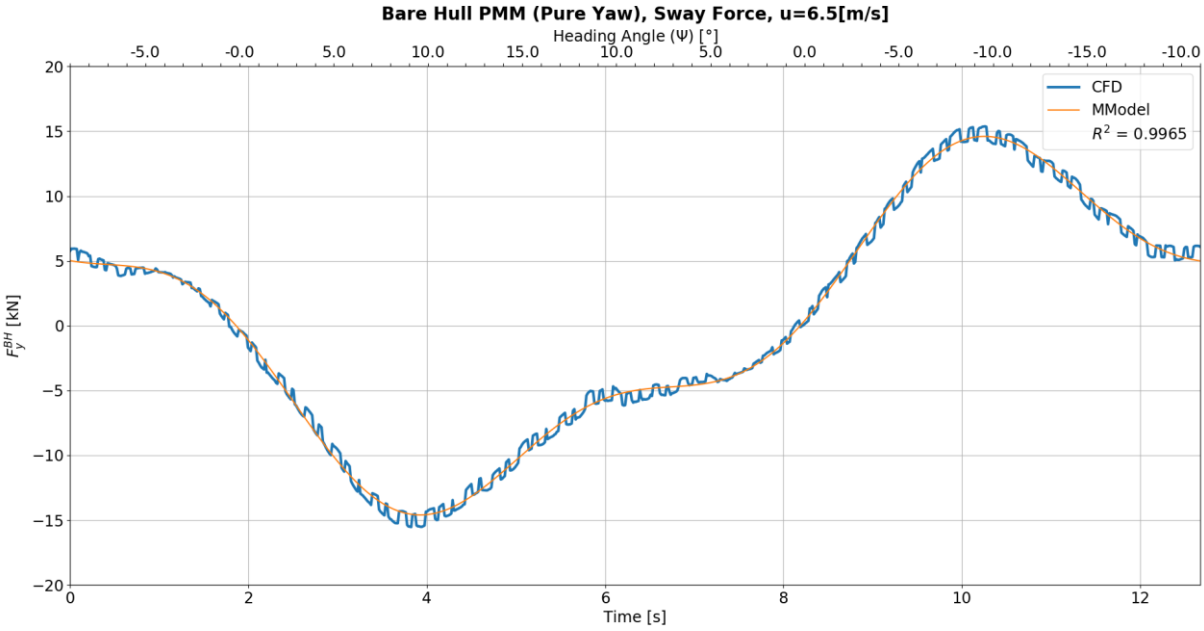

Figure 11.22.: Bare hull sway force due to yaw motion: CFD vs Mathematical model.

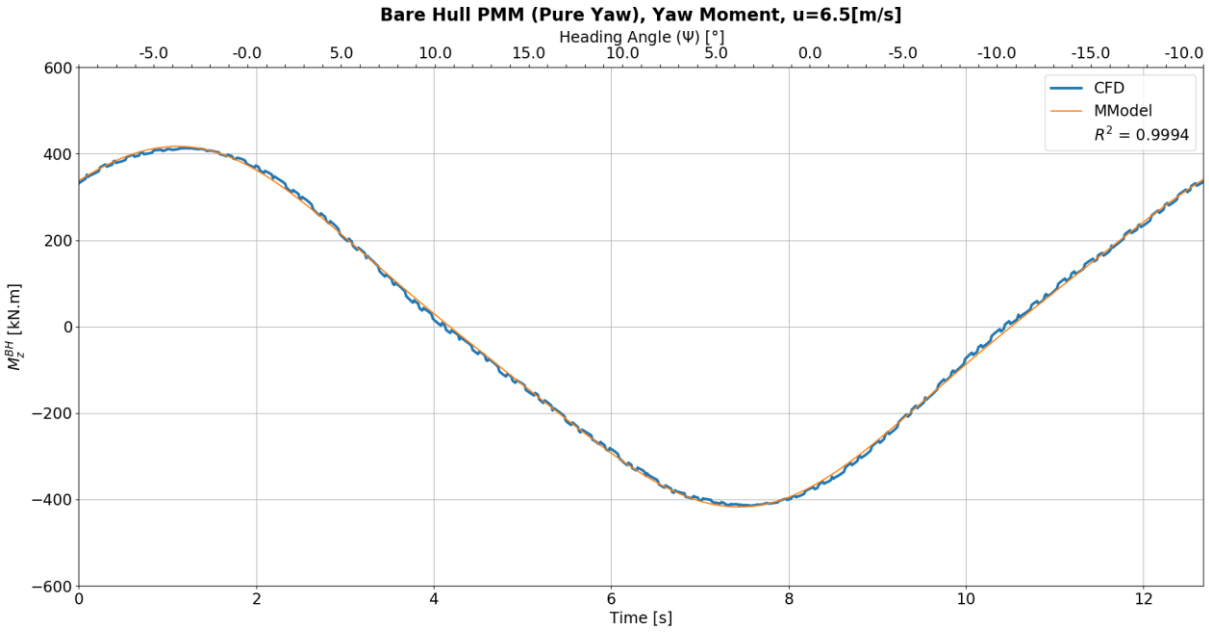

Figure 11.23: Bare hull yaw moment due to yaw motion: CFD vs Mathematical model.

A.4 HYDRODYNAMIC COEFFICIENTS

A.4.1 Bare Hull

Table 11.4: Bare Hull hydrodynamic coefficients. The hydrodynamic coefficients are non-dimensionalized considering $V = 6.5\ [m/s]$, $L = 25\ [m]$ and $\rho = 1025\ [kg/m^3]$.

Coefficients	Non-Dimensional Value	Origin
$X'_{\dot{u}}$	-3.6789×10^{-4}	*Tristan et al.*, [77]
X'_{u}	1.2823×10^{-4}	Straight ahead *CFD* runs
X'_{uu}	-1.6113×10^{-3}	
X'_{vv}	-8.051×10^{-3}	*OTT*
$X'_{\dot{v}\dot{v}}$	-8.7921×10^{-4}	*PMM pure-sway*
X'_{rr}	-1.2882×10^{-5}	*PMM pure-yaw*
$X'_{\dot{r}\dot{r}}$	-2.4282×10^{-4}	
$Y'_{\dot{v}}$	-5.2159×10^{-3}	*PMM pure-sway*
Y'_{v}	-1.3061×10^{-2}	*OTT*
Y'_{vvv}	-2.3193×10^{-1}	*OTT*
Y'_{r}	5.6623×10^{-4}	*PMM pure-yaw*
Y'_{rrr}	-6.8338×10^{-3}	
$Y'_{\dot{r}}$	-5.3972×10^{-4}	
$Y'_{\dot{r}\dot{r}\dot{r}}$	-5.6162×10^{-4}	
$N'_{\dot{r}}$	-1.1265×10^{-4}	*PMM pure-yaw*
N'_{r}	-1.9562×10^{-3}	
N'_{rrr}	-2.0145×10^{-3}	
$N'_{\dot{v}}$	5.6888×10^{-4}	*PMM pure-sway*
$N'_{\dot{v}\dot{v}\dot{v}}$	-2.2936×10^{-2}	
N'_{v}	-4.5876×10^{-3}	*OTT*
N'_{vvv}	-2.3264×10^{-2}	
$K'_{\dot{p}}$	-3.9561×10^{-6}	*Tristan et al.*, [77]
K'_{p}	-5.5071×10^{-4}	
$K'_{\dot{v}}$	-3.0196×10^{-5}	*PMM pure-sway*
$K'_{\dot{v}\dot{v}\dot{v}}$	-1.2227×10^{-2}	
K'_{v}	3.8653×10^{-4}	*OTT*
K'_{vvv}	1.6486×10^{-3}	
K'_{vvvvv}	-1.6276×10^{-1}	

A.4.2 Hull with Hull Vane – Integrated Approach

Table 11.5: Hull (with Hull Vane) hydrodynamic coefficients. Hull Vane integrated approach. The hydrodynamic coefficients are non-dimensionalized considering a speed of 6.5 $[m/s]$, 25 $[m]$ length and $\rho = 1025$ $[kg/m^3]$.

Coefficients	Non-Dimensional Value	Origin
$X'_{\dot{u}}$	-3.6789×10^{-4}	*Tristan et al.,* [77]
X'_{u}	9.8928×10^{-5}	Straight ahead *CFD* runs
X'_{uu}	-1.1589×10^{-3}	
X'_{vv}	-1.1698×10^{-2}	*OTT*
$X'_{\dot{v}\dot{v}}$	-1.7765×10^{-3}	*PMM pure-sway*
X'_{rr}	-1.8717×10^{-5}	*PMM pure-yaw*
$X'_{\dot{r}\dot{r}}$	-3.7497×10^{-4}	
$Y'_{\dot{v}}$	-5.4374×10^{-3}	*PMM pure-sway*
Y'_{v}	-8.7222×10^{-3}	*OTT*
Y'_{vvv}	-3.5161×10^{-1}	*OTT*
Y'_{r}	5.6623×10^{-4}	*PMM pure-yaw*
Y'_{rrr}	-1.3354×10^{-2}	
$Y'_{\dot{r}}$	-6.2102×10^{-4}	
$Y'_{\dot{r}\dot{r}\dot{r}}$	-3.1696×10^{-3}	
$N'_{\dot{r}}$	-1.6020×10^{-4}	*PMM pure-yaw*
N'_{r}	-1.9145×10^{-3}	
N'_{rrr}	-2.2797×10^{-3}	
$N'_{\dot{v}}$	4.2341×10^{-4}	*PMM pure-sway*
$N'_{\dot{v}\dot{v}\dot{v}}$	-4.2544×10^{-2}	
N'_{v}	-3.6457×10^{-3}	*OTT*
N'_{vvv}	-4.8268×10^{-2}	
$K'_{\dot{p}}$	-3.9561×10^{-6}	*Tristan et al.,* [77]
K'_{p}	-5.5071×10^{-4}	
$K'_{\dot{v}}$	-3.1299×10^{-5}	*PMM pure-sway*
$K'_{\dot{v}\dot{v}\dot{v}}$	-2.1736×10^{-2}	
K'_{v}	5.7765×10^{-4}	*OTT*
K'_{vvv}	-9.2061×10^{-3}	
K'_{vvvvv}	-3.2192×10^{-1}	

A.4.3 Interaction Coefficients

Table 11.6: Summary of the interaction coefficients derived in *Chapter 5*

Coefficients	Expression/Value	Section
$w_{out} \times 10^5$	$-9.279\beta_p^3 + 271.31\beta_p^2 - 624.86\beta_p + 2713.9$	5.1
$w_{in} \times 10^5$	$12.828\beta_p^3 - 237.24\beta_p^2 + 1072.1\beta_p + 2813.5$	
t	0.04	5.2
$\gamma_R^{out}, \gamma_R^{in,1}, \gamma_R^{in,2}$	$1.578, 0.783, -0.072$	5.3
a_H, x_{RH}	$0.056, -7.963$	5.4
$\Gamma_s^0, \Gamma_s^1, \Gamma_s^2, \Gamma_s^3 \times 10^3$	$285.29, -1088.8, 53.646, -0.695$	5.6

visit & mail us:

Nude 46

6702 DM, Wageningen

The Netherlands

contact us:

T +31 (0) 317 451573

info@oossanen.nl

follow us:

www.oossanen.nl

@oossanen